ԵՐԵՎԱՆԻ ՊԵՏԱԿԱՆ ՀԱՄԱԼՍԱՐԱՆ

ՀԱՅԱՍՏԱՆԻ ՀԱՆՐԱՊԵՏՈՒԹՅԱՆ ԳԻՏՈՒԹՅՈՒՆՆԵՐԻ
ԱԶԳԱՅԻՆ ԱԿԱԴԵՄԻԱ

ԿԻՍԱՀԱՂՈՐԴՉԱՅԻՆ ՄԻԿՐՈ- ԵՎ ՆԱՆՈԷԼԵԿՏՐՈՆԻԿԱ

ՏԱՍՆԱՄԵԿԵՐՈՐԴ ՄԻՋԱԶԳԱՅԻՆ ԳԻՏԱԺՈՂՈՎԻ ՆՅՈՒԹԵՐ
ԵՐԵՎԱՆ, 23-25 ՀՈՒՆԻՍ

SEMICONDUCTOR MICRO- AND NANOELECTRONICS

PROCEEDINGS OF THE ELEVENTH INTERNATIONAL CONFERENCE
YEREVAN, ARMENIA, JUNE 23-25

Երևան

ԵՊՀ հրատարակչություն

2017

ՀՏԴ 621.3.049.77:620:06
ԳՄԴ 32.85+30.3
Կ 510

ICSMN ORGANIZING COMMITTEE

Տպագրվում է Երևանի պետական համալսարանի ռադիոֆիզիկայի ֆակուլտետի գիտական խորհրդի որոշմամբ:

Կ 510 **ԿԻՍԱՀԱՂՈՐԴՉԱՅԻՆ ՄԻԿՐՈ- ԵՎ ՆԱՆՈԷԼԵԿՏՐՈՆԻԿԱ ՏԱՍՆԱՄԵԿԵՐՈՐԴ ՄԻՋԱԶԳԱՅԻՆ ԳԻՏԱԺՈՂՈՎԻ ՆՅՈՒԹԵՐ ԵՐԵՎԱՆ, 23-25 ՀՈՒՆԻՍԻ**. – Եր.: ԵՊՀ հրատ., 2017. - 207 էջ:

Ժողովածուի մեջ զետեղված են 2017 թ. հունիսի 23-25-ը Երևանում անցկացված «Կիսահաղորդչային միկրո- և նանոէլեկտրոնիկա» գիտաժողովում զեկուցված նյութերը: Աշխատանքները խմբավորված են ըստ հետևյալ բաժինների.

1. Ֆիզիկական երևույթները միկրո- և նանոկառուցվածքներում,
2. Գազային և կենսաքիմիական սենսորներ,
3. Նյութագիտություն և ճարտարագիտություն,
4. Ինտեգրալ սխեմաների մշակում և մոդելավորում:

Ժողովածուն տպագրության է պատրաստվել փորձագիտական և խմբագրական հանձնախմբի կողմից:

ՀՏԴ 621.3.049.77:620:06
ԳՄԴ 32.85+30.3

ISBN 978-5-8084-2197-4

After independence, since 1991 Armenian scientists carry out intensive investigations in the field of physics and technology of semiconductors, semiconductor micro- and nanosize devices and nanotechnologies. Since 1997, we have been constantly holding conferences devoted to the problems of semiconductor micro- and nanoelectronics. Over the past 20 years, our conference has acquired international significance. Over the years new important and interesting results in the field of micro- and nano-electronics are obtained. Many investigations of Armenian scientists made in co-authorship with colleagues from various countries. Important results were obtained in the last few years in Armenia when studying phenomena in physical and chemical sensors for various purposes, IR and UV photodetectors and solar cells, transistor-like nanostructures, large ICs, in the field of low-dimensional effects, low-frequency noises, noise spectroscopy, etc. The geography of our Conference is expanding. We hope that the conference will take place in a favorable and scientific atmosphere, where new scientific ideas and results will be presented and discussed, which can form the basis for new joint projects.

The Organizing Committee wishes the conference participants useful work, fruitful discussions, interesting polemics, the genesis of new ideas and concepts!

The Organizing Committee is grateful for the State Committee of the Ministry of Education and Science of Armenia, the "Barva" Innovation Center and CJSC "Synopsys" for financial support.

ICSMN ORGANIZING COMMITTEE

PHYSICAL PHENOMENA IN MICRO- & NANOSTRUCTURES

PHOTOELECTRICAL PROPERTIES OF SEMICONDUCTOR NANOWIRES

S.G. Petrosyan

Russian-Armenian (Slavonic) University, H. Emin str. 123, Yerevan, 0051, Armenia
Institute of Radiophysics and Electronics, NAS RA, Alikhanyan Brs. Str.1, Ashtarak, 0203, Armenia
E-mail: stepan.petrosyan@rau.am

1. Introduction

Recently a great number of experimental works has been reported to fabrication, synthesis and characterization of semiconductor nanowires (NW) in different material systems. Among other nanostructures, semiconductor NWs with a diameter of several hundred *nm* and aspect ratios as high as 10^2, even without quantum size effects, offer exciting possibilities as building blocks for nanoelectronics, optoelectronics, biological and chemical sensors. In addition, the possibility to integrate functionality in NW structure, such as radial or axial homo- a heterojunctions within single NW device or NW arrays, enables large scale integration. Due to the exchange of electrons between the surface and extension of the order of the NW diameter or even inversion effects, which can strongly influence the electric and photoelectric characteristics of NWs and NWs based devices.

Here several aspects of nanowire electronic and photolectrical properties will be presented.

2. Critical Radius of full depletion in Semiconductor Nanowires

Control of the depletion layer thickness is important for the operation of NW devices as photoconductive optical detectors, solar cells and field-effect transistors. To better understand these effects the solution of Poisson`s equation must be carried out in order to provide a comprehensive model of NW surface depletion as a function of surface (or interface) state density and their energetic distribution, NW radius and doping level. We presented a simple analytical model for estimating critical radius of full depletion in semiconductor nanowires due to charge carrier trapping at surface states and resulting radial band bending. The model describes the critical radius functional dependences on doping level, surface states parameters and appears as a very useful tool to understand nanowires transport properties limited particularly by surface effects.

3. Conductivity type switching in Nanowires

Due to high surface-to-volume ratio surface states (traps) play an important role in nonequilibrium properties of semiconductor nanowires and nanowire based devices. Recently it was experimentally demonstrated that surface traps effect even can induce conductivity type inversion in semiconductor NWs. We have performed detailed theoretical analyzes of the influence of charge trapping by surface states on semiconductor nanowire conductivity. Different semiconductor materials and surface traps densities have been considered. The effect of surface traps was analyzed in case of low-doped as well as for highly doped semiconductor nanowires. The Poisson equation with consideration of both type of mobile charges and acceptor like surface sates was solved for different radii and doping level. It was shown that for small radii the conductivity type can be switched from n- to p- type. The accuracy of analytical calculations has been validated with numerical data and as well as the results have been qualitatively compared with published experimental data.

4. Photoconductivity of Semiconductor Nanowires

One of the most studied phenomena in nanowires is their high sensitivity to light, which is emerging as a very promising NW application for photo detectors, photovoltaics, optical switches, optical interconnect and solar cells. NW based photo detectors can yield higher light

sensitivity than their bulk or thin film counterparts due to the large surface-to volume ratio and small dimensions comparable to the carrier diffusion length .

We developed an analytical theory for the photoconductivity (PC) of semiconductor nanowires (NWs). The model takes into account the enhanced role of surface recombination in the lifetime of nonequilibrium carriers in NW due to large surface-to-volume ratio. The main peculiarities of the NW PC are governed by radius and time dependent recombination barrier, which varies in time with interplay between the NW quasi-neutral core radius and the space charge layer thickness near the surface. Assuming acceptor-like-traps located on the surface of NW we find the relationship between the thickness of space-charge region and nonequilibrium surface charge density in NW and thus calculate the size-dependent PC. Time variation of surface band bending in the course of carrier capture by surface states leads to a non-exponential character of transient PC. The instantaneous relaxation time grows with time after turning of the illumination and it can become so large that persistent PC can be observed even at room temperatures. The results are in good agreement with available experimental data.

5. Single Nanowire solar cells

Radial p–n junction solar cells have been theoretically predicted to have better efficiency than their planar counterparts due to decrease in the distance required to collect minority carriers compared to carrier diffusion length. This advantage is also significantly enhanced when the diffusion length is much smaller than the absorption length. The NW based solar cell has several advantages over conventional planar analogues, in particular associated with the fact that the collection and the generation of charge carriers takes place in mutually perpendicular directions. We have studied silicon single core/shell NW with radial p-n junction under the illumination taken as blackbody radiation at 5800°K temperature. It was found that low open circuit voltages experimentally often observed for such solar cells can be caused by large surface recombination at the NW sidewall the role of which is increased as the diameters become smaller and the ratio of NW surface to volume is increased. Optimization of nanowire geometry and proper choice of doping densities are mandatory to improve the cell efficiency. The developed model gives good understanding for designer to choose the optimal geometrical parameters for a single NW to get the satisfactory values of photocurrent, open-circuit voltage and cell efficiency.

ON THE THEORY OF INTRAVALLEY RAMAN SCATTERING IN INTRINSIC GRAPHENE

S.V. Melkonyan

Yerevan State University, Yerevan, Armenia, E-mail: smelkonyan@ysu.am

Introduction

Raman spectroscopy is one of the effective tools for accurate structural characterization of materials, for investigating phonon spectra, electron-phonon and phonon-phonon interactions in crystalline structures. Basic parameters of Raman spectrum are Raman line frequencies (Raman lines positions), Raman line widths and intensities of Raman peaks' (or bands). Graphite and graphene (single-layer, bilayer, few-layer and multilayer) Raman spectra are measured and widely discussed in mass of publications (see, e.g. [1 - 5]). The actual measurements are usually carried out by using a laser in the visible region with different excitation energies (wave numbers), for example, $E_l = 1.58$ eV ($q_l = 0.8\times10^5$ cm^{-1}), $E_l = 1.96$ eV ($q_l = 1\times10^5$ cm^{-1}), $E_l = 2.41$ eV ($q_l = 1.2\times10^5$ cm^{-1}) cm^{-1}, respectively. Main intensive Raman peaks of graphite and graphene are the so-called D (~ 1360 cm^{-1}), D' (~ 1620 cm^{-1}), G (~ 1560 ÷ 1580 cm^{-1}) and G' (or 2D) (~ 2690 ÷ 2700 cm^{-1}) bands. As it is well-known Raman spectrum is directly related to crystalline lattice vibrations. Graphite and graphene phonon spectra are practically similar for the major part of Brillouin zone (see, e.g. [4 - 6]). iLO and iTO phonon branches are degenerate at the Γ point (Brillouin zone centre): $\omega_\Gamma^{iLO} = \omega_\Gamma^{iTO} \approx 1583$ cm^{-1}, and at the K point: $\omega_K^{iTO} \approx 1232$ cm^{-1}, $\omega_K^{iLO} \approx 1300$ cm^{-1} (detailed, see [4, 5]). Literature data analysis shows that physical mechanisms of Raman bands origin [1 - 5] require more detailed qualitative and quantitative discussion.

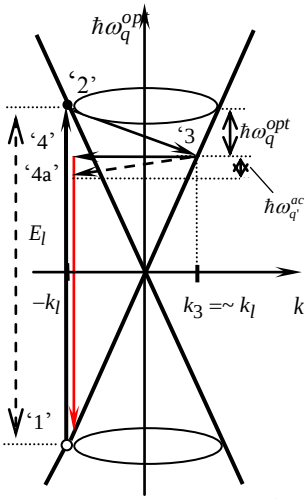

Fig.1. Graphical representation of double-resonant intravalley scattering scheme for the Raman D' peak for a single-layer graphene sample.

Theory

The task of the Raman peaks intensity is closely related to physical the mechanism of its origin. Here the Raman D' peak has been discussed mainly. D' peak is accepted to be interpreted via the mechanism of intravalley double-resonant Raman (DRR) scattering [1 - 4]. In the case of a single layer graphene with high concentration of lattice defects the process of DRR scattering is qualitatively shown in fig.1 in the form of '1'-'2'-'3'-'4'-'1' electron transitions. '1'-'2' and '2'-'3' are the resonant transitions (double resonant) and '3'-'4' transition is conditioned by electron-defect elastic scatterings.

It is of principal importance, to firstly analize the case of a defect-free single-layer graphene with intrinsic conductivity. For the high-quality (defect-free) graphene sample a physical model of intravalley DRR scattering is illustrated on the fig.1 as '1'-'2'-'3'-'4a'-'1' electron transitions. The microscopic interpretation of transitions is the following. The electron in the initial state '1' of valence π band is excited to the conduction π^* band state '2' by absorbing an incident photon with the energy $E_l = \hbar\omega_l$. After that, in the result of '2'-'3' intravalley scattering the electron

appears in the state ‘3’ emitting a photon with energy $\hbar\omega_{\mathbf{q}}$. The electron is then scattered back returning to the initial state ‘1’ through intermediate virtual state ‘4a’ (transition ‘3’-‘4a’-‘1’) by emitting a phonon with the enrgy $\hbar\omega_{q'}$ (transition ‘3’-‘4a’) and a photon with a much smaller energy $\hbar\omega_r = E_l - \hbar\omega_q - \hbar\omega_{q'}$ (transition ‘4a’-‘1’). The processes within a closed cycle where the electron performs the role of a mediator (catalyst), through which the photon-phonon interaction is realized.

DRR scattering involves two phonons at least one of which must be optical. The energy of the emitted (scattered) photon $\hbar\omega_r$ is determined by the sum $\hbar\omega_q^{opt} + \hbar\omega_{q'}^{ac}$ (or $\hbar\omega_q^{opt} + \hbar\omega_{q'}^{opt}$). Depending on the wave vector the phonon frequencies (energies) vary, for example, the frequencies of iLO optical and iLA acoustic modes in graphene first Brillouin zone varies within the ranges $\sim 1232 \div \sim 1583$ (cm^{-1}) and $0 \div \sim 1232$ (cm^{-1}), correspondingly [4, 5]. For the estimation of the possible numerical values of scattered photon energies $\hbar\omega_r$ it is necessary to base on the theory of intrinsic absorption of light by semiconductor taking into account the specificity of the two-phonon processes. According to intrinsic light absorption theory as a result of $\hbar\omega_l$ photon absorption an electron-hole quasi-particle pairs appear. However, for the real absorption of light it a disipative subsystem which will change the state of electron or hole is required, so that they will not be immediately annihilated (recombined) irradiating absorbed photons. In defect-free crystals such a disipative subsystem is the phonons of the lattice. But in the case of Raman scattering we deal with the opposite situation. Unlike real absorption of light, processes which bring to immediate annihilation of electron-hole pairs are responsible for Raman scattering.

According to quasi-particle method of probability calculation a two-phonon process of electron scattering is represented as two consecutive one-phonon transitions which can take place via real or virtual intermediate states. Probability of an electronic transition through a real intermediate state, as a rule, is much higher [8]. The only electron intravalley scattering is possible when the quasi-momentum transfer to the lattice is small. There are three types of two-phonon processes. If a pair of phonons, $\mathbf{q}$ and $\mathbf{q}'$ is emitted or absorbed, their wave vectors should be almost exactly opposite: $\mathbf{q} \approx -\mathbf{q}'$, if one phonon is absorbed and the other is emitted, their wave vectors should be almost equal: $\mathbf{q} \approx \mathbf{q}'$ [8]. Note, the phonons may belong to different regions of different branches.

These well-known features of the two-phonon processes allow assessing the $\hbar\omega_r$ energies of the scattered photon. So, near to the graphene allowed bands extremum (Dirac *K* points) the dispersion relation is linear,

$$E_k = \pm\hbar v_F |\mathbf{k}| = \pm\hbar v_F \sqrt{k_x^2 + k_y^2} \ ,$$

where v_F is the electron group (Fermi) velocity, $\mathbf{k}$ is the electron wave vector, (+) and (-) sings refer to conduction and valence bands, respectively. The magnitude of the wave vector $\mathbf{k}$ is measured from the Dirac *K* point. For ‘1’-‘2’ photo-transition owing to the energy and quasi-momentum conservation laws

$$v_F |\mathbf{k}'| = -v_F |\mathbf{k}| + c|\mathbf{q}_l| \ ,$$

$$\mathbf{k}' = \mathbf{k} + \mathbf{q}_l \ .$$

Here c is the light velocity, $\mathbf{q}_l$ is the light wave vector, $\mathbf{k}$, E_k and $\mathbf{k}'$, $E_{k'}$ is the electron wave vector and energy in the states '1' and '2', respectively.
Taking into account inequality $v_F << c$ from the conservation laws we obtain:

$$k = q_l c / 2v_F = E_l / 2\hbar v_F \equiv k_l .$$

Therefore, '1'-'2' photo-transition can be carried out by the electrons having quasi-momentun $\sim \hbar k_l$ (or energy $E_l / 2$). Note, the $\hbar k_l$ depends on the photon energy E_l via linear proportional law.

For '2'-'3' transition when an acoustic or optical phonon is emitted owing to conservation laws:

$$v_F|\mathbf{k}'| = v_F|\mathbf{k}| - \omega_q^{ac} , \qquad v_F|\mathbf{k}'| = v_F|\mathbf{k}| - \omega_q^{opt} , \tag{1.a-1.b}$$

$$\mathbf{k}' = \mathbf{k} - \mathbf{q} , \tag{2}$$

where $\mathbf{k}$ and $\mathbf{k}'$ are electron wave vectors in the states '2' and '3', respectively.

For the simplicity of calculations optical phonon dispersion can be ignored ($\omega_q^{opt} = \omega_0 = const$) and for acoustic phonons the linear dispersion law $\omega_q = v_{ac} q$ [4, 5, 7] is used, where v_{ac} is the velocity of longitudinal acoustic phonon. Taking into account inequality $v_{ac} / v_F << 1$ ($v_{ac}^{LA} \approx 2\times10^4$ m/s, $v_F \approx 10^6$ m/s [5, 7]), from equations (1.a) and (2) the well-known result is obtained: $0 \le q \le 2k$. Phonons with $q \approx 2k$ wave vectors provide effective change of electron quasi-momentum [8]. From equations (1.b) and (2) it follows that $k > k_0$, $\frac{k_0}{2} < k < k_0$ and $0 < k < k_0 / 2$ electrons interact with $k_0 < q < 2k - k_0$, $2k - k_0 < q < k_0$ and $k_0 - 2k < q < k_0$ optical phonons, respectively. Here $k_0 \equiv \omega_0 / v_F = 4.7 \cdot 10^5$ cm^{-1} is the electron characteristic wave number.

Taking into account inequality $k_0 / k_l = 2\hbar\omega_0 / E_l < 1$ it can be stated that DRR scattering involes acoustic and/or optical phonons whose wave numbers should be equal: $q \approx 2k_l$. Therefore, for the scattered photons one can have $\hbar\omega_r = \hbar\omega_{q=2k_l}^{ac} + \hbar\omega_{q=2k_l}^{opt}$ and $\hbar\omega_r = \hbar\omega_{q=2k_l}^{opt} + \hbar\omega_{q=2k_l}^{opt}$. From relation $q = 2k_l = E_l / \hbar v_F$ it follows that Raman peak position is determined by the phonon spectrum as well as by excitation laser energy $E_l = \hbar\omega_l$. Particularly, at excitation laser energy $E_l = 2.41$ eV one have $k_l = 2\times10^7$ cm^{-1}. As it follows from the experimental curves of phonon spectrum [4, 5], the phonon wave number $q = 2k_l = 4\times10^7$ cm^{-1} corresponds to $\omega_{q=2k_l}^{iLO} \approx 1620$ cm^{-1}, $\omega_{q=2k_l}^{iTO} \approx 1550$ cm^{-1}, $\omega_{q=2k_l}^{iLA} \approx 400$ cm^{-1} and $\omega_{q=2k_l}^{iTA} \approx 200$ cm^{-1} phonon frequencies. Phonons from the same as well as from different branches can participate in two-phonon processes. Therefore, according to DRR scattering mechanism in high-quality graphene sample, Raman peaks may be expected at following frequencies:

- related to optical and acoustic phonon branches:

$$\omega_{q=2k_l}^{iTO} + \omega_{q=2k_l}^{iTA} \ (1750 \text{ cm}^{-1}), \quad \omega_{q=2k_l}^{iLO} + \omega_{q=2k_l}^{iTA} \ (1820 \text{ cm}^{-1}),$$

$$\omega_{q=2k_l}^{iTO} + \omega_{q=2k_l}^{iLA} \ (1950 \text{ cm}^{-1}), \quad \omega_{q=2k_l}^{iLO} + \omega_{q=2k_l}^{iLA} \ (2020 \text{ cm}^{-1}), \tag{3a}$$

- related to the same optical branch:

$$2\omega^{iLO}_{q=2k_l} \ (3240\ \text{cm}^{-1}) \text{ ы } 2\omega^{iTO}_{q=2k_l} \ (3100\text{cm}^{-1}). \quad (3b)$$

If an acoustic phonon is not emitted, but absorbed at electron transition, one may have

$$\omega^{iTO}_{q=2k_l} - \omega^{iTA}_{q=2k_l} \ (1350\ \text{cm}^{-1}), \quad \omega^{iLO}_{q=2k_l} - \omega^{iTA}_{q=2k_l} \ (1420\ \text{cm}^{-1}),$$

$$\omega^{iTO}_{q=2k_l} - \omega^{iLA}_{q=2k_l} \ (1150\ \text{cm}^{-1}), \quad \omega^{iLO}_{q=2k_l} - \omega^{iLA}_{q=2k_l} \ (1220\ \text{cm}^{-1}), \quad (3c)$$

According to multiphonon scattering theory [8] transition probability per unit time of the '1' - '1' cycle process can be presented by the following form

$$W = \sum_{\mathbf{k}_l^{\pi^*}, \mathbf{k}_3^{\pi^*}} W_{\mathbf{k}_l^{\pi} \to \mathbf{k}_l^{\pi^*}} \tau_{\mathbf{k}_l^{\pi^*}} W_{\mathbf{k}_l^{\pi^*} \to \mathbf{k}_3^{\pi^*}} \tau_{k_3^{\pi^*}} W^{(2v)}_{\mathbf{k}_3^{\pi^*} \to \mathbf{k}_l^{\pi}}, \quad (4)$$

where $W_{k_l^{\pi} \to k_l^{\pi^*}}$ and $W_{k_l^{\pi^*} \to k_3^{\pi^*}}$ are probabilties of the transitions '1'-'2' and '2'-'3', respectively, $W^{(2v)}_{k_3^{\pi^*} \to k_l^{\pi}}$ is the probapility of the transition '3'-'1' through virtual intermediate electronic state '4a', $\tau_{k_l^{\pi^*}}$ and $\tau_{k_3^{\pi^*}}$ are electron lifetimes in the real states '2' and '3', respectively, which carachterize '2' and '3' energy level broadening, $\mathbf{k}_3^{\pi^*}$ is the electron wave vector in state '3'. Factor $\tau_{k_3^{\pi^*}} W^{(2v)}_{\mathbf{k}_3^{\pi^*} \to \mathbf{k}_l^{\pi}}$ is the conditional probability that the electron in state $\mathbf{k}_3^{\pi^*}$ will afterwards transfer specifically into $\mathbf{k}_l^{\pi^*}$ state. Here the particular case of emition of two phonons with $\mathbf{q} = \mathbf{q}' = 0$ wave verctors should be noted. For acoustic-optical phonon pair taking into account $\omega^{ac}_{q=0} = 0$ peculiarity, it can be stated that the two-phonon process is expanded to the one-phonon process. At transition is emitted one iLO (or iTO) optical phonon with $q = 0$ wave number. Then energy of the scattered phonon is determined as $\hbar\omega_r = \hbar\omega^{ac}_{q=0} + \hbar\omega^{opt}_{q=0} = \hbar\omega^{opt}_{q=0}$. It corresponds to the Raman band with frequency $\omega_r = \omega^{iLO}_{q=0} = \omega^{iTO}_{q=0} = 1583\ \text{cm}^{-1}$.

Conclusions

The task of intensity of Raman bands is closely related to Raman scattering mechanism. On the base of energy and quasi-momentum conservation laws the peculiarities of intravalley double-resonant Raman scattering processes are discussed above. In the high-quality intrinsic graphene set frequencies of Raman peaks is given by equations (3). Those frequencies depend on phonon spectrum as well as excitation laser energy E_l. However, the theoretical results practically do not coincide with the corresponding experimental data. So, the measurement results at $E_l = 2.41$ eV show [9] that in defect-free graphene G (~ 1580 cm^{-1}) and G' (or 2D) (~ 2700 cm^{-1}) relatively high intensity peaks and D (~ 1350 cm^{-1}) and 2D' (~ 2350 cm^{-1}) very weak intensity peaks have basically been observed; D' band is absent. Note D' band requires a defect and is observed only in non perfect samples with structural defects. The frequency $\omega_r = \omega^{iLO}_{q=0} = \omega^{iTO}_{q=0} = 1583\ \text{cm}^{-1}$ is in good agreement with measured Raman G band of graphene and graphite. That band, unlike the collection (3), is due to the single-phonon scattering of electron (single-resonant Raman scattering). On the other hand, it is currently assumed that the Raman G' band relates to the intervalley two-phonon scattering of an electron. Usually, as a rule, the probability of a single-phonon scatterings is higher and, therefore, is a more intensive process than a two-phonon one. Therefore, the intensity of the G band I_G must be much higher than the intensity of the G' band

$I_{G'}$. However according to the measurement data in defect-free grapene one comes accross the opposite situation, $I_G < I_{G'}$ (more than four time).

Thus, by comparing the results of the above presented theoretical analyses and experimental data the following can be concluded: the accepted double-resonant Raman scattering concept fails to give a successful and accurate explanation of the origin of Raman spectrum peaks and intensities of purely crystalline (without defects) intrinsic grapheme.

References

1. ***D. Yoon, H. Moon, H. Cheong.*** Journal of the Korean Physical Society, **55**, 1219 (2009).
2. ***A.C. Ferrari.*** Solid State Communications, **134,** 47 (2007).
3. ***R. Narula, S. Reich.*** Phys. Rev., **B78,** 165422-1 (2008).
4. ***H. Yanagisawa, T. Tanaka, Y. Ishida et al.*** Surf. Interface Anal., **37,** 133 (2005).
5. ***M. Mohr, J. Maultzsch, E. Dobardžić et al.*** Phys. Rev., **B76,** 035439-1 (2007).
6. ***J. Maultzsch, S. Reich, C. Thomsen et al.*** Phys. Rev. Lett., **92**, 075501-1 (2004).
7. ***D. Singh, J. Y. Murthy, T. S. Fisher.*** J. Appl. Phys., **110**, 094312 (2011).
8. ***V. F. Gantmakher, Y.B. Levinson.*** Carrier *scattering* in metals and semiconductors, Elsevier, 1987.
9. ***A.C. Ferrari, J. C. Meyer, V. Scardaci et al***. Phys. Rev., **97**, 187401 (2006).

ELECTRON LATTICE MOBILITY FLUCTUATIONS IN EQUILIBRIUM SEMICONDUCTORS

T.A. Zalinyan, S.V. Melkonyan

Yerevan State University, Yerevan, Armenia, E-mail: tigran.zalinyan@ysumail.am

Introduction

The development of the theory of electron mobility fluctuations could serve as good basis for further explanation of the basic mechanism of low frequency current noises in semiconductors. The main arguments for this are the results of recently publicated various experimental studies (see, e.g., [1, 2]). The main sources of carrier mobility fluctuations are: random intraband scattering, generation-recombination transitions, and the shot effect [3, 4]. It is discovered [5, 6] that unlike electron concentration fluctuations, lattice mobility fluctuations attenuate over time more slowly, by non-exponential law. In order to specify the nature of this pecularity that has a very important meaning for the theory of low frequency 1/f noises [7], it is necessary to clarify the role of the phonon subsystem in the interacting electron-phonon system of the semiconductor. For that purpose electron lattice mobility fluctuations, conditioned by electron-phonon random scatteringare considered in this work. As a result of phonon absorption or emission by electron both the equilibrium of electron and phonon systems are disturbed. It is known [8] that the disturbance of the phonon subsystem equilibrium restores much faster than the disturbance of the equilibrium electron system. Therefore, here neglecting phonon fluctuations it has been assumed that the phonon system is in equilibrium state.

Theory

It was established [9] that in general cases electron mobility fluctuation $\tilde{\mu}$ is the result of the fluctuations of the electron quasi-momentum relaxation time τ_k ($\tilde{\tau}_k$ -source) and the occupancy of energy levels of the conduction band n_k ($\tilde{n}_k$ -source). As shown in Ref. [9] for the theory of 1/f-noise the $\tilde{n}_k$ component of the mobility fluctuations is of basic interest which can be presented as [4, 9]

$$\tilde{\mu} \equiv \sum_{\mathbf{k}} (\bar{\mu}_k - \bar{\mu}) \tilde{n}_k / \bar{n} V \ . \tag{1}$$

Here $\bar{n}$ is the statistical average concentration of conduction electrons, V is the semiconductor volume, $\mathbf{k}$ is the quasi-wave vector of a conduction electron, $\bar{\mu}$ is the statistical average mobility of the electron, $\bar{\mu}_k$ is the statistical average component of "local" mobility which is determined by the statistical average quasi-momentum relaxation time $\bar{\tau}_k$ as $\bar{\mu}_k = e\bar{\tau}_k / m$, m is the electron effective mass. The summing takes place within the range of Briluen's first zone (*BZ*). Herein and below, the statistical average and the fluctuation components of the corresponding quantities are denoted by the symbols « – » and « ~ », respectively, vector quantities and their magnitudes are denoted by boldface and non-boldface symbols, respectively.

The occupancy fluctuations $\tilde{n}_k$ are expressed by $\tilde{f}^0_{\mathbf{k}}$ fluctuations of the equilibrium distribution function of conduction electrons $f^0_{\mathbf{k}}$ as below [4, 9]:

$$\tilde{n}_k = -\frac{1}{3} k \frac{d\tilde{f}^0_k}{dk} \ . \tag{2}$$

Here $f_{\mathbf{k}}^{0}(t) = \bar{f}_{\mathbf{k}}^{0} + \tilde{f}_{\mathbf{k}}^{0}(t)$, $\bar{f}_{\mathbf{k}}^{0}$ is the statistical average distribution function of the equilibrium electron system which is determined by the Fermi-Dirac (or Boltzmann) statistics, $\tilde{f}_{\mathbf{k}}^{0}(t)$ is time dependent function which describes random disturbances (fluctuations) of the equilibrium state. By the index "0" of distribution functions it is emphasized the important fact that fluctuations are equilibrium fluctuations which arise in equilibrium semiconductors, too.

As a result of occupancy fluctuations $\tilde{n}_{\mathbf{k}}$ the equilibrium electron system of the semiconductor transmits to the non-equilibrium state. The $\tilde{n}_{\mathbf{k}}$ and $\tilde{f}_{\mathbf{k}}^{0}(t)$ functions, which characterise the non-equilibrium state of the electron system may be represented as a sum of symmetric $\tilde{n}_{\mathbf{k}}^{s}(t)$, $\tilde{f}_{\mathbf{k}}^{0,s}(t)$ (i.e. $\tilde{n}_{\mathbf{k}}^{s}(t) = \tilde{n}_{-\mathbf{k}}^{s}(t)$, $\tilde{f}_{\mathbf{k}}^{0,s} = \tilde{f}_{-\mathbf{k}}^{0,s}$) and asymmetric $\tilde{n}_{\mathbf{k}}^{a}(t)$, $\tilde{f}_{\mathbf{k}}^{0,a}(t)$ (i.e. $\tilde{n}_{\mathbf{k}}^{a}(t) = -\tilde{n}_{-\mathbf{k}}^{a}(t)$, $\tilde{f}_{\mathbf{k}}^{0,a} = -\tilde{f}_{-\mathbf{k}}^{0,a}$) components as below:

$$\tilde{n}_{\mathbf{k}}(t) = \tilde{n}_{\mathbf{k}}^{s}(t) + \tilde{n}_{\mathbf{k}}^{a}(t), \qquad \tilde{f}_{\mathbf{k}}^{0}(t) = \tilde{f}_{\mathbf{k}}^{0,s}(t) + \tilde{f}_{\mathbf{k}}^{0,a}(t).$$

From expression (1) it follows:

$$\tilde{\mu} = \sum_{\mathbf{k}} (\bar{\mu}_k - \bar{\mu}) \tilde{n}_{\mathbf{k}}^{s} / \bar{n}V + \sum_{\mathbf{k}} (\bar{\mu}_k - \bar{\mu}) \tilde{n}_{\mathbf{k}}^{a} / \bar{n}V = \sum_{\mathbf{k}} (\bar{\mu}_k - \bar{\mu}) \tilde{n}_{\mathbf{k}}^{s} / \bar{n}V . \tag{3}$$

Here we have taken into account that summing takes place within the range of Brillouin's zone and due to asymmetry of $\tilde{n}_{\mathbf{k}}^{a}(t)$ the corresponding sum is zero. Therefore, one can state that the electron mobility fluctuations are caused by the symmetric component $\tilde{n}_{\mathbf{k}}^{s}(t)$ of the occupancy fluctuations $\tilde{n}_{\mathbf{k}}$ (or taking into account relation (2): by the symmetric component of the electron distribution function fluctuations $\tilde{f}_{\mathbf{k}}^{0,s}(t)$). Moreover, asymmetric components $\tilde{n}_{\mathbf{k}}^{a}(t)$ or $\tilde{f}_{\mathbf{k}}^{0,a}(t)$ have no contribution to the mobility fluctuations. $\tilde{f}_{\mathbf{k}}^{0,s}(t)$ is a symmetric function, which means that it depends only on electron energy $\varepsilon_{\mathbf{k}}$ (or the magnitude of the quasi-wave vector k), and, of course, on the time, too. Therefore, hereafter we can also use the notation $\tilde{f}_{\varepsilon_{\mathbf{k}}}^{0,s}(t)$ for the function $\tilde{f}_{\mathbf{k}}^{0,s}(t)$.

Using the Refs. [10-12] results, it can be shown that in the simple case of the semiconductor with a standard band structure in case of intraband scattering of conduction electrons on acoustic phonons we get the following expression for the electron mobility fluctuation:

$$\tilde{\mu}(t) = \mu_0 \int_0^{\infty} dx \tilde{f}_x^{0,s}(t), \tag{4}$$

where

$$\mu_0 = \frac{\bar{\mu}(2mk_BT/\hbar^2)^{3/2}}{4\pi^{3/2}\bar{n}}. \tag{5}$$

Here k_B is the Boltzmann's constant, $\hbar$ is the reduced Planck's constant, T is the temperature, and $x \equiv \varepsilon_{\mathbf{k}} / k_BT$ is the dimensionless quantity.

From Eq. (4) one can notice that to find out the features of the time dependence of the mobility fluctuations $\tilde{\mu}(t)$, first of all, we need to find out the time dependence of the symmetric component of the electron distribution function fluctuations $\tilde{f}_x^{0,s}(t)$. In present study this problem was solved by linearization of Boltzmann kinetic equation.

The movement of the electron along the energy axis is a chaotic movement which is known as diffusive movement of an electron along the energy axis [13]. This movement is described by the symmetric component of the fluctuations of the electron distribution function $\tilde{f}_x^{0,s}(t)$. As a result, we obtain the following equation for $\tilde{f}_x^{0,s}(t)$:

$$\frac{d\tilde{f}_x^{0,s}(t)}{dt} = \frac{1}{\tau_M}\left[x^{3/2}\frac{d^2\tilde{f}_x^{0,s}}{dx^2} + \left(x^{3/2} + 2\sqrt{x}\right)\frac{d\tilde{f}_x^{0,s}}{dx} + 2\sqrt{x}\,\tilde{f}_x^{0,s}\right], \tag{6}$$

where

$$\frac{1}{\tau_M} \equiv \frac{2\pi\varepsilon_{def}^2 (k_B T)^{1/2}\hbar(2m/\hbar^2)^{5/2}}{(2\pi)^2\rho}.$$

Here ρ is the mass density of the crystal, ε_{def} is the acoustic deformation potential constant. Eq. (6) is the Fokker-Planck's equation in $\mathbf{k}$-space [14] which describes the chaotic movement of the electron along the energy axis (one-dimensional diffusion in $\mathbf{k}$-space).

Intraband scattering cannot change the concentration of conduction electrons n. It is easy to show that Eq. (6) satisfies the condition $d\tilde{n}(t)/dt = 0$.

From expression (4) one can notice that to determine electron lattice mobility fluctuations caused by electron-acoustic phonon scattering and to find out patterns of time-dependence $\tilde{\mu}(t)$, first of all, one needs to solve Eq. (6). But the analysis of literature data on linear second order partial differential equations in two variables (see, e.g., Refs. [15-17]) shows that analytic solutions of equations of parabolic type (6) practically are not investigated. In the given case it is possible to find only approximate solutions of Eq. (6) based on the known approximate methods [17]. But before passing on to approximate solutions, first of all, by using Eq. (6) we should try to find another equation for $\tilde{\mu}(t)$. To do this, let us differentiate Eq. (4) with respect to time:

$$\frac{d\tilde{\mu}(t)}{dt} = \mu_0 \int_0^\infty dx \frac{d\tilde{f}_x^{0,s}(t)}{dt}, \tag{7}$$

then substituting $d\tilde{f}_x^{0,s}/dt$ from Eq. (6) into the right-hand side of Eq. (7). After simple integration by parts one obtains the following equation:

$$\frac{d\tilde{\mu}(t)}{dt} = \frac{\mu_0}{\tau_M}\int_0^\infty dx\left(-\frac{1}{4\sqrt{x}} + \frac{1}{2}\sqrt{x}\right)\tilde{f}_x^{0,s}. \tag{8}$$

Now, differentiating Eq. (8) over time t one obtains:

$$\frac{d^2\tilde{\mu}(t)}{dt^2} = -\frac{\mu_0}{4\tau_M}\int_0^\infty dx\frac{d}{dt}\left(\frac{\tilde{f}_x^{0,s}}{\sqrt{x}}\right) + \frac{\mu_0}{2\tau_M}\int_0^\infty dx\frac{d}{dt}\left(\sqrt{x}\,\tilde{f}_x^{0,s}\right). \tag{9}$$

The second term on the right-hand side of this equation is equal to zero. One can calculate the first integral on the right-hand side of Eq. (9) using Eq. (6) again. For this, let us multiply Eq. (6) by $dx/\sqrt{x}$ and integrate over dx in the range $[0,\infty)$. Then, integrating by parts and taking into account Eq. (4), we obtain:

$$\frac{d}{dt}\int_0^\infty dx\left(\frac{\tilde{f}_x^0}{\sqrt{x}}\right)=\frac{1}{\tau_M}\int_0^\infty dx\tilde{f}_x^0=\frac{1}{\tau_M}\frac{\tilde{\mu}}{\mu_0}. \tag{10}$$

Substituting Eq. (10) into Eq. (9), for electron lattice mobility fluctuations one obtains the following equation:

$$\frac{d^2\tilde{\mu}(t)}{dt^2}=-\frac{1}{4\tau_M^2}\tilde{\mu}(t). \tag{11}$$

The solution of Eq. (11) is a stochastic harmonic function:

$$\tilde{\mu}(t)=A\cos\left(t/2\tau_M+\varphi\right), \tag{12}$$

where $1/2\tau_M=\omega$ is the vibration frequency, and the amplitude A and the initial phase φ are random quantities.

Conclussions

Processes described by an equation of type (12) are known as harmonic oscillations with random parameters (amplitude A and initial phase φ). Note that in the discussed case the amplitude A can take any value, but the initial phase φ can take only two values: 0 and π. $\varphi=0$ corresponds to the case when the mobility initial fluctuation is positive, $\tilde{\mu}(t=0)=A>0$, and $\varphi=\pi$ corresponds to the case when the mobility initial fluctuation is negative, $\tilde{\mu}(t=0)=-A<0$. Statistical characteristics of stochastic parameters A and φ, e.g. the probability density and the variance, depend on peculiarities of intraband electron transitions. So, for example, at a relatively high temperature range where we can neglect spontaneous transitions of electrons, one can assume values of the initial phase $\varphi=0$ and $\varphi=\pi$ equally probable. As can be seen from the solution Eq. (12), the mobility fluctuation does not decay over time, it varies harmoniously with the characteristic frequency $\omega=1/2\tau_M$. The characteristic time τ_M can be represented in a more convenient form for numerical estimations:

$$\frac{1}{\tau_M}=\frac{8}{3\sqrt{\pi}}\frac{mv_0^2}{k_BT}\frac{1}{\bar{\tau}},$$

where $\bar{\tau}$ is the electron mean free time due to electron-acoustic phonon scattering. In particular, for Si at room temperature $v_0\approx 8.4\div 9.4\times10^5$ cm/s, $m\approx 0.3m_0$ [18] and one obtains following estimation $\tau_M\approx 120\bar{\tau}$. The period of mobility fluctuations oscillations $T=2\pi/\omega=4\pi\tau_M\approx 1.5\times10^3\bar{\tau}$ is approximately three orders of magnitude longer than the electron mean free time $\bar{\tau}$. Eq. (6), and therefore Eq. (12) were obtained by linearization of the Boltzmann equation, when second order nonlinear terms were neglected. We get a very important result: in the linearization approximation equilibrium of the electron system does not restore. It is obvious that for the decay of electron mobility fluctuations and for restoration of equilibrium of the

electron system we need to refuse the linearization approximation and take into account nonlinear terms. In that case it can expected that mobility fluctuations will decay over time not exponentially but by amore slowly power law.

References

1. ***T. Kang***. Optimization of Signal-to-Noise Ratio in Semiconductor Sensors via On-Chip Signal Amplification and Interface-Induced Noise Suppression, PHD, The University of Michigan, 2015.
2. ***M.D. Hammig, T. Kang, M. Jeong, M. Jarrett.*** **60**, 2831 (2013).
3. ***S.V. Melkonyan, F.V. Gasparyan, H.V. Asriyan.*** **6600,** 66001K-1 (2007).
4. ***S.V. Melkonyan.*** Physica B, **405**, 379 (2010).
5. ***S.V. Melkonyan, V.M. Aroutiounian, F.V. Gasparyan, H.V. Asriyan.*** Physica B, **382**, 65 (2006).
6. ***S.V. Melkonyan, V.M. Aroutiounyan, F.V. Gasparyan, C.E. Korman.*** Physica B, **357**, 398 (2005).
7. ***S.V. Melkonyan.*** Physica B, **403**, 2029 (2008).
8. ***V.L. Gurevich.*** Kinetics of Phonon Systems, Nauka, Moscow, 1980. (In Russian)
9. ***S.V. Melkonyan, H.V. Asriyan, Ash.V. Surmalyan, J.M. Smulko.*** Arm. J. of Phys., **4,** 62 (2011).
10. ***C. Hamaguchi.*** Basic Semiconductor Physics, Springer, 2010.
11. ***B.M. Askerov.*** Electron Transport Phenomena in Semiconductors, World Scientific Publ. Co. Inc, 1994.
12. ***A.I. Anselm.*** Introduction to Semiconductor Theory, Prentice Hall **Publ.,** 1982**.**
13. ***V.F. Gantmakher, I.B. Levinson.*** Carrier *Scattering* in Metals and Smiconductors, Elsevier Science Ltd., 1987.
14. ***E.M. Lifshitz, L.P. Pitaevskii.*** Physical Kinetics, Butterworth-Heinenann Ltd, Oxford, 1999.
15. ***A.D. Polyanin, V.E. Nazaikinskii.*** Handbook of Linear Partial Differential Equations for Engineers and Scientists, Chapman & Hall/CRC Press, Boca Raton-London-New York, 2016.
16. ***A.D. Polyanin, V.F. Zaitsev.*** Handbook of Exact Solutions for Ordinary Differential Equations, Chapman & Hall/CRC Press, Boca Raton, 2003.
17. ***E. Kamke.*** Differentialgleichugen Losungsmethoden und Losungen, Springer, 1977.
18. ***A. Dargys, J. Kundrotas.*** Handbook on physical properties of Ge, Si, GaAs and InP, Science and Encyclopedia Publishers, Vilnius, Lithuania, 1994.

COMPETING NUCLEATION OF ISLANDS AND NANOPITS IN ZINC-BLEND AND WURTZIT GaN-InN-AlN QUATERNARY MATERIAL SYSTEM

K.M. Gambaryan, A.K. Simonyan and Y.M. Baghiyan

Yerevan State University, Armenia. E-mail: kgambaryan@ysu.am

1. Introduction

During the last two decades, the use of quantum dots (QDs), corresponding semiconducting materials and their band gap engineering, opens up entirely new functionalities of traditional devices as well as new challenges for the fabrication of devices with unique properties. In particularly, single photon sources for quantum cryptography, quantum dot lasers, single photon detectors, single electron transistors, resonant tunneling diodes, etc [1-4]. Indeed, the physical properties of QDs depend on QDs size and shape, as well as on the mechanism of their formation. The most useful approach for the fabrication of QDs is Stranski–Krastanow growth mode, where the sum of the surface free energy and the interface free energy is about the same as the substrate free energy. In this case, the wetting layer is compressively strained in a few percent. Interestingly note that in the original publication by Stranski and Krastanow, no strain effects were considered. The strain relaxation leads to the formation of coherent (dislocation free) islands on top of a thin wetting layer. Depending on the strain value and its sign, the growth of QDs, the formation of nanopits or even QDs–nanopits cooperative structure can be achieved. Binary III-V compound semiconductors, especially nitrides and their ternary and quaternary alloy are very attractive for several applications [5]. For instance, GaInN alloys are used for fabrication of blue and green light emitted diodes, as well as for violet and blue lasers [6]. Since the band gap of GaInN can be varied from 2.0 to 3.5 eV by increasing of GaN concentration, the potential operating wavelengths cover nearly the entire visible spectra range [7, 8]. High-speed field effect transistors, high-temperature electronic devices, UV and blue light emitters, detectors and gas sensors were made of GaN [9]. Among III-nitride semiconductors, InN has lowest effective mass and small band gap. Therefore, InN-related solid solutions can extend the emission or absorption from the UV to near infrared regions. The photovoltaic (PV) and thermo-PV cells were also fabricated using InN [9]. While cubic film/cubic substrate combinations have been analyzed previously, systems involving hexagonally oriented material as either the film or substrate have not been thoroughly investigated to date. Examples of important semiconductor materials that exist in the hexagonal crystal structure include the wide band gap compound semiconductors GaN, SiC and many II–VI semiconductors. These materials are promising candidates for use in optoelectronic applications including visible and ultraviolet emitters, high power–high temperature electronics. The growth of hexagonal materials has been extensively studied experimentally; quantitative calculation of the inherent strain energy has not been fully performed. Furthermore, the effect of the strain energy on the resulting equilibrium has not been addressed. In [13], elastic compliance equations are developed and their relationship to the overall strain energy of a hexagonally oriented film and substrate are presented. These general relations are then applied to the growth of GaN on different substrates. Additionally, the sufficient lattice mismatch between the III-N binary compounds allows growing of nanostructures in Stranski–Krastanow growth mode.

Regarding the research and development of III-nitride QDs, there are three main kinds of formation mechanism for the growth of QDs. First, it has been proposed [14] that nanoscale indium composition fluctuation due to InGaN phase separation or indium segregation results in the formation of indium-rich clusters, which acts as QDs (QDs-like). Hence, QDs-like system acts as an extremely sophisticated quantum capture system, and in QDs, the charge carriers are deeply localized so as to hinder their migration toward nonradiative defects (dislocations). Therefore, high

luminescence efficiency could be expected if the density of QDs is much higher than that of dislocations. Second, it has been shown that nitride QDs can be self-organized using the strain-induced Stranski-Krastanow growth mode [15]. Third, another way to form nitride QDs is to take advantage of surfactants or antisurfactants, which are often used to change the surface free energy of heterostructure interface. However, the self-assembled nitride QDs can be fabricated by molecular-beam epitaxy or by metalorganic chemical vapor deposition [14, 15] without using any antisurfactants. High-density GaN/AlN QDs for deep UV LED with high quantum efficiency [16] have been also successfully grown by molecular beam epitaxy.

In this paper, the growth mechanism of QDs, nanopits and collaborative QDs-nanopits structures in GaN-InN-AlN material system both for zinc-blend and wurtzit configurations is theoretically investigated using the continuum elasticity model proposed by J. Tersoff (IBM) [1, 10].

2. Total energy of island–pit structure in GaN-InN-AlN material system

Here, according to [10] we assume that the zinc-blend GaN substrate has only discrete orientations and therefore only one angle can be used. We also assume that islands and pits have a shape as schematically presented in figure 1(*a*). High-resolution SEM images of the InAsSbP composition pyramidal island and a nanopit [4] grown on InAs(100) substrate are presented in Figures 1(*b,c*).

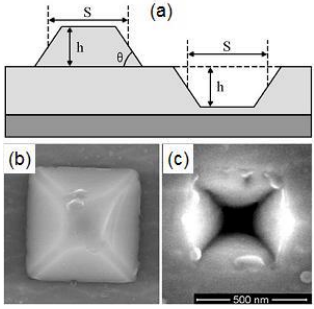

Fig. 1. Schematic view of the island-nanopit structure's cross section – (*a*), high-resolution SEM images of the InAsSbP composition pyramidal island and a nanopit – (*b, c*).

As it is known [10], the energy for the formation of an island (or a pit) can be written as $E = E_S + E_R$, where E_S and E_R are the change in surface energy the reduction of the strain energy by elastic relaxation, respectively. Considering island's volume as a constant, in the case of $s = t = h\ cot\ \theta$, where *s*, *t*, *h* and θ are the length, width, height (depth) and contact angle, as in figure 1(*a*), the energy is equal to:

$$E = 4\Gamma V^{2/3} Tan^{1/3}\theta - 6cVTan\theta, \quad (1)$$

where $\Gamma = \gamma_e Csc\theta - \gamma_s Cot\theta$. For the crystals with a zinc-blend symmetry, $\gamma_s = \frac{1}{2}\epsilon^2(C_{11} + C_{44})d_{wet}$, $c = \sigma_b^2 \frac{(1-\nu)}{2\pi\mu}$, $\sigma_b = \epsilon(C_{11} + C_{44})$. Here γ_s and γ_e are the surface energy per unit area for the normal orientation and the beveled edge, respectively, $\varepsilon = \frac{\Delta a}{a}$ is the lattice mismatch ratio (strain) and d_{wet} is the wetting layer thickness. The value for γ_e can be found from Young equation $\gamma_{sl} = \gamma_s - \gamma_e Cos\theta$ [11], where for Stranski–Krastanow growth mode $\gamma_{sl} = 0$ is the surface energy corresponding to the solid-liquid interface, $\nu = \frac{\lambda}{2(\lambda+\mu)}$ is the Poisson ratio, λ, μ and C_{ij} are the Lame coefficients and the elastic modulus of the substrate. Finally, the expression for the total energy for the crystals with a zinc-blend and a wurtzit symmetry, respectively, can be written as:

$$E = 4\left(\gamma_e Csc\theta - \frac{1}{2}\epsilon^2(C_{11} + C_{44})d_{wet}(\varepsilon)Cot\theta\right)V^{2/3}Tan^{1/3}\theta - 3\epsilon^2(C_{11} + C_{44})^2\frac{(1-\nu)}{\pi\mu}VTan\theta, \quad (2)$$

$$E = 4\left(\gamma_e Csc\theta - \frac{1}{S_{11}+S_{12}}\epsilon^2 d_{wet}(\varepsilon) Cot\theta\right) V^{2/3} Tan^{1/3}\theta - 3\epsilon^2 \left(\frac{S_{11}-S_{12}}{S_{11}^2-S_{12}^2}\right)^2 \frac{(1-\nu)}{\pi\mu} VTan\theta\,, \quad (3)$$

where $S_{11} = \frac{(C_{11}\cdot C_{33}-C_{13}^2)}{(C_{11}-C_{12})(C_{11}C_{33}+C_{12}C_{33}-2C_{13}^2)}$, $S_{12} = \frac{(C_{13}^2-C_{12}\cdot C_{33})}{(C_{11}-C_{12})(C_{11}C_{33}+C_{12}C_{33}-2C_{13}^2)}$ [13].

Next, we performed a mathematical approximation of experimental data [12] in order to evaluate for the GaInAlN material system an analytical expression for the dependence of wetting layer thickness versus strain. In our calculations we used the following expressions for d_{wet} in monolayers (ML): (*i*) if the deformation strain is positive, then $d_{wet} = 0.05\varepsilon^{-3/2}$ at $\varepsilon > 0.03$ [12] and $d_{wet} = 24.184e^{-31.034\varepsilon}$ at $0 < \varepsilon < 0.03$ (accuracy of approximation $R^2 = 0.9635$), (*ii*) if the deformation strain is negative, then $d_{wet} = 0.15|\varepsilon|^{-3/2}$ at $|\varepsilon| > 0.035$ [12], and $d_{wet} = 45.162e^{-23.034|\varepsilon|}$ at $0 < |\varepsilon| < 0.035$ (accuracy of approximation $R^2 = 0.9934$).

The results of theoretical calculations of the dependence of GaInAlN composition islands energy on volume at different strains for zinc-blend and wurtzit symmetry, calculated at $\gamma_e = 10.15\text{x}10^{-5}$ J/cm^2, $\mu = 30.34\text{x}10^4$ J/cm^3 $C_{11} = 272.3\text{x}10^3$ J/cm^3, $C_{44} = 130.3\text{x}10^3$ J/cm^3, $\nu = 0.361$ and $\theta = 0.785$ (45°) and $\gamma_e = 2\text{x}10^{-5}$ J/cm^2, $\mu = 106\text{x}10^4$ J/cm^3, $C_{11} = 296\text{x}10^3$ J/cm^3, $C_{12} = 130.3\text{x}10^3$ J/cm^3, $C_{13} = 158\text{x}10^3$ J/cm^3, $C_{33} = 267\text{x}10^3$ J/cm^3, $C_{44} = 241\text{x}10^3$ J/cm^3, $\nu = 0.37$ $\theta = 0.785$ (45°) are presented in Figure 2(*a*, *b*) and figure 3 (combined), respectively. The dependence of islands critical volume versus strain for the zinc-blend and wurtzit symmetry are presented in figure 4(*a*, *b*), respectively.

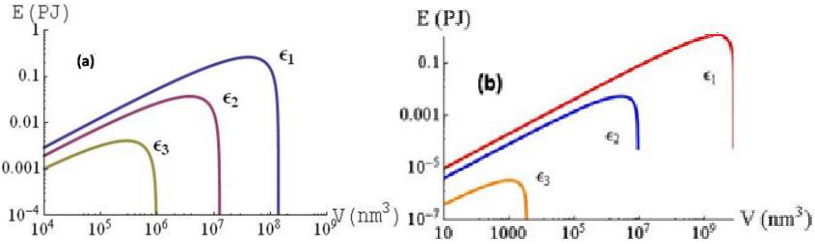

Fig. 2. Dependence of the GaInAlN composition islands energy on volume at different strain for zinc-blend and wurtzit symmetry at different strain ($\varepsilon_1 = 0.02$, $\varepsilon_2 = 0.025$, $\varepsilon_3 = 0.03$ and $\varepsilon_1 = 0.004$, $\varepsilon_2 = 0.008$, $\varepsilon_3 = 0.01$), respectively.

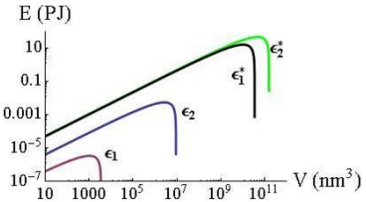

Fig. 3. Dependence of the GaInAlN composition islands energy on volume at different strain for zinc-blend and wurtzit symmetry at $\epsilon_1 = \epsilon_1^* = 0.008$, $\epsilon_2 = \epsilon_2^* = 0.01$.

As it can be seen from figures 2 and 3, in order to attain a stable geometry the island must first overcome the energy barrier E^* which occurs at volume V^*. It is also quite visible that both E^* and V^* strongly depend on the strain and dramatically decrease at the increasing of the strain. At the critical strain of $\varepsilon^* = 0.039$ for zinc-blend and $\varepsilon^* = 0.01$ for wurtzit symmetry, the sign of critical volume (Fig. 4) is changed. We assume that at $\varepsilon = \varepsilon^*$ the mechanism of the nucleation is changed from the growth of dots to the nucleation of pits. Clearly, at small misfit ($\varepsilon < \varepsilon^*$), the bulk

nucleation mechanism dominates. However, at $\varepsilon > \varepsilon^*$, when the energy barrier becomes negative as well as a larger misfit provides a low-barrier path for the formation of dislocations, the nucleation of pits becomes energetically preferable. The results of theoretical calculations also show that the critical strain for the wurtzit symmetry at least three times smaller than that for zinc-blend symmetry.

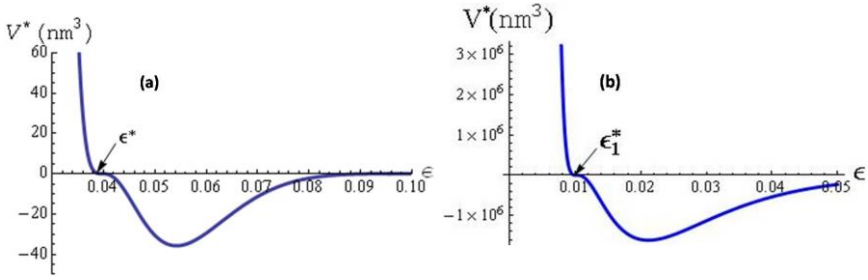

Fig.4. Dependence of the GaInAlN composition islands critical volume versus strain for zinc-blend and wurtzit symmetry, respectively.

3. Conclusion

Thus, the growth mechanism of quantum dots (QDs), nanopits and collaborative QDs-nanopits structures in GaN-InN-AlN material system is theoretically investigated using the continuum elasticity model. The islands energy versus their volume, as well as the critical energy and volume versus the island and wetting layer lattice constants relative mismatch ratio (strain ε), are calculated. It was shown that when the zinc-blend GaN is used as a substrate and when the strain between the wetting layer and a substrate overcomes critical $\varepsilon^* = 0.039$ value, instead of QDs nucleation, the formation of nanopits becomes energetically preferable. Otherwise, when wurtzit GaN is used as a substrate the critical strain is equal to ε^*=0.01, i.e. at least three times smaller. Revealed features have to be taking into account not only at QDs engineering, but also at the growth of bulk crystals and epitaxial thin films in GaInAlN material system.

References

1. ***J. Tersoff and F.K. Le Goues.*** Phys. Rev. Lett., **72,** 3570 (1994).
2. ***K.M. Gambaryan, V.M. Aroutiounian and V.G. Harutyunyan.*** Infrared Phys. and Technol., **54,** 114 (2011).
3. ***K.M.Gambaryan.*** Nanoscale Res. Lett., **5,** 587 (2010).
4. ***V.M. Aroutiounian, K.M. Gambaryan and P.G. Soukiassian.*** Surf. Sci., **604,** 1127 (2010).
5. ***H. Ihsiu and G.B. Stringfellow.*** Appl. Phys. Lett., **69,** 18 (1996).
6. ***S. Nakamura, M. Senoh, N. Iwasa and S. Nagahama.*** Jpn. J. Appl. Phys., **34,** L79 (1995).
7. ***S. Nakamura, M. Senoh, S. Nagahama, H. Iwasa, et al.*** Jpn. J. Appl. Phys., **35,** L74 (1996).
8. ***S. Strite and H. Morkoc.*** J. Vac. Sci. Technol., B **10,** 1237 (1992).
9. ***H.W. Kim, H.S. Kim, H.G. Na, J.C. Yang, et al.*** Chem. Eng. Journal **165,** 720 (2010).
10. ***J. Tersoff and R.M. Tromp.*** Phys. Rev. Lett., **70** (18), 2782 (1993).
11. ***M. Żenkiewicz.*** J. Achievements in Materials and Manufacturing Engineering **24**(1), 137 (2007).
12. ***M. Biehl, F. Much and C. Vey.*** Int. Series of Numerical Mathematics **149,** 41 (2005).
13. ***J. Shen, S. Johnston, S. Shang, T. Anderson.*** Journal of Crystal Growth **240**, 6 (2002).
14. ***J.G. Lozano, A.M. Sánchez, R. García, D. González.*** Appl. Phys. Lett., **87**, 263104 (2005).
15. ***Z. Bi, D. Lindgre, B.J. Johansso, et al.*** Phys. Stat. Solidi (c) **11**, 3 (2014).
16. ***W. Yang, J. Li, Y. Zhang, et al.*** Scientific Reports **4,** 5166 (2014).

OPTOELECTRONIC PROPERTIES OF InAsSbP QUANTUM DOT PHOTOCONDUCTIVE CELLS

V.G. Harutyunyan, K.M. Gambaryan, V.M. Aroutiounian

Department of Physics of Semiconductors and Microelectronics, Yerevan State University, 1 A. Manoogian, Yerevan 0025, Armenia, E-mail: harutyunyan@ysu.am

1. Introduction

In recent years, quantum dots (QDs) have been intensively studied for applications in transistors, solar cells, LEDs, photodetectors, quantum computing systems, etc. The manipulation of the matter at the nanoscale is the key challenge of nanotechnology. Because of quantum confinement effects quantum nanostructures can be considered as artificial atoms and like the natural atoms show a discrete spectrum of energy levels [1]. More than natural atoms, their electronic and optical properties can be tuned on demand adjusting structural parameters, such as size, composition and morphology. For instance, the authors of [2] theoretically showed that the absorption edge of ellipsoidal QDs depends on their semiaxis. The latter parameter is very important to control the properties of nanostructures, as tiny variations in morphology can cause significant changes [3]. The mid-wavelength infrared (MWIR) region of 3-5 μm has many important applications. The importance of this range is related to the atmosphere transmission, appropriate absorption spectra of several industrial gases, etc. Due to QDs peculiarities, QD based photodetectors are expected to show fascinating operation. To satisfy the demands of the state-of-the-art infrared photodetectors, quantum well infrared photodetectors (QWIP) and quantum dot infrared photodetectors (QDIP) are of great interest. QDIPs are predicted to have superior performances compared to QWIPs [4, 5], such as sensitivity to normal incidence infrared radiation, low dark current, high responsivity and detectivity. In addition, this technology is important in remote sensing, chemical and biological detection, as well as in photovoltaic (PV) [6] and thermo-PV (TPV) applications [7]. Some researchers use long-wavelength infrared (LWIR) QDIPs for spectroscopic applications. Bhattacharya et al. presented several heterostructure designs to obtain improved responsibility for InGaAs/GaAlAs mid- and far-infrared QDIPs [8]. HgCdTe (MCT) is a well-established alloy, which has been the dominant system for MWIR and LWIR infrared photodetectors. However, MCT suffers from instability and non-uniformity problems over large area due to the high Hg vapor pressure. Theoretical studies predicted that only type-II superlattice photodiodes and QDIPs are expected to compete with HgCdTe photodiodes [9]. Another potential material system for MWIR applications is InAs-InSb-InP. This quaternary system has been applied to grow diode heterostructures [10, 11]. In recent years, InAsSbP QDs have been successfully grown on InAs substrates for the purpose of MWIR application too [11-17].

In this paper, we report our efforts to fabricate and investigate MWIR photoconductive cells with InAsSbP QDs grown on the surface of an n-InAs(100) substrate. The results of structural characterization, as well as optoelectronic properties of fabricated photodetectors are presented.

2. Experiment

To grow InAsSbP QDs on InAs substrates, we used a modified liquid phase epitaxy (MLPE) technique. The growth process was performed in a slide-boat crucible under a hydrogen atmosphere purified by a palladium filter. The liquid phase consisted of In (7N) solvent and InAs, InP, Sb (6N) solutes was used to nucleate QDs. The substrate used was n–InAs industrial single crystal with 11 mm in diameter, (100) orientation, background electron concentration of 2×10^{16} cm^{-3}, and electron mobility of 40.000 $cm^2V^{-1}s^{-1}$ at 78 K. The QDs were grown in Stranski-Krastanow mode [18, 19] by providing appropriate lattice mismatch between the substrate and wetting layer. To investigate the morphology and crystalline properties of grown nanostructures, atomic force microscope (AFM) and scanning tunneling microscope (STM) were used. MWIR photodetectors were fabricated in the form of photoconductive cells (PCC). Actually, the QD PCC

consists of InAs substrate and InAsSbP QDs grown on its surface (Fig. 1). The capacitance-voltage characteristic of the QD PCC was measured by a high precision LCR meter (QuadTech-1920). In addition, an infrared He-Ne laser was used to investigate the relative conductivity change of fabricated photodetector at different wavelengths. The photoresponse spectrum measurements were performed by an IRS-21 spectrometer.

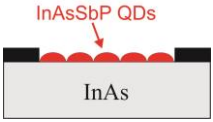

Fig. 1. Schematic of the QD PCC.

3. Results and discussion

The oblique view AFM image of grown QDs is presented in Fig. 2(a). Additional studies have shown that the average surface density and heights of the QDs are in the range of (4-8)×10^9 cm^{-2} and 0.5-21 nm, respectively. In average, the diameter of the QD exceeds the height by about 3 times. The STM image of a single InAsSbP QD is presented in Fig. 2(b).

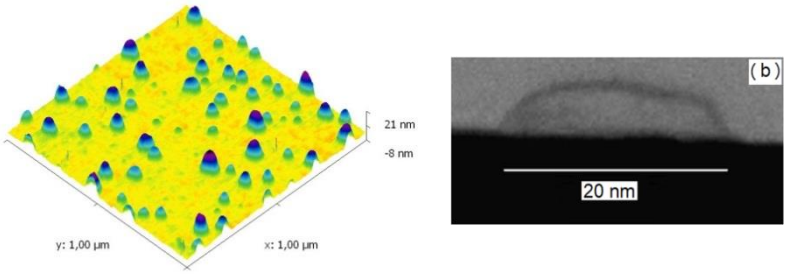

Fig. 2. (a) - AFM image of InAsSbP QDs (oblique view), (b) - STM image of a single InAsSbP QD.

The capacitance-voltage characteristics (C-V) of the QD PCC were measured at signal frequency of 10^6 Hz (Fig. 3). In the figure, the arrows show the voltage change direction during the measurement. One can notice that a capacitance hysteresis is revealed, i.e. at increasing and decreasing of voltage the value of capacitance does not remain the same (see Fig. 3). The remnant capacitance (ΔC) is 270 pF. Detected hysteresis can be explained by the remnant polarization occurred in type-II InAsSbP QDs [12, 16] due to spatial separation of electrons and holes.

The photoresponse spectrum of fabricated photodetector was measured at room temperature applying biases up to 6 mV. It was found that the spectrum is extended up to 4 μm with main peak at 3.48 μm (Fig. 4). This peak coincides with the energy bandgap of InAs (E_g=0.355 eV) at room temperature. The observed additional peaks are the results of charge carrier transitions via energy levels created by InAsSbP QDs. Figure 5 shows the dependence of the relative surface conductance ($\Delta\sigma/\sigma_d$) of the QD PCC on power density under irradiation at different wavelengths, where $\Delta\sigma$ is the change of conductance under irradiation and the dark conductance σ_d.

In the case of irradiation at 1.15 μm, the relative surface conductance change of up to 16 % was measured. As for 3.39 μm, the relative surface conductance change was found to be up to 7 % (Fig. 5(b)). Note that the intensity range of radiation at different wavelengths is different. To make a comparison, we extrapolated the experimental data obtained for 1.15 μm and calculated the

conductance change value for power density of 0.065 W/cm^2. By comparing that value with the average value measured at the same power density for 3.39 μm, we obtained about 1 % higher conductance change. Although the photon energy of radiation at 3.39 μm coincides with the InAs bandgap, the obtained value for 1.15 μm is about 3 times higher than the value for 3.39 μm. This could be explained by the multiple electron-hole generation phenomenons observed in QDs [20].

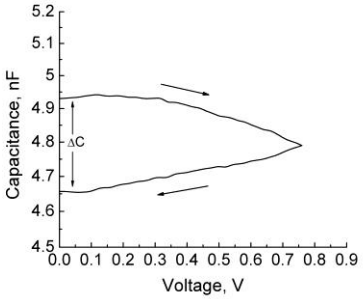

Fig. 3. Capacitance-voltage characteristic of the QD PCC at room temperature.

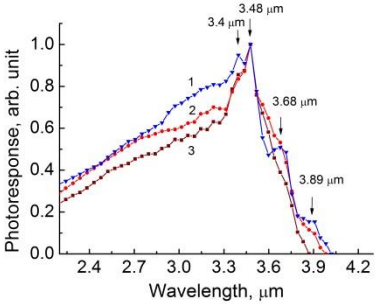

Fig. 4. Photoresponse spectrum of the QD PCC at different biases: 1 – 6 mV, 2 – 2 mV, 3 – 1 mV.

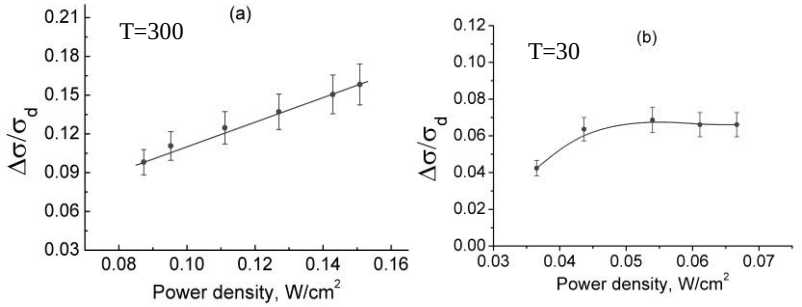

Fig. 5. Relative conductivity change ($\Delta\sigma/\sigma_d$) versus power density at (a) – 1.15 μm and (b) – 3.39 μm.

4. Conclusion

Thus, the results of investigations of InAsSbP quantum dot photoconductive cells are presented. The quantum dots are grown on an InAs(100) substrate by modified liquid phase epitaxy. During measurements, a capacitance hysteresis with remnant capacitance of 270 pF is revealed. The photoresponse spectrum of the photoconductive cell is in the range of 2.2 - 4 μm. The relative surface conductance change of up to 16 % is detected at room temperature.

Acknowledgments: This work was performed in the frame of the project № 15T-2J137 funded by the RA MES State Committee of Science, as well as in the frame of award № YSSP-13-08 funded by NFSAT, AYF and CRDF Global.

References

1. ***M.A. Kastner***, Physics Today **46**, 24 (1993).
2. ***K.G. Dvoyan, D.B. Hayrapetyan, E.M. Kazaryan***, Nanoscale Res. Lett. **4**, 106 (2009).
3. ***J. Li and L.-W. Wang***, Nano Lett., **3**, 1357 (2003).
4. ***V. Ryzhii***, Semicond. Sci. Technol., **11**, 759 (1996).
5. ***J. Phillips***, J. Appl. Phys., **91**, 4590 (2002).
6. ***V.M. Aroutiounian, S.G. Petrosian, A. Khachatryan, K. Touryan***, J. Appl. Phys., **89**, 2268 (2001).
7. ***K.M. Gambaryan, V.M. Aroutiounian, T. Boeck, M. Schulze***, Physica Status Solidi C **6**, 1456 (2009).
8. ***P. Bhattacharya, X.H. Su, S. Chakrabarti, G. Ariyawansa, A.G.U. Perera***, Appl. Phys. Lett., **86**, 191106 (2005).
9. ***P. Martyniuk, A. Rogalski***, Progress in Quantum Electronics **32**, 89 (2008).
10. ***V.A. Gevorkyan, V.M. Aroutiounian, K.M. Gambaryan, I.A. Andreev, L.V. Golubev and Yu.P. Yakovlev***. Technical Physics Letters **34**, 69 (2008).
11. ***K.M. Gambaryan, V.M. Aroutiounian, V.G. Harutyunyan***, ISESCO JOURNAL of Science and Technology **7**, 35 (2011).
12. ***K.M. Gambaryan***, Nanoscale Res., Lett. **5**, 587 (2010).
13. ***K.M. Gambaryan, V.M. Aroutiounian, V.G. Harutyunyan, O. Marquardt, P.G. Soukiassian***, App. Phys. Lett. **100**, 033104 (2012).
14. ***K.M. Gambaryan, V.M. Aroutiounian, V.G. Harutyunyan***, App. Phys. Lett., **101**, 093103 (2012).
15. ***K.M. Gambaryan, V.M. Aroutiounian, V.G. Harutyunyan, O. Marquardt, E.P. O'Reilly***, Villa Conference on Energy, Materials and Nanotechnology (VCEMN-2011), Las Vegas, Nevada, USA, April 21-25, 2011, Book of Abstracts, 260 (2011).
16. ***K.M. Gambaryan, V.M. Aroutiounian, V.G. Harutyunyan***, Infrared Phys. Technol., **54**, 114 (2011).
17. ***V. Harutyunyan, K. Gambaryan, V. Aroutiounian***, J. Nanosci. Nanotechnol., **13**, 799 (2013).
18. ***I. Stranski, L. Krastanow***, Math.-Naturwiss., **146**, 797 (1938).
19. ***A. Baskaran, P. Smerek***, J. App. Phys. **111**, 044321 (2012).
20. ***A.J. Nozik***, Chemical Physics Letters **457,** 3 (2008).

OPTICAL AND SURFACE PROPERTIES OF SELF-ASSEBLED GRAPHENE LAYERS

N. Margaryan[1], H. Karayan[2], A. Avagyan[3]

[1]National Polytechnic University of Armenia, Yerevan, Armenia
[2]Yerevan State University, Yerevan, Armenia
[3]"Almast Synthesis"
E-mail: n.margaryan@polytechnic.am

1. Introduction

At present, carbon nanostructures, and especially graphene, have their unique place among the world-wide actively researched nanostructures. That is why, intensive research taking place in the world to develop simple low-temperature methods for the synthesis of graphene and related materials [1]. Also, a promising method is the self-assembling method of obtaining nanostructured and nanofilms [2, 3]. Obtained in this way films have fractal structure (fractal character) [4]. Due to their fractal essence, self-assembled graphene layers have very rich optical absorbance spectra. In turn, graphene quantum dots (GQDs) are forming in self-assembled graphene systems, which have fractal behavior too [5]. In spite their similar origin, these quantum dots have different sizes and geometric shapes, and the dependencies on this have different effects on the absorption spectra [6]. Especially in [6] absorption spectra for three typical GQDs of 12, 17, and 22 nm average sizes dispersed in DI water and a graphene sheet is presented. Due to the presence of graphene quantum dots, the peak position of the absorption spectrum changes and shifts to the side of high energies with decreasing of linear size of dot. Also, the studying of absorbance spectra is a good method to understand the internal structure of formed films. So, due to the analysis of the absorption spectrum, it is possible to detect the presence of the sp2 carbon phase [7]. But in the case of nanofilms (and especially graphene), the exciton absorption component begins to play a significant role [8-10]. As follows from [8-10] and other articles, in graphene and graphene based quantum dots the peak of the absorption spectrum corresponds approximately to the energy of 4.6 eV. On the other hand, there are works devoted to the effect of the dielectric confinement on the binding energy of the exciton and on the excitoниц component of the absorption spectrum [11]. In this case, the substrate can appreciably affect on the optical properties of graphene.

In this paper a method of obtaining of self-assembled graphene layers is discussed, which is based on joining of graphene fractal flakes (clusters and nanocrystals). Atomic force and scanning electron microscopes (AFM and SEM) are used to describe the spatial form and surface properties of obtained films. To reveal the optical properties of these films and influence of presence quantum dot on those, optical absorbance spectrum for various samples is studied.

2. Experiment and measurements

As already mentioned in the introduction, a method of obtaining self-assembled graphene layers is developed by us. In experiment powder of highly oriented pyrolytic graphite (HOPG) is used, as source of necessary clusters. The process realised in water environment, in presence acetone as mixture, which plays role of carrying plasma. Also, ultrasonic vibrations were used for two purposes. First of all, ultrasonic vibrations are used to crush the graphite powder and to obtain nanocrystals with suitable linear size. And the second important effect of ultrasonic vibration on the process of film formation is that it leads to the grouping of nanocrystals. To the grouping of nanocrystals, als, leads the hidrofob character of this nanocrystals (graphene flakes). Another important factor in this process is the surface tension forces.

As it is known, HOPG consists of atomic layers of carbon, in the plane of which act chemical forces of type σ, and the forces between these layers are type π. The latter, in comparison with the forces of σ, are very weak, so that the above-described graphite layers are easily separated from each other, due to the influences of water surfaces forces and ultrasonic acoustic waves. Obtained layers were substituted on the surface of silicon, amorphous sapphire, monocrystal salt and plastic substrate. Due to their mechanical strength and elasticity obtained films keep their continuity when removed from the

water and placed on a substrate. Already on the substrate, the film undergoes final machining, which is aimed at cleaning the graphene layers from other carbon-bearing structures.
On Fig. 1 a) and b) images of obtained layers on water surface and on silicon substrate correspondly are presented. In the first case (Fig. 1 a)) formed layers are visible by reflecting light from the water surface. And in the second case (Fig. 2 b)) we have the image of formed film, which is done by USB microscope. In this case too, the image of graphene is visible only due to the light reflecting, because angles of reflectance for graphene and silicon surfaces are different. The black dots in Fig. 1 are remains of graphite powder, which cling to the film, when the latter is removed from the water. Mentioned remains are removed during the final machining. In addition to real images, to study the surface properties, also important the AFM and SEM images of these films, which allow you to conduct research on the nano level. Using AFM microscopy it is also possible to study surface potential of obtained film and potential transition between it and substrate. Such studies are done using the Kelvin probe method, when the AFM works in a semi contact mode. The essence of this method is to measure the work function-the minimum thermodynamic work (i.e. energy) needed to remove an electron from a solid to a point in the vacuum immediately outside the solid surface. Here "immediately" means that the final electron position is far from the surface on the atomic scale, but still too close to the solid to be influenced by ambient electric fields in the vacuum. The work function is not a characteristic of a bulk material, but rather a property of the surface of the material (depending on crystal face and contamination).

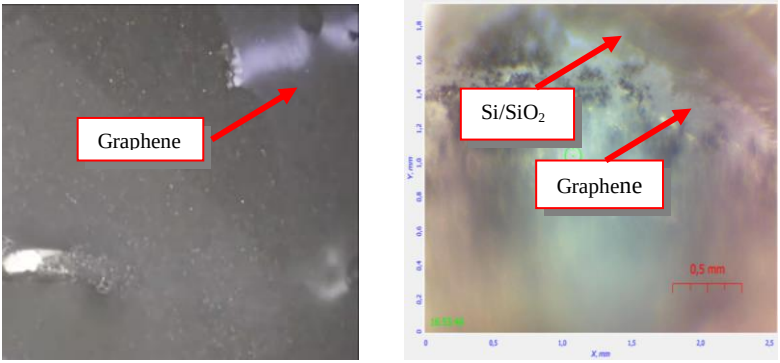

a) b)

Fig.1. Graphene on water surface (a) and on Si/SiO_2 substrate (b).

The AFM image of the obtained self-assembled carbon layer (Fig. 2) shows , that formed film surface is smooth and have waviness less than 0,5 nm. To ensure that graphene is obtained with a large surface area and that on the well-polished (14 sample) surface of silicon is formed a very thin layer of carbon; a scanning electron microscope (Fig. 4) is used.
On the other hand, silicon substrate is a not very suitable substrate for our carbon films; when one measure the optical absorption spectra. For this purpose, we used in our experiment substrates made of single-crystal feed salt (NaCl) and amorphous sapphire (from sapphire glass), which do not absorb the light of the measuring range (from 200 nm to 1100 nm).
The optical absorption of graphene, mainly, is due to the π -π^* interband transition corresponding to the point M of the wave vector. Mentioned excitonic transition and graphene band diagram corresponding to its hexagonal structure Briolluoin zone are shown on Fig. 4 a. And on Fig. 4 b absorption spectrum of graphene substrated corresponds on NaCl (уппер curve) and amorphous sapphire substrates (lower curve). As we can notice, characteristic peak of absorption for amorphous sapphire case is shifted to the side of short waves (high energy) (blue shift effect), which is result of

dielectric confinement effect, because dielectric constant of graphene exceeds the value of dielectric constant of amorphous sapphire (sapphire glass).

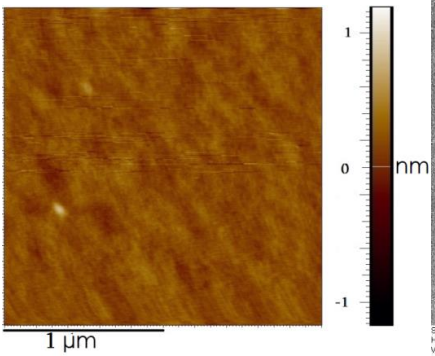

Fig. 2. AFM image of grapheme.

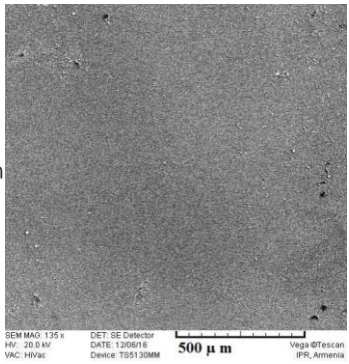

Fig. 3. SEM image of grapheme.

In addition to graphene with an integral surface, graphene quantum dots with different linear size are also obtained. They can be connected to each other and form a layer with a fractal edge. And since in the case of graphene quantum dots, we are dealing with a decrease in dimensionality (the number of space constraints increases by one), the absorption spectra will again care changes, that is "blue shift" effect will take place (Fig. 5a). Of course, the linear measure of the quantum dot will have an important influence on the absorption spectra. Of course, the linear measure of the quantum dot will have an important influence on the absorption spectrum, because, due to the dimensional quantization of the energy spectrum, the excitonic absorption spectrum will change. And in case, when we have set of quantum dots with substantially different sizes, the absorption spectrum will be a combination of the absorption spectra of these quantum dots (Fig. 5 b).

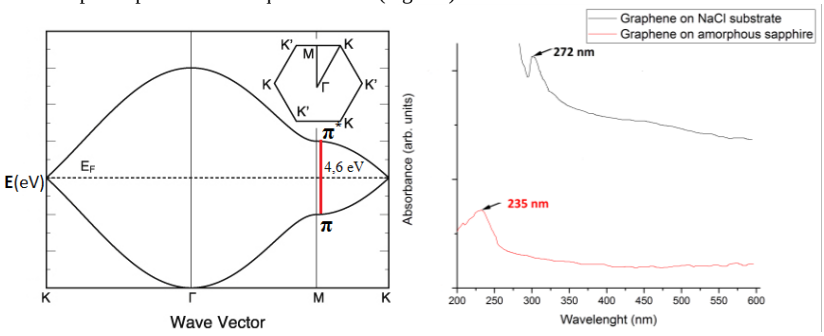

a b

Fig. 4. Band diagram of graphene (a) and optical absorption spectrum (b).

3. Conclusion

The method of obtaining graphene layers by self- assembling is a promising method, since they are released at low temperatures and are not expensive. If the appropriate technological conditions are met, this method can produce graphene with a large surface area. Usually, such films have a fractal character, which is expressed in its surface and optical properties. On the other hand, the optical properties of the fractal graphene layers are also influenced by the graphene based quantum dots. The analysis of the absorption spectra of the films discussed in this paper indicates the excitonic

type of absorption typical for graphene and graphene based quantum dots. The effect of the dielectric confinement on the absorption spectrum is noticeable when the substrate material changes.

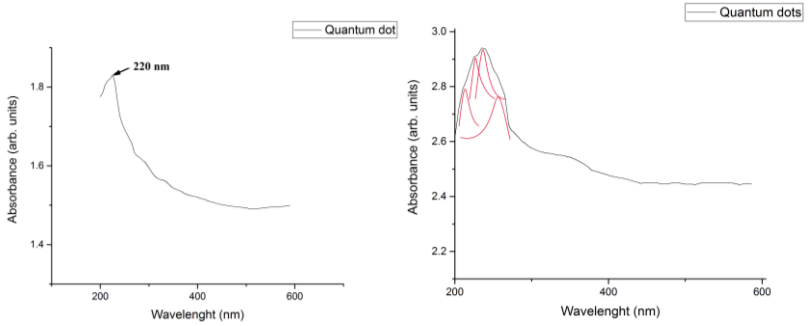

a b

Fig.5. The "blue shift" effect (a) and optical absorption spectrum (b).

References

1. ***K.S. Novoselov, A.K. Geim, et al.*** Scinece, **306**, 666 (2004).
2. ***M. Massicotte, V. Yu, et al.*** Nanotechnolog , **24**(32) 325601 (2013).
3. ***M. Asif, Y. Tan, et al.*** J. Phys. Chem. C, **119**, 3079 (2015).
4. ***D. Geng, B. Wu, et al.*** J. American Chem. Society, 135 (17), 6431 (2013).
5. ***Y. Ujiie, N. Yumoto, et al.*** J. Physics: Conf Series, **109,** 012035 (2008).
6. ***S. Kim, S. W. Hwang, et al.*** ACS Nano, **6**(9), 8203 (2012).
7. ***Q. Lai, Sh. Zhu, et al.*** AIP Advances, **2**, 032146 (2012).
8. ***L. Yang,*** Nano Letters, 11(9) 3844 (2011).
9. ***H. Ajiki.*** J. Phys.: Condens. Matter, **24**, 483001 (2012).
10. ***D.-H. Chea, T. Utikal, et al***. Nano Letters, 11(3), 1379 (2011).
11. ***K. Aharonyan, N, Margaryan.*** NASA Reports, Physics**, 116**(1) (2016).

QUANTUM ENTANGLEMENT IN TWO COUPLED KERR-NONLINEAR RESONATORS

H.S. Karayan, A.G. Chibukhchyan

Yerevan State University, Republic of Armenia, Email: agchibukhchyan@gmai.com

Introduction

Quantum computers and quantum computing function on the basis of algebra of quantum logic. The "if …, to …" argument in quantum logic is a reversible binary operation that is physically realized only by the conditional dynamics of the coherently correlated combined system of qubits. Such dynamic does not have a classical analog and it is performed exclusively by entangled quantum states. Such states are obtained by various physical systems that must ensure the reliability and stability of quantum computing, fights with errors and decoherence due to dissipation dephasing during interaction with the environment or with imperfect control of computer equipment [1].

Entanglement is an important physical resource that underlies the quantum information protocols, including quantum cryptography [3] and teleportation [4]. For any quantum algorithm operating on pure states, the presence of multiparticle (multiple-qubit) entanglement is necessary for exponential acceleration by classical calculations [5]. Therefore, the ability to control entangled states is one of the basic requirements for building quantum information systems.

The Hamiltonian of the combined systems of qubits A and B should have the form:

$$H = H_A + H_B + H_{AB} + H_C(t)\cdot \tag{1}$$

Here H_A and H_B are the Hamiltonians of subsystems A and B respectively, H_{AB} is the interaction energy of qubits A and B, which is responsible for the existence of entanglement, $H_C(t)$ is the energy of the control signal responsible for transitions between different states. To have such a Hamiltonian for obtaining quantum entangled states, we will consider two coupled Kerr-nonlinear resonators and calculate the probability of these states.

Quantum entanglement and violation of inequality for two nonlinear resonators

Let us consider two Kerr-nonlinear resonators interacting with one another under pulsed excitation. The Hamiltonian describing our system in the approximation of a rotating wave has the form:

$$H = \Delta_1 a_1^{+} a_1 + \Delta_2 a_2^{+} a_2 + \chi_1 \left(a_1^{+}\right)^2 a_1^{\,2} + \chi_2 \left(a_2^{+}\right)^2 a_2^{\,2} + g\left(a_2^{+} a_1 + a_1^{+} a_2\right) + \hbar \mathrm{f}(t)\left(\Omega \mathrm{a}^{+} + \Omega^{*} \mathrm{a}\right)\cdot \tag{2}$$

Here the coupling constant, depending on the time Ωf (t), which is proportional to the amplitude of the leading field Ω, consists of Gaussian pulses of duration T separated by time intervals τ,

$$\mathrm{f}(t) = \sum e^{-\left(t - t_0 - n\tau\right)^2 / T^2}\,. \tag{3}$$

a_j Bose annihilation operators associated with modes, g is the Jaynes-Cummings connection constant, which we consider real without substantial loss of generality. χ_1, χ_2 nonlinearity forces in each oscillator, $\Delta_1 = \omega_{01} - \omega$, $\Delta_2 = \omega_{02} - \omega$ is the detuning between the average frequency of the exciting field and the frequency for each oscillator. This model is represented experimentally feasible and can be realized in several physical systems. The quantum optical behavior of our system is completely described by the master equation for the density matrix

$$\frac{d\rho}{dt} = \left[H, \rho\right] + \frac{\Gamma}{2}\sum_{n=1}^{2}\left(2a_n \rho a_n^{\dagger} - a_n^{\dagger} a_n \rho - \frac{1}{2}\rho a_n^{\dagger} a_n\right)\cdot \tag{4}$$

The second and third terms on the right-hand side of this equation are Lindblad members, necessary for describing the Markov connection between the system and the random environment.

They describe, respectively, dissipation and pure dephasing of processes [6]. Here $n_j = a_j^\dagger a_j$ the filling operator of the j mode (the number of photons). Equation (3) can be solved by expanding the density matrix over the basis of the number of particles in the same way as in [16].
Our goal is to demonstrate the continuous variable entanglement between the modes in the first and the third quantum boxes and to calculate the probability of states distribution | 00>, | 10>, | 01> and | 11>. By analogy with Bell's result for discrete variable entanglement, continuous variable entanglement is characterized by a violation of the inequality [7, 8]:
By analogy with Bell's result for a discrete variable entanglement, the CV-interlacing between the modes n and m is characterized by a violation of the inequality [9, 10]

$$1 \le S_{nm} = V\left(\hat{p}_n - \hat{p}_m\right) + V\left(\hat{q}_n - \hat{q}_m\right), \tag{4}$$

where the amplitude and phase operators are defined as

$\hat{p}_n = (\hat{a}_n + \hat{a}_n^\dagger)/2$ and $\hat{q}_n = (\hat{a}_n - \hat{a}_n^\dagger)/(2i)$. The variance of the operator is defined by $V\left(\hat{O}\right) = \hat{O}^2 - \hat{O}^2$.

To be sure that inequality (4) indicates entanglement, if it is present, it may be necessary to minimize the value of S_{12} regarding to the phase counts of different modes. Local operations allow to make transformation $\hat{a}_n \to \hat{a}_n e^{-i\phi_n}$ and the minimum value of S_{nm}, obtained when $\phi_m + \phi_n$ is an integral multiple of 2π, is given by formula

$$S_{nm} = 1 + \hat{a}_n^\dagger \hat{a}_n + \hat{a}_m^\dagger \hat{a}_m - \hat{a}_n^\dagger \hat{a}_n - \hat{a}_m^\dagger \hat{a}_m - 2\sqrt{\hat{a}_n^\dagger \hat{a}_m^\dagger - \hat{a}_n^\dagger \hat{a}_m^\dagger} - \sqrt{\hat{a}_n \hat{a}_m - \hat{a}_n \hat{a}_m} \tag{5}$$

According to calculations based on the von Neumann equations [6] the WFMC (wave function Monte Carlo) approach demonstrates cohesion between the first and second modes in the system via violation of the inequality $1 \le S_{12}$. We have solved the basic equation Eq. (5) and obtained dependence of S_{12} value from time, which is shown in Fig. 6

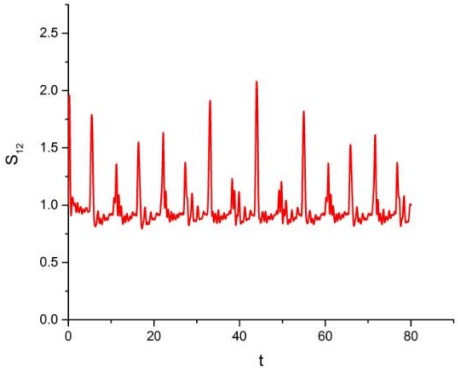

Probability distribution of entanglement states

We solve the master equation Eq. (3) numerically based on quantum state diffusion method. The applications of this method for NDO studies can be found in [29]-[32].

In Figs. 1-4 the solid (A) lines show the probability of state in the first resonator, dotted (B) lines in second one. Considering the pulsed regimes of Kerr-nonlinear reservoir, we assume that the spectral pulse-width, i.e. the spectral width of pulses, should be smaller than the nonlinear shifts of the oscillatory energy levels. It means that the duration of pulses should be greater than $1/\chi$.

Thus, for strong nonlinearities $\chi/\gamma > 1$, we arrive at the following inequalities for the duration of Gaussian pulses $1/\gamma > T > 1/\chi$. The parameters are: $\chi/\gamma = 15$, the maximum amplitude of pump field $\Omega/\gamma = 6$, $\tau = 5.5\gamma^{-1}$, $T = 0.4\gamma^{-1}$, $g = 3$.

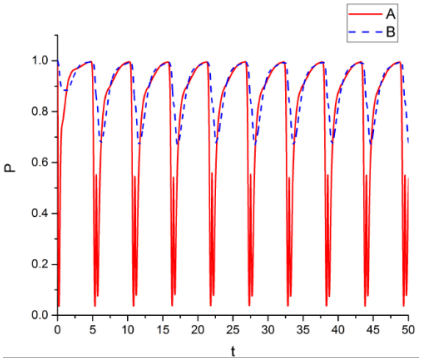

Fig. 1. Quantum entanglement state |00⟩ probability for entanglement qubits A and B.

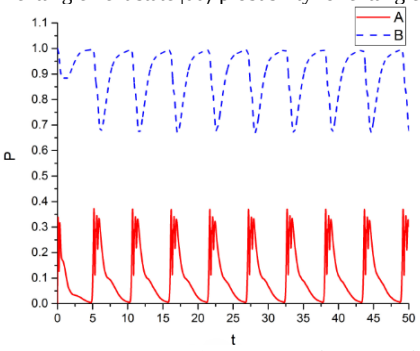

Fig. 2. Quantum entanglement state |01⟩ probability for entanglement qubits A and B.

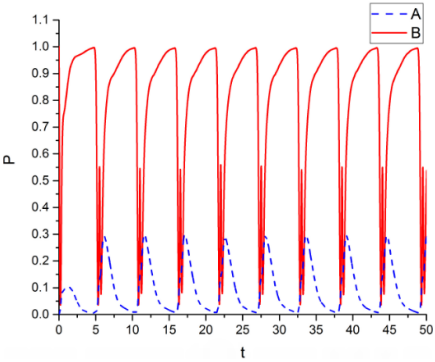

Fig. 3. Quantum entanglement state |10⟩ probability for entanglement qubits A and B.

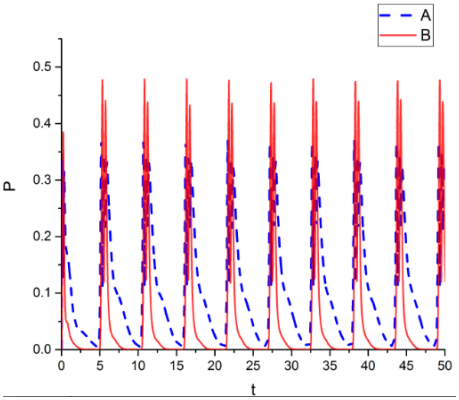

Fig. 4. Quantum entanglement state |11⟩ probability for entanglement qubits A and B.

Conclusion

In this work, we have calculated entanglement between two modes of coupled Kerr-nonlinear resonators which satisfies the condition of quantum entanglement. We have also calculated the probability of the state of states |00⟩, |01⟩, |10⟩ and |11⟩. These states can be used in quantum computer algorithms.

References

1. ***C. Miquel, J. P. Paz, W.H. Zurek.*** Phys. Rev. Lett., **78**, 3971 (1997).
2. ***G. Benenti, G. Casati, S. Montangero, and D.L. Shepelyansky.*** Phys. Rev. Lett., **87**, 227901 (2001).
3. ***A. Ekert.*** Phys. Rev. Lett., **67**, 661 (1991).
4. ***C. Bennett, G. Brassard, C. Crépeau, R. Jozsa, A. Peres, K. Wootters***. Phys. Rev. Lett., **70**, 1895 (1993).
5. ***R. Jozsa, N. Linden.*** Proc. R. Soc. London, Ser. A 459,2011 (2003).
6. ***D.F. Walls, M.J. Collet and G.J. Milburn.*** Phys. Rev., **D 32** 3208 (1985).
7. ***C. Lang, D. Bozyigit, C. Eichler, L. Steffen, J.M. Fink, A.A. Abdumalikov, Jr., M. Baur, S. Filipp, M.P. da Silva, A. Blais, and A. Wallraff.*** Phys. Rev. Lett., **106**, 243601 (2011).
8. ***T.C.H. Liew, V. Savona.*** Phys. Rev. Lett., **104,** 183601 (2010).
9. ***L.-M. Duan, G. Giedke, J.I. Cirac, P. Zoller***. Phys. Rev. Lett., **84,** 2722 (2000).
10. ***S.R. Peres.*** Phys. Rev. Lett., **84** 2726 (2000).
11. **F. Grosshans and P. Grangier.** Phys. Rev. **A 64**, 010301(R) (2001).
12. ***M.D. Reid.*** Phys. Rev**. A 62**, 062308 (2000).
13. ***D. Gottesman and J. Preskill.*** Phys. Rev**. A 63**, 022309 (2001).
14. ***M. Hillery.*** Phys. Rev. **A 61**, 022309 (2000).
15. ***N. J. Cerf, M. Levy, and G. Van Assche.*** Phys. Rev. **A 63**, 052311 (2001).
16. ***G.H. Hovsepyan, A.R. Shahinyan, and G.Yu. Kryuchkyan.*** Phys. Rev. **A 9**0, 013839 (2014).

IMPLEMENTATION OF QUANTUM RECURSIVE ALGORITHMS WITH THE KERR EFFECT CONSIDERING THE DISSIPATION

A.G. Chibukhchyan

Yerevan State University, Republic of Armenia, Email: agchibukhchyan@gmail.com

Introduction

Rapid development of semiconductor integral microtechnology led to the creation of high-performance computers and data processing systems. This, in turn, induced creations of the artificial intelligence (AI). The main tasks of AI (pattern recognition, image identification, inference, decision-making, forecasting, and management) is to bring to the point of forming knowledge about something (the feature of thinking) and gaining knowledge. Their model can be represented as a triple of formal structures $\{V_{in}, A, V_{out}\}$ with input V_{in} and output V_{out} of data and mapping A (algorithm of transformation V_{in} to V_{out}). Among them there may also be unfamiliar ones, but at least one of them must be unknown, which is to be found (the formation of knowledge about it). Generally this problem belongs to the class of hard-to-solve (NP-non-polynomial) problems with an iterative solution procedure, which puts forward the possibility of its physical fulfillment. The decision of A. Kolmogorov and V. Arnold formulated in 1900 helps in this, the thirteenth problem of Hilbert on the representability of a function of n variables by a superposition of continuous functions of two variables [1, 2]. Moreover, they proved that any continuous function of any number of variables can be represented as a sum of continuous functions of one variable and addition (displacement):

$$f(x_1, x_2, \ldots x_n) = \sum_{k=0}^{2n} F_k\left(\sum_{i=1}^{n} G_{k,i}(x_i)\right). \quad (1)$$

In addition, the functions F_k and $G_{k,i}(x_i)$, not counting the zero ones, require no more than (n+1)(2n+1) pieces, particularly, for two variables - no more than 15, for three - not more than 28.

On the basis of relation (1) in 1987, R. Hecht-Nielsen proved the theorem on physical realizability (1) by two-layer neural networks, that is, circuits of elements with deterministic sigmoidal characteristics [3]. As a corollary, it is proved that any function continuous on a compact set can be uniformly approximated by the computed neural networks. Thus, a good elemental base is found that is sufficient to create AI and, moreover, to implement the algebra of more general logic, Zade's fuzzy logic [4].

However, despite the great achievements in this area, with such an elementary base is impossible to perform NP-class algorithms, that is, to obtain a "strong" AI. To overcome such a barrier, it is necessary to maximally expand the algebra of logic up to the quantum one. Processes in the microcosm, particularly, in a system of coherently correlated qubits, occur in quantum indeterminate logic, and the AI is organized by a neural network with reverse connections based on deterministic logic. The combination is not trivial, since the reverse connection requires knowledge of the state of the system without destroying it, which is impossible for a closed quantum system. Knowledge at a moment of time of the state of a quantum system either projects it into one of its own state, or destroys coherent correlation, responsible for the efficiency of processing information, that is, the advantage of quantum computing. The problem of replacing deterministic logic with an indeterminate, that is, the organization of "quantum feedback", is solved by G.S. Karayan in [5-6] with the help of the quantum element of the "cycle number shift $\hat{T}_n$. Its physical implementation can be carried out in different ways, depending on the choice of the qubit and the control of its dynamics. Here we consider the possibility of performing the "shift of the cycle number" $\hat{T}_n$ with the help of the nonlinear optical Kerr effect.

Theory

The operator $\hat{T}_n$ is described in the following way. Let $|\psi_n(0)\rangle$ and $|\psi_n(\tau)\rangle$ be respectively the state vectors of the quantum system at the beginning and at the end of the nth iteration cycle with

duration τ, and $\hat{U}_\tau$ the unitary operator describing the conditional dynamics of the system in the flow τ, i.e.

$$|\psi_n(\tau)\rangle = \hat{U}_\tau|\psi_n(0)\rangle\,. \tag{2}$$

Then the function of the operator $\hat{T}_n$ is the transformation of the state of two qubits $\begin{pmatrix}|\psi_n(0)\rangle\\|\psi_{n-1}(\tau)\rangle\end{pmatrix}$ in the state $\begin{pmatrix}|\psi_{n+1}(0)\rangle\\|\psi_n(\tau)\rangle\end{pmatrix}$, i.e. $\hat{T}_n\begin{pmatrix}|\psi_n(0)\rangle\\|\psi_{n-1}(\tau)\rangle\end{pmatrix} \rightarrow \begin{pmatrix}|\psi_{n+1}(0)\rangle\\|\psi_n(\tau)\rangle\end{pmatrix}$. (3)

Generally $\hat{T}_n$ affects on three qubits, from which the third one is internal (intermediate) with the initial and final states $|0\rangle$. The condition for the dynamics of the combined qubits is given by the symmetric difference ("distance") of the final states of subsequent cycles

$$\Delta_n \equiv ||\psi_n(\tau)\rangle - |\psi_{n-1}(\tau)\rangle| \tag{4}$$

for $n < n_{np}$ there will be a $\hat{T}_n \equiv \hat{T}$, since the structure of the operators $\hat{T}_n$ of all cycles is the same and is denoted by $\hat{T}$ [6]:

$$\hat{T} \equiv \hat{I}(2)\hat{S}_w(2,3)\hat{C}_N(3,2)\,\hat{S}_\varphi\,(2,1)\hat{C}_N(3,2)\,\hat{U}_\tau(2)\,\hat{C}_N(1,2). \tag{5}$$

Here $\hat{S}_\varphi$,$\hat{C}_N$,$\hat{S}_w$ and $\hat{C}_N$ are the operators of controlled phase shift, conditional NOT, exchange of qubit states and initialization respectively. Here in order to avoid cumbersome for the formation of knowledge, it is necessary that the considered system proceed to the established state when $\Delta_n = 0$. In turn, this requires that when, in some cycles with the number $n = n_{np}$ the difference $\Delta_n = 0$, then the operator $\hat{T}_n$ becomes the identity operator. Then it follows from (3) and (4) that $\hat{T}_n$ will be the identity for all $n \geq n_{np}$, and the matrix form of the record, in parentheses each operator has the qubit number on which it acts, and for binary operators, the first number refers to the supervisor , the second one refers to the controlled qubits. As usual, the operators in composition (5) act from the right to the left (in quantum schemes they are represented in the reverse order, in the direction of time).

Then any convergent iteration process is represented by the operator [6]:

$$\hat{T}_{it}=\hat{1}\hat{1}\ldots..\hat{T}_{n_{np}}\hat{T}_{n_{np}-1}\quad\ldots\hat{T}_2\hat{T}_1 \equiv \left(\hat{T}\right)^{n\geq n_{np},} \tag{6}$$

In the formulas (5) and (6), the action of the operator $\hat{I}(2)$, i.e. the initialization on the auxiliary qubit at the end of each cycle results in the loss of information and the irreversibility of the operators $\hat{T}$ and $\hat{T}_{it}$. This procedure is similar to the procedure for input-output of information into the quantum system, but also differs in that it is an "internal" process and it is possible to avoid losing data by increasing the hardware costs. The remaining operators in (5) and (6) are unitary, if we assume that the quantum system is closed. However, there is no such case in real quantum information systems, therefore, in many works (see [7,8] and the papers cited there), dissipation phenomena, both in the sense of decoherence and in the sense of information loss are taken into account. Particularly, in [7, 8] were studied superpositional and entangled states of Kerr systems considering the dissipation , and in [9], based on the obtained results, were found the conditions for performing a series of frequently used unary and binary operations. On this basis, it is not difficult to find the protocol for the fulfillment of relations (5) and (6) in the form of a time dependence of the Hamiltonian f(t):

$$f(t)=\begin{cases} f_C, when\ t\ \in [0,\tau_C] \\ f_U, when\ t\ \in [\tau_C,\ (\tau_C+\tau_U)] \\ f_C, when\ t\ \in [(\tau_C+\tau_U),(2\tau_C+\tau_U)] \\ f_\varphi, when\ t\ \in \left[(2\tau_C+\tau_U),(\tau_U+2\tau_C+\tau_\varphi)\right] \\ f_C, when\ t\ \in \left[(\tau_U+2\tau_C+\tau_\varphi),(\tau_U+3\tau_C+\tau_\varphi)\right] \\ f_I, when\ t \in \left[(\tau_U+3\tau_C+\tau_\varphi),(\tau_U+3\tau_C+\tau_\varphi+\tau_I)\right] \end{cases} \tag{7}$$

Here we denote by f_C, f_U,f_φ,f_S,f_I and τ_C,τ_U,τ_φ,τ_S,τ_I the values of the control signals and their duration for the operation $\hat{C}_N$,$\hat{U}_\tau$, , $\hat{S}_\varphi$,$\hat{S}_w$ and $\hat{I}$ respectively.

Essentially, the protocol (7) is a mechanic program for realizing a "quantum feedback" or, what is the same thing, performing a conditional shift operation of the cycle number of the iteration of quantum computation.

Conclusion

Thus, it was established that on the basis of the optical Kerr resonator it is possible to realize the "quantum feedback" in quantum circuits, and with its help, the implementation of the "cycle number shift" $\hat{T}_n$, which is important for obtaining the AI. In this case, seven control signals are required to perform each transition of the iteration cycles $n \longrightarrow (n + 1)$. Then, according to the algorithm (6), the formation is achieved about $(10^3 - 10^4)$ of the control signals, which must act until the coherence of the correlation of the qubits is destroyed.

References

1. ***А. Н. Колмогоров.*** ДАН СССР, **114**, 953 (1957).
2. ***В. И. Арнольд.*** Матем. сб. **48, 3** (1959).
3. ***Р. Хехт-Нильсен.*** Нейрокомпьютинг. История, состояние, перспективы, Открытые системы, 1998, N_o 4, (***R. Hecht-Nielsen.*** The nature of real-world data. Workshop on Self-Organizing maps. Helsinki, June 1997).
4. ***В.В. Круглов, М.И. Дли, Р.Ю. Голунов.*** Нечеткая логика и искусственные нейронные сети. М.: ФИЗМАТЛИТ, 2001.
5. ***Г.С. Караян.*** Изв. НАН РА, сер. Техн. Науки, **LX**, 608 (2007).
6. ***Karayan H.S.*** Quantum Mechanics and physical calculations, 2nd International Symposium on the Modern Physics of Compact Stars and Relativistic Gravity IOP Publishing Journal of Physics: Conference Series 496 (2014).
7. ***G.Yu. Kryuchkyan, H.S. Karayan, A.G. Chibukhchyan, and A.R. Shahinyan.*** Arm. J. of Physics, **10** (1). 64. 1829 (2017).
8. ***H.S. Karayan, A.G. Chibukhchyan***. Proc. YSU: Series Phys. & Math. Sci., **51**, 200 (2017).

MEASURING SURFACE POTENTIAL OF CARBON NANOSTRUCTURED FILMS, COMING OUT OF CONCEPT OF THERMODYNAMIC WORK FUNCTION

N. B. Margaryan[1], H.S. Karayan[2]

[1]*National Politechnic University of Armenia*
[2]*Yerevan State University, n.margaryan@polytechnic.am*

1. Introduction

Today, semiconducting nanostructures are under extensive investigation, since they have an exceptional importance for application in optoelectronics, solar energy conversion and etc. [1]. The development of these technologies is closely connected with the miniaturization of sample size. In particular, in case of semiconducting layers the thickness is a critical parameter. In thin layers some physical characteristics of the material dominate which should not be of high importance. Consequently, the surface characteristics are very important in revealing the physical properties of nanostructures. A *NT-MDT Solver* AFM microscope was used to investigate the surface properties of carbon layers grown by Chemical Vapor Deposition (CVD) method [2]. Using Atomic Force Microscopy , surface topological images of carbon nanostructured films are obtained. Surface potential with Kelvin probe method are measured for the same samples. The microscope was used in semi-contacting mode which enabled to measure the surface potential of a sample along with topological characterization.

2. Method Description

As it is mentioned in Abstract, semi-contacting mode was used in this study. It enables one to register the surface potential distribution over the surface of a layer with sufficient accuracy, which is of a key importance in investigation of complicated surface (interface). A very important characteristics of nanostructures is so called work function, which is the minimum thermodynamic work which is needed to remove an electron from the layer surface to "reasonable far" distance. Here "reasonable far" means that the final position of the electron is far from the layer surface by atomic size but the electron is under the influence of the electric field formed in vacuum. The latter is described in the following way [3]:

$$W = -e\varphi - E_F,$$

where e is the electron charge, φ is the potential of electric field in the vacuum near the surface and E_F is Fermi energy: By Kelvin probe method the difference of work function is measured.
This method is based on registration of electric field (gradient of potential) between the sample under study and the material with known characteristics used as a microscope probe, which in turn with normalization yields the voltage between the probe and the sample. In Fig. 1 the corresponding energy diagram is shown.

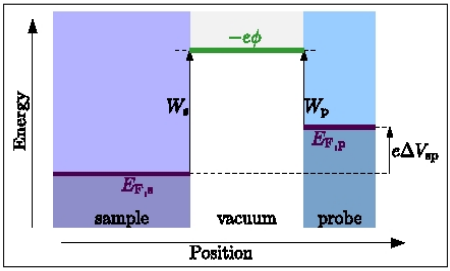

Fig. 1. Energy diagram of the measurement by Kelvin method.

Thus, measuring the voltage we can calculate the difference between the sample and the probe by the following formula:

$$e\Delta V_{sp} = W_s - W_p.$$

Though only the difference between the work functions is measured by Kelvin method, it enables to calculate the work function of a sample, knowing the corresponding parameters of the probe material.

Measured in this work along with the surface topology, the surface potential $\Delta V_{sp}$is measured by AFM, which gives an opportunity to consider the change in surface potential during surface formation case of CVD.

3. Measurements and numerical analysis

Among nanostructured diamond like carbon (DLC) layers, layers obtained by CVD method are of special importance due to their exceptional physical and chemical properties. Investigated in this work DLC layers, the process of their formation and fractural regularities are discussed in [4], are obtained by CVD method with the use of ion and magnetron sources. The surface potential at different stages of layer deposition is also important to study. In Fig. 2 the topology of the surface of DLC layers obtained for different deposition time of 20; 30; 40 minutes are shown.

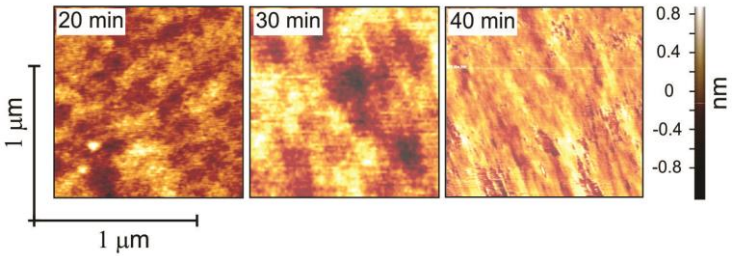

Fig. 2. The topology of the surface of DLC layers obtained for different deposition time of 20; 30; 40 minutes.

As can be noted from Fig. 2 during CVD formation of DLC layer isles of thin (about 0.34 nm thick) are formed, which expand with deposition duration and finally spread all over the sample surface. Now let us to compare these images with corresponding surface potential measured by Kelvin probe method [5-7] (Fig. 3).

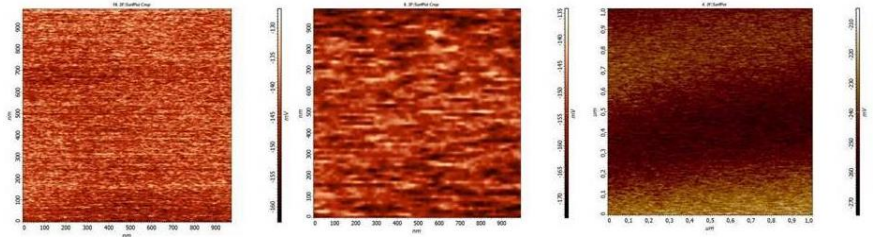

Fig. 3.The surface potential of DLC layers obtained for different deposition time of 20; 30; 40 minutes.

As it is seen from Fig. 3, with the expansion of thin layer the module of surface potential increases remaining negative though (correspondingly -140mV; -165mV; -250mV, the last in case when the surface is almost wholly covered by atomically thin layer), which in turn, means that the layer

formed at the surface is a potential well for the whole layer. Actually, at the surface of DLC studied in this work, an atomically thick layer is formed the potential of differs from that of the rest of the layer and can affect the surface properties of the layer.

3. Conclusion

Kelvin probe method, which is based on measuring of work function of corresponding surface, is perspective method for investigation nanostructured films surface potential and other surface properties. During deposition process on surface of CVD DLC films surface as upper layer atomic layers are forming. Formed on film surface layers directly affect on surface potential of film and are Potential wells compared with the whole film.

References

1. ***H. Mariguchi, H. Ohara, M. Tsujioka*.** SEI Technical Review, 52 (2013).
2. ***Zh. Panosyan, A. Gharibyan, A. Sargsyan, et al.*** Proceedings of SPIE, Nanophotonic Materials VII, edited by Stefano Cabrini, Taleb Mokari, vkm 7755, p. 77550Q1, (2010).
3. ***Ch. Kittel.*** Introduction to Solid State Physics (7th ed.). Wiley.
4. ***N. Margaryan, Zh. Panosyan, A. Mailyan, S. Voskanyan.*** Nanotech France 2016, Book of Abstracts, p. 153.
5. ***L. Yan, Ch. Punckt. et al.*** AIP Conf. Proc. **1399**, 819 (2011).
6. ***O.Kazakowa, V. Panchel, T. L Burnett***. Crystals, **3**, 191 (2013).
7. ***C. Barth, T. Hynninen, et al.*** New Journal of Physics, **12**, 093024 (2010).

COULOMB INTERACTION IN THE FINITE DIELECTRIC ENVIRONMENT BASED MOSFET STRUCTURES

K.H. Aharonyan[a, c], E.M. Kazaryan[b], E.P. Kokanyan[c]

[a]National Polytechnic University of Armenia, Yerevan, Armenia,
E-mail: ahkamo@yahoo.com
[b]Russian-Armenian State University, Yerevan, Armenia
[c]Armenian State Pedagogical University, Yerevan, Armenia

1. Introduction

The metal–oxide–semiconductor field-effect transistors (MOSFETs) for more than four decades have been traditionally scaled on silicon (Si) mainly due to its native thermal oxide SiO_2 proper gate dielectric properties, as well as their outstanding performance, ease in use and manufacturing.

As nowadays MOSFETs scaling is reaching its physical and best possible limits since devices have been getting smaller, both use of the semiconductors with higher carrier mobility and the scaling down into sub-nanometer equivalent oxide thickness range by dielectric layer with a high (relative to SiO_2) dielectric constant value (high – κ dielectric) are of decisive significance [1]. Thus, that is exactly reasonable to replace the SiO_2 by a high – κ gate dielectric with hafnium (HfO_2) or zirconium oxides (ZrO_2) with dielectric constants value $\varepsilon_D = 25$ and 26 respectively.

Certainly, for that an alternative semiconductor environment with higher carrier mobility could be used as the MOSFET high mobility channel. Materials such as III-V key semiconductors (InAs, InSb, InGaAs), few-layer graphene and metal dichalcogenides are promising candidates for ultra-low power, high-speed MOSFET application as well as innovative structures due to their high electron (hole) mobility properties as compared to Si [2-4]. At present there is technologically available to replace the SiO_2 by a gate dielectrics with a much higher dielectric constant such as HfO_2, or ZrO_2 in the surface-channel inversion-mode III–V MOSFETs with atomic layer deposition [5]. At the same time, the downscale technology is expanding in alternative direction as well, i.e. using the gate dielectric layer with a low dielectric constant value relative to SiO_2 (low – κ dielectric) of the same thickness. This may reduce particularly the parasitic capacitance, which enables to the faster switching speeds and lower heat dissipation performances of the device. The most proposed and promising materials for the low –k dielectric performance technology now are: fluorinated glass (SiOF), hydrogen silesquioxane (HSQ), SiOC polymers, organosilicates and porous oxides with dielectric constant values $\varepsilon_D = 3.5 \div 1.1$ comparatively [6, 7, 8].

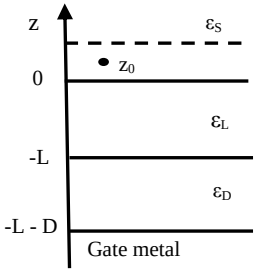

Fig. 1. Four layer MOSFET system

Regardless of the progress both in the fabrication and in component materials unusual combination choice, all MOSFET systems for their functioning demonstrate common feature is that it requires one or several strongly finite thickness dielectric layer media, exhibiting important polarization effects due to the difference between dielectric constants of the channel and barriers regions. As a result, the spatial proximity of the metal gate and finite thickness dielectric environment would reasonably modify the interaction potential in inversion channel region in comparison with the host semiconductor environment itself.

Calculation of Coulomb interaction properties in MOSFET structures has been carried out by number of authors [9-11], where except for Ref. [9] mainly the infinitely large oxide width values were taken into account. Recently in Ref. [12] contribution in Coulomb potential related Green's function coming from the finite dielectric stack of four-layer MOSFET structure is evaluated with the aim of re-normalization of dielectric screening function for Si-inversion layer.

Comprehensive calculation of the MOSFET structure inversion channel region related real-space Coulomb interaction properties in account of inhomogeneous and finite dielectric background is the main aim of the presented paper.

2. Coulomb interaction potential in a four-layer MOSFET structure

Let have a four-layer heterogeneous MOSFET structure in which the region $z \le -(L+D)$ is occupied by a gate metal, the region- $-(L+D) < z \le -L$ by a dielectric oxide layer with dielectric constant ε_D of thickness D, region $-L < z \le 0$ by an intermediate dielectric layer with dielectric constant ε_L of thickness L and the region $0 < z \le \infty$ by a semiconductor substrate with dielectric constant ε_S as shown in Fig. 1. The z axis is perpendicular to the interfaces. The point charge e at the site with coordinates $\rho = 0$, $z = z_0$ (ρ - is two-dimensional (2D) plane coordinate) placed in the oxide/semiconductor junction region with 2D inversion layer. The Coulomb interaction potential $\varphi(\rho, z)$ of point charge is related to Poisson's equation as

$$\nabla_{\vec{r}}^2 \varphi(\vec{r}) = -\frac{4\pi e}{\varepsilon_S}\delta(\vec{r} - \vec{r}_0) \tag{1}$$

where $\delta(\vec{r} - \vec{r}_0)$ is Dirac-delta function, $r = r(\rho, z)$ and $r_0 = r_0(0, z_0)$.

Here we are utilizing the cylindrical coordinate system ρ, φ, z. For that we are expressing the interaction potential in Fourier components $\varphi(k, z)$ with respect to the coordinate ρ as

$$\varphi(\vec{r}) = \varphi(\vec{\rho}, z) = \frac{1}{(2\pi)^2}\int_0^\infty e^{i\vec{k}\vec{\rho}}\varphi(k, z)\, d^2\vec{k} = \frac{1}{2\pi}\int_0^\infty J_0(k\rho)\varphi(k, z)\, k\, dk \tag{2}$$

where $\vec{k}$ is the electron 2D plane vector and J_0 is the 0-th order Bessel function.

The Poisson's equation (1) with Exp. (2) for the discussed system then gets the form

$$\nabla_z^2 \varphi(k, z, z_0) - k^2 \varphi(k, z, z_0) = \begin{cases} -\dfrac{4\pi e}{\varepsilon_s}\delta(z - z_0) & z \ge 0 \\ 0 & z < 0 \end{cases}. \tag{3}$$

The appropriate solution of the equation (3) possess both inhomogeneous

$$\varphi^{in\,\mathrm{hom}}(k, z, z_0) = \frac{e^{-k|z - z_0|}}{k} \tag{4}$$

and homogeneous

$$\varphi^{\mathrm{hom}}(k, z, z_0) = \frac{2\pi e}{\varepsilon_S} \cdot \begin{cases} C_1 e^{-kz} & z \ge 0 \\ C_{2a}e^{-kz} + C_{2b}e^{kz} & 0 \ge z > -L \\ C_{3a}e^{-kz} + C_{3b}e^{kz} & -L \ge z > -(L + D) \\ 0 & z \le -(L + D) \end{cases} \tag{5}$$

parts, respectively, where $C_{3b} = C_{3a}e^{k(D+L)}\left(e^{k(2D+L)} - e^{-kL}\right)$.

Combining expressions (4), (5) with Maxwell boundary conditions

$$\begin{cases} \varphi(k,z,z_0)\big|_{-(L+D)} = 0 \\ \begin{cases} \varphi(k,z,z_0)\big|_{z_i^-} = \varphi(k,z,z_0)\big|_{z_i^-} \\ \varepsilon_{i^+} \dfrac{\partial \varphi(k,z,z_0)}{\partial z}\bigg|_{z_i^+} = \varepsilon_{i^-} \dfrac{\partial \varphi(k,z,z_0)}{\partial z}\bigg|_{z_i^-} \end{cases} \\ z_i = -L;\ 0 \end{cases}, \tag{6}$$

the general solution of Poisson's equation (3) is given by

$$\varphi(k,z,z_0) = \frac{2\pi e}{\varepsilon_S}\left\{ e^{-k|z-z_0|} + e^{-k(z+z_0)} \cdot \frac{\varepsilon_S - \varepsilon_D cth(kD) - \varepsilon_L th(kL) + \frac{\varepsilon_S \varepsilon_D}{\varepsilon_L} cth(kD)\, th(kL)}{\varepsilon_S + \varepsilon_D cth(kD) + \varepsilon_L th(kL) + \frac{\varepsilon_S \varepsilon_D}{\varepsilon_L} cth(kD)\, th(kL)} \right\} \tag{7}$$

which is the comprehensive expression of the Coulomb interaction potential related to the inversion layer region for the discussed four-layer structure.

From Exp. (7) follows specific Coulomb potential particular expressions for the heterogeneous structures such as:

1. In the absence of any dielectric layer, i.e. $D = L = 0$, Exp. (7) reduces to the classic expression of the non conductor/ conductor junction case

$$\varphi(k,z,z_0) = \frac{2\pi e}{\varepsilon_S}\left\{ e^{-k|z-z_0|} - e^{-k(z+z_0)} \right\}; \tag{8}$$

2. In the presence of one dielectric layer, i.e. $L = 0$, the interaction potential (7) goes to expression

$$\varphi(k,z,z_0) = \frac{2\pi e}{\varepsilon_S}\left\{ e^{-k|z-z_0|} + e^{-k(z+z_0)} \cdot \frac{\varepsilon_S - \varepsilon_D cth(kD)}{\varepsilon_S + \varepsilon_D cth(kD)} \right\} \tag{9}$$

for the semiconductor/dielectric layer/metal junctions case [9].

3. In the absence of both metal and any one dielectric layer, i.e. $L = 0$ with $D \to \infty$ (D=0 with $L \to \infty$)), the interaction potential (7) reduces to semiconductor/bulk dielectric junction corresponding expression *) [13]

$$\varphi(k,z,z_0) = \frac{2\pi e}{\varepsilon_S}\left\{ e^{-k|z-z_0|} + e^{-k(z+z_0)} \cdot \frac{\varepsilon_S - \varepsilon_{D(L)}}{\varepsilon_S + \varepsilon_{D(L)}} \right\}. \tag{10}$$

3. Real- space Coulomb interaction potential in a three-layer MOSFET structure

Let now discuss Coulomb interaction potential properties after the Exp. (9) in a three-layer structure. As well known, the effective thickness of the inversion layer in discussed structures is of the order of $d \sim (a_0 / n_S)^{1/3} << r_0$, where n_S is the surface density of the electrons in the layer, $r_0 = n_S^{-1/3}$ - is the average distance between electrons, and a_0 is the effective Bohr radius in a bulk semiconductor. Thus, an important role will be played subsequently by values of ρ that are large compared with d. For the latter there exists in the 2D wave vector k interval such that $k\, d << 1$. Therefore, Exp. (9) should be averaged under the conditions $k\, z << 1$ and $k\, z_0 << 1$, and the result is

$$\varphi(k) = \frac{4\pi e}{k} \frac{1}{\varepsilon_S + \varepsilon_D cth(kD)}. \tag{11}$$

In turn, for a thin enough dielectric layer with thickness $D \sim d$, which usually holds in real structures, for the aforementioned long wave related k vectors the additional condition $k\, D \leq 1$ can be fulfilled as well. For that case Exp. (11) then can lead to the specific result in the form

$$\varphi(k) = \frac{2\pi e}{(\varepsilon_S / 2)} \frac{1}{k + (1/\varepsilon_r D)} \,. \qquad (12)$$

where $\varepsilon_r = \varepsilon_S / \varepsilon_D$ is the dielectric constants ratio of semiconductor and dielectric oxide. Here an expression of the three-layer FET structure Coulomb interaction potential Fourier-image is obtained, which with Eq. (2) will lead to the real–space e and $-e$ point charge interaction potential $V(\rho) = -e\,\varphi(\rho)$ final form such as

$$V(\rho) = -\frac{e^2}{\varepsilon_S / 2}\left\{\frac{1}{\rho} - \frac{\pi}{2}\frac{1}{\varepsilon_r D}\left[H_0\left(\frac{\rho}{\varepsilon_r D}\right) - N_0\left(\frac{\rho}{\varepsilon_r D}\right)\right]\right\}, \qquad (13)$$

where $H(x)$ and $N(x)$ are Struve and Neumann functions.

As we obtain, the Coulomb interaction potential in discussed case holds both the same k - and ρ - dependences as corresponding potential in semiconductor / dielectric two- [13] and three- [14] layer dielectrically homogeneous systems in presence of two-dimensional electron gas (2DEG). As follows, the metal gate here modifies the Coulomb interaction in the same manner such as the 2DEG by means of the statically screening effect in aforementioned systems.

Thereby, the metal gate in this case effectively shields the interaction of charges in the inversion channel towards of weakening, which is to be expected. The quantity $\rho_D = \varepsilon_S D / \varepsilon_D$, analogous to the screening parameter in noted homogeneous systems, here in Exps. (12) and (13) depends on both from the dielectric oxide layer thickness and the neighboring media dielectric constants ratio. For the aforementioned cases the 2D screening parameter is expressing by bulk sample Bohr radius only [13, 14]. In turn, the Coulomb interaction potential after Exp. (13) due to the factor $\varepsilon_S/2$ in the denominator is enhanced twice which is the characteristic feature of discussed structure. The noted factor appears just in the two-layer system inversion channel with the strong low-k environment case [13,15] and in strong "one-side" low-k environment three-layer case [16]. At this moment we have not imposed any restrictions on the both semiconductor and oxide layer dielectric constant values. Since the interaction potential after Exp. (13) strongly depends on both the oxide layer thickness and dielectric constant value, by mutual manipulating of these quantities with ε_S we receive the access to discuss the coulomb characteristic phenomena specific to both low-k ($\varepsilon_S >> \varepsilon_D$) and high-k ($\varepsilon_D >> \varepsilon_S$) environment cases.

Let discuss both cases separately.

1. The low – k dielectric contrast case with $\varepsilon_r = \varepsilon_S / \varepsilon_D >> 1$**.**

With the joint combination of the conditions $k D \leq 1$ and $\varepsilon_S >> \varepsilon_D$ there are distinct 2D distance ρ ranges, such as $\rho_D = \varepsilon_r D >> \rho \geq D$ and $\rho >> \rho_D = \varepsilon_r D$ that Eq.(13) possesses the following analytical features.

(i) For the moderate small wave vectors with $k D \leq 1$ and 2D distances $\rho_D = \varepsilon_r D >> \rho \geq D$ in the first approximation we get

*) Obtained in [12] Coulomb interaction potential expression, corresponding only to the case of very thin intermediate dielectric layer ($kL<<1$) in four-layer FET structure, goes into Eq. (9) barely under the condition $L = 0$.

$$V(\rho) = -\frac{e^2}{(\varepsilon_S / 2)}\frac{1}{\rho}\left[1 + \left(\frac{\rho}{\varepsilon_r D}\right)\ln\left(\frac{\rho}{\varepsilon_r D}\right)\right] \,. \qquad (14)$$

We argue that the appearance of an analytic spatial dependence in the form of Exp.(14), which is essentially absent in a homogeneous dielectric medium case, is strictly a consequence of taking into account the low-k dielectric contrast effect. For comparison, note that in the presence of the latter effect corresponding potential in the two-layer system inversion channel in the first approximation has the form $V(\rho) = -2e^2/(\varepsilon_S + \varepsilon_D)\rho$ for the 2D distances $\rho >> d$ [13, 15].

(ii) For the small enough wave vectors with $k D << 1$ and large 2D distances $\rho >> \rho_D = \varepsilon_r D$ we obtain

$$V(\rho) = -\frac{e^2}{\varepsilon_S / 2}(\varepsilon_r D)^2 \frac{1}{\rho^3} \ . \qquad (15)$$

As follows, at large 2D distances interaction potential falls off as ρ^{-3} and at the same time strongly depends on the oxide layer parameters such as ε_D and D.

2. The high – k dielectric contrast case with $\varepsilon_r = \varepsilon_S / \varepsilon_D < 1$ **.**

For the long wave related $k \leq 1 / D$ vectors there are 2D distance ρ ranges such as $\rho \geq D$ that the variable $\rho / \varepsilon_r D$ in Exp.(13) by condition $\varepsilon_r = \varepsilon_S / \varepsilon_D < 1$ is always greater than unity. Thereby for the moderate small wave vectors case Exp. (13) preserves but for the small enough wave vectors case Exp. (15) would be consistent as well.

4. Numerical calculation of the real-space Coulomb interaction potential

We carried out the numerical analysis of the obtained three-layer MOSFET structure Coulomb interaction potential after Exp.(13) in two cases of oxide layer thickness D=2.5 nm and 5nm.

At first we demonstrate Coulomb interaction energy properties with **Si/SiO₂** *low–k dielectric contrast case* where the following material parameters are adopted: ε_S = 11.7, ε_D = 3.9 and the Bohr radius in the bulk Si sample a_0 = 6.27 nm.

In Fig.2 we outline interaction potential $V(\rho)$ (scaled by meV) as a function of the intercharge planar distance ρ (scaled by bulk sample Bohr radius a_0). The bold and thin solid curves are relating to the D=2.5 nm and D=5 nm cases correspondingly. For comparison, the graphical curve (dashed line) relating to the two-layer (for that $D \to \infty$ and, thus, metal gate is absent) low–k dielectric contrast case $\varepsilon_S / \varepsilon_D > 1$ described by expression $V(\rho) = 2e^2 / (\varepsilon_S + \varepsilon_D)\rho$ [13] is demonstrated as well. The latter, as expected, holds highest position since screening by metal gate is excluded. By decreasing D the influence of the metal gate is enhancing and interaction energy is weakening.

In Fig. 3 we draw Coulomb interaction energy properties with **InSb/SiO₂** *low–k dielectric contrast case* where the following material parameters are adopted ε_S = 16.8, ε_D = 3.9, the Bohr radius in the bulk InSb sample a_0 = 65.8 nm. The details here are the same as in Fig. 1. As follows, the Coulomb interaction energy here is more enhanced than in Si/SiO_2 based MOSFET case. At the same time, the graphical lines particularly in the region with $\rho > (D \div 3D)$ are closer to each other which means that for this case with decreasing oxide layer thickness the influence of the metal gate grows slowly. The latter is a consequence of dielectric enhancement of Coulomb interaction (dielectric confinement effect) which for the noted planar distances balances the metal gate induced interaction energy weakening tendency. Finally let numerically discuss the *high–k dielectric contrast case*. In Figs. 4 and 5 the Coulomb interaction energy properties both with **Si/HfO₂ and InSb/HfO₂** MOSFET structures respectively is demonstrated where the oxide layer dielectric constant value is taken as ε_D = 25 (the details are the same as in Figs. 1, 2). As we can see, two graphical lines relating to oxide layer width D = 2.5nm and 5nm cases in both graphs are located far below from two-layer metal gate absent ($D \to \infty$) related line. This is because that metal gate induced screening and already dielectric de-confinement ($\varepsilon_S < \varepsilon_D$) effects act together and significantly weaken the Coulomb interaction in MOSFET channel region. At the same time, since the dielectric de- confinement effect for the InSb based structure is manifested relatively more less than in Si based counterpart thus in the region with $\rho > (D \div 3D)$ the Coulomb interaction efficiency is more obvious.

From the foregoing, it can be concluded that the efficiency of Coulomb interaction intensity in aforementioned MOSFET structures except **Si/HfO₂** case is quite effective, which would be enough ground to discuss the prospective problems related to Coulomb binding states in these structures.

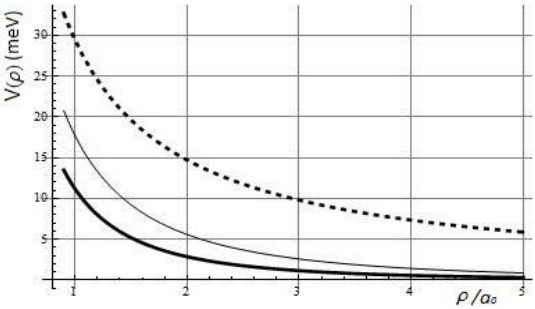

Fig. 2. *V(ρ)* (scaled by *meV*) as a function of planar distance ρ (scaled by a_0) for the **Si/SiO$_2$** MOSFET structure. The bold and thin solid curves are related to the D =2.5 nm and D=5 nm cases respectively. The dashed curve related to the two-layer ($D\to\infty$) metal absent case.

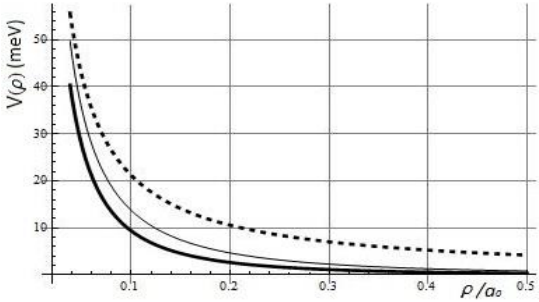

Fig. 3. *V(ρ)* (scaled by *meV*) as a function of planar distance ρ (scaled by a_0) for the **InSb/SiO$_2$** MOSFET structure. The bold and thin solid curves are related to the D=2.5 nm and D=5 nm cases respectively. The dashed curve related to the two-layer ($D\to\infty$) metal absent case.

5. Conclusions

Comprehensive analysis of MOSFET structure inversion channel region related real-space Coulomb interaction potential properties in account of inhomogeneous and finite dielectric oxide background is provided. In particular, the explicit dependence of the Coulomb potential on the thickness of the oxide layer is established. It is shown that the efficiency of the Coulomb interaction on a number of existing structures is the highest in **InSb/SiO$_2$** MOSFET system.

References

1. ***H.-D.Trinh, et al.*** Appl.Phys. Lett., **103,** 142903-1-5 (2013).
2. ***J.M.S. Orr, et al.*** Phys. Rev. ***B, 77***, 165334-1 (2008).
3. ***J. Lee, et.al.,***Thin Solid Films, **520,** 5382 (2012).
4. ***R.A. Aliev, et al.*** Semiconducters, **51,** 383 (2017).
5. ***J. Robertson, R.M. Wallace.*** Materials Science and Engineering: R: Reports, **88**, 1 (2015).

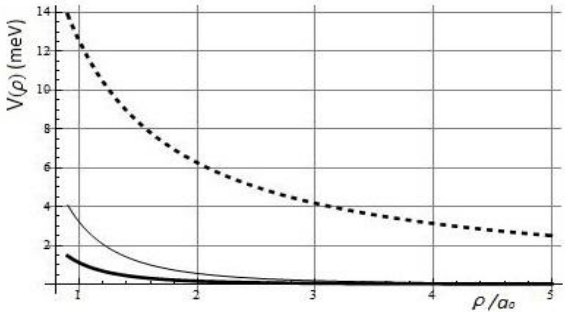

Fig. 4. $V(\rho)$ (scaled by *meV*) as a function of planar distance ρ (scaled by a_0) for the **Si/HfO$_2$** MOSFET structure. The bold and thin solid curves are related to the D=2.5 nm and D=5 nm cases respectively. The dashed curve related to the two-layer ($D\to\infty$) metal absent case.

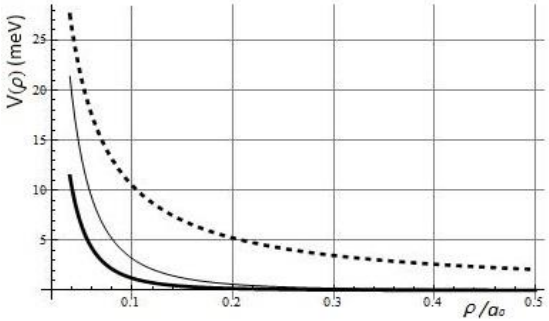

Fig. 5. $V(\rho)$ (scaled by *meV*) as a function of planar distance ρ (scaled by a_0) for the **InSb/HfO$_2$** MOSFET structure. The bold and thin solid curves are related to the D=2.5 nm and D=5 nm cases respectively. The dashed curve related to the two-layer ($D\to\infty$) metal absent case.

6. ***C. Wu, Y. Li, M.R. Baklanov, K. Croes.*** ECS Journal of Solid State Science and Technology, **4,** N3065 (2015).
7. ***S.M. Sze, K.K. NG.*** Physics of Semiconductor Devices, John Wiley & Sons, Inc., Hoboken, New Jersey, 2007.
8. ***D. Shamiryan1,T. Abell, F. Iacopi, K. Maex.*** Materials to day, **7,** 34 (2004).
9. ***A.V. Chaplik.*** Zh. Eksp. Teor. Fiz. **62**, 746 (1972).
10. ***N.S. Averkiev, G.E. Pikus, G.E. Shmatov.*** Solid State Physics, **30,** 3276 (1988).
11. ***S.I.Beril,E.P.Pokatilov,A.S.Zotov,M.Farakh, L.K.Faj.*** Semiconductors, **27,** 12 (1993).
12. ***A. Konar, M. Bajaj, R.K. Pandey, K.V.R.M. Murali.*** J.Appl. Phys., **114,** 113707-1 (2013).
13. ***F. Stern, W.E. Howard.*** Phys. Rev., **163**, 816 (1967).
14. a) ***N.S. Rytova***. Soviet Physics–Doklady, **10**, 754 (1965).
    b) ***N.S. Rytova.*** Vestnik Mosk. Univ. Fizika, Astronomia, **30**, 30 (1967).
15. ***A.V. Chaplik,*** Zh. Eksp. Teor. Fiz. **60**, 1845 (1971).
16. ***K.H. Aharonyan, E.M .Kazaryan,*** Thin Solid Films, **105**, 149 (1983).

SELECTIVELY SENSITIVE PHOTODETECTOR

V.Sh. Meliqyan, D.S. Khudaverdyan, M.G. Khachatryan, S.Kh. Khudaverdyan

National Polytechnic University of Armenia, e mail: xudaver13@mail.ru

1. Introduction

The spectrophotometric semiconductor photodetectors are applied for the optical spectral analysis. They will be put an end to the use of high accuracy mechanical devices, light filters, prisms and diffraction gratings. The photodetectors are used for creating the multi-purpose monitoring systems which meet the current requirements, for obtaining the information on the composition of the environment under study and for solving the important identification problems from the security viewpoint [1,2]. The application of the developed photodetector is conditioned by the large market demand [3]. The work done in this direction is still on the research level [4-7]. The reason is the relatively complex manufacturing technology and special conditions required for the work.

From this perspective, the creation of the high-resolution system for the spectral analysis, on the basis of the semiconductor detector with spectral selective sensitivity,and the implementation of the system in various fields will be a great achievement, since it will be cheap, fast-acting, handy and fit for use in field conditions. The photoelectronic processes occurring in $p^+ - n - p^+$ structuresunder the absorption of electromagnetic radiationare studied. The dependence of the correlation of the saturation currents generated by the counteracting potential barriers on the degree of the abruptness of $p^+ - n$ and $n - p^+$ barriers isfound. The processes of the attraction of individual waves into the radiation absorbing environment conditioned by the change of the depth of that environment, the motives and the possibilities of the determination of the intensity and the length of the waves are explained. The necessity of the developed semiconductor photodetector structure for the creation of the cheap, fast-acting, highly sensitive system of spectral analysis, fit for use in field conditions is analyzed. The problems with the spectral selective sensitivity of the photodetectror and the solutions to those problems are examined in the process of the decoding of the radiation spectra of three different LEDs (blue, green, red). The comparative analysis of the photodetectors under study and the multicolored semiconductor photoreceivers in which multilayer structures or the cascade chain of active layers with different base thicknesses, describedin the modern literature, is made in terms of the spectral selective sensitivity and complexity of the technology.

The qualitative connection between the radiation intensity and the oscillation changes of the values of the spectral photocurrentis studied. The possibilities of the optical spectral analysis with the help of the developed structure without high accuracy mechanical devices, light filters, prisms and diffraction gratings, and the use of the structure for the creation of multi-purpose monitoring systems, the obtainment of the data on the composition of the environment under study and the solution of the important identification problems in terms of securityare observed.

2. The object under study

The experimental samples of the photodetector with $p^+ - n - p^+$ planar structure are studied. They consist of vertically arranged p- n junctions. The electromagnetic radiation falls from the side of the surface $p^+ - n$ barrier (longitudinal absorption of the radiation) and propagates to wards the registration range of the rear $n - p^+$ barrier. Fig. 1 shows the schematic diagram of the photodetector. Contact 3 is removed from the n – base, which enables the independent study of photoelectric properties of the counteracting $p^+ - n$ and $n - p^+$ barriers with the help of Contacts 1 or 2. The $p^+ - n$ barrier is the silicide of Ti and has the height of 0.84 eV [8]. The positionof the Fermi level in the n – base is 0.27 eV when mixture density is10^{15} cm^{-3}. Thus, the height of the surface barrier deepening to the baseis 0.57 eV, and it covers the 0.87 microns section of the base, while the height of the calculated potential barrier of the rearn - p^+ junction is 0.76 eV, and itcovers the 1 micron section of the base. The counteracting barriers cover almost 2- micron - thick base.

When the external voltage is applied, one of the barriers is always forward-biased and the other one is back-biased, depending on the polarity. Thus, the change of the voltage brings to the change of the width of one barrierat the expense of the width of the other barrier.

Figures 2 and 3 show the current-voltage characteristics (CVC) of the individual barriers. At the longitudinal absorption of the radiation incident from the side of the silicide barrier, the rear p^+ - n junction of the barrier, that has greater height, provides the greater value of the saturation current and the small change of that current (Fig. 2) than the p^+ - n junction (Fig. 3). It is due to the greater abruptness of the rear junction and the relatively greater value of the wave absorption depth $\lambda = 705$ nm.

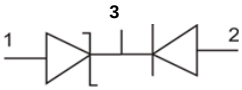

Fig. 1. Schematic diagram of the photodetector

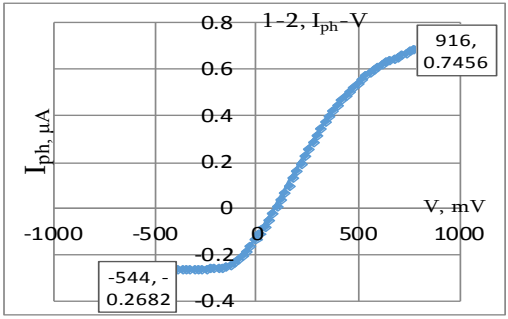

Fig. 2. Current-voltage charactristics of p^+ - n - p^+ structure at the influence of the electromagnetic radiation when the wavelength $\lambda = 705$ nm.

Figure 2 shows the CVC of the p^+ - n - p^+ structure and the wave absorption $\lambda = 705$ nm when the voltage is applied to Contacts 1 and 2. The change of the sign of the voltage value brings to the saturation of the photocurrents of the counteracting potential barriers, each in its opposite bias range. When the voltage is negative, the saturation photocurrent is conditioned by the rear n - p^+ junction, and when the voltage is positive, the photocurrent is conditioned by the near surface p^+ - n junction. In the second case, the saturation process is relatively smooth which is probably due to the increase of the voltage and the conserved resistance of the rear potential barrier with the greater height. While in the first case, as compared with the rear barrier, the small height of the surface potential barrier results inthe small resistance and the abrupt saturation of the photocurrent conditioned by the rear barrier. In case of the relevant polarity of the external voltage, the rear potential barrier expands at the expense of the decrease of the surface barrier, and the new waves get successively involved into the rear section of the current generation, which leads to the change of the photocurrent. Thus, in the registration range of the photoreceiver, starting from the most deeply absorbed wave, the registration is carried out successively by moving from the depth to the surface. It enables to develop an algorithm for the detection of the separate waves and the determiantion of their intensities, as well as for the determination of the absorbing material, the degree of the absorption and the amount of the material [9].

The experimental example of the spectrum obtained from the developed photodetector is shown in Fig. 3. It presents b) the calibrated and a) the spectral dependences obtained by the radiation of L-813SRC-J14 (AlGaInP) LEDs absorbed in the p^+ - n - p^+ structure. The calibrated spectral maximum is in the wavelegth $\lambda_{max} = 660$ nm. It is evident that the calibrated and the obtained spectra are very close to each other.

*3. **Conclusion***

The photoelectronic processes of the double-barrier photodetector are studied. The possibility of the selective registration of waves is obtained experimentaly, which opens up opportunities for the creation of semiconductor spectrophotometers.
https://www.ncbi.nlm.nih.gov/pmc/articles/PMC3927122/

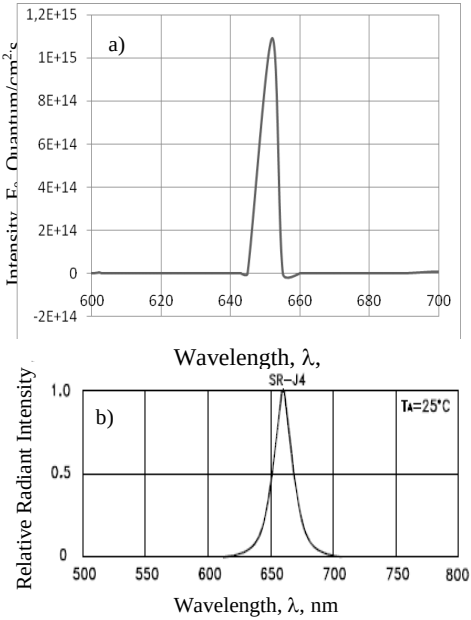

Fig. 3. a) The experimental and b) the calibrated spectral dependences of the intensities of L-813SRC-J4 (AlGaInP) LED.

References

1. ***P. Jiang, H.B. Xia, Z.Y. He and Z.M. Wang***. Sensors, **9** (2009).
2. ***P.I. Normatov, R. Armstrong, I.S. Normatov and N. Narzulloev.*** Russian Meteorology and Hydrology. p. 347 (2015).
3. Technavio Releases New Report on Global Spectroscopy Market. http://www.businesswire.com/news/home/20160127005709/en/Technavio-Releases-Report-Global-Spectroscopy. 2016.
4. ***Ç.S. Elif, et al.*** https://www.ncbi.nlm.nih.gov/pmc/articles/PMC3927122, 2014.
5. ***Th. Kautzsch***. Patent US 8916873 B2. (2014).
6. ***V.A. Gergel, A.V. Lependin, Y.I. Tishin, et al.*** Proc. SPIE, **6260** (2006).
7. ***M.K. Nader and N. Fereydoon.*** Refer to SSC-00072 (2004).
8. ***S.M. Sze.*** Physics of Semiconductor Devices. New York, 1981.
9. ***S.Kh. Khudaverdyan, M.G. Khachatryan, D.S. Khudaverdyan, S.H. Tsaturyan and A.K. Vaseashta.*** NATO Science for Peace and Security. Series B: Physics and Biophysics. Springer, 261 (2013).

ON A NEW METHOD OF SPECTRAL ANALYSIS

D.S. Khudaverdyan

National Polytechnic University of Armenia, e-mail:xudaver13@mail.ru

1. Introduction

With a view to securing the environmental safety, it is necessary to create a user-friendly sensor and a system of the optical spectral analysis of various environments, based on that sensor [1-4]. At present, the optical spectral analysis is carried out with the help of light filters, prisms and diffraction gratings. At the same time, high-accuracy mechanical and optical devices are used [5,6]. The spectrophotometric systems like this are deprived of versatility, and the performance of every new function requires additional facilities, which makes these systems expensive and unsuitable for the use in the field conditions. One of the most effective and up-to-date solutions to the above-stated problem is the development of such a semiconductor structure in which the electronic processes will provide high accuracy spectral analysis of the electromagnetic radia+-tion.

The research paper studies the electronic processes occurring in the specially designed semiconductor sensor which receives the primary information of the optical signal, and the possibilities of the spectral analysis with the help of these sensors.

2. The object under study

The research [7] shows that if the high-resistance semiconductor interlayer is covered by the space charges of oppositely directed barriers on both sides, then the thickness of each of the barriers changes linearly within the thickness of the interlayer, depending on the value of the external voltage. Such structures are able to register the spectral distribution of the intensity, thereby identifying different impurities and determining their amounts [8-9]. There is research done in the area of multicolored [10,11] and cascade [12] selectively sensitive photodetectors. However, these photodetectors require special working conditions and are difficult to use. Therefore, they have not been widely adopted.

The current research studies the two-barrier structures (Fig. 1). The surface barrier is silicide and has a semimetal interlayer p+ underneath. The rear barrier is the n-p junction.

Fig. 1 presents the structure where the *n*-base is an epitaxial layer doped with phosphorus and has the impurity density $N_d = 10^{15}$ cm^{-3}. The rear p^+ layer is doped with boron and has the impurity density 10^{18} cm^{-3}. The impurities are ionized at room temperature and determine the densities of the main charge carries n_n and p_p within the certain range. The charge density of silicon is $n_i = 1.6 \times 10^{10}$cm^{-3}, the thermal energy kT/q is 0.26 eV at room temperature, the height of the silicide barrier PtSi created by Pt is $\varphi_b =<$ PtSi $-$ nSi $>= 0.84$ eV, and the height of the potential barrier of the p-n junction is ln $\varphi_2 = (kT/q)\ln(p_p n_n/n_i) = 0.76$ eV [13]. The Fermi level in the base is far from the conduction band edge $E_C - E_F = kT \times \ln(N_c/N_d) = 0.266$ eV, where $N_C = 2.8 \times 10^{19}$cm^{-3} is the effective density of states in the conduction band.

Thus, the height of the surface barrier is $\varphi_b - |E_C - E_F| = 0.57$ eV, and the difference between the oppositely directed potential barriers is $\varphi_2 - \varphi_1 = \Delta\varphi_k = 0.76 - 0.57 = 0.17$ eV. The calculations in [13] were made when the width of the surface barrier was 0.87μm and the width of the rear barrier was equal to 1 μm. Thus, the base width $d = 2 \pm 0.2$ μm was almost entirely occupied by the oppositely directed barriers. Under the circumstances, the linear movement of x_m by the external voltage changes the contribution made by the barriers in the public photocurrent, and creates the possibility for the detection of the waves of the absorbed radiation and for the determination of their intensities [8].

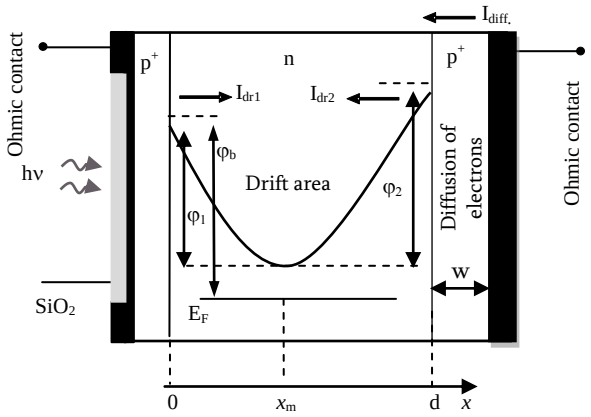

Fig. 1. p^+-n-p^+ structure and current direction.

When electromagnetic radiation is absorbed, the generation rate of electron-hole pairs changes exponentially, depending on the coordinate,

$$G(x) = J_0 \times \alpha \times e^{-\alpha x}.$$

Here J_0 is the incident photon flux per unit area per unit time, is equal to $W \times (1-R)/S \times h\vartheta$, where R the reflection coefficient, α the absorption coefficient, W the radiation capacity, S the photosensitive platform area. The electrons $G(x)$ generated at point x per unit time make a contribution $q \times G(x)$ into the drift photocurrent flowing through the field.

The density of the drift photocurrent conditioned by the first junction is presented by,

$$J_{dr1} = q \int_0^{x_m} G(x)dx = -q \times J_0(1 - e^{-\alpha x_m}). \quad (1)$$

The photocurrent density of the rear junction is conditioned by the photogeneration in the regions $d - x_m$ and the rear p^+ (Fig. 1). Taking into account the diffusion component of the p^+ region, the photocurrent density of the rear barrier will be,

$$J_2 = J_{dr2} + J_{diff} = q \times F_0 \times \left(e^{-\alpha x_m} - \frac{e^{-\alpha d}}{1-\alpha L_n}\right). \quad (2)$$

The resulting density of the photocurrent flowing through the structure under study, taking into account the reflection coefficient *R*, can be represented as,

$$J_{tot} = J_{dr1} - J_{dr2-} - J_{diff} = (1-R)\left[q \times F_0 \times \left(1 - 2e^{-\alpha x_m} + \frac{e^{-\alpha d}}{1-\alpha L_n}\right)\right]. \quad (3)$$

As a result of the absorption of the integral radiation flux, the photocurrent can be presented as,

$$\sum_{i,j} I_{Ph\ i,j} = (1-R)\left[S \times q \times \sum_{i,j} F(_{\lambda_i})\left(1 - 2e^{-\alpha_i x_{mj}} + \frac{e^{-\alpha_i d}}{1-\alpha_i w}\right)\right], \quad (4)$$

where the diffusion length of the minority charge carriers L_n in the rear p^+ layer is bigger than the width w of that layer, and that is included in expression (4). ($j = 1,2,3 \ldots$) changes in the integral flux with the change of the emission wavelength, and ($j = 1,2,3 \ldots$) changes with the change of bias voltage, $F_0(\lambda_i)$ is the total flux of incident photons with the wavelength λ_i.

In the expressions (3) and (4) the reflection coefficient is determined by the correlation of the experimental and calculated values of the current. It introduces a correction for the wave length and flow algorithm described in [9]. The length and the intensity of the most deeply penetrated wave is determined when the value of the external voltage is zero or is very close to zero. Then the subsequent steps described in [10] are taken.

When the algorithm was tested, the data on the light and volt-ampere characteristics of the above-described sample at the monochromatic wavelength $\lambda = 560$ nm and $\lambda = 705$ nm were used. Fig. 2 and Fig. 3 show the spectral dependencies of the received intensities. Besides the principal

maximum, the influence of the background radiation is also present, which corresponds to the testing conditions.

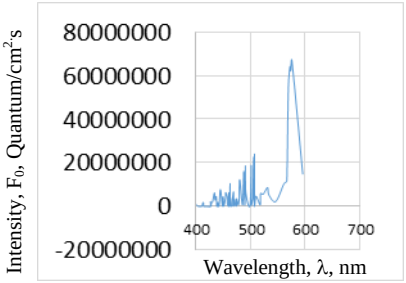

Fig.2

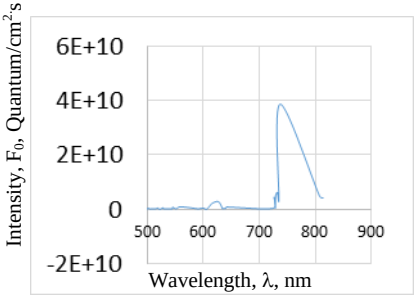

Fig.3

Conclusion

Thus, the research paper describes the possibility of carrying out the optical spectral analysis by means of the photodetector described above.

References

1. ***P. Jiang, H.B. Xia, Z.Y. He and Z.M. Wang***. Sensors. **9**, 6411 (2009).
2. ***P.I. Normatov, R. Armstrong, I.S. Normatov and N. Narzulloev.*** Russian Meteorology and Hydrology. p. 347 (2015).
3. ***M. Vaganov.*** Saint-Petersburg State University of Aerospace Instrumentation Saint-Petersburg, Russia. 2012. p. 1.
4. ***G.N. Pshinko S.A. Kobets, and L.N. Puzyrnayain.*** Journal of Water Chemistry and Technology, **35**, 145 (2013).
5. https://oceanoptics.com/product/flame-spectrometer/
6. http://mrclab.com/productDetails.aspx?pid=81561
7. ***S. Kh. Khudaverdyan, J.G. Dokholyan, A.A. Kocharyan, A.M. Kechiyantz and D.S. Khudaverdyan.*** J. Solid State Electronics, **49**, 634 (2005).
8. ***S. Khudaverdyan, M. Khachatryan, D. Khudaverdyan, S. Tsaturyan and A. Vaseashta.*** NATO Science for Peace and Security Series B.- Physics and Biophysics. Springer, 261 (2013).
9. ***S. Khudaverdyan, A. Avetisyan, D. Khudaverdyan, A. Vaseashta.*** NATO Science for Peace and Security Series B: Physics and Biophysics. Springer, 183 (2013).
10. ***I.V. Vanyushin, V.A. Gergel, V.A. Zimoglyad, Yu. I. Tishi*****n.** Russian Microelectronics. **34**, 155 (2005).
11. ***V.A. Gergel, A.V. Lependin, Y.I. Tishin, et al***. Proc. SPIE, **6260** (2006).
12. ***M.K. Nader and N. Fereydoon.*** 2004. Refer to SSC-00072.
13. ***S. Sze.*** Physics of semiconductor devices. Wiley-Interscience, New York. 1981.

REGISTRATION OF CHARGED PARTICLES & ROLE OF THE WATER CLUSTERS IN THE SEMICONDUCTORS OF DETECTORS

K.S. Ohanyan H.G. Badalyan

Yerevan State University, Yerevan, Armenia, E-mail: kohanyan@ysu.am, hbadal@ysu.am

1. Introduction

Water molecules endowed with the dipole momentum by blocking in the micro-defects of the silicon crystal generate there water clusters which could be considered, for the charged particles, as capture or scattering centers, and for the heavy charged particles – interaction centers. Due to the losses of the charged particles' ionization energy, the generated free charged particles (electrons) by interacting with the identical centers (traps) existing in the silicon crystals, are absorbed by flow absorption constant value, as given below:

$$\sum \lambda = \left(1 - e^{-\sigma n d}\right). \quad (1)$$

And correspondingly, are absorbed by the number of occupied charged particles in the traps:

$$\sum N = N_0\left(1 - e^{-\sigma n d}\right). \quad (2)$$

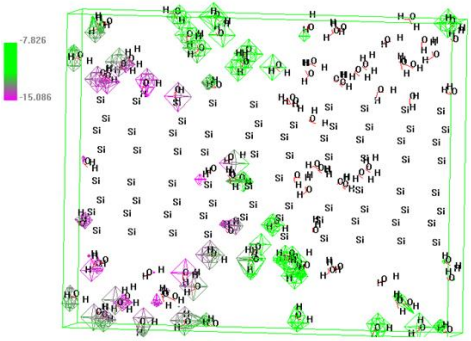

Fig. 1(a). The distribution of the potentials of electrical field in the Si crystal in case of the "line" and "point" models.

Some part of the occupied charged particles is re-combined, the other part, by staying in the constant fluctuation process, gains sufficient kinetic energy for being able to get rid of the traps and for being included in the flow of the charged free particles with delay, thereby by lengthening the tailing part of the charged particles' amplitude spectrum. On the other hand, the delay time, with a little error, coincides to the charged particles, occupied in the traps, average lifetime. The lifetime of the charged particles occupied in the traps could be described as an empirical dependence, as follows:

$$\tau_{m1} = \frac{1}{\nu_{n(p)}} exp\left(-\frac{E_{m1}}{kT}\right). \quad (3)$$

Where, τ_{m1} is the lifetime of the electron in the m_1 type trap, that has E_{m1} energy, $\nu_{n(p)}$ is the frequency factor.

2. Research methodology

In the present work we've built the crystal of silicon with the «Hyperchem» computer modeling program and immersed it into the box full of water, thereafter we've analyzed the generation characteristics of the water clusters in the Si monocrystalline's micro-defects and the distribution of the potentials of electrical field within the structures surroundings.

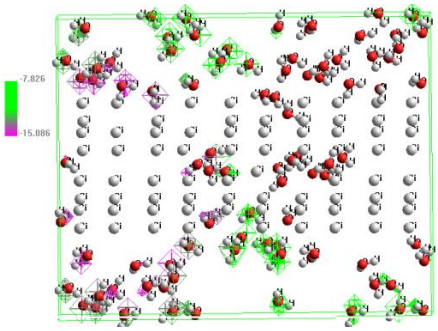

Fig. 1 (b). The distribution of the potentials of electrical field in the Si crystal in case of the "blob" and "point" models.

From the **«Molecular dinamics»** calculation mechanism we've chosen the **PM**^{3} method, which is, for our case, a common method for calculation of the generated potential fields for all atoms, system energy and molecular dynamics. As a modeling result it was obtained that regardless of the amount of water in the "box" the structure of water clusters in micro-defects depends on the sizes of the defects, rather than the quantity of water in the surroundings. If the sizes of a defect are smaller from $5A^0$, then the maximum amount of water molecules in clusters is 3. Otherwise the penetration of water into the hollow of the micro-defect is not beneficial from the point of view the energy.

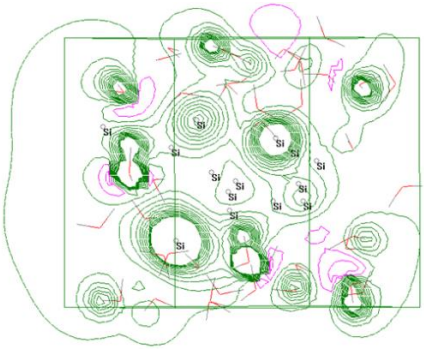

Fig. 2. The distribution of the potentials of electrical field in case of the small sizes of the defects (~5Å).

The amount of the Hydrogenated water molecules is calculated by the equation (4), where ρ - is the density, $G(r)$ - is the radial distribution, and r – is the radius vector.

$$N = 4\pi\rho \int_0^{2\pi} G(r) r^2 dr \,. \quad (4)$$

Based on the energetic results of the radial distribution, it was obtained that water penetrates into the micro-defects by the associated form, which is beneficial from point of view the energy in case of the 3 water molecules, which are arranged in such a way, that the dipole momentum of the associate decreases, and makes it beneficial from point of view the energy [1]. However, in the

literature [2], there exists information that the unique (independents) molecule of water could penetrate into the 0.5 nm micro-defect. This would mean that the deployment of the beryllium network by the water molecule occurs, which is not energetically beneficial (for the beryllium the network constants are a=2,286 Å; c=3,584 Å). Along with the increase of the defect sizes the amount of water molecules increase not constantly, but partially, by generating five-pointed, pentagonal structures, where the interaction energy is greater than for the hexagonal case (pic. 6). For that purpose the energetic levels of water molecules are denser, and the potentials of the surroundings are more, and because of the small sizes of the micro-defects the negative electric field intensity in the edges of micro-defects became $10^7 – 10^9$ V/m, which could act as scattering or capture centers for alpha particles and electrons.

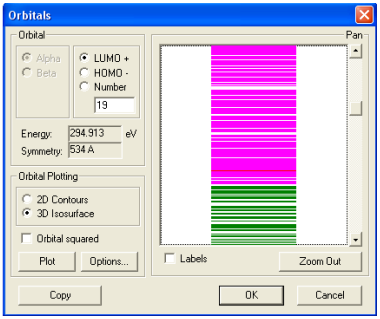

Fig. 3. The energetic levels of the Hydrogenated water molecules at the edge of the microdefect.

In case of large defects water clusters are generated with several layers of pentagonal structures, while the following layers have more dilapidated, fragile structure rather than the first layers which are directly interacting with the atoms of Si [3-5]. It can be seen from Fig. 4 and Fig. 5 that there exist also 2 small distribution peaks, the half-width of which is more than the first one. It means that the third and subsequent layers are having worse arrangements and finally the last layers become not arranged. We are sure about that when we're taking the option of the molecular dynamic in considering the radial distributions of Si, oxygen and hydrogen.

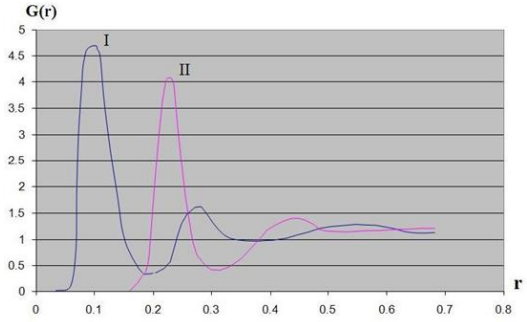

Fig. 4. The radial distribution curve dependence from the radius r from oxygen I and hydrogen II.

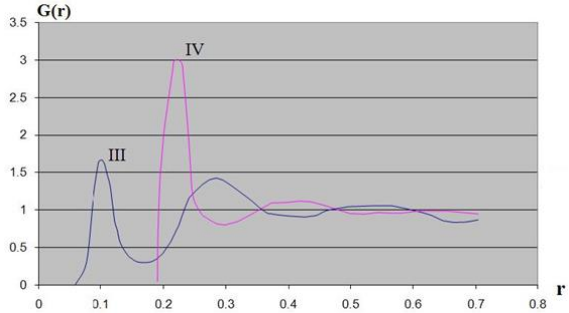

Fig. 5. The radial distribution curves for Si-oxygen and Si-hydrogen.

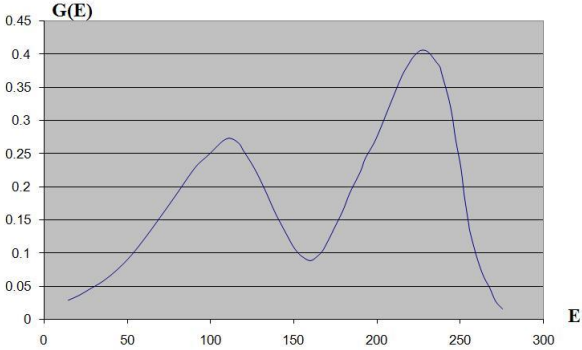

Fig. 6. The dependence of the radial distribution from energy.

This leads to the fact that in the edges of the defects the energetic field potential becomes greater because of the smaller radius. Consequently, the tension of the field in the defects increases from 10^5 to 10^7 V/m. So, it turns out that there exists an effective size of the defect for the occupation of positive particles, which is 10^7 V/m. The free charges occupied by the water clusters with pentagonal structures in the volume of Si generate local centers, which lead to the re-distribution of the electrons. As a result in the monocrystalline of Si the electric field becomes inhomogeneous by the $E = E(x)$ function, and in the traps a great electric field tension is generated, where the water energetic levels reach up to 294 eV, which corresponds to the gamma domain's electronic transitions, where the usual, as well as tunnel crossings of the proton are possible.

The big tension of the electric field in the traps is a condition for the tunnel crossing for protons and for the generation of oxygen atoms with free electrons (particles) within the volume of Si. In work [1] it was registered as a tunnel cross of oxygen, however in our case it is a tunnel cross of proton, which is more likely in our opinion [6].

3. Conclusions

The amplitude spectrum investigations of the registered alpha particles show that the associates embedded into the Si monocrystalline, which have other structure rather than water, could be as occupational or distributional centers for "alpha" particles, and for the electron-hollow pairs which are caused due to the losses of ionization, they could be as occupational and release centers.

References

1. ***H.G. Badalyan. G.L. Grigoryan.*** Chem. Phys., **25,** 17 (2006).
2. ***H. Johnston, A. Kolesnikov.*** «Physicists discover new state of the water molecule» Institute of Physics IOP Physics World May 6, 2016. Chemical and Engineering Materials Division, Oak Ridge National Laboratory, Oak Ridge, Tennessee 37831, USA.
3. ***J. Carrasco, A. Michaelides, M. Forster, S. Haq, R. Raval & A. Hodgson***. Nature Mater. **8,** 427 (2009).
4. ***M.A. Henderson.*** Surf. Sci. Reports, **46**, 1 (2002).
5. ***T.G. Trudeau, K.C. Jena, and D.K. Hore.*** Phys. Chem. C, **113**, 20002 (2009).
6. ***A.I. Kolesnikov, GF. Reiter, N. Choudhury, T.R. Prisk, E. Mamontov, A. Podlesnyak, G. Ehlers, A.G. Seel, D.J. Wesolowski, and L.M. Anovitz.*** Phys. Rev. Lett., **116**, 167802 (2016).

CRITICAL RADIUS OF FULL DEPLETION IN SEMICONDUCTOR NANOWIRES CAUSED BY THE EXISTENCE OF SURFACE TRAPS

S.R. Nersesyan[1], V.A. Khachatryan[2]

[1]Institute of Radiophysics and Electronics, NAS RA, AlikhanyanBrs 1, Ashtarak 0203, Armenia
[2]Russian-Armenian (Slavonic) University, H. Emin Str.123, Yerevan 0051, Armenia.
E-mail: vars.khachatryan1990@gmail.com

Introduction

Among other nanostructures, semiconductor nanowires with a diameter on typically on the order of 10 *nm* to 100 *nm* and aspect ratios as high as 10^2, even without quantum size effects, offer exciting possibilities as building blocks for different photovoltaic devices, in particular, for photosensitive elements in highly integrated optoelectronic devices [1] and for third generation of solar cells [2]. Nanowire based photo detectors can yield higher light sensitivity than their bulk or thin film counterparts due to the large surface-to volume ratio and small dimensions comparable to the carrier diffusion length [3,4].

Because of inherently large surface-to-volume ratio, nanowires contain an extremely high density of surface states very often causing Fermi level pinning near the middle of the bandgap. Due to the exchange of electrons between the surface and volume and their trapping at surface states, nanowires can exhibit a depletion space charge layer with an extension of the order of the nanowire diameter or even inversion effects [5], which can strongly influence the electric and photoelectric characteristics of nanowires and nanowire based devices. Control of the depletion layer thickness is important for the operation of nanowire devices as field-effect transistors [6], photoconductive optical detectors [7] and solar cells [8]. To better understand these effects several solutions of Poisson`s equation have been presented [9] in order to provide a comprehensive model of nanowire surface depletion as a function of surface (or interface) state density and their energetic distribution, nanowire radius and doping level [5]. Because of interrelation between the surface states filling, potential and mobile charge radial variation and surface potential Poisson equation is not liner and must be solved self-consistently. In general all these theoretical calculations have shown that for the given doping level small diameters result in full-depletion of nanowires, thus minimize the dark current. Therefore it is important for many applications to establish simple analytical approach for estimating radius of full depletion in nanowires. Here we will present a simple approach to find the critical radius for full depletion in relationship to surface states density, ionization energy and bulk doping level.

Later we will assume that the nanowire radius R is greater than de Broglie wave length, so we can neglect in our calculations all quantum size effects.

The size dependent surface band bending and critical radius

Here we consider nanowire of n-type conductivity with uncompensated concentration of shallow donors N_D and acceptor-like recombination traps on the surface with the concentration N_s, capturing electrons from the volume. For the simplicity we assume that only one type of acceptor-like states with ionization energy E_s exists on the surface. The negative charge of surface states give rise to a positively charged depleted region, which is formed near the surface of the nanowire and has the width W. This causes surface band bending with the equilibrium potential barrier. The band bending diagrams for nanowires with different radiuses are illustrated in Fig. 1 [10].

The decrease of the nanowire diameter leads to its complete depletion at a critical radius R_c (Fig. 1.b). We must note that such situation is possible if N_s is enough large and all electrons from the volume of NW trapped by surface are not able to fill all surface states i. e $N_S > \frac{N_D R}{2}$. Further decreasing of the radius causes the reduction of surface potential barrier and the total space charge (Fig. 1.c). So the surface recombination barrier becomes size dependent.

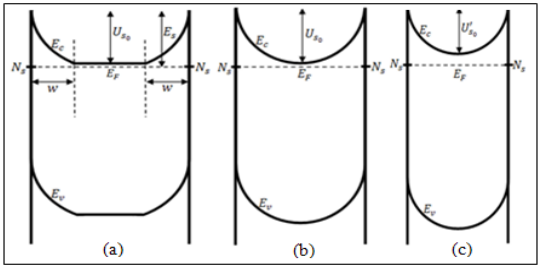

Fig 1. The band bending in nanowires with different radiuses.

To define the critical radius of nanowire we must solve the Poisson equation for the electrostatic potential $\varphi(r)$ in the space charge region $R - W \le r \le R$ written in the standard cylindrical coordinates:

$$\frac{1}{r}\frac{d}{dr}\left(r\frac{d\varphi}{dr}\right) = -\frac{eN_D}{\varepsilon\varepsilon_0},$$

where e is the elementary charge, ε_0 is the electric constant, ε is the dielectric constant of nanowire. We have the following boundary conditions;

$$\begin{cases} \varphi(R-W) = 0 \\ \varphi'(R-W) = 0 \\ \varphi'(R) = -\frac{en_s}{\varepsilon\varepsilon_0} \end{cases},$$

where n_s is the surface concentration of electrons and

$$n_s = \frac{N_s}{1+\exp\left[\frac{E_S - E_F}{kT}\right]}.$$

Here E_F is the Fermi level, k is the Boltzmann constant, T is the absolute temperature. Solving Poisson equation by using boundary conditions we get for $R_c(W = R)$

$$1 + \frac{N_C}{N_D}\exp\left[-\frac{E_s}{kT}\right]\exp\left[\frac{e^2 N_D R_c^2}{4\varepsilon\varepsilon_0 kT}\right] = \frac{2N_s}{N_D R_c},$$

where N_C is the effective density of states in the conduction band.
Now we can examine the dependence of critical radius of semiconductor nanowires on doping level, surface states density and their ionization energy (Figs. 2-4).

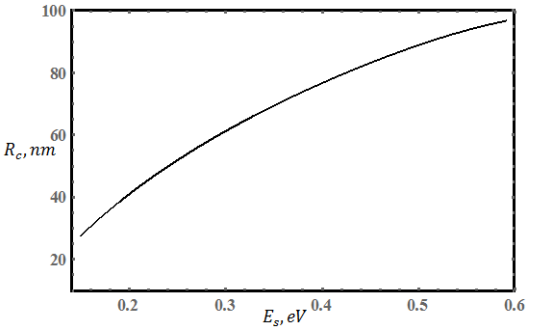

Fig. 2. Critical radius dependence on ionization energy of surface states for Si-nanowire ($N_s = 5x10^{11}sm^{-2}$, $N_D = 10^{17}cm^{-3}$).

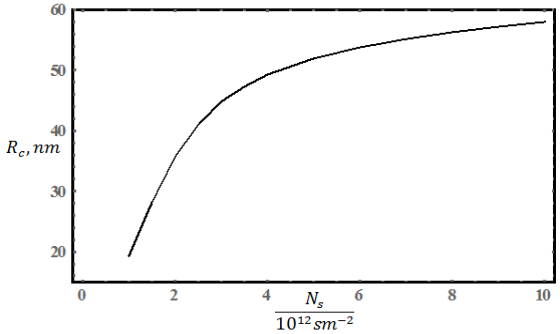

Fig. 3. Critical radius dependence on surface states concentration for Si-nanowire ($E_s = 0.25$ eV, $N_D = 10^{17} cm^{-3}$).

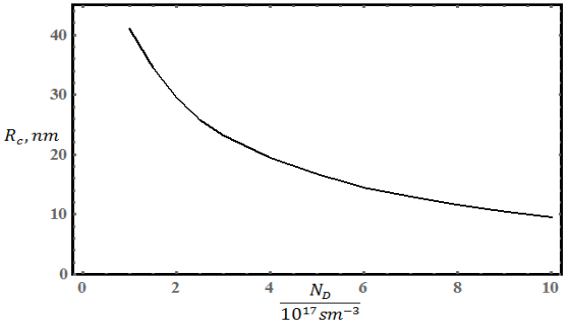

Fig. 4. Critical radius dependence on doping level for Si-nanowire ($E_s = 0.2$ eV, $N_s = 5x10^{11} cm^{-2}$).

Conclusions

When the radius of semiconductor nanowire is comparable with the Debye screening length there is a critical radius when the nanowire is fully depleted. The Poisson equation is solved to find potential distribution in nanowires as a result of surface depletion for different parameters of surface states. The dependence of critical radius on doping level, surface states density and their ionization energy is examined and it is shown that the change of that parameters has a great influence on the values of critical radius.

References

1. ***C. Soci, A. Zhang, X-Y.Bao, H. Kim et al.*** J. Nanosci. Nanotechnol., **10**, 1 (2010).
2. ***V. Sivakov, G. Andra, A.Gawlik et al.*** Nano Lett., **9**(4), 1549 (2009).
3. ***G Mariani, R.B. Laghumavarapu, B. Tremolet et al.*** Appl. Phys.Lett, **97**, 013107 (2010).
4. ***G Mariani, P.-S. Wong, A.M. Katzenmeyer et al.*** Nano Lett., **11**, 2490 (2011).
5. ***R-S.Chen, H.Y.Chen, C.Y.Lu et al.*** Appl. phys. Lett., **91**, 223106 (2007).
6. ***H. Kind, H.Yan, B. Messe et al.*** Adv. Mater. **14**(2), 158 (2002).
7. ***R. Calarco, M. Marso, T. Richter et al.*** Nano Lett., **5**, 981 (2005).
8. ***V. Schmidt, S. Senz, and U. Gosele.*** Appl. Phys. A:Mater. Sci.Process, **86**, 187 (2004).
9. ***B. S. Simpkins, M.A. Mastro, C.R. Eddy et al.*** J.Appl. Phys., **103**, 104313(1-6) (2008).
10. ***S.G. Petrosyan, S. Nersesyan, A. Yesayan.*** Arm. J. of Phy., **6**(2), 72 (2013).

GAS, BIO- & CHEMICAL SENSORS

NANOWIRES OF METAL OXIDES FOR GAS SENSING APPLICATIONS

E. Comini[1,3], D. Zappa[1], V. Galstyan[1], V. Sberveglieri[2] and G. Sberveglieri[1,3]

[1]*SENSOR, Dept. of Information Engineering, University of Brescia, Via Branze 38, Brescia, Italy*
[2]*CNR - Institute of Biosciences and Bioresources, Sesto Fiorentino Florence, Italy*
[3]*NANO SENSOR SYSTEMS srl, Via Branze 38, Brescia, Italy, giorgio.sberveglieri@unibs.it*

Abstract

Chemical **s**ensors based on metal oxides semiconductors are known since 1954 – 1962, when the effects of reaction of metal oxides with the surrounding atmosphere were discovered and the first commercial gas sensor was developed in Japan from FIGARO company. Since then they attracted the attention of researchers working on sensors thanks to low costs of fabrication, simple preparation and operation, large number of potential detections and applications together with the possible device miniaturization. Recently, the growing demand for Internet of Things (IoT) technology further pushed the requirements for the sensor community, including very low power consumption, low limit of detection, high sensitivity on a large spectrum of concentration, the long term stability, to name but a few. Also due to increasing interest for IoT applications the chemical research community produced more that 50000 publications only on sensor sensibility. Nanowires in particular present a high surface to volume ratio and lateral size comparable with the depletion region that provide a way to enhance the effects of surface phenomena, moreover they may be single crystalline and have well defined crystal orientations, leading to controlled reactions and increased stability. Metal oxide quasi-1D nanostructures have been prepared according to the recently proposed evaporation-condensation process with Vapour-Liquid-Solid growth mechanism, consisting of thermally-driven evaporation of bulk metal oxides followed by condensation and by the thermal oxidation method. Structural characterization has been performed in order to confirm the amount of material deposited on nanowires. Batches of conductometric sensors (chemiresistors) based on nanowires have been fabricated and tested towards different gases to compare their functional properties. To develop gas sensors featuring different response spectra, useful to gain selectivity through the exploitation of an Electronic Nose system, we followed two routes: i) the preparation of chemiresistors layers based on different oxides, namely SnO_2, ZnO, CuO; ii) the functionalization of nanowires with catalytic nanoparticles such as Au, Ag, CuO. To investigate the morphology of metal oxide nanostructures and the effectiveness of the functionalization process, a field-emission scanning electron microscope SEM LEO 1525 equipped with EDX detector was used (Figure 1 (a) – (d)). The different effect of the working temperature on the response to NO_2 and ethanol are shown in figure 2 (a) – (b) for ZnO and SnO_2 based gas sensors. Moreover, results on heterostructured nanomaterials (such as ZnO/NiO), and their functional properties will be discussed together with the exploitation of innovative transduction principles (optical and magneto-optical chemical sensors). As the next step to develop a more complete and performing sensing instrument, the talk will further focus on the integration of metal oxide gas-sensors in a portable and reliable instrument, often referred as electronic-nose (EN), based on an array of different sensors, whose collective response is handled by means of a pattern recognition software. In particular, the authors have developed, in cooperation with the spin off of University of Brescia Nano Sensor Systems srl, an EN called S3 (Small Sensor System). This allows to obtain selectivity and analysis capability also working with atmospheres as complex as those encountered in security ad food safety applications. In these fields, targets are not single molecules, but smells composed by hundreds (if not thousands) of compounds, whose analysis through analytical chemical techniques remain a challenge. The S3 EN has been successfully employed in various areas including food quality control and safety. Regarding food applications where including the diagnosis of microbial pathogens contamination. While regarding the security

filed the EN was applied for hidden-people detection, using its capability to detect odour related to human-sweat. To this aim, artificial sweat samples have been prepared starting from a chemical blend simulating the human-sweat environment and here inoculating bacteria typical of human-skin. Our results show the potentiality and flexibility of the proposed NWs MOX technology in both security field or food safety.

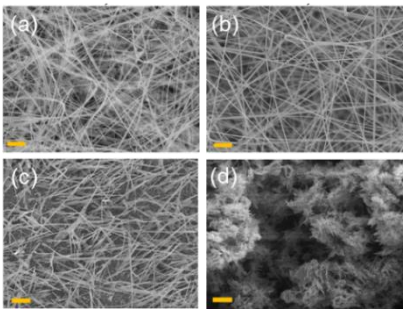

Fig. 1. SEM images of the different morphologies obtained for znc (a), tin (b) oxides prepared by thermal evaporation and copper (c) and zinc (d) oxides prepared by thermal oxidation (The bar is 1 micron). Sensor temperature effects on the ZnO and SnO_2 based gas sensors to ethanol (e) and NO_2 (f).

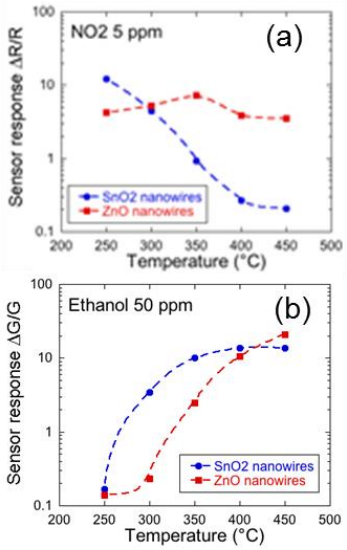

Fig. 2. Sensor temperature effects on the ZnO and SnO_2 based gas sensors to ethanol (a) and NO_2 (b).

Acknowledgement: This work was partially supported by the FP7 project N. 313110 "Sniffer for concealed people discovery (SNOOPY)"and the project N. 611887 "MSP: Multi Sensor Platform for Smart Building Management" by the European Community's 7th Framework Programme.

SMALL SENSOR SYSTEM (S3) DEVICE TO CONTROL FOODSTUFF FROM FARM TO FORK

E. Núñez Carmona[c], V. Galstyan[c], M. Soprani[c], V. Sberveglieri[a,b]
[a]CNR-IBBR, Via Madonna del Piano, 10, 50019 Sesto Fiorentino (FI), Italy
E-mail:veronica.sberveglieri@ibbr.cnr.it
[b]Nano Sensor Systems srl (NASYS), Via Brozzoni, 9, 25125 Brescia, Italy
[c]University of Brescia, Department of Information Engineering,
Via Branze, 38, 25123 Brescia, Italy

1. Introduction

Aroma is one of the most significant parameters of foods from the sensory point of view. The characteristic flavour of VOCs, so called fingerprint, may offer information about safety and quality of food, performing sometimes as an indicator of process mistakes as well.
Indeed, some volatile compounds can be originated from biochemical processes of food, as a consequence of technological food chain or product storage.
Unwanted smell, so-called off-flavour, may involve substances originating from the metabolism of spoilage microorganisms, bacteria, and fungi that adulterate naturally or unintentionally the products before or during its production. On the other hands consumers have become always more aware and interested about the quality and the safety of the consumed food. Microbial contamination creates a large amount of losses every year and a represent big challenge to the quality control labs. This can occur due to the contaminated or non-treated raw material or due to problems in the production plants.
An important part of the development of more efficient ENs is related to the progress in materials science. Focusing on metal oxide based chemiresistors, which are among the widest used sensors, in recent years metal oxides with nanowire structure have been proposed as effective materials for gas sensing applications.
In the last decade, electronic noses (EN) have become very popular as monitoring tools in evaluating food quality and safety.
In this paper, important applications of EN in food control were examined, concerning different relevant issues in the food field of food quality and control.

a) The water microbiological pollution represents one of the most hazard for the human health due to the pathogenic contamination.
b) The ripening process of high quality Parmigiano Reggiano PDO cheese that influences the quality and the authenticity of the cheese.
c) Microorganisms like *Listeria monocytogenes*, *Salmonella tiphymurium* and *Candida lbicans* that have the potentiality to create problems in the food industry, may also come from the human skin microbiota, called, cross-contamination.

Another main target of this work was to illustrate the broad spectrum of potential uses of sensor technology in this field and to show the potential of the new Nanowire technology.

2. Methods

2.1. Sensors preparation and electronic nose

The electronic nose used in the present work merges two metal oxide sensor technologies, namely thin films and nanowires.
Thin films have been fabricated according to the rheotaxial growth and thermal oxidation (RGTO) technique. Briefly, RGTO metal oxide layers are grown by deposition of the related metallic layer by means of sputtering using a 50 W power in argon pressure keeping the substrate at the temperature of 400◦C. The metallic film is then oxidized in two steps: a 4-h annealing at the temperature of 250 ◦ C followed by a 6-h treatment at 600◦C. Such a procedure was shown to be effective to promote the complete oxidation of the metallic layer and induce nanostructured morphology. Metal oxide nanowires were synthesized directly on the active transducers by evaporation-condensation technique.
Bulk tin and zinc oxide powder were placed in the middle of an alumina furnace at high temperature

(1370 ^{o}C) to evaporate the material. An inert gas flow (Argon, 100 sccm) was injected into the furnace, to move the cloud of material towards a colder region of the furnace (≈800 ^{o}C) where the substrates are located. Prior to nanowires synthesis, noble metal nanoparticles (platinum) were deposited on the substrates by RF magnetron sputtering as a catalyst for nanowires growth. The evaporated metal oxide material condensates on the substrates, forming a dense mat of nanowires. The pressure inside the furnace was set at 100 mbar, and the deposition time was 5 min. A new Small Sensors System (S3) model designed and built at SENSOR Laboratory, Brescia, Italy. This portable device consists of six MOS gas sensors as sensing elements, flow sensors, temperature and humidity sensors, and actuators (valves, pumps), all enclosed in a compact cell. The multi-sensor array was interfaced with an autosampler head space system HT280T (HTA srl, Brescia, Italy) which consisted of a 40-loading-site carousel and a shaking oven to equilibrate the sample head space (Fig. 1).

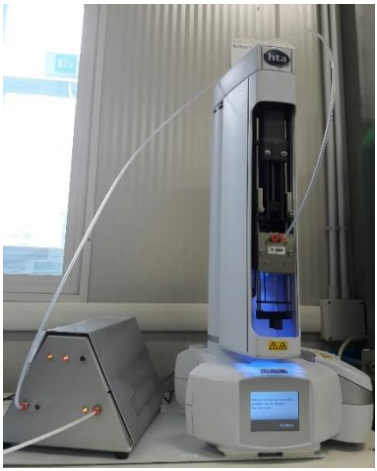

Fig. 1. Complete set-up showing the S3 sensor device connected with an HT280T autosampler head space system for cheese analysis.

This set-up has been applied to 3 different fields mentioned before are illustrated as follows:

a) In order to carry out the analysis, three samples have been used: drinking water from bottle, tap water and a pathogenic indigenous microorganisms' solution. The pathogenic microorganisms were isolated from river wastewater with the use of "filtration membrane" and therefore specific microorganism solution was developed depending on the incubation temperature, the incubation time and the selective culture medium.

b) Eight grated cheese samples of Parmigiano Reggiano from different provinces of origin, altitude zone, and different ripening times were procured from Consorzio del Formaggio Parmigiano Reggiano (CFPR), Reggio Emilia, Italy. The cheese samples were ripened for 11, 13, 18, 24, 30, and 36 months. They were stored at 4 °C before performing the color measurements, S3 analysis and sensory evaluation.

c) Different works have been addressed to investigate the most reliable receipt to prepare an artificial solution simulating the environment offered by human sweat to microbiota (Table1). Based on these works, one of the most accredited receipts is here adopted. Its composition is as follows:

–0,5%NaCl(w/v)(85mM),
–0,1%KCl(w/v)(13mM),
– 0,1% Lactic Acid (w/v) (17 mM),

– 0,1% Urea (w/v) (16 mM).
All the compounds should be diluted in distillate sterilized water. The pH of the solution was adjusted using NaOH solution 4 M, until it reached a pH of 5.5, which is the normal pH of the human skin.

Table. 1 Blend of microrganism used for the inoculation in artifical sweat.

BLEND	**KIND OF MICROORGANISMS**		
	BACTERIA	**YEAST**	**FUNGI**
MIX A	*Listeria Monocytogenes*	*Trichosporon spp.*	MMSI
MIX B	*Escherichia coli*	*Rhodotorula spp.*	FGO3
MIX C	*Salmonella enteritidis*	*Candida Albicans*	FGB2
CONTROL	CSS whit no microbial species inoculated		

i. Samples were diluted till reaching a measurable optical density (ODs).
ii. The optical density (ODs) of such diluted sample was measured at 600 nm.
iii. Using the McFarland Microbial Standard, it is possible to obtain the microbial concentration in the diluted sample. The number 3 of the McFarland Standards corresponds to 9 × 108 CFU/ml. It is necessary to measure also the OD of this solution (ODmf).
iv. To calculate the microbial concentration in the stock solution is enough to multiply for the dilution factor (DF).

3. Conclusions

In this work, metal oxide nanowire and RGTO thin film technologies have been merged into an electronic nose, which has been adopted to assist the analysis of microbiological growth in an artificial sweat solution, microbial development in water and quality standards of Parmigiano Reggiano. The achieved results show that depending on the headspace developed by the microorganisms and the cheese samples, the electronic nose can be used to discriminate the microorganism Blends from their medium (artificial chemical sweat), and to follow the different stages of the culture development microbial water contaminant, and provide information about the ripening and the production area of the Parmigiano Reggiano. These results open an important prospective for the exploitation of metal oxide and electronic nose technologies in different fields such as medicine, food safety and quality control.

References

1. ***E. Nunez Carmona, V. Sberveglieri, A. Ponzoni, V. Galstyan***, ***D. Zappa, A. Pulvirenti, E. Comini.*** Sensors and Actuators B, **238,** 1224 (2017).
2. ***V. Sberveglieri, E. Comini, D. Zappa, A. Pulvirenti, and E. Núñez Carmona.*** "Electronic nose for the early detection of different types of indigenous mold contamination in green coffee," Seventh Int. Conf. on Sensing Technology (ICST), Wellington, NZ, pp. 461-465, 2013.
3. ***V. Sberveglieri, M. Falasconi, E.Gobbi, E. Núñez Carmona, G. Zambotti, and A. Pulvirenti.*** Procedia Eng., **87**, 584 (2014).
4. ***E. Núñez Carmona, V. Sberveglieri, E. Comini, D. Zappa, and A. Pulvirenti.*** Procedia Eng., **87**, 1453 (2014).
5. ***E. Comini, C. Baratto, I. Concina, G. Faglia, M. Falasconi, M. Ferroni, V. Galstyan, E. Gobbi, A. Ponzoni, A. Vomiero, D. Zappa, V. Sberveglieri and G. Sberveglieri,*** "Metal Oxide Nanoscience and Nanotechnology for Chemical Sensor", Elsevier. Pp. 3-20.

Co-DOPED SnO_2 SENSOR FOR DETECTION OF CHEMICAL AGENTS

V.M. Arakelyan[1], M.S. Aleksanyan[1], A.G. Sayunts[1], G.E. Shahnazaryan[1], M. Vrnata[2], P. Fitl[2], J. Vičeк[2], K.S. Gharajyan[3], H.S. Kasparyan[3]

[1]Yerevan State University, Yerevan, Republic of Armenia, E-mail: kisahar@ysu.am
[2]University of Chemistry and Technology, Prague, Czech Republic
[3]National Bureau of Expertises SNPO, Yerevan, Republic of Armenia

1. Introduction

Threat of military operations and terrorist acts with application of chemical agents is not only maintained, but also unfortunately rises in the modern world. Two sarin gas attacks in Japan (Matsumoto and Tokyo, 1994-1995) and recent military operations in Syria confirm this horrible reality. Therefore, in all countries the researchers continue to investigate the possibility of developing of sensors for detection of chemical agents. Note that chemical agents include chemical warfare agents (e.g., sarin, soman, tabun, ethyl sarin, sulfur mustard, nitrogen mustard, hydrogen cyanide, arsine, chlorine, phosgene et.al.) and toxic industrial chemicals (hydrogen cyanide, nitrous oxide, carbon monoxide, dichloromethane, phosphorus pentafluoride et al.). Sensors for detection of chemical agents should be sensitive to very low concentrations of agents – considerably lower than immediately dangerous to life or health concentrations. Note also that because of extremely high toxicity of CWAs their handling in laboratory, when testing the related sensor, is very dangerous risk. Therefore, many researchers in place of SWAs usually utilize an appropriate simulants for the testing of sensor devices. For example, dimethyl-methyl-phosphonate is often studied as a simulant of nerve agents such as sarin and soman, 1,5-dichloropentane and di(propyleneglycol) methyl ether are considered as simulants of mustard gas (vesicants agents), acetonitrile known as a simulant for cyanide agents. Several techniques have been developed to detect the chemical warfare agents (CWAs) and toxic industrial chemicals (TICs) such as infrared spectrophotometry, raman spectroscopy, colorimetric indicators, ion mobility spectrometer and mass spectrometers combined with gas chromatographs. Several kind of gas sensors have been developed based on different sensing materials and various transduction platforms. The main classes of gas-sensing materials include metal oxide semiconductors, metal-oxide/polymer composite, carbon nanotube, graphene and other novel materials. Now arrays of chemically sensitive micro resistors produced from semiconductor metal oxide are considered as one of the most promising basic technologies for detection of chemical agents. These metal oxide based chemiresistive semiconducting sensors offer advantages such as their very low cost, high sensitivity, fast response and recovery times, easy in manufacturing, small size, simple electronic interface, low power consumption and portability [1-4]. SnO_2 is the most studied material and SnO_2-based gas sensors have been used to detect CWAs and TICs [5-8], but other semiconductor metal oxide such as TiO_2, WO_3, ZnO, CuO, In_2O_3 have also been considered [9-11]. In this paper we report about the development of technology and fabrication of a Co-doped SnO_2 nanostructured films based sensors for detection such CWAs as sarin and yperite, and such TICs as dichloroethane, dichloromethane, dimethylformamide and propylene glycol. The Co-doped SnO_2 thin films were

synthesized by the high-frequency magnetron sputtering method and their sensing properties were investigated.

2. Materials and measurements methods

Ceramic targets made of metal oxide SnO_2 doped with 2 at.% Co were synthesized by the method of solid-phase reaction in the air. The powders of initial oxides (SnO_2 and Co_2O_3) were weighed in the applicable quantities. This mixture was carefully intermixed and pressed. The compacted samples SnO_2<Co> were exposed to thermal treatment in the programmable furnace Nabertherm, HT O4/16 with the controller C 42. The annealing was carried out at 500 °C (five hours), 700 °C (five hours), 1000 °C (five hours) and 1100 °C (five hours) consecutive. Then, the synthesized compositions were subjected to mechanical treatment in the air in order to eliminate surface defects. Thus, smooth, parallel targets with a diameter ~ 40 mm and thickness ~ 2 mm were prepared.

Chemical composition of prepared SnO_2 <Co> targets was studied using Niton™ XL3t GOLDD+ XRF Analyzer. The results of this investigation have shown that the real content of cobalt's atom on the surface of the prepared ceramic targets was equal 1.3% (Fig. 1).

Prepared semiconductor SnO_2<Co> targets had sufficient conductance and were used for deposition of nanosize films using the high-frequency magnetron sputtering method. An alumina or Multi-Sensor-Platforms (purchased from TESLA BLATNÁ, Czech Republic) were used as substrate for films. In last case, when the Multi-Sensor-Platforms were used as substrates, the chip can be kept at constant temperature using heat resistance. The platform integrates a temperature sensor (Pt 1000), a heater and interdigitated electrode structures in platinum thin film on a ceramic substrate. Heater and sensor are covered with an insulating glass layer. Gas sensitive layer made of SnO_2<Co> was deposited onto the non-passivated electrode structures. That way the Multi-Sensor-Platform was converted into gas sensor. The following working conditions of the high-frequency magnetron sputtering were chosen: the power of the magnetron generator unit was 60 W; the substrate temperature during sputtering was 200 °C; duration of the sputtering process was equal to 20 minutes for SnO_2<Co>. The sensing device was completed through the ion-beam sputtering deposition of palladium catalytic

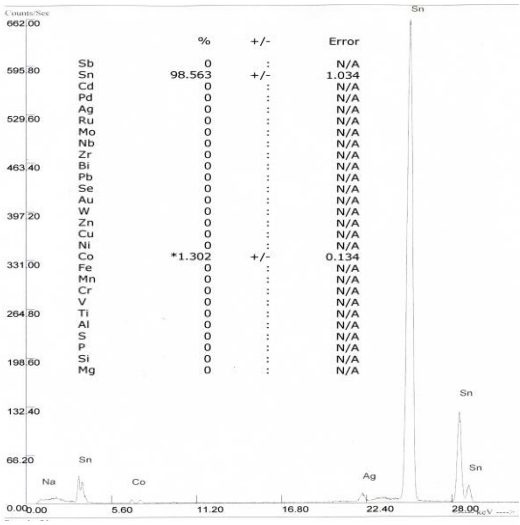

	%	+/-	Error
Sb	0	:	N/A
Sn	98.563	+/-	1.034
Cd	0	:	N/A
Pd	0	:	N/A
Ag	0	:	N/A
Ru	0	:	N/A
Mo	0	:	N/A
Nb	0	:	N/A
Zr	0	:	N/A
Bi	0	:	N/A
Pb	0	:	N/A
Se	0	:	N/A
Au	0	:	N/A
W	0	:	N/A
Zn	0	:	N/A
Cu	0	:	N/A
Ni	0	:	N/A
Co	*1.302	+/-	0.134
Fe	0	:	N/A
Mn	0	:	N/A
Cr	0	:	N/A
V	0	:	N/A
Ti	0	:	N/A
Al	0	:	N/A
S	0	:	N/A
P	0	:	N/A
Si	0	:	N/A
Mg	0	:	N/A

Fig. 1. The result of chemical analysis of the SnO_2<Co> target.

particles (the deposition time ~ 3 seconds). The interdigited gold contacts were deposited (the deposition time was 1 hour) by ion beam sputtering method on the surface of the sensing layers when the alumina substrate was used. Further annealing of the manufactured structures in the air was carried out at temperature 350 °C during 2 hours to obtain homogeneous films and eliminate mechanical stress.

The thickness of the deposited doped metal oxide films was measured by Ambios XP-1 profilometer (see Fig. 2). The thickness of the SnO_2<Co> films was equal 160 nm.

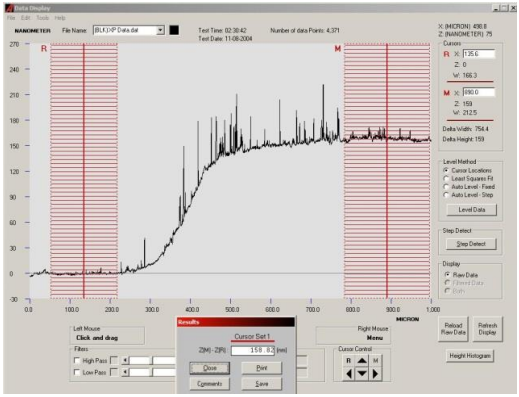

Fig. 2. The thickness measurement result for the Co-doped SnO_2 films.

Morphology of the deposited Co-doped SnO_2 films was studied by scanning electron microscopy using Mira 3 LMH (Tescan). The result of the study of morphology for the deposited doped metal oxide films is presented on the Fig. 3. The average size of nanoparticles was equal 18.7 nm.

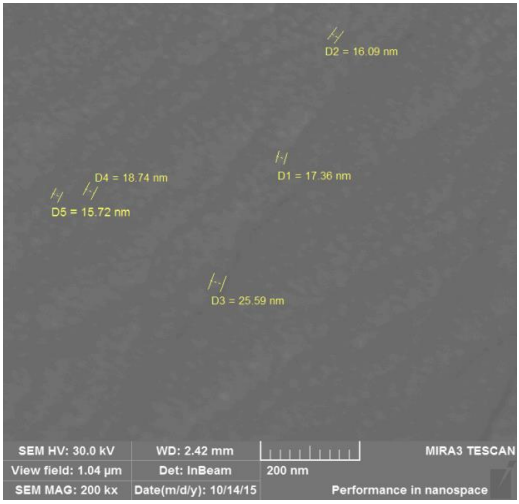

Fig. 3. The SEM image for the SnO_2<Co> films.

Gas sensing properties of prepared sensors made from Co-doped SnO_2 metal oxide films under the influence of TICs were measured in YSU using home-made developed and computer-controlled static gas sensor test system [12]. The sensors were reheated and studied at different operating temperatures. When the electrical resistance of sensors was stable, the vital assigned amount of compound in the liquid state for sensors testing was injected in measurement chamber by a microsyringe. Moreover, the target matters were introduced into the chamber on the special hot plate designed for the quick conversion of the liquid substance to its gas phase. After its resistance reached a new constant value, the test chamber was opened to recover the sensors in the air. The sensor on alumina substrate is put on the heater which allows raising temperature of the sensor

working body up to 350 °C. Testing of the SnO_2<Co> semiconductor sensors responses to the different gases such as dichloroethane, dichloromethane, dimethylformamide and propylene glycol vapors was carried out at the different operating temperatures (from room temperature up to 350 °C). All measurements were carried out at sensor applied voltage 0.5 V. Investigations of the sensitivity of the prepared sensors made of Co-doped SnO_2 films to CWAs such as sarin and yperite were carried out at University of Defence (Vyshkov, Czech Republic). Measuring system for gas sensor testing works as vacuum-type, where gaseous sample from sample bag flows through 3-way valve to glass measuring chamber and then through flowmeter to membrane pump, which generates vacuum. Sample bags are multi-layer foil chromatography bags (Supelco brand) with aluminum foil. Measuring glass chamber can be equipped by 4 different gas sensors connected via electrical feedthroughs. Resistance of sensitive layer is recorded by DC measurement by Agilent 34970A data logger unit with multiplexer card. Gaseous sample with concentration in ones of ppm are prepared by procedure, where in the first step we fill the sample bag with defined volume of ambient air (the same air we fill also to the second bag as reference), then we inject calculated volume of liquid agent by Hamilton syringe via septum to the sample bag. Sample bags were kept for at least an hour prior measurement until injected agent evaporates in the bag fully. Prepared sample bags with contain of agent and with reference air are connected to 3-way valve, by which we can switch desired atmosphere. These measurements were carried out at the operating temperature 210 °C.

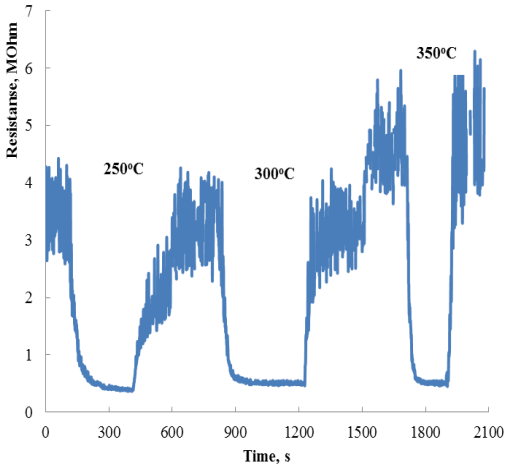

Fig. 4. The SnO_2<Co> sensor resistance variation under the influence 200 ppm of dichloromethane at different work body temperatures.

3. Results and discussion

We investigated the sensitivity of prepared SnO_2<Co> sensors to such TICs as dichloroethane ($C_2H_4Cl_2$), dichloromethane (CH_2Cl_2), dimethylformamide (C_3H_7NO) and propylene glycol ($C_3H_8O_2$). The sensors manufactured by us are resistive, i.e., their operation is grounded on changes in the resistance of gas sensitive semiconductor layer under the influence of target gas due to an exchange of charges between molecules of both the semiconductor film and adsorbed target gas. As known there are ions O_2^-, O^- and O^{2-} on the surface of semiconductor films. They originate due to electrons which are captured by adsorbed oxygen on the surface of oxide:

$$O_2\,(gas) \leftrightarrow O_2\,(ads), \quad (1)$$

$$O_2\,(ads) + e^- \leftrightarrow O_2^-\,(ads), \quad (2)$$

$$O_2^-\,(ads) + e^- \leftrightarrow 2O^-\,(ads), \quad (3)$$

$$O^-\,(ads) + e^- \leftrightarrow O^{2-}\,(ads). \quad (4)$$

The exchange of charges takes place between these surface oxygen species and target gas molecules. So, the reaction between oxygen species and dichloroethane, dichloromethane, dimethylformamide and propylene glycol can be simply described by reactions (5), (6), (7) and (8), respectively.

$$C_2H_4Cl_2 + 3O^- \rightarrow 2HCl\uparrow + 2CO_2\uparrow + H_2O\uparrow + 3e^-, \quad (5)$$

$$CH_2Cl_2 + 2O^- \rightarrow 2HCl\uparrow + CO_2\uparrow + 2e^-, \quad (6)$$

$$2C_3H_7NO + 21O^- \rightarrow 6CO_2\uparrow + 4NO_2\uparrow + 7H_2O\uparrow + 21e^-, \quad (7)$$

$$C_3H_8O_2 + 8O^- \rightarrow 3CO_2\uparrow + 4H_2O\uparrow + 8e^-. \quad (8)$$

A variation of the sensor resistance takes place variation of resistance was fixed as sensor response.

The typical curve demonstrating the changing of the sensor resistance under the influence of the target gas at invariable temperature of the work body is presented on the Fig. 4.

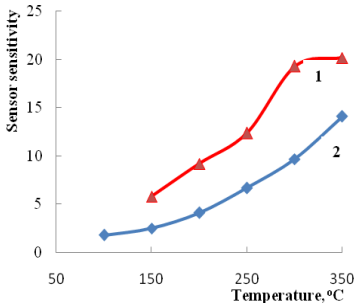

Fig. 5. The SnO_2<Co> sensor sensitivity dependence on temperature to 500 ppm dimethylformamide (1) and 350 ppm dichloroethane (2).

Fig. 5. The SnO_2<Co> sensor sensitivity dependence on temperature to 500 ppm dimethylformamide (1) and 350 ppm dichloroethane (2).

The sensor sensitivity was determined as the ratio R_{air}/R_{gas}, where R_{gas} is the sensor resistance in the presence of target gas in the air and R_{air} is the sensor resistance in the air without target gas. The dependence of the SnO_2<Co> sensor sensitivity to 350 ppm dichloroethane and 500 ppm dimethylformamide on temperature of the work body is presented on the Fig. 5. Investigated Co-doped SnO_2 metal oxide sensors demonstrate response to 350 ppm dichloroethane starting from 100 °C. The resistance of the SnO_2<Co> sensor was changed more than on order under the influence of 500 ppm dimethylformamide at operating temperature 300 °C. The SnO_2<Co> sensor sensitivity to 200 ppm dichloromethane and 650 ppm propylene glycol at different work body temperatures is presented on the Table 1. The response to 200 ppm dichloromethane and 650 ppm to propylene glycol was detected for prepared SnO_2<Co> sensors starting at 150 °C. The best sensitivity was achieved at operating temperature 200 °C and 300 °C to 200 ppm dichloromethane and 650 ppm to propylene glycol, respectively. The sensitivity of our SnO_2<Co> sensors to vapours of sarin and yperit was measured in the University of Defence (Vyskov, Czech Republic). As shown from the presented results of these measurements (Fig. 6 and Fig. 7), the sensor is exposed comparatively greater concentration of gas (200 ppm sarin and 100 ppm yperite) in the beginning of the measurements. Thus, the stabilization of the sensor parameters occurs. After that the SnO_2<Co> sensor was sensitive to yperite starting from 25 ppm. The sensitivity to 50 ppm and 12.5 ppm sarin were equal ~8 and ~15, accordingly, at the operation temperature 210 °C.

Table 1. The Co-doped SnO_2 sensor sensitivity

Temperature	dichloromethane (200 ppm)	propylene glycol (650 ppm)
150 °C	3.5	2
200 °C	36	22.7
250 °C	10.4	282
300 °C	9	417
350 °C	13.5	207

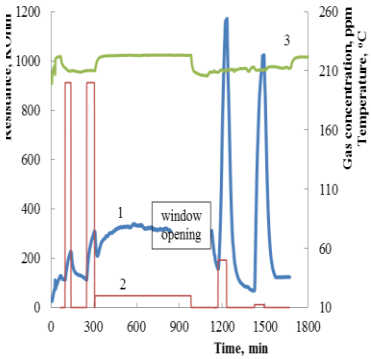

Fig. 6. The resistance variation under influence of sarin for the Co-doped SnO_2

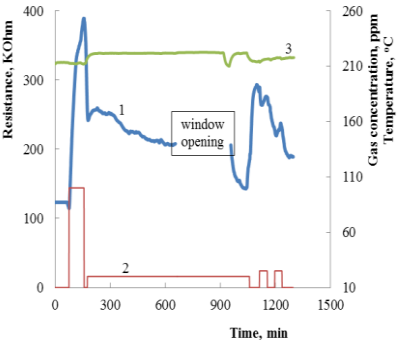

Fig. 7. The resistance variation under influence of yperite for Co-doped SnO_2 sensor (1). Curves (2) and (3) - gas concentration and work body temperature, accordingly.

3. Conclusions

The technology for the manufacturing of semiconductor sensor made of Co-doped SnO_2 was developed. Nanostructured films SnO_2<Co> were deposited onto the alumina substrate and Multi-Sensor-Platforms using the high-frequency magnetron sputtering method. The thickness of sensitive layer was measured; its chemical composition and surface morphology were studied. Specimens detecting CWAs and TICs were manufactured and investigated. The response of the prepared thin-film Co-doped SnO_2 sensors to different concentrations of sarin and yperite was measured at the operating temperature 210 °C. The responses to various TICs (propylene glycol, dichloroethane, dichloromethane and dimethylformamide) were measured at different temperatures of the SnO_2<Co> sensor work body.

Acknowledgments: This investigation was carried out within the framework NATO EAP SFPP 984597 project. Authors express gratitude to Dr. V. Kuzanyan for help in the measurements of thickness of our samples.

References

1. ***A.A. Tomchenko, G.P. Harmer, B.T. Marquis.*** Sensors and Actuators B, **108**, 41 (2005).
2. ***T. Alizadeh, L.H. Soltani.*** Sensors and Actuators B, **234**, 361 (2016).
3. ***L.A. Patil, A.R. Bari, et al.*** Sensors and Actuators B, **161**, 372 (2012).
4. ***E. Comini, C. Baratto, et al .***Sensors and Actuators B, **179**, 3 (2013).
5. ***S.C. Lee, H.Y. Choi, S.J. Lee, W.S. Lee, J.S. Huh, D.D. Lee, J.C. Kim.*** Sensors and Actuators B, **138**, 446 (2009).
6. ***N.J. Choi, J.H. Kwak, Y.T. Lim, et al.*** Sensors and Actuators B, **108**, 298 (2005).
7. ***S.C. Lee, S.Y. Kim, W.S. Lee, S.Y. Jung, et al.*** Sensors, **11**, 6893 (2011).
8. ***L. Liu, Y. Zhang, G. Wang, S. Li, L. Wang, Y. Han, X. Jiang, A. Wei.*** Sensors and Actuators B, **160**, 448 (2011).
9. ***G.N. Dar, A. Umar, S.A. Zaidi, et ali.*** Sensors and Actuators B, **173**, 72 (2012).
10. ***T. Alizadeh, L.H. Soltani.*** Sensors and Actuators B, **234**, 361 (2016).
11. ***R. Yoo, S.Yoo, D. Lee, J. Kim, S.Cho, W. Lee.*** Sensors and Actuators B, **240**, 1099 (2017).
12. ***A.Z. Adamyan, Z.N. Adamyan, et al.*** Intern. Journal of Hydrogen Energy, **32**, 4101 (2007).

MANUFACTURING AND INVESTIGATIONS OF HYDROGEN PEROXIDE VAPORS SENSOR

V.M. Aroutiounian[1], V.M. Arakelyan[1], M.S. Aleksanyan[1], G.E. Shahnazaryan[1], P. Kacer[2], P. Picha[2], J.A. Kovarik[2], J. Pekarek[2], B. Joost[3]

[1]Yerevan State University, Yerevan, Republic of Armenia, E-mail: kisahar@ysu.am
[2]University of Chemistry and Technology, Prague, Czech Republic
[3]Institute for Pharmaceutical Technology, Muttenz, Switzerland

1. Introduction

Hydrogen peroxide (H_2O_2) is subsumed under the category of matters that are dangerous for man with certain maximum permissible concentration. Therefore, the development of sensors for determination of the H_2O_2 concentration in the environment is important and attracts interest of chemists, physicians, industrial engineers, etc. The H_2O_2 stable sensors can be used in analytical chemistry, in various fields of the industry (food, textile, pharmaceutical), for an environmental control, in clinical diagnostic for prompt and reliable specification of diagnoses of different diseases and check of a course of treatment.

Several techniques have been developed for a reliable and sensitive detection of H_2O_2, such as chemiluminesce, fluorimetry, liquid chromatography, spectrophotometry and fluorescence. These techniques are complex, expensive and time consuming. Now the electrochemical sensors are wide used [1-6]. A large range of materials such as ferric hexacyanoferrate (Prussian blue) and other metal hexacyanoferrates, redox proteins, metallophthalocyanines and metalloporphyrins, transition metals and metal oxides have been applied in these sensors. Advantages of these sensors are simplicity of manufacturing, good response and a capability of control in a real time. In recent years, nanotechnology progress is promoted advance in the field of manufacturing of the H_2O_2 electrochemical sensors. For example, carbon nanotubes and graphene can be used either as substrates with high specific area for catalytic materials or as electrocatalysts by themselves. Note that process of chemical decontamination can be carried out in two different ways: the first is the wet approach using water or any other solution of H_2O_2 (certain concentration) and the second one is the dry method using H_2O_2 in vapor phase [7]. The correct selection of the H_2O_2 concentration during the sterilization of the equipment technological surfaces and also control of the H_2O_2 content in air after completion of disinfection cycle are very important. Therefore, the development and manufacturing of stable and reproducible sensors sensitive to H_2O_2 vapors are extremely required. The H_2O_2 vapor phase checking is also crucially significant in connection with counterterrorism efforts. The most used method is based on the determination of the concentration of H_2O_2 vapors after cooling down and being absorbed in the water. An amperometric sensor for detection of H_2O_2 vapors made of an agarose-coated Prussian-blue modified thick-film screen-printed carbon-electrode transducer was investigated [8]. Near infrared spectrophotometry was used for the monitoring of the concentration of H_2O_2 vapors in the course of sterilization [9]. It was reported about manufacturing of organic core/sheath nanowires with waveguiding core and chemiluminogenic cladding and manufacturing of organic single-wire optical sensor for H_2O_2 vapors [10]. The chemiresistive films made from organic p-type semiconductors phthalocyanines metalized with elements of p-, d-, and f-blocks were also sensitive to H_2O_2 vapors [11].

The aim of the present paper is development of technology, manufacturing and investigations of solid-state hydrogen peroxide vapors sensors made from semiconductor metal oxide nanostructured ZnO<La> films.

2. Experimental

Ceramic targets made of metal oxide ZnO doped with 1 at.% La were synthesized by the method of solid-phase reaction in the air in the programmable furnace Nabertherm, HT O4/16 with the

controller C 42. The following program of annealing for the compact samples of ZnO<La> was chosen: rise of temperature from room temperature up to 1300 °C for three hours, soaking at this temperature during four hours, further decrease in temperature for three hours prior to room temperature. Then, the synthesized compositions were subjected to mechanical treatment in the air in order to eliminate surface defects. Thus, smooth parallel targets with a diameter ~ 40 mm and thickness ~ 2 mm were manufactured.

Prepared semiconductor ZnO<La> targets had sufficient conductance and were used for deposition of films using the high-frequency magnetron sputtering method. An alumina or Multi-Sensor-Platforms (purchased from TESLA BLATNÁ, Czech Republic) were used as substrate for nanosize films. In last case, when the Multi-Sensor-Platforms were used as substrates, the chip can be kept at constant temperature using heat resistance. The platform integrates a temperature sensor (Pt 1000), a heater and interdigitated electrode structures in platinum thin film on a ceramic substrate. The heater and sensor are covered with an insulating glass layer. Gas sensitive layer made of ZnO doped with 1 at.% La was deposited onto the non-passivated electrode structures. This way the Multi-Sensor-Platform is converted into gas sensors. The following working conditions of the high-frequency magnetron sputtering were chosen: the power of the magnetron generator unit was 60 W; the substrate temperature during sputtering was 200 °C; the sputtering process was carried out during 15 and 30 minutes for preparing films with different thickness. The sensing device was completed through the ion-beam sputtering deposition of palladium catalytic particles (the deposition time was 3 seconds). The interdigited titanium contacts were deposited (the deposition time was 50 minutes) by ion beam sputtering method on the surface of the sensing layers when the alumina substrate was used. Further annealing of the manufactured structures in the air was carried out at temperature 250 °C to obtain homogeneous films and eliminate mechanical stress. The thicknesses of the deposited doped metal oxide films were measured by Ambios XP-1 profilometer. Morphology and chemical composition of the deposited ZnO<La> films were studied by scanning electron microscopy (SEM) using Mira 3 LMH (Tescan) and energy-dispersive X-ray spectroscopy using Quantax 200 with XFlash 6|10 detector (Bruker) with resolution of 127 eV, respectively. Response of the prepared sensors made of doped metal oxide films under the influence of H_2O_2 vapors was measured in YSU using a home-made system [12]. Sensors were placed in a hermetic chamber. A certain quantity of H_2O_2 water solution was placed in the chamber to reach a corresponding concentration of H_2O_2 vapors. Measurements of the manufactured sensors response (the sensor resistance changes under the H_2O_2 vapors influence) were carried out at different concentrations of H_2O_2 vapors. The sensor on alumina substrate is put on the heater which allows raising temperature of the sensor working body up to 350 °C. A platinum heater on a front side of the sensor on Multi-Sensor-Platforms ensures a necessary temperature of the work body. All measurements were carried out at sensor applied voltage 0.5 V.

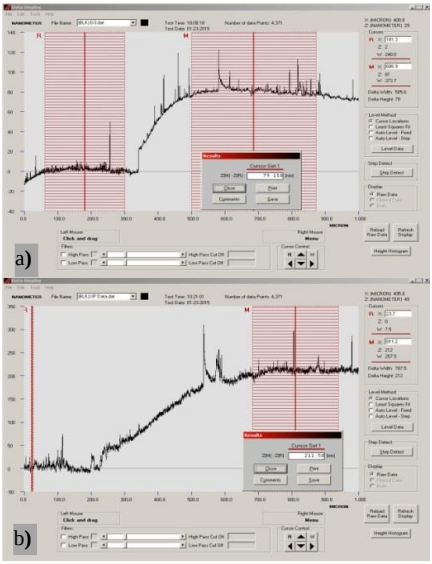

Fig. 1. The thicknesses measurement resultes for ZnO doped with 1 at.% La films with sputtering duration of 15 (a) and 30 minutes (b).

Investigations of the sensitivity of the prepared sensors to H_2O_2 vapors with concentration below than 100 ppm were carried out at University of Chemistry and Technology (Prague). In particular, the temperature dependence of sensitivity to 100 ppm H_2O_2 vapors was investigated. Measurements of the sensitivity of the ZnO<La> sensors to 10 ppm H_2O_2 vapors were carried out by the following way. Firstly, an atmosphere containing 10 ppm of H_2O_2 vapors was prepared in a laboratory model of an isolator. This H_2O_2 vapors concentration decreased by spontaneous decomposition of H_2O_2. When a reference device (Dräger Sensor® H_2O_2 HC) could not detect any H_2O_2 vapors, the sensor was inserted into the model isolator. Then, sensor responded immediately. When the maximum response was reached, the sensor was taken out into an atmosphere without any traces of H_2O_2 vapors. This process was repeated three times.

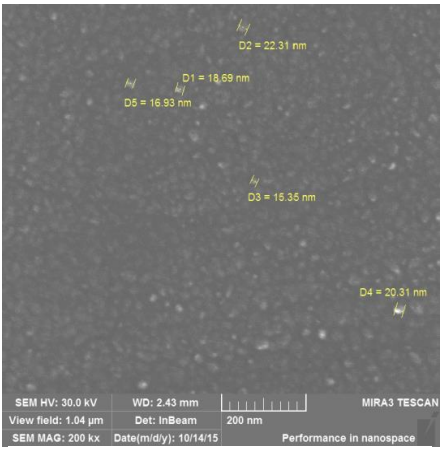

Fig. 2. SEM images for ZnO doped with 1 at.% La films.

3. Results and discussion

The thickness of the ZnO doped with 1 at.% La films prepared during 15 and 30 minutes was equals 80 nm and 210 nm, respectively (Fig. 1). Results of the study of morphology for the deposited doped metal oxide films are presented on the Fig. 2. The average size of nanoparticles was equal 18.7 nm. The sensor manufactured by us is resistive, i.e., its operation is grounded on changes in the resistance of gas sensitive semiconductor layer under the influence of H_2O_2 vapors due to an exchange of charges between molecules of the semiconductor film and adsorbed H_2O_2 vapors. A variation of the sensor resistance takes place as a result of such exchange of charges. This variation of resistance was fixed as sensor response.

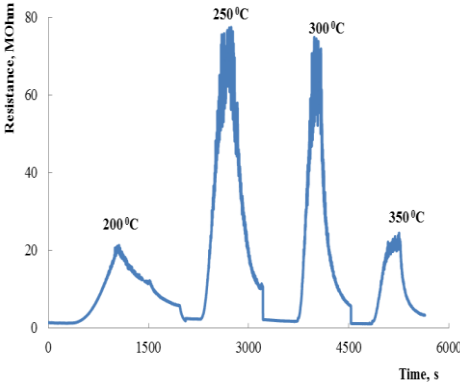

Fig. 3. The resistance variation of the ZnO<La> (80nm) sensor under the influence 1800 ppm of H_2O_2 vapors at different work body temperatures.

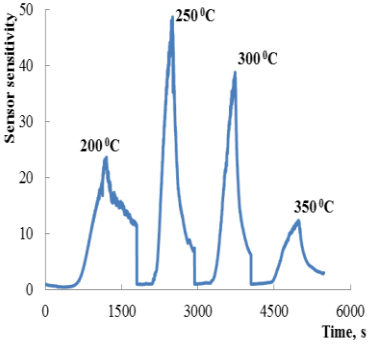

Fig. 4. The ZnO<La> (210 nm) sensor sensitivity to 1800 ppm of H_2O_2 vapors at different work body temperatures.

The sensor resistance variation under the influence of H_2O_2 vapors at invariable temperature of the work body was measured using a special home-made computer program. Results of such measurements are presented on the Fig. 3 for ZnO<La> (80 nm) sensors. The response and recovery times were determined as the time required for reaching the 90% resistance changes from the corresponding steady-state value of each signal and were equals on the average 6 and 10 minutes respectively at the pointed temperatures. The sensor sensitivity was determined as the ratio R_{vapors}/R_{air}, where R_{vapors} is the sensor resistance in the presence of H_2O_2 vapors in the air and R_{air} is the sensor resistance in the air without H_2O_2 vapors. The sensitivity of ZnO<La> (210 nm) sensor at different work body temperatures is presented on the Fig. 4. Note that the resistance of prepared sensors has changed in order of magnitude under influence of H_2O_2 vapors already at operation temperature 100 °C. However in such temperature a long time was needed for recovery of sensors parameters. Pulsed increasing of work body temperature is needed for decreasing of the recovery time of investigated sensors.

The sensitivity of the prepared sensors is decreased, when the working body temperature excesses some certain value (about 250 °C). An amount of matter, adsorbed on a surface and generally held by Van der Waals forces (physical adsorption), is decreased with the increase of temperature. More intensive exchange of electrons between the absorber and the absorbed matter takes place when the stronger chemical nature bond is established between them, originates at capping of electronic shells of both adsorbent and adsorbate atoms. Amount of chemisorbed matters increases with the temperature growth. Desorption prevails over the adsorption when a temperature is increased above certain value and, therefore, the sensor sensitivity is decreased. As it has already been noticed, H_2O_2 concerns to materials dangerous for man with certain maximum permissible concentration. The permissible limit of exposure 1.0 ppm has established by Occupational Safety and Health Administration (OSHA, USA) [10, 11]. It is immediately dangerous for life and health when its concentration reaches 75 ppm [13]. Therefore, the investigations of the prepared sensors sensitivity to H_2O_2 vapors with concentration below than 100 ppm were also carried out at University of Chemistry and Technology (Prague). The results of measurements of response to 100 ppm of H_2O_2 vapors at invariable temperature of the work body are presented on the Fig. 5 for the ZnO<La> sensors preparing on the Multi-Sensor-Platforms substrates. Results of these measurements show, that the structure made of ZnO<La> exhibits a response to 100 ppm of H_2O_2 vapors at the operating temperature starting at 100 °C. The ZnO<La> sensor exhibited enough response (sensitivity was equal ~ 2) to 100 ppm of H_2O_2 vapors at the operating temperature 200 °C. The investigations of the ZnO<La> sensors sensitivity to very low concentrations (0-10 ppm) of H_2O_2 vapors were carried out. The sensitivity to 10 ppm of H_2O_2 vapors was equal ~ 2 for the ZnO<La> sensors at the work body temperature 220 °C. Note that the DrägerSensor® H_2O_2 HC reference device was not sensitive to 10 ppm of H_2O_2 vapors (Fig. 6). The results of investigations of the sensitivity at different concentrations of H_2O_2 vapors are presented on the

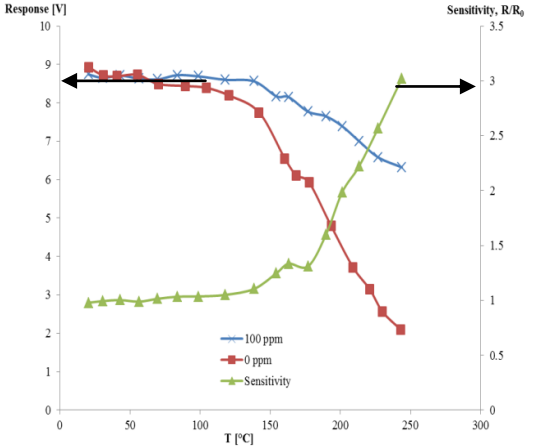

Fig. 5. The temperature dependence of sensitivity to 100 ppm H_2O_2 vapors for ZnO<La> sensor.

Fig. 7 for prepared made of ZnO<La> sensors. As can see, this dependence of sensors sensitivity on H_2O_2 vapors concentration has a linear character and can be used for determination of H_2O_2 vapors concentration.

3. Conclusions

The technology for the manufacturing of semiconductor sensors made from ZnO doped with 1 at.% La nanostructured films was developed. Sensitive ZnO<La> layers were deposited onto alumina substrate and the Multi-Sensor-Platforms using the high-frequency magnetron sputtering method. Thicknesses of deposited doped metal oxide films were measured and its morphology was investigated. The thicknesses of the deposited ZnO<La> films were equals 80 nm and 210 nm. The aaverage size of nanoparticles was equals 18.7 nm for both structures. Specimens detecting H_2O_2 vapors were manufactured and investigated. The sensitivity of the prepared sensors was measured at different temperatures of the sensor work body and concentrations of H_2O_2 vapors. It was found that La-doped ZnO sensors exhibit a good response to H_2O_2 vapors at the operating temperature starting at 100 °C. Sensors made of ZnO<La> were sufficient sensitive to 10 ppm of H_2O_2 vapors at the work body temperature 220 °C. It was established that the dependencies of the sensitivity on H_2O_2 vapors concentration at the operation temperature 220 °C have a linear character for prepared structured and can be used for determination of H_2O_2 vapors concentration. Our future work will be directed on the long-time stabilization of sensors parameters and the improvements of such characteristics as operation speed and recovery time.

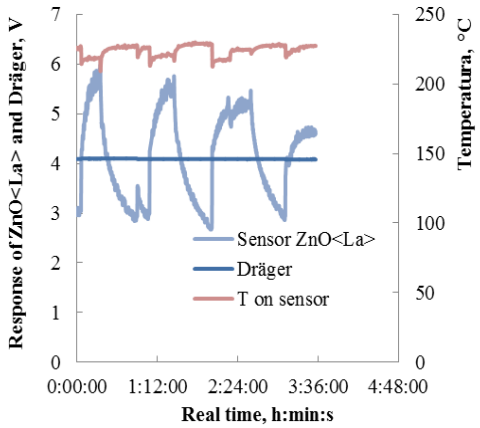

Fig. 6. ZnO<La> sensors response to 10 ppm of H_2O_2 vapors, work body temperature 220°C.

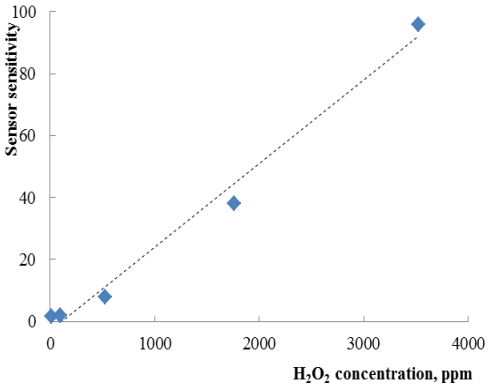

Fig. 7. The sensitivity dependence on H_2O_2 vapors concentration at operating temperature 220 °C.

Acknowledgments: This investigation was supported by the Swiss National Science Foundation FNSNF within the framework of the SCOPES DecoComp project. Authors express gratitude to Dr. V. Kuzanyan for help in the measurements of thickness of our samples.

References

1. ***W. Chen, S. Cai, Q.-Q. Ren, W. Wen, Y.-D. Zhao.*** Analyst, **137**, 49 (2012).
2. ***X. Chen, G. Wu, Z. Cai, M. Oyama, X. Chen.*** Microchim Acta, **181**, 689 (2014).
3. ***E.A. Puganova, A.A. Karyakin.*** Sensors and Actuators B, **109**, 167 (2005).
4. ***C.-Y. Lin, C.-T. Chang.*** Sensors and Actuators B, **220**, 695 (2015).
5. ***X. Yang, Y. Ouyang, F. Wu, Y. Hu, Y. Ji, Z. Wu.*** Sensors and Actuators B, **238**, 40 (2017).
6. ***Z.-L. Wu, C.-K. Li, J.-G. Yu, X.-Q. Chen.*** Sensors and Actuators B, **239**, 544(2017).
7. ***P. Kačer, J. Švrček, K. Syslová, J. Václavík, D. Pavlík, J. Červený, M. Kuzma.*** Organic pollutants ten years after the Stockholm Convention – environmental and analytical update, chapter 17, 399 (2012).
8. ***J. Benedet, D. Lu, K. Cizek, J. La Belle, J. Wang.*** Anal. Bioanal. Chem., **395**, 371(2009).
9. ***S. Corveleyn, G. M. R. Vandenbossche, J. P. Remon.*** Pharmaceutical Research, **14**, 294 (1997).
10. ***J.Y. Zheng, Y. Yan, X. Wang, W. Shi, H. Ma, Y. S. Zhao, J. Yao.*** Adv. Mater., **24**, OP194 (2012).
11. ***F.I. Bohrer, C.N. Colesniuc, J. Park, I.K. Schuller, A.C. Kummel, W.C. Trogler.*** J. Am. Chem. Soc., **130**, 3712 (2008).
12. ***V.M. Aroutiounian, A.Z. Adamyan, E.A. Khachaturyan, Z.N. Adamyan, K. Hernadi, Z. Palai, Z. Nemeth, L. Forro, A. Magrez, E. Horvath.*** Sensors and Actuators B, 177, 308 (2013).
13. ***J. Sun, C. Li, Y. Qi, S. Guo, X. Liang.*** Sensors, **16**, 584 (2016).

SYNTHESIS AND IMPROVEMENT OF SENSING PROPERTIES OF HIGHLY ORDERED TITANIA NANOSTRUCTURES FOR THE FABRICATION OF SMALL-SIZE SENSOR DEVICES

V. Galstyan[1,2], A. Ponzoni[1,2], E. Comini[1,2], V. Sberveglieri[3,4], N. Poli[1], G. Sberveglieri [1,2,4]

[1]Sensor Lab, Department of Information Engineering, University of Brescia, Via Valotti 9, 25133 Brescia, Italy
[2]Sensor Lab, CNR-INO, Brescia unit, Via Branze 45, 25123 Brescia, Italy
[3]IBBR-CNR, Via Madonna del Piano, 10, 50019 Sesto Fiorentino, Florence, Italy
[4]NANO SENSOR SYSTEMS srl, Via Branze 38, Brescia, Italy
E-mail: vardan.galstyan@unibs.it

Introduction

The importance of low-cost and small-size gas sensor devices is rapidly increasing for a wide range of applications, including detection of harmful chemical vapours and explosives in public spaces, government and military facilities, and chemical processing plants. Consequently, the development of the chemical gas sensors is a highly critical research area that involves health, safety and environmental risks. Metal oxide nanostructures have been extensively investigated for the applications in gas sensing devices because of their advantages, such as good chemical stability, low cost, easy production, simple measuring electronics, etc.[1] The conductance of the metal oxide materials is changed when oxidizing or reducing species in air chemisorb onto its surface. These conductivity changes are exploited for fabrication of conductometric chemical sensors. Among the transition metal semiconducting materials TiO_2 is one of the widely investigated structures for chemical sensing due to its excellent chemical and physical properties. Especially TiO_2 nanotubes with the large surface area have been considered as promising structures for the applications in gas sensors.[2] However, the improvement of the sensing performance of TiO_2 is remaining as a challenging issue for the fabrication of highly sensitive and small size sensing devices. Herein, we report the synthesis of pure and niobium (Nb) containing TiO_2 nanotubes and investigation of their gas sensing properties in a wide range of operating temperatures.

Experimental

The TiO_2 nanotubes were obtained by the electrochemical anodization of metallic Ti and Nb-Ti thin films deposited on alumina substrates. Then, the metallic films were anodized by potentiostatic mode using a two-electrode configuration. Anodization process was carried out at room temperature. The formation and the growth mechanism of the obtained tubular structures were investigated. Afterwards, the obtained samples were annealed at 400 °C. The morphological and the structural analyses of the obtained materials have been carried out. The sensing properties of the samples have been studied toward different gases, such as CO, H_2, NO_2, acetone and ethanol.

Conclusions

Well-aligned and highly ordered pure and doped TiO_2 nanotube arrays have been obtained by means of anodization of metallic films followed by post-growth annealing. Structural analysis of the samples confirms the presence of anatase in the structure. Investigations have shown that presence of Nb in TiO_2 has increased the gas sensing performance of prepared samples. Sensors were obtained without Pt, Pd or other catalytic layers. The obtained results showed that this low cost and low temperature fabrication method can be easily integrated into chemical sensor devices on a large scale platform. The fabricated sensors were also incorporated into the TO 39 case and installed in an array of other MOX sensors for applications in food quality analyses.

Acknowledgement: This work has been supported by the FP7 project N. 313110 “Sniffer for concealed people discovery (SNOOPY)” and the project N. 611887 “MSP: Multi Sensor Platform for Smart Building Management” by the European Community’s 7th Framework Programme.

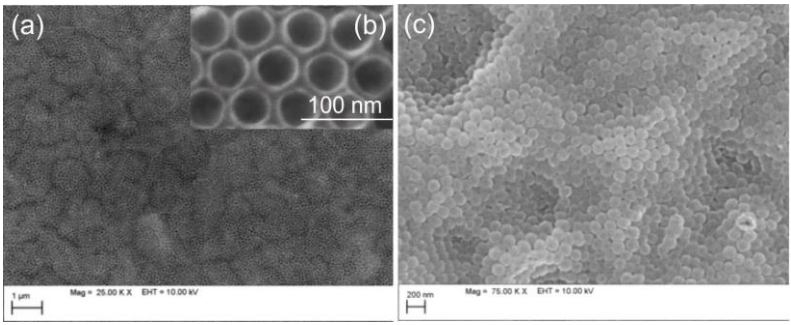

Fig. 1. (a) and (b) SEM images of the Nb-TiO_2 nanotubes with the different magnifications. (c) The bottom-view of the tubular arrays.

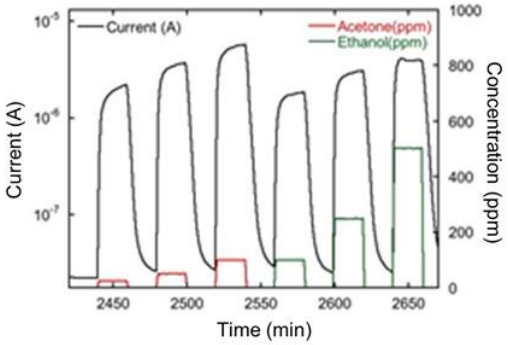

Fig. 2. Variation of the nanotubes conductance as a function of the introduction of different concentrations of acetone (10, 50 and 100 ppm) and ethanol (100, 250 and 500 ppm).

References

1. ***V. Galstyan, E. Comini, A. Ponzoni, V. Sberveglieri, G. Sberveglieri***. Chemosensors, 4(2), 6 (2016).
2. ***V. Galstyan, E. Comini, G. Faglia, G. Sberveglieri***. Sensors, **13**(11), 14813 (2013).

STUDY OF MWCNTs/SnO_2 NANOCOMPOSITE FORMALDEHYDE GAS SENSOR

Z.N. Adamyan, A.G. Sayunts, E.A. Khachaturyan, V.M. Aroutiounian

Center of Semiconductor Devices and Nanotechnologies at Yerevan State University, Yerevan, Armenia, E-mail:zad@ysu.am

Introduction

Formaldehyde (FA) is a colorless, water-soluble gas with a pungent odor which used in making building materials and many household products such as particleboard, plywood and fiberboard, glues and adhesives, textiles, paper and their product coatings. It is also used to make other chemicals. Formaldehyde is also used extensively as an intermediate in the manufacture of industrial chemicals. It can also be used as a preservative in some foods and in products, such as antiseptics, medicines, and cosmetics [1]. FA impacts on human organs when it exists in the air at levels higher than 0.1 ppm. For example, it can cause burning sensations of the eyes, nose, and throat, coughing, wheezing, nausea, skin irritation. Besides, exposure to relatively high amounts of formaldehyde can increase the risk of leukemia and even cause to some types of cancer in humans. But the effect of exposure to small amounts is less clear [2]. Hence, formaldehyde gas sensors have a huge application for detecting and continuous monitoring this gas, in the spheres where it is used. There are many formaldehyde gas sensors. For instance, FA gas sensors based on graphene or polymers which are working at room temperature [3,4]. On the other hand, FA gas sensors based on metal-oxide materials have advantages such as small sizes, low power consumption and price, repeatability and long reliability [5]. However pure metal-oxide structures react on FA at higher operating temperatures (300-400^{o}C) [6,7] or at room temperature with the assistance of UV LED [8,9]. Nanomaterial such as carbon nanotubes (CNTs) are widely used in gas sensing for their excellent responsive characteristics, mature preparation technology, and low cost of mass production. Due to the covering of CNTs walls with metal-oxide nanoparticles, specific surface area of such gas-sensitive nanocomposites increases more. Moreover, nanochannels in the form of hollows of CNTs promote penetration of gas molecules deeper down in the nanocomposite sensitive layer. Hence, it can be expected that application in gas sensors technology of nanocomposite structures composed of metal oxide functionalized with CNTs should lowering the gas sensor operating temperature [10].

The choice of tin oxide as a component of tin oxide multiwall (SnO_2/MWCNTs) nanocomposite structure is conditioned by the fact that SnO_2 is well known and studied basic material for metal-oxide gas sensors. We expected that coating of functionalized MWCNTs with SnO_2 nanoparticles with admissible, sizes should provide the improved performance of the gas sensor and lowered the temperature of its operating [5]. Here, we present the characteristics of the FA vapor sensors based on ruthenated thick-films MWCNT/SnO_2 nanocomposite structures.

Material and Samples Preparation

MWCNTs membranes, kindly provided to us by our colleagues from the University of Szeged, Hungary, were used for preparation of nanocrystalline MWCNTs/SnO_2 powder. MWCNTs were prepared by the decomposition of acetylene (CVD method) using Fe, Co/$CaCO_3$ catalyst [11,12]. This growth procedure using $CaCO_3$ catalyst enables a highly efficient selective formation of clean MWCNTs, suitable for effective bonding between CNT and metal-oxide, particularly, SnO_2 precursors.

For a functionalization of nanotube walls with oxygen-containing hydroxyl (OH), carbonyl (C=O), and carboxylic (COOH) functional groups, MWCNTs from the membranes were transferred to slurry in HNO_3/H_2SO_4 acids mixture during 1 h. Such a functionalization of the CNTs is very important and necessary for the following synthesis of SnO_2 nanoparticles on the MWCNTs walls since these oxygen-containing groups act as sites for the nucleation of nanoparticles. After rinsing with distilled water and drying at 80^{o}C, MWCNTs were poured and treated in deionized water in

the ultrasonic bath for 5 min. The preparation of SnO_2/MWCNT nanocomposite materials was carried out by a hydrothermal method. The purified MWCNTs is well dispersed in water via sonication. As a precursor solution, calculated amount of $SnCl_2 \cdot 2H_2O$ dissolved in water is used. The chose of water as a solvent, instead of e.g. ethanol, was preferably for us in the view of expected improvement in gas sensing characteristics, taking in account the fact that cover the overwhelming parts of CNTs with SnO_2 nanoparticles is ensured at that [13]. The target final mass ratio of the MWCNT/SnO_2 nanocomposite components for this study was chosen 1:200, respectively. This hydrothermal process described elsewhere in [14-16], in detail. SEM and TEM images of the sensors surface revealed that the average size of SnO_2 nanoparticles covered the nanotubes walls is about 14 nm. The thick films were obtained on the base of MWCNTs/SnO_2 nanocomposite powder. The paste for the thick film deposition made by mixing powders with α-terpineol ("Sigma Aldrich") and methanol was printed on chemically treated surface of the alumina substrate over the ready-made Pt interdigitated electrodes. The thin-film Pt heater was formed on the back side of the substrate. Obtained nanocomposite structures were cut into 3×3 mm pieces. After annealing and cooling processes, the MWCNTs/SnO_2 thick films were surface ruthenated by dipping its into the 0.01 M $RuOHCl_3$ aqueous solution for 20 min whereupon dried at 80°C for 30 min and then annealing treatment was carried out again at the same regime. The choice of the ruthenium as a catalyst was defined by its some advantages [14].

Results and Discussions

Gas sensing properties of the MWCNTs/SnO_2 nanocomposite structures were measured by home-made developed and computer-controlled static gas sensor test system [17]. The sensors were reheated and studied at different operating temperatures. When the electrical resistance of all studied sensors was stable, the vital assigned amount of compound in the liquid state for sensors testing was injected by a microsyringe in measurement chamber. Moreover, the target matters were introduced into the chamber on the special hot plate designed for the quick conversion of the liquid substance to its gas phase. After its resistance reached a new constant value, the test chamber was opened to recover the sensors in air. The sensing characteristics were studied in the 20-300°C operating temperature range and the gas response of the sensors determines as R_a/R_g where R_a and R_g are the electrical resistances in the air and in target gas-air atmosphere, respectively. The response and recovery times are determined as the time required for reaching the 90% resistance changes from the corresponding steady-state value of each signal.

Firstly, we should determine the operating temperature of the sensors. As a result of measurements of the sensor resistance in air and air/gas environment, the maximal response to 1160 ppm of FA vapor was revealed at 200°C operating temperature (Fig. 1). Dependence of the response and recovery times of MWCNTs/SnO_2 FA vapor sensor on operating temperature is shown in Fig.2.

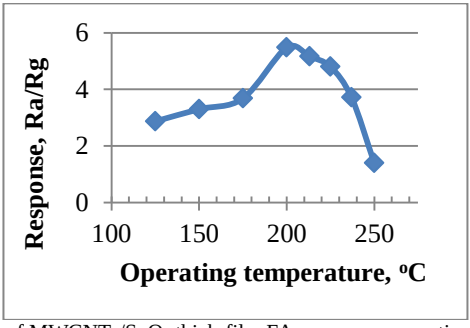

Fig. 1. Response of MWCNTs/SnO_2 thick-film FA sensors vs operating temperature.

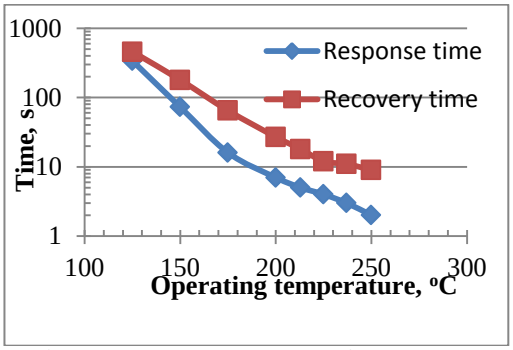

Fig. 2. Dependence of the response and recovery times of MWCNTs/SnO_2 FA vapor sensor on operating temperature.

Dependence of the resistance and response of MWCNTs/SnO_2 sensor on FA vapor concentration is shown in Fig. 3 and Fig. 4 respectively. As it is obvious from the figures, the sensor response occurs down to gas concentrations but the response approximately linearly depends on the gas concentration.

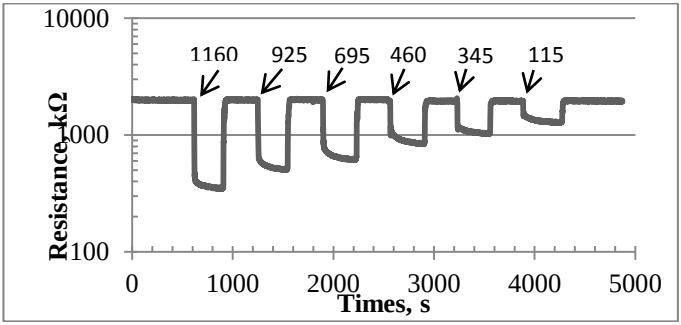

Fig. 3. The response/recovery curves observed at different FA gas concentrations (values of the ppm are mentioned within the picture) exposure measured at 200°C operating temperature.

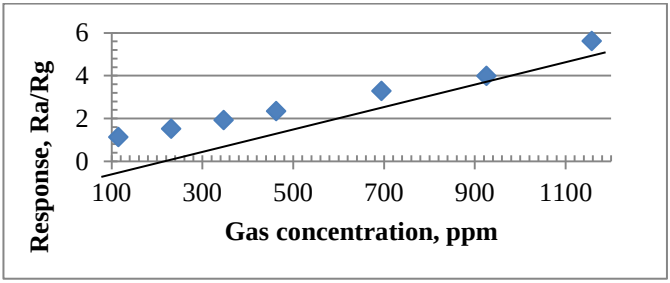

Fig.4. Dependence of the response of MWCNTs/SnO_2 FA vapor sensor on gas concentration measured at 200°C operating temperature.

FA gas sensing mechanism is not fully researched so far. It is proposed that the HCHO sensing process can be described by the commonly accepted gas sensing mechanism for n-type semiconducting metal oxides including SnO_2. Namely, as a result of adsorption-oxidation and desorption processes sensor surface is covered by chemisorbed oxygen ions, such as O^- and O^{2-}. When sensor exposed with FA gas HCHO molecules interact with the adsorbed oxygen according to the following reactions.

$$2O^- + HCHO \leftrightarrow H_2O + CO_2 + 2e^- ,$$
$$2O^{2-} + HCHO \leftrightarrow H_2O + CO_2 + 4e^- .$$

These reactions lead to enhance the free electron concentration which causes the decrease of the resistance of SnO_2. The role of carbon nanotubes in this case, apparently, is that the presence of nanotubes in the nanocomposite prevents the formation of SnO_2 agglomerates of nanoparticles, thereby providing a more developed and porous surface. In addition, hollow nanotubes facilitate the penetration of gas molecules into the interior of the nanostructured film and the yield of the products of the chemisorption reaction to the atmosphere. These facts lead to an increase in the sensitivity of the film to the acting gas, and to an improvement in the operation speed of the sensors (both the response and recovery times are on the order of seconds).

Conclusion

In this paper, we have carried out the investigation of obtaining ruthenated MWCNTs/SnO_2 thick-film nanocomposite sensors using hydrothermal synthesis and sol-gel technologies. The maximal response of FA vapor was revealed at 200^{o}C operating temperature. Response and recovery times of the sensors decrease with the increase in the operating temperature. The responses and short response and recovery times of the sensors (at the order of seconds) are observed under all gas concentrations influence at 200^{o}C operating temperature. The lowest FA gas concentration at which the perceptible signal ($R_a/R_g = 1.4$) is registered is 115 ppm.

Due to the linear dependence of the response on the concentration of FA gas, it is possible to easily measure the concentration of this gas in the atmosphere.

Acknowledgment: This work was supported by NATO EAP SFPP 984.597.

References

1. ***M.-A. Lefebvrea, W.J.A. Meulingb et al.*** Regulatory Toxicology and Pharmacology, **63**, 171, (2012)
2. ***L. Zhang, X. Tang, N. Rothman et al.***. Cancer Epidemiol Biomarkers Prev, **19**, 80, (2010)
3. ***W.-Y. Chuang, S.-Y. Yang, W.-J. Wu, C.-T. Lin.*** Sensors, **15**, 28842, (2015)
4. ***J. Flueckiger, F.K. Ko, K.C. Cheung.*** Sensors, **9**, 9196, (2009)
5. ***V.M. Aroutiounian.*** NATO Science for Peace and Security, Series B: Physics and Biophysics, Chapter 9, (2012)
6. ***K. Xu, D. Zeng, S. Tian, S. Zhang, C. Xie.*** Sensors and Actuators B, **190**, 585, (2014)
7. ***H.J. Park, N.-J. Choi et al***. Sensors and Actuators B, **203,** 282, (2014)
8. ***F.-C. Chung, R.-J. Wu, F.-C. Cheng.*** Sensors and Actuators B, **190,** 1, (2014)
9. ***X. Li, X. Li, J. Wang, S. Lin.*** Sensors and Actuators B, **219,** 158, (2015)
10. ***V.M. Aroutiounian.*** Journal of Contemporary Physics, **50**, 333, (2015)
11. ***E. Couteau, et al.*** Chem. Phys. Lett., **378**, 9, (2003).
12. ***A. Magrez, J.W. Seo, R. Smajda, M. Mionić, L. Forró.*** Materials, **3**, 4871, (2010)
13. ***Z. Nemeth, B. Reti, Z. Pallai et al.*** Phys. Status Solidi B, **251**, 1, (2014)
14. ***V.M. Aroutiounian, A.Z. Adamyan et al.*** Sensors and Actuators B, **177**, 308, (2013)
15. ***Z. Nemeth, Z. Pallai et al.*** J. of Coating Science and Technology, **1**, 137, (2014)
16. ***V. Aroutiounian et al.*** Int. J. of Emerging Trends in Science and Technology (IJETST), **01/08**, 1309, (2014)
17. ***A.Z. Adamyan.*** Izvestiya NAN RA and GIUA, Tekhnicheskie nauki, LIX, **1**, 155, (2006).

ADSORPTION OF CO MOLECULES ON SNO_2 (110), (100), (101), (001) SURFACE ORIENTATIONS: DENSITY FUNCTIONAL THEORY STUDY

H. Zakaryan

Yerevan State University, Yerevan, Armenia, E-mail: zhayk91@gmail.com

Introduction

Carbon monoxide (CO) is tasteless and transparent substance, which is known as an "invisible killer" due to the high level of toxicity. It is extremely poisonous and can even cause health effects up to a certain extent – 9 ppm, therefore, the detection of CO in the environment is quite vital. For the above reasons, chemical sensors are used to precisely monitor the concentration of the target compounds in the air. Usually, the SnO_2 semiconductor is used as a sensing material in such detectors, because of high sensitivity and low response time for wide variety of molecules, such as CO, H_2, CH_3OH, NO_x, etc. [1–2]. In order to increase the sensitivity of the detectors, it is crucial to deeply investigate adsorption mechanism of CO compounds.

Several models, which are named as Langmuir Hishelwood [3], Eley Redeal [4] and the MvK [5], have been developed to describe the mechanisms that are responsible for CO adsorption on oxide semiconductors. The MvK adsorbtion mechanism is in a good agreement with the experiments on SnO_2–(110) surface [6]. Apparently, the MvK mechanism consists of following steps; *I)* adsorbed CO molecule is reacting with tin dioxide oxygen and forms CO_2 compound, leaving oxygen vacancy in the material; *II)* then remained vacancy fills by adsorbed O_2 molecule from the environment; *III)* and finally, another CO molecule is reacting with already bonded O_2 and forms CO_2, leaving material in its initial undisturbed state.

We would like to stress that there are plenty of manuscripts dedicated to the investigation of CO absorption on SnO_2 surfaces, using first principle and ab initio DFT calculations [7]. Some calculations were done particularly for pristine (110) surface orientation, oxygen reach and tainted surfaces [8]. However, very few are devoted to other surface orientations (100), (101) [9] and (001). In practice, surface orientation immensely influences sensor parameters such as sensitivity, time response etc.

In this manuscript, we explore CO adsorption on various surface orientations (110), (100), (101), (001) of SnO_2 and determine the most optimal configurations for adsorption, using ab initio DFT calculations in order to shed the light on the atomic scale processes that still remains elusive and unclear. Here, we will rise following issues: *I)* Does MvK mechanism similarly describing adsorption processes for all surface orientations of SnO_2? *II)* What is the exact amount of charge transferred between the surface and adsorbed CO molecule? *III)* Which surface orientation is more prominent to the interaction with the CO molecule?

Models and computational methods

Calculations were done using conventional ab initio DFT [10] method implemented in Vienna ab initio Simulation Package (VASP) [11]. DFT relaxations were done within Perdew-Burke-Ernzerhof (PBE) generalized gradient approximation (GGA) [12]. The 500eV cutoff energy was chosen due to the total energy convergence from that value. Surface structures were relaxed until the threshold net force on atoms become less than 0.01 eV/A. The Monkhorst-Pack scheme was used to sample the Brillouin zone, using 6x6x1 k-points mesh. After relaxation, the Bader charge analysis was done to find out charge transfer [13].

Stable adsorbed configurations were found using the following equation:

$$E_{ads}=E_{surf}-E_{clean}-E_{CO}\,, \qquad (1)$$

where E_{ads} is adsorption energy, E_{surf} is total energy of SnO_2 surface and adsorbed CO, E_{clean} is total energy of pure surface without CO and E_{CO} is total energy of the gas molecule. It is clear from this equation that if E_{ads} is negative the configuration of adsorbed site is stable, in other words, the

process is exothermic. In the case of positive E_{ads}, the process is endothermic: the molecule will not adsorb to the surface and will remain in the non-interacting state.

Bulk SnO_2 has rutile, tetragonal structure, corresponding to the $P4_2/mnm$ space group. The lattice parameters of SnO2 from [14] are a = 4.82 Å, c = 3.23 Å and u = 0.607. In our calculations (see Fig. 1) each (110), (100), (101), (001) surface consists of 4 layers and relative stability has the following sequence (110), (100), (101), (001) [15].

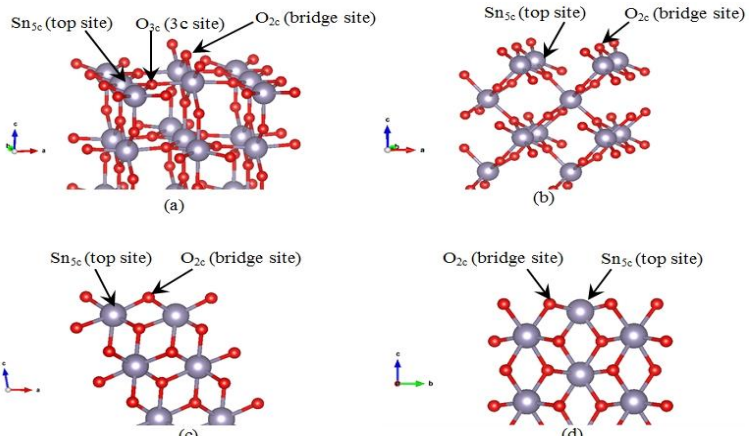

Fig. 2. Different surfaces of SnO_2 and possible adsorption sites on it: a) (110), b) (100), c) (101), d) (001).

Here, number of layers was tuned to check the convergence of surface energy. However, after getting all results, we double checked the obtained data by recalculating stable structures with a big substrate of 12 atoms of tin and 24 atoms of oxygen and make sure that the results are reliable. For all calculations, we choose vacuum thickness of 15 Å, which is greater than substrate thickness.

Results and Discussion

This SnO_2 (110) surface orientation consists of 4 layers, each comprising of 3 subsequent layers. Top sublayer represents oxygen, where each atom (O_{2c}) is connected by the covalent bond to 2 Sn atoms. The Second sublayer has 2 Sn atoms and 2 oxygen atoms. Third one is similar to the first layer. So, together these 3 sublayers can be treated as one layer which is continually repeated 4 times (see Fig1 a). There are 3 possible adsorption sites: top site (t), bridge site (br), three-coordinated oxygen site (3c). For each site, we consider 2 configurations: *I)* C atom in a CO molecule is closer to the surface (C down configuration) and *II)* the vice versa configuration (O down configuration). Thus, we end up with 6 possible configurations for (110) surface.

For each separate configuration we calculated adsorption energies, and found out that O down configuration for all surfaces is completely unstable. In the case of C down configuration, (110) surface has 3 stable sites. However, there is only one that is transferring the charge form molecule to the surface, and it is corresponding to the event when molecule approaches to br-site, reacts with oxygen and takes it away forming a CO_2 molecule and leaves oxygen vacancy on the surface (E_{ads}=-0.48 eV). Here, vacancy could be an adsorption site for O_2 or CO molecule, as described in [7]. The Bader charge analysis shows charge transport to the surface of 1.7e. Such processes examined in a number of experimental and theoretical studies [6]. It is important to note, that for this particular configuration and surface orientation the first step of MvK mechanism is preserved, and the distance between CO_2 molecule and surface is 3.1 Å. For other sites (top and 3c) the CO molecule does not exchange electrons, which serves as a confirmation that we have physisorption

process onto the surface. In these cases, distances from carbon to tin atoms are 2.46, 2.61 Å, respectively.

The unit cell of SnO2 (100) surface orientation, also consists of same 4 layers, where each layer can be divided into 3 sublayers: O-Sn-O layers. The top atom of the surface is 2 coordinated oxygen as in (110) surface, see Fig. 1 b. Adsorption energies for O_{2c} site is the minimal and equal -0.48 eV. According to the calculations interaction of CO with the O_{2c} site of oxygen leads to the formation of CO_2 molecule and also leaves a vacancy on the surface (Fig. 2 a). In this case, the first step of MvK mechanism is also conserved and it leads to charge transfer of 1.6e to the surface.

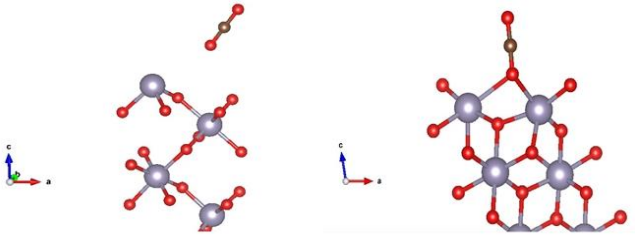

Fig. 3. (a) Desorbed CO_2 molecule from (100) surface: (b) Adsorbed CO on (101) surface (red circle is oxygen, grey is Sn, brown is C atoms)

The Second possible adsorption site is top(t) on Sn atom (E_{ads}=-0.16 eV). Here as for (110), the CO is physisorbed and no charge transfer has been observed. Due to physisorption, the distance from a carbon atom of CO molecule to the oxygen atom of the surface is 2.65 Å.

For the SnO_2 (101) surface orientation, each of 4 layers consists of 3 subsequent layers of 2O, 2Sn, 2O. There are 3 possible sites of adsorptions O_{2c}, Sn atom and 3 coordinated O, which is located in third sub layer as it is shown in Fig. 1 (c). Here, only one configuration has negative adsorption energy (E_{ads}=-0.47 eV) and it is O_{2c}. The CO molecule adsorbs by the surface and remains connected to it in O_{2c} site with a distance of 1.18 Å (see Fig. 2(b)). During that process, the distance between O_{2c} oxygen and Sn atom increases up to 2.5 Å. The Bader charge analysis shows that there is 1.9e charge transferred to the surface, which make it more conductive. Thus, adsorption mechanism on (101) surface differs from MvK, because no CO_2 desorption observed.

In the SnO_2 (001) surface case, we have a completely different situation. Instead of 4 layers that consist of 3 subsequent layers, we have got only one that consists of one atom of Sn and 2 oxygen atoms. There are two possible sites: on top of Sn (t) site and O_{2c} (2c) site Fig. 1 (d). Moreover, there are 2 equivalent 2c sites in one unit cell, thus we should take into account two possible coverage. The first is when both sites are occupied by the CO molecule (E_{ads}=-1.24 eV) and form one mono layer (ML=1) The second possible coverage is when only one site is occupied (E_{ads}=-1.19 eV) and half mono layer of CO forms (ML = 0.5). For ML = 0.5, carbon monoxide adsorbed and stay bounded with a distance of 1.16 Å (Fig. 3) to the O_{2c} atom, transferring 2e charge to the substrate.

For ML = 1, one CO molecule adsorbed and one physisorbed in a 1.255 and 2.6 Å distances, respectively. In fact, for (001) only ML=0.5 coverage can happen, because when one CO adsorbed, the second one will be physisorbed. Bader charge analysis shows that 1.83e was transferred to the surface. Physisorption occurs for the top site (E_{ads}=-0.19 eV) with distance 2.41 Å.

Conclusion

Previously, it was considered that adsorption on SnO_2 surfaces follows MvK mechanism; however, here we have proven that CO adsorption on SnO_2(101), (001) is different. Here, the C atom of the

CO molecule remains bonded to surface's O atom. For (110) and (100) surfaces, we establish that adsorption obeys MvK mechanism, where its first stage CO_2 molecules are forming during CO-surface interaction. For all adsorption cases, O down configuration was not stable, due to positive adsorption energy.

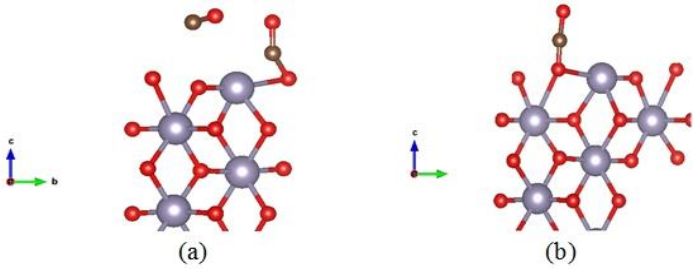

Fig. 4. Adsorption when ML=1. (b) eDoS before and after adsorption, when ML=1 (b) Adsorption when ML= 0.5 (d)

The Bader charge analysis reveals that charge transfer to (101), (001) surfaces are 1.9e, 2e respectively and 1.7e, 1.6e for (110), (100) surfaces. The Bader analysis shows that (101), (001) surface orientations gather more electrons than the rest orientations, thus, those should be considered as a better platform for the interaction of the CO molecules with SnO_2 surfaces. We believe that our findings will pave the way for the fabrication of SnO2 based CO sensors with higher sensitivity and lower response time.

Acknowledgements: This work was supported by NATO project Science for Peace [Ggrant numbers 984597]. We are grateful to Prof. Artem Oganov for opportunities to perform the DFT calculations on the Rurik supercomputer at Moscow Institute of Physics and Technology (State University).

References

1. ***V. Aroutiounian***. Int. J. Hydrog. Energy. **32,** 1145 (2007).
2. ***V.M. Aroutiounian.*** Lith. J. Phys., **55,** 319 (2015).
3. ***R.H. Nibbelke, M.A.J. Campman, J.H.B.J. Hoebink, G.B. Marin***. J. Catal., **171**, 358 (1997).
4. ***C.C. Cheng, S.R. Lucas, H. Gutleben, W.J. Choyke, J.T. Yates***. J. Am. Chem. Soc., **114** 1249 (1992).
5. ***P. Mars, D.W. van Krevelen.*** Chem. Eng. Sci., **3,** 41 (1954).
6. ***Y. Sun, F. Lei, S. Gao, B. Pan, J. Zhou, Y. Xie.*** Chem. Int. Ed., **52,** 10569 (2013).
7. ***Z. Lu, D. Ma, L. Yang, X. Wang, G. Xu, Z. Yang.*** Phys Chem. Phys., **16,** 12488 (2014).
8. ***Y.B. Xue, Z.A. Tang***. Sens. Actuators B Chem., **138,** 108 (2009).
9. ***S. Gong, J. Liu, J. Xia, L. Quan, H. Liu, D. Zhou***. Sci. Eng. B., **164,** 85 (2009).
10. ***P. Hohenberg, W. Kohn***. Phys. Rev. **136,** B864 (1964).
11. ***G. Kresse, J. Hafner***. Phys. Rev., B. **47,** 558 (1993)–561.
12. ***J.P. Perdew, K. Burke, M. Ernzerhof***. Phys. Rev. Lett., **77,** 3865 (1996).
13. ***G. Henkelman, A. Arnaldsson, H. Jónsson.*** Comput. Mater. Sci., **36,** 354 (2006).
14. ***T.T. Rantala, T.S. Rantala, V. Lantto***. Surf. Sci., **420,** 103 (1999).
15. ***C. Xu, Y. Jiang, D. Yi, S. Sun, Z. Yu***. J. Appl. Phys., **111,** 063504 (2012).

STABILIZATION AND LINEARIZATION OF HIGH RESISTANCE GAS SENSOR'S OUTPUT CHARACTERISTIC

B.O. Semerjyan

Yerevan State University, Yerevan, Armenia
E-mail: semicsemer@ysu.am

Introduction

One of the major advantages of high resistance gas sensors (HRGS) based on MWCNT/S_nO_2 nanocomposite is the relatively high variation of the output parameter. However, HRGS have several specific features making the processing of gas registration and measurement results difficult. These features involve distribution of resistance at very low registration values of gas concentration (P), and considerable non-linearity of load characteristic as a result of inversely proportional character of transformation function from gas concentration to resistance [1]. Elimination of these unfavorable characteristics is possible to perform in input measurement circuits through proportional changing of HRGS conductivity to electric signal.

Gas sensor shunt effect on its output characteristic

HRGS resistance (R) shunting by constant resistance R_{sh} leads to significant change in loading characteristics as $R=f(P)$ (P – gas concentration in air) (Fig. 1a). Index of shunting (shunt characteristic) is a ratio: $g=R/R_{sh}$, which is determined at $R=R_0$. Equivalent resistance of two-terminal "HRGS-Shunt" is $R_1^1=RR_{sh}/(R+R_{sh})$. At absence of HRGS gas environment $R_{sh} \ll R$, then $R_1 \approx R_{sh}$. The latter means that two-terminal resistance with HRGS at air environment without registered gas is determined by shunt resistance. Consequently, HRGS shunting make it possible to eliminate zero uncertainty. The major disadvantage of shunting is the decrease of HRGS sensitivity. Value of relative sensitivity variation – β is detected at P_{nom} (nominal concentration of detected gas):

$$\beta = \frac{\Delta R_1/R_1}{\Delta R/R} \times 100\% , \quad (1)$$

where $\Delta R_1 = R_1 - R_1^1$; R_1^1 - two-terminal's resistance with HRGS at air environment with registered gas.

Expressing

$$R_{sh} = R/g;\ R_1 = R/(1+g) \quad \text{and} \quad S_R = \Delta R/R, \quad (2)$$

where S_R is the relative variation of HRGS resistance. It is followed that:

$$\Delta R_1 = R\Delta R/[R + g(R - \Delta R)]\,(1+g) = RS_R/[1 + g(1 - S_R)](1+g) \quad (4)$$

and

$$\beta = R \times 100\%/[R + g(R - \Delta R)] = 100\%/[1 + g(1 - S_R)] \times 100\% . \quad (5)$$

Obviously, along with reduction of shunt resistance (with increasing g) the nonlinearity of characteristic is sharply reduced at values $g \leq 5$ (at $g = 5$ nonlinearity decreases twice). Further increase in g will lead to slow decrease of nonlinearity.

Wheatstone bridge circuit design

Essential distinguishing feature of nanocomposites-based HRGS is the instability of R_0 and high values of $\Delta R/R_0$ which alter the design method and the parameters of the circuit. Consequently, in Wheatstone bridge circuit design for HRGS considers mainly the optimal value of shunt R_{sh}, expressing the highest sensitivity at the least nonlinearity of the load characteristic of HRGS.

Output signal voltage - U_C in the bridge circuit is determined by expression

$$U_C = E\left(\frac{R_1 - \Delta R_1}{R_1 - \Delta R_1 + R_2} - \frac{R_3}{R_3 + R_4}\right), \quad (6)$$

where E is the bridge supply voltage; $R_1 - R_1 R_2, R_3, R_4$ are the bridge arms' resistances (Fig. 1a).

Consider an example of the Wheatstone bridge parameters circuit design with "HRGS-Shunt" two-terminals included in one of the bridge arms with symmetry relatively to diagonal of power supply,

i.e. $R_1 = R_3$ and $R_2 = R_4 = mR_1$. According to [2] nonlinearity of bridge output characteristic N(m) is determined from equation:

$$N(m)=(4+m)\Delta R_1/4(1+m)R_1\ . \tag{7}$$

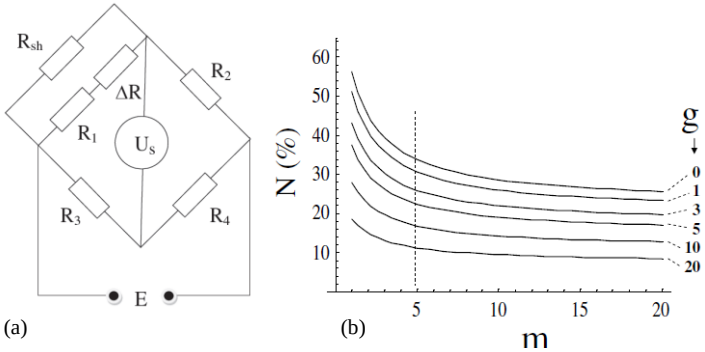

Fig. 1. (a) The Wheatstone bridge circuit with gas sensor ($R_1 + \Delta R$) and (b) the dependence of nonlinearity of the bridge circuit output characteristic on parameter m at different values of g.

Substituting expression (4) in (7), we receive:

$$N(m)= (4+m)\,\Delta R/4(1+m)[R+g(R-\Delta R)] = (4+m)\,S_R/4(1+m)[1+g(1-g(1-S_R)]. \tag{8}$$

If $R= 0.5G\Omega$ and $\Delta R/R = 0.9$, we can construct $N= N(m)$ dependence plot at several values of g (Fig. 1b). From received family of curves we can obtain m on assumption of reasonable N-value of output characteristic's nonlinearity. Obviously, the higher is the m (at prescribed value of g), the less is the nonlinearity of the characteristic. However, increase of m above 10÷20 is undesirable since the characteristic nonlinearity N decrease is insignificant, while E-power supply voltage of the circuit sharply increases. Hence, the choice of m value of the bridge is limited by power supply voltage. Determination of power supply voltage of bridge circuit is performed based on HRGS operating current value I:

$$E = I(R-\Delta R) + (I+I_{sh})R_2, \tag{9}$$

where I_{sh}- current in shunt R_{sh}. It is obvious,

$$I_{sh} = \frac{I(R-\Delta R)}{R} = I(1-S_R)g. \tag{10}$$

Expressing R_2 in

$$R_2 = mR/(1+g) \tag{11}$$

and making the substitution (10) into (9), it is obtained that:

$$E= I[(\mathrm{R}-\Delta R) + \frac{mR+(R-\Delta R)gm}{1+g}]=IR\left\{(1-S_R) + \frac{m[1+g(1-S_R)]}{1+g}\right\} = Ir\ . \tag{12}$$

Hence, the bridge power supply voltage is a function of both HRGS operating current and circuit common resistance r depending on bridge parameters, particularly, the coefficients m and g. To set the bridge power supply voltage ($R= 0.5G\Omega$ and $\Delta R/R = S_R = 0.9$) we construct dependence $r=r(m)$ at several values of g (Fig. 2a). It follows from the graph that along with increase of m there is significant elevation of r as well as the bridge power supply voltage.

The output signal voltage bridge of measuring diagonal at HRGS resistance altered from R to $\mathrm{R}-\Delta R$ and the internal resistance of registering voltmeter $R_l = \infty$, can be determined from expression (6). After substitution of (2), (3) and (10) into (6), we receive:

$$U_S = \frac{Em\Delta R}{(m+1)\Delta R-(m+1)^2[R+g(R-\Delta R)]} = E\frac{mS_R}{(m+1)S_R-(m+1)^2[1+g(1-S_R)]} = EK(m). \tag{13}$$

Analogously with preceding construction (R= $0.5G\Omega$ and $S_R = \Delta R/R = S_R = 0.9$) we construct graphs of K= $K(m)$ dependence at several values of g (Fig. 2b) and determine expected value of signal voltage. For example, if m= 5, g= 5, I= $50nA$, then E= $30V$, K= 0.093, and $U_S = 2.78V$.

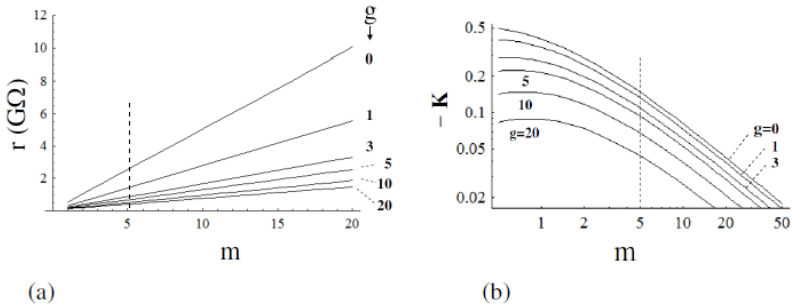

Fig. 2. The dependence of the bridge circuit common resistance r (a) and coefficient K (b) on parameter m at different values of g.

Conclusions

The Wheatstone bridge parameters (the nonlinearity of output characteristic N, the common resistance r, the power supply voltage of circuit E and the output signal voltage U_s) are calculated with two-terminal "HRGS-Shunt" included in one of the bridge arms with symmetry relatively to diagonal of power supply in dependence on m= R_2/R_1 at several values of g= R/R_{sh}. From received family of curves we have obtained terms for HRGS performance linearization at preserved considerably high gas sensitivity and stability that permits applying standard electronics for registration of bridge readings.

Acknowledgement: The author wishes to thank Dr. Z.N. Adamyan for fruitful discussion.

References

1. ***V.M. Aroutiounian, A.Z. Adamyan, E.A. Khachaturyan, Z.N. Adamyan, K. Hernandi, Z. Pallai, Z. Nemeth, L. Forro, A. Magrez, E. Harvath.*** Sensors and Actuators B: Chemical, **177**, 308(2013).
2. ***Л.С. Ильинская.*** Полупроводниковые тензодатчики, М., Энергия, 1975

BIOCHEMICAL SENSORS BASED ON SILICON NANORIBBON FETs Part 1: Samples Fabrication, CVCs, pH-sensitivity

F. Gasparyan[1,2], I. Zadorozhnyi[2], H. Khondkaryan[1], A. Arakelyan[1], S. Vitusevich[2]

[1]Yerevan State University, 1 Alex Manoogian St., 0025, Yerevan Armenia
[2]Peter Grünberg Institute (PGI-8), Forschungszentrum Jülich, 52425 Jülich, Germany

1. Introduction

Over the past decade, nanosized silicon structures have been under intensive study due to their promising electrical, optical, chemical, thermal and mechanical properties. Compared to larger structures, nanoscale field-effect transistors (FET) are capable of measuring electrical, optical and other types of very small signals due to increased surface-to-volume ratio of the sample. The small sizes of nanostructures make them ideal for sensing of small sample volumes with low analyte concentrations. For example, in the field of medical diagnostics an incredibly small volume structures aiming the integration of 1D nanostructure such as carbon nanotubes, metallic and semiconducting nanowires (NW) and nanoribbons (NR) can be utilized for a variety of applications. Among the mentioned structures, silicon nanoribbon (NR) and nanowire (NW) field – effect transistor (FET) structures open prospects for label-free, real-time and high-sensitive detection of biomolecules using affinity-based detection [1]. The sensitivity of different NR dimensions was studied in [1]. It was illustrated that the new integrated NR sensor with reference NR can be utilized for real-time error monitoring during pH-sensing [1]. New features and functions are continuously added to the electronic devices, i.e. health monitoring mobile systems and wearable devices. Despite the success of such personal health monitoring systems [2], the next generation of wearable devices is expected to include also a portable "lab-on-a chip" – set of medical biosensors which can be used for the detection and diagnosis of various medical conditions[3,4]. In order to be able to monitor and detect the early stages of disease, the size of the sensor transducer has to be comparable with the biological markers. Therefore biosensors based on NWs and NRs have to be capable to monitor the biological events that occur at very small dimensions. Another important area of application is optoelectronic, where the interaction of different wavelengths of light with nanostructures may be used for future optical device applications. Sub-wavelength diameters and proximity effects may lead to interesting optical properties such as low reflectance and thus high absorption. Investigations of SiNW optical absorption have shown the strong size-dependent effects [5,6]. Studies of the broadband optical absorption showed increased total optical adsorption spectra for SiNW samples [7]. SiNWs lead to a significant reduction of the reflectance compared to the solid silicon films [7,8]. Optical absorption increases while the wavelength decreases. It should be noted that, unlike the bulk material, nanosized Si structures may be direct band gap semiconductors. Such properties make them excellent choice for optical applications [6,9-12]. On the other hand, the size scaling brings to the increased band gap [9]. This may result in a successful shift of the absorption spectra to short wavelengths [6,12]. With size decrease the limitations regarding current and voltage have also be considered. For devices operating at weak signal levels internal noise plays crucial role [13-15]. It determines one of the most important parameters of sensors - signal-to-noise ratio (SNR). As it is shown for double gated SiNW sensors pH-sensitivity increases with the liquid gate voltage and SNR has higher value (~10^5) [6,12]. The nanoribbon approach opens up for large scale CMOS fabrication of highly sensitive biomolecule chips for potential use in medicine and biotechnology [16].

The present work is devoted to the study of silicon nanoribbons-based FETs and consists of two parts. In the first part, the sample fabrication technology, and chip characterization - their dark

and light current-voltage characteristics (CVC) and pH-sensitivity are presented. In the second part low-frequency noise studies, size-dependent effects of the pH-sensitivity and source-drain currents are described. We demonstrate that silicon nanoribbons, in this case, a thin sheet of silicon on an oxidized silicon substrate, can have high pH-sensitivity fairly close to the Nernst limit.

2. Samples and experimental technique

Silicon nanoribbon (NR) structures were fabricated on the basis of silicon-on-insulator (SOI) wafers purchased from SOITEC. The process starts from the thermal oxidation to form 20 nm thick silicon oxide hard masks. The active silicon layer thickness is 50 nm. NRs of various geometries are then patterned in hard mask using optical lithography with following reactive ion etching process step. The pattern is transferred into silicon using wet chemical etching in the tetramethylammonium hydroxide (TMAH) solution. Gate dielectric which also serves as a channel protection from liquid environment was thermally grown 8nm thick silicon oxide. The NR channel was almost undoped Si NR channel with hole concentration of 10^{15} cm^{-3}. Source and drain contacts were highly doped to form good ohmic contact. For the connection to electronics Aluminum contacts were patterned using a lift-off process. Finally chips were passivated with polyimide layer to protect metal feed lines from liquid environment.

3. CVCs and pH-sensitivity

Figures 2 and 3 show source-drain current-voltage characteristics (CVCs) of samples under study measured at back gate voltages of -1V and -5 V, correspondingly. Characteristics measured in the dark conditions as well as under specific power illuminations of 0.85 W/cm^2 and 1.6 W/cm^2 at room temperature. Light excitation is performed using incandescent lamps located at a distance of 15 cm from the sensor. The CVC dependencies demonstrate typical behavior which is similar to the solid silicon FET CVCs [17] since the samples under investigation have relatively large dimensions of $l \times w \times t = (2 \div 10) \times 10 \times 0.05$ μm (l, w and t are the channel length, width and thickness, correspondingly). Presented in Figs. 2-3 CVCs can be described as:

$$I_{ds} = I_{ds,d} + I_{ds,ph}, \quad (1)$$

where $I_{ds,d}$ and $I_{ds,ph}$ are the dark and photo current components. Dark current can be described by the well-known expression of CVC for the n-channel MOSFETs for $V_{ds} \le V_{gs} - V_{th}$ [17]:

$$I_{ds,d} = \frac{w\mu_n C_{ox}}{l}\left(V_{gs} - V_{th} - \frac{V_{ds}}{2}\right)V_{ds}. \quad (2)$$

Here $C_{ox} = \varepsilon_{ox}/t_{ox}$ is the oxide layer capacitance per unit area, ε_{ox} and t_{ox} are the permittivity and thickness of the gate oxide layer, V_{gs} and V_{th} are gate-source and threshold voltages.

In the approximation the Eq. (2) can be applied for the n-channel. We can present photo current as following:

$$I_{ds,ph} = A_{ch} e\mu_p \Delta p \frac{V_{ds}}{l} = A_{ch} e\mu_p \eta\alpha\tau_p \frac{W}{h\nu}\frac{V_{ds}}{l}. \quad (3)$$

Here $A_{ch} = wt$ is the current channel cross-section area, Δp the concentration of excess photo carriers (holes), α the illumination absorption coefficient, η the quantum yield, τ_p the hole's life time, $h\nu$ the photon energy, W the illumination specific power in [W/cm^2].

In Eq. (3) we assumed that the electric field strength is uniformly distributed along the channel length and the value of A_{ch} slightly varies along the length of the channel. It should be noted that this assumption is valid in the main part of the channel, which is far from source and drain contacts.

At low voltages V_{ds}, the source-drain current I_{ds} grows approximately linearly with voltage and tends to saturation at high voltages. The magnitude of the I_{ds} increases, with increasing light specific power. Figs. 4-5 shows CVCs of the investigated device at the several front gate voltages (V_{FG} = -1 V, -5 V) measured in an aqueous solution with pH= 6.2, 7 and 8.3. We can see that increasing of the pH-value results in the increase of the channel current, I_{ds}. This is in a good agreement with model of the solution contact with the oxide layer surface, then on the oxide/solution interface caused hydroxyl groups SiOH. Concentration and behavior of those

hydroxyl groups depends on value of the pH. The case when the surface is not charged is called zero charge point. For the SiO_2 dielectric layer the point is reached at $pH_0 = 2.2$. At the pH-values lower pH_0 the oxide surface is charged positively, at higher values of the pH, oxide surface is charged negatively. In the case of buffer solution with pH = 7 silicon oxide surface charge will be charged negatively, correspondingly Therefore, at the applied negative gate potential the absolute value of the negative charge on the surface oxide increases. As a result, the concentration of the majority carriers in the current channel (holes in p-Si) and therefore current increases.

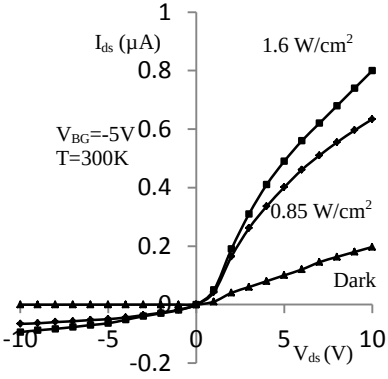

Fig. 2. Output CVCs of SiNR FET sample with length $l = 10$ μm, measured in the dark and at excitation by the light specific power 0.85 W/cm^2 and 1.6 W/cm^2 at V_{BG} = -1V, T = 300 K.

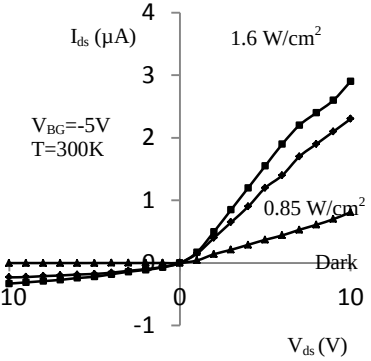

Fig. 3. Output CVCs of SiNR FET sample with length $l = 10$ μm, measured in the dark and with excitation by the light specific power 0.85 W/cm^2 and 1.6 W/cm^2 at V_{BG} = -5 V, T = 300 K.

Figures 4 and 5 show the CVCs of the SiNR structures working in biochemical sensing mode. In [18] pH-sensitivity of the biochemical sensors was introduced as

$$R_{pH} = \frac{R_{ch}\Delta I_{ds}}{\Delta pH}. \quad (4)$$

Here ΔI_{ds} and ΔpH are the elementary changes in I_{ds} and pH. Note that pH-sensitivity is the measurable value. In the solution medium with the increased pH value the source-drain current increases. This allows the registration of the pH variation in any bio liquids with high accuracy. For example, for $V_{BG} = -5$ V at the V_{ds}=5 V the sensitivity is equal to R_{pH}≈56.4 mV/pH. At the $V_{BG} = -10$ V the pH-sensitivity grows up to 59.3 mV/pH and approaches the Nernst limit 59.5 mV/pH [19]. The pH-sensitivity grows with increase of back-gate voltage. For example from Figs. 4 and 5 at the V_{ds}=8 V we obtained the ratio $(R_{pH})_{V_{BG}=-5\,V}/(R)_{V_{BG}=-1\,V} \approx 5.17$, i.e. approximately 5 times improved sensitivity.

4. Conclusion

Silicon nanoribbon FET biochemical sensors of various lengths were fabricated. Their static dark and light-induced CVCs as well as the behavior of these sensors in an aqueous solution with different values of pH are investigated. The static dark CVC dependencies show that the characteristics correspond to high quality silicon FET CVCs. With increasing light intensity, the source-drain current grows because of the increase in the conduction of the current channel. The pH-sensitivity increases with the increasing of the back gate voltage and approaches to the Nernst limit of 59.5 mV/pH.

Acknowledgments: This work was supported by the SCS MES of Armenia in the framework of research Project No. 15T-1C 279. F. Gasparyan greatly appreciates the support from the German

Academic Exchange Service (DAAD) in the form of a research grant. The authors would like to acknowledge for the Innovation Award of RWTH Aachen University in the framework of RWTH transparent 2016.
The list of used literature is given in the second part of this work.

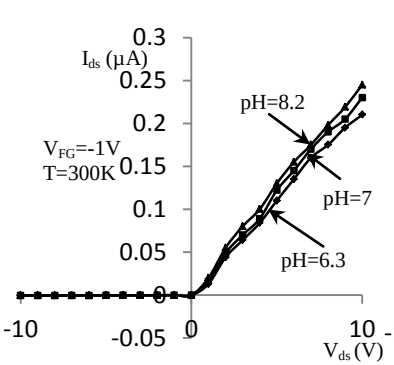

Fig. 4. Output CVCs of SiNR FET with length $l = 10$ µm, measured in the dark and pH concentrations 6.3, 7, 8.2 at V_{FG} =-1 V, T =300 K.

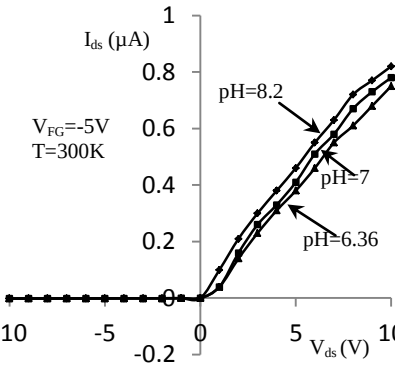

Fig. 5. Output CVCs of SiNR FET with length $l = 10$ µm, measured in the dark and pH concentrations 6.3, 7, 8.2 at V_{FG} =-5 V, T =300 K.

BIOCHEMICAL SENSORS BASED ON SILICON NANORIBBON FETs
Part 2: Low-frequency noise and size-dependent effects

F. Gasparyan[1,2], I. Zadorozhnyi[2], H. Khondkaryan[1], A. Arakelyan[1], S. Vitusevich[2]

[1]*Yerevan State University, 1 Alex Manoogian St., 0025, Yerevan Armenia*
[2]*Peter Grünberg Institute (PGI-8), Forschungszentrum Jülich, 52425 Jülich, Germany*

1. Low-frequency noise properties

The noise spectra of Si NR structures were measured at the constant current in the ohmic CVC mode. Figure 6 shows the source-drain current low-frequency (LF) noise spectral density measured in dark conditions as well as under irradiation at back gate voltage of $V_{BG} = -1$ V and $I_{ds} = 0.1$ μA. Noise spectra, measured in dark, demonstrate $1/f^{\gamma}$ noise behavior with noise parameter equal to $\gamma = 1$. LF noise level rises with the increase of the light irradiation intensity. The increase of the illumination intensity results in the growth of the majority carrier's concentration. This in turn causes the growth of mobility fluctuations in the channel because of increased interaction and scattering rates as result of: first, scattering between carriers and secondly between the carriers and acoustic phonons, as well as on different impurity traps [20].

As the noise measurements were performed at the constant current in the ohmic CVC mode, the channel resistance linearly changes with the applied voltage V_{ds}. As it is known the $1/f$-noise spectral density is proportional to the voltage in power 2:

$$S_V = \frac{\alpha_H V_{ds}^2}{N R_{ch}^2 f^{\gamma}} = \frac{\alpha_H V_{ds}^2}{p\Omega R_{ch}^2 f^{\gamma}} = \frac{\alpha_H V_{ds}^2}{R_{ch}^2 f^{\gamma}} \frac{e\mu_p \rho}{Al} = \frac{\alpha_H V_{ds}^2}{f^{\gamma}} \frac{e\mu_p}{l^2} \frac{1}{R_{ch}} \propto \frac{1}{R_{ch}}, \quad \frac{f^{\gamma} S_V}{V_{ds}^2} \propto \frac{1}{R_{ch}}. \tag{6}$$

Here R_{ch} is the current channel resistance; Ω, A and l is the volume, the cross-section area and the length of the current channel, respectively; μ_p is the majority carriers (holes) mobility and ρ is the channel specific resistance. The decrease of the channel resistance leads to growth of the noise spectral density. At the light excitation of NR FET sample with the special power W we have:

$$S_{V,L} = \frac{\alpha_H V_{ds}^2}{N R_{ch}^2 f^{\gamma}} = \frac{\alpha_H V_{ds}^2}{p\Omega R_{ch}^2 f^{\gamma}} = \frac{\alpha_H V_{ds}^2}{\Omega f^{\gamma}} \frac{1}{p(\rho l/A)^2} = \frac{\alpha_H V_{ds}^2}{\Omega f^{\gamma}} \frac{A^2\sigma^2}{pl^2} = \frac{\alpha_H V_{ds}^2}{\mathrm{A}lf^{\gamma}} \frac{A^2 e^2 p\mu_p^2}{l^2} =$$
$$= \frac{\alpha_H V_{ds}^2}{f^{\gamma}} \frac{A}{l^3} e^2 \mu_p^2 (p_d + \Delta p) = \frac{\alpha_H V_{ds}^2}{f^{\gamma}} \frac{A}{l^3} e^2 \mu_p^2 \left(p_d + \eta\alpha\tau_p \frac{W}{h\nu}\right). \tag{7}$$

Here p_d is the concentration of holes in the dark conditions, σ is the specific conductivity. The noise level increases proportionally to the intensity of the illumination.

We calculate values of the noise parameter γ, using the curves presented in Fig. 6. The following parameters are obtained for samples, measured in dark and at light excitation of different powers:

$$\gamma(\text{dark}) \approx 1.0, \quad \gamma(0.85\ \text{W/cm}^2) \approx 0.5 \quad \text{and} \quad \gamma(1.6\ \text{W/cm}^2) \approx 0.2.$$

Under irradiation the value of the noise parameter γ decreases. This can be explained as follows. With increasing light power, the conductivity of the current channel increases. As a result, the lifetime of minority carriers τ_n rises and reaches values $\tau_n \geq (10^{-3} \div 10^{-2})$ s. As is known, generation-recombination (g-r) noise has the Lorentzian shape

$$S_{V,g-r} \sim \frac{1}{1+(2\pi f\tau_n)^2}. \tag{8}$$

Here f is the frequency. It is clear that the section of the plateau on dependence $S_{V,g-r}(f)$ is determined by the condition

$$2\pi f_c \tau_n \leq 1. \tag{9}$$

It should be noted that with the increase in the lifetime of the electrons, first of all the value of the cut-off frequency f_c decreases. The characteristic frequency of the g-r noise shifts to the low-frequency region. Since the conductivity σ and lifetime τ_n increase with increasing illumination power, the f_c decreases with increasing W, correspondingly:

$$f_c \propto \frac{1}{\tau_n} \propto \frac{1}{W}. \quad (10)$$

Secondly, the growth of g-r processes leads to an increase in the g-r noise level. These two processes result in the screening of the 1/f noise part under the g-r noise plateau. The fact explains the decrease in the value of the noise parameter γ with increasing illumination power. Note that the decrease in the value of the parameter γ can also be related to the growth of thermal noise due to the increase in the conductivity of the current channel.

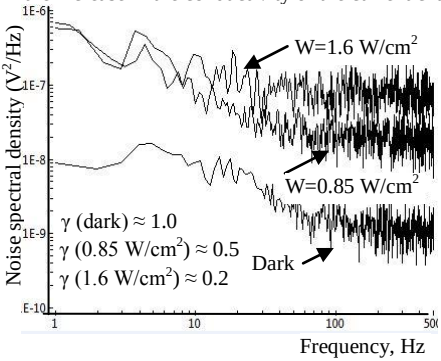

Fig. 6. Spectral dependence of LF noise, measured for NR FET sample with l = 10 μm under illuminations 0.85 W/cm^2; 1.6 W/cm^2, and in the dark, T=300K.

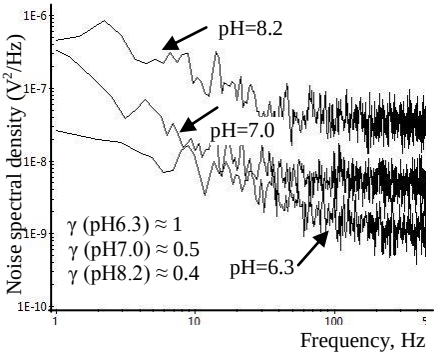

Fig. 7. Spectral dependence of LF noise for NR with length, l = 10 μm, measured at T= 300K and several pH values: 6.3, 7.0 and 8.2.

Figure 7 illustrates spectral dependency of the LF noise power spectrum of Si NR FET sample, measured at the $V_{FG} = -1$V, $I_{ds} = 0.1$ μA in solution at the several pH values: 6.3, 7.0 and 8.2. Noise parameter decreases with the increasing of the pH-value: γ(pH=6.3) ≈ 1.0; γ(pH=7.0) ≈ 0.5; γ(pH=8.2) ≈ 0.4. LF noise level increases and its slope decreases with increase of the pH-value. The increase in pH-value leads to a decrease in channel resistance, which is caused by the accumulation of negative charges at the semiconductor-oxide interface. Decreasing of the slope of $S_V(f)$ dependence can be explained taking into account the effect of the channel conductivity increasing.

2. Size-depending effects

In this section, we present the results of a study of the effect of SiNR characteristic length on the current transport mechanisms, pH-sensitivity, and also the behavior of LF noise. The magnitude of the current is inversely proportional to the length of the current channel, which justifies the application of the drift approximation for transport mechanism, as well as the assumption of a uniform distribution of the electric field strength along the length of the current channel (Fig. 8). The influence of light excitation, leads to an increase in the magnitude of the source-drain current. The pH-sensitivity increases with the current channel elongation and tends to the Nernst limit of 59.5 mV/pH, characteristic for micro-size sensors [19] (see Fig. 9). This behavior can be explained as follows. First, as the length of the channel l decreases, the area of the pH-sensitive surface decreases, and consequently the number of measurable H^+ ions in the aqueous solution decreases. Second, according to Eq.(2) the current I_{ds} increases with decreasing l, which leads to a decrease in the resistance of the current channel at constant voltage V_{ds}. As the resistance of the channel R_{ch} decreases, its modulation is hampered under the influence of the H^+ ions; hence the pH- sensitivity decreases.

Figure 10 illustrates the LF noise spectral density dependencies on the length of the current channel. These curves are plotted using the spectral dependences of the LF noise measured in the dark conditions, under illumination with an intensity of 0.85 V/cm^2, and in an aqueous solution with a pH=7 of SiNRs of different lengths. Calculated value of the slope of those parallel curves is equal to $\log(500/10) \approx 2.7$ (see Fig. 10).
This value is near the value (equal to 3) obtained theoretically using Eqns. (6) and (7), $S_V \propto l^{-3}$ with error about 10%. The difference between the theoretically expected and measured value of dependence $S_V(l)$ can be explained by relatively high level of thermal noise.

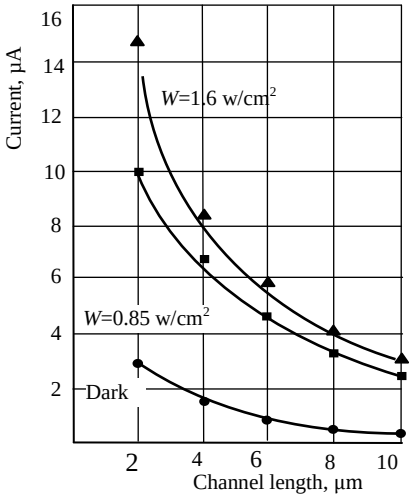

Fig. 8. Plot of channel current vs channel length.
$V_{FG} = -10$ V, $V_{ds} = -5$ V, $R_{ch} = 1.26$ MΩ.

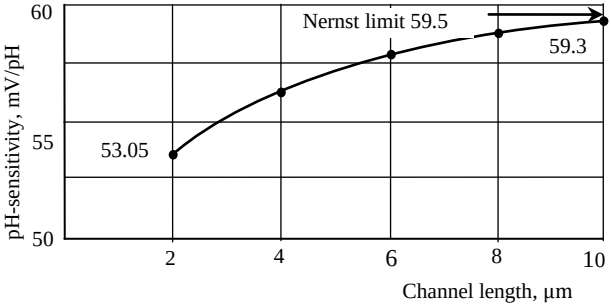

Fig. 9. Plot of pH-sensitivity vs channel length.
$V_{FG} = -10$ V, $V_{ds} = -5$ V, $R_{ch} = 1.26$ MΩ.

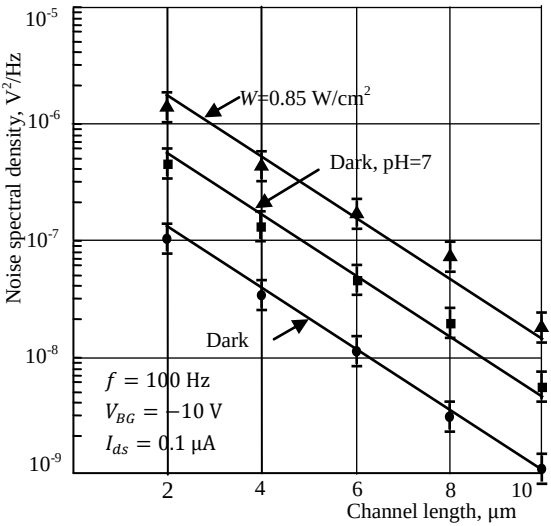

Fig. 10. Plot of noise spectral density vs channel length.

3. Conclusion

The spectral density of the LF noise increases both under the action of the pH solution and the illumination, and in both cases the frequency dependence of the noise is weakened and the value of the noise parameter γ decreases. With increasing of the pH and illumination power the 1/f noise is screened by the G-R plateau and the characteristic frequency of the G-R noise component decreases with increasing illumination power. LF noise level increases and its slope decreases with increase of the pH value. The magnitude of the channel current is approximately inversely proportional to the length of the current channel. The pH-sensitivity increases with the current channel elongation and approaches to the Nernst limit value of 59.5 mV/pH. It is shown that the measured value of the slope of noise spectral density dependence on the current channel length is 2.7 that are close to the theoretically predictable value 3.

Acknowledgments: This work was supported by the SCS MES of Armenia in the framework of research Project No. 15T-1C 279. F. Gasparyan greatly appreciates the support from the German Academic Exchange Service (DAAD) in the form of a research grant. The authors would like to acknowledge for the Innovation Award of RWTH Aachen University in the framework of RWTH transparent 2016.

References

1. ***R. Afrasiabi.*** Silicon Nanoribbon FET Sensors: Fabrication, Surface Modification and Microfluidic Integration. Doctoral thesis. Stockholm, Sweden 2016.
2. ***K.S. McKeating, A. Aubé, and J.-F. Masson.*** Analyst, **141**, 429 (2016).
3. ***H. Craighead.*** *Nature, **442**, 387 (2006).*
4. ***S.S. Bhinder, and P. Dadra.*** Asian J. of Chem., **21**, 5167 (2009).
5. ***G. Chen and L. Hu.*** SPIE Newsroom, 1087 (2008).
6. ***F. Gasparyan, H. Khondkaryan, A. Arakelyan, I. Zadorozhnyi, S. Pud, and S. Vitusevich*****.** J. of Appl. Phys., **120,** 064902-(1-8) (2016).

7. ***L. Tsakalakos, J. Balch, J. Fronheiser, M.-Y. Shih, S. F. LeBoeuf, M. Pietrzykowski, P. J. Codella, B. A. Korevaar, O. Sulima, J. Rand, A. Davuluru, and U. Rapolc.*** J. Nanophotonics, **1**, 013552 (2007).
8. ***E. Garnett and P. Yang.*** Nano Lett., **10**, 1082 (2010).
9. ***V. Parkash and A. K. Kulkarni.*** IEEE Trans. Nanotechnol., **10**, 1293 (2011).
10. ***G. Sanders and Y.C. Chang.*** Phys. Rev., **B 45**, 9202 (1992).
11. ***A. Miranda, R.Vazquez, A. Dıaz-Mendez, and M. Cruz-Irisson.*** Microelectron. J., **40**, 456 (2009).
12. ***M. Bruno, M. Palummo, S. Ossicini, and R. D. Sole.*** Surf. Sci., **601**, 2707 (2007).
13. ***F.V. Gasparyan.*** Chapter 11: Noise Reduction in (Bio-) Chemical Sensors Functionalized with Carbon Nanotube Multilayers. Advanced Sensors for Safety and Security, NATO Science for Peace and Security Series B: Physics and Biophysics, A. Vaseashta and S. Khudaverdyan (eds.), DOI 10.1007/978-94-007 7003-4 11, © Springer ScienceCBusiness Media Dordrecht 2013, pp. 139-150.
14. ***S. Vitusevich, F. Gasparyan.*** Chapter 11: Low-Frequency Noise Spectroscopy at Nanoscale: Carbon Nanotube Materials and Devices. In: "Carbon Nanotubes Applications on Electron Devices" Ed. by J.M. Marulanda, PH InTech, 2011, pp. 257-296.
15. ***F.V. Gasparyan, A. Poghossian, S.A. Vitusevich, M.V. Petrychuk, V.A. Sydoruk, J.R. Jr. Siqueira, O.N. Oliveira, A. Offenhäusser, M.J. Schöning.*** IEEE Sensors Journal, **11**, 142 (2011).
16. ***N. Elfström, A.E. Karlström and J. Linnros.*** *Nano Lett.,* **8**, 945 (2008).
17. ***T. Ytterdal, Y. Cheng and T. A. Fjeldly.*** Device Modeling for Analog and RF CMOS Circuit Design. John Wiley & Sons, Ltd, 2003.
18. ***F.V. Gasparyan, H.D. Khondkaryan.*** Proc. of the 10th Int. Conf. Semicond. Micro-and Nanoelectronics, Yerevan, Sept. 11-13, 2015, pp.68-71.
19. ***K. Bedner, V. A. Cuzenko, A. Tarasov, M. Wipf, R. L. Stoop, D. Just, S. Rigante, W. Fu, R. L. A. Minamisawa, Ch. David, M. Calame, J. Gobrecht, and Ch. Sch€onenberger.*** Sens. Mater, **25**, 567–576 (2013).
20. ***S.V. Melkonyan, V.M. Aroutiounian, F.V. Gasparyan, H.V. Asriyan.*** Physica, B: Physics of Condensed Matter, **382**, 65 (2006).

LABEL-FREE BIOSENSING USING CAPACITIVE FIELD-EFFECT STRUCTURES MODIFIED WITH GOLD NANOPARTICLES

Arshak Poghossian and Michael J. Schöning

Institute of Nano- and Biotechnologies, FH Aachen, Campus Jülich, 52428 Jülich, Germany

1. Introduction

Last decade, enormous efforts have been devoted to the research field of nanoelectronic and molecular devices, resulting in the realization of various kinds of single-electron transistors [1] or molecular transistors [2]. Nevertheless, the replacement of Si with "nanoobject-only" or "molecule-only" technologies in the near future is considered to be a challenging task [3]. On the other hand, the hybrid device concept, which is based on a combination of bio- and nanomaterials within hybrid systems and their integration with macroscopic electronic transducers might be a more realistic concept for a new generation of biosensors and biochips [4,5]. In this context, the coupling of charged molecules (proteins, antibodies, DNA, polyelectrolytes, dendrimers, etc.), nanoobjects (e.g., nanoparticles, carbon nanotubes) and inorganic/organic functional nanohybrids with semiconductor field-effect devices based on an electrolyte–insulator–semiconductor (EIS) system represents a very promising strategy for the label-free biosensing [6–9].

2. Functioning of AuNP-modified capacitive EIS sensors

Assemblies of AuNPs on a macroscopic transducer surface are an emerging and highly attractive class of chemically and electrically tunable functional materials. Fig. 1 schematically shows the cross-section of a capacitive Al–p-Si–SiO_2 sensor structure after silanisation of the SiO_2 surface (a), deposition of negatively charged citrate-capped AuNPs (b), adsorption of positively charged molecules on the AuNPs (c) and the expected shift of a high-frequency *C–V* (capacitance-voltage) curve of the EIS sensor after these surface modification steps (d). The EIS sensor detects the charge changes in AuNP/molecule inorganic/organic hybrids induced by the molecular adsorption or binding events. The binding of negatively charged citrate-capped AuNPs to the silanised SiO_2 surface (Fig. 1b) will decrease the width of the depletion layer in the Si within regions under surface areas covered with AuNPs. This will result in an increase of the total capacitance of the sensor and in a shift of the *C–V* curve in the direction of more positive (or less negative) gate voltages. In contrast, the electrostatic adsorption or binding of positively charged molecules to the negatively charged citrate-capped AuNPs (Fig. 1c) will lead to a local increase of the width of the depletion layer, resulting in a shift of the *C–V* curve in the direction of more negative (or less positive) gate voltages (see Fig. 1d). A large sensor signal can be expected by a high surface coverage of AuNPs, a large number of highly charged, adsorbed molecules per AuNP and by measurements in low ionic-strength solutions (i.e., by a reduced counterion-screening effect).

Since the surface of AuNPs can be easily modified with variously charged shell molecules and because the vast majority of biomolecules or polyelectrolyte macromolecules are charged under physiological conditions, AuNP-modified EIS sensors can provide a universal and efficient platform for label-free electrical detection of a wide variety of molecules by their intrinsic molecular charge. Recently, we demonstrated the potential of this approach by realizing capacitive EIS sensors consisting of an Al–p-Si–SiO_2–silane–AuNP structure for the label-free electrostatic detection of positively charged small proteins (cytochrome c, CytC) and macromolecules (poly-D-lysine) as well as for monitoring the consecutive adsorption of positively/negatively charged polyelectrolyte multilayers [3]. In the following, the experimental results related to the label-free detection of CytC molecules are exemplarily presented.

3. Label-free detection of cytochrome c molecules by their intrinsic charge

EIS chips (with sizes of 10 mm x 10 mm) consisting of an Al (300 nm)–p-Si–SiO_2 (30 nm) structure were fabricated by standard microfabrication processes. Before deposition of AuNPs, the surface of the SiO_2 gate was silanised with 3-mercaptopropyl trimethoxysilane. The negatively

charged citrate-capped AuNPs were prepared using the well-established chloroauric acid ($HAuCl_4$) reduction method [10,11]. The AuNPs were deposited on the silanised SiO_2 surface from a water solution of citrate-stabilised AuNPs [3,12]. Fig. 2 shows scanning electron microscopy (SEM) and atomic force microscopy (AFM) images of the AuNP-modified EIS sensor surface. The average diameter and density of AuNPs evaluated from several SEM images were approximately 18 ± 2 nm and N = (0.8–1.2) × 10^{11} AuNPs/cm^2, respectively. For details of surface silanisation, AuNP preparation and deposition steps, see [3].

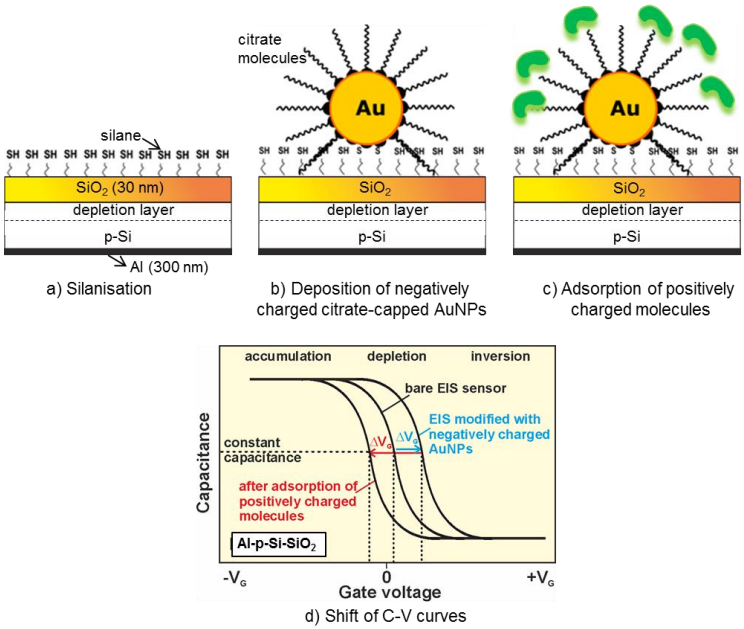

Fig. 1. Schematic cross-section of the capacitive field-effect Al–p-Si–SiO_2 EIS sensor after silanisation (a), deposition of negatively charged citrate-capped AuNPs (b), adsorption of positively charged molecules on the AuNPs (c) and the corresponding *C–V* curves with typical accumulation, depletion and inversion regions (d).

Figure 3 shows an example of the label-free electrical detection of CytC molecules by means of the EIS sensor modified with citrate-capped AuNPs. CytC is a small protein and an essential component of the electron transport chain in mitochondria [13]. It is positively charged at neutral pH value with the net positive charge of approximately +9*e* (*e* is the elementary charge, 1.6 × 10^{-19} C) [14]. CytC rapidly binds to an AuNP due to electrostatic interactions between the positively charged CytC and negatively charged citrate-capped AuNP, resulting in a large shift of the *C-V* curve of about 400 mV in the depletion region. The number (*N*) of adsorbed CytC molecules per AuNP, evaluated using the experimentally observed potential change of ΔV_G = 400 mV, amounted to be approximately *N* = 56 (for simulation details, see [3]).

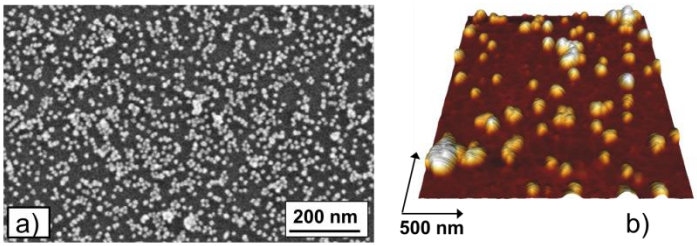

Fig. 2. SEM (a) and tapping-mode AFM (b) images of an AuNP-modified EIS sensor surface.

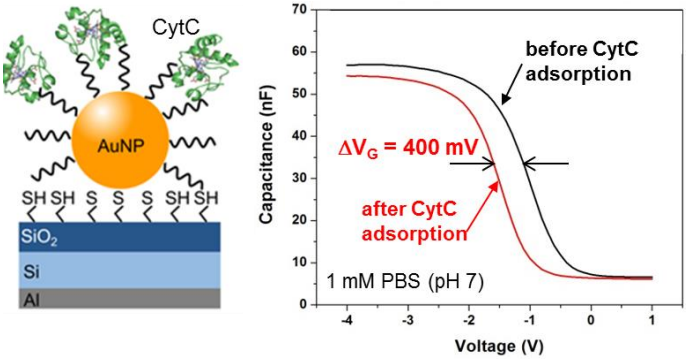

Fig. 3. Label-free electrical detection of positively charged CytC molecules by means of the EIS sensor modified with negatively charged citrate-capped AuNPs (left). For the CytC adsorption, the sensor was exposed to 1 mM PBS (phosphate buffer solution, pH 7) containing 50 μM CytC for 10 min. The high-frequency *C*–*V* curves (right) were recorded in 1 mM PBS (pH 7) before and after the adsorption of CytC molecules. Left figure is reproduced from Ref. 3 with permission of the Royal Society of Chemistry.

4. Conclusions

During the last years, label-free biosensing has become one of the most reported research fields for semiconductor field-effect devices based on nanomaterial-modified EIS systems. In this work, we exemplarily presented results of label-free electrostatic detection of small proteins such as positively charged CytC molecules using EIS sensors modified with citrate-stabilized negatively charged AuNPs. The functioning mechanism of the AuNP-modified EIS sensor is based on the detection of charge changes in AuNP/ligand hybrids induced by molecular adsorption or binding events. Since most of the biomolecules are charged under physiological conditions, AuNP-modified EIS sensors represent a powerful and universal platform for label-free electrical detection of a wide variety of biomolecules.

Acknowledgements:The authors thank P. Mehndratta and M. Bäcker for technical support and D. Mayer for valuable discussion.

References

1. ***Y. Noguchi, M. Yamamoto, H. Ishii, R. Ueda, T. Terui, K. Imazu, K. Tamada, T. Sakano, K. Matsuda.*** Jpn. J. Appl. Phys., **52**, 110102 (2013).

2. ***I. Diez-Perez, Z. Li, S. Guo, C. Madden, H. Huang, Y. Che, X. Yang, L. Zang, N. Tao*****.** ACS Nano, **6**, 7044 (2012).
3. ***A. Poghossian, M. Bäcker, D. Mayer, M.J. Schöning*****.** Nanoscale, **7**, 1023 (2015).
4. ***A. Samanta, I.L. Medintz.*** Nanoscale, **8**, 9037 (2016).
5. ***S. Mehrabani, A.J. Maker, A.M. Armani*****.** Sensors, **14**, 5890 (2014).
6. ***S.W. Boettcher, N.C. Strandwitz, M. Schierhorn, N. Lock, M.C. Lonergan, G.D. Stucky*****.** Nat. Mater., **6**, 592 (2007).
7. ***J. Gun, V. Gutkin, O. Lev, H.G. Boyen, M. Saitner, P. Wagner, M. D'Olieslaeger, M.H. Abouzar, A. Poghossian, M.J. Schöning*****.** J. Phys. Chem. C, **115**, 4439 (2011).
8. ***J.R. Jr. Siqueira, M.H. Abouzar, M. Bäcker, V. Zucolotto, A. Poghossian, O.N. Jr. Oliveira, M.J. Schöning*****.** Phys. Status Solidi A, **206**, 462, (2009).
9. ***J. Gun, M.J. Schöning, M.H. Abouzar, A. Poghossian, E. Katz*****.** Electroanalysis, **20**, 1748 (2008).
10. ***I. Kruglenko, Yu. Shirshov, J. Burlachenko, A. Savchenko, O. Kukla, O. Belyaev*****.** Sens. Actuators B, **170**, 109 (2012).
11. ***Y.C. Yeh, B. Creran, V.M. Rotello*****.** Nanoscale, **4**, 1871 (2012).
12. ***J. Gun, D. Rizkov, O. Lev, M.H. Abouzar, A. Poghossian, M.J. Schöning*****.** Microchim. Acta, **164**, 395 (2009).
13. ***A. Vinu, V. Murugesan, O. Tangermann, M. Hartmann*****.** Chem. Mater., **16**, 3056 (2004).
14. ***S. Imabayashi, T. Mita, T. Kakiuchi*****.** Langmuir, **21**, 1470 (2005).

MATERIAL SCIENCE AND ENGINEERING

MAGNETIZATION PLATEAUS AND ENTANGLEMENT IN SPIN-1 Ni ^{II} CONTAINING POLYMER

V. Abgaryan[1], N. Ananikian[2], A. Sadrolashrafi[2]

[1]Laboratory of Information Technologies, JINR, 141980 Dubna, Russia
[2] Alikhanyan National Science Laboratory, Alikhanian Br. 2, 0036 Yerevan, Armenia,
E-mail: afsaneh@mail.yerphi.am

1. Introduction

The μ-azido bridging ligand is a good candidate for divalent metal ions, mainly Cu^{II}, Ni^{II}, Co^{II}, Cd^{II}, Fe^{II}, and Mn^{II} [1] and it is one of the most adaptable and flexible for creation of new materials with different magnetic properties. Meanwhile, it is very functional in the studying of magnetization structure and magnetic correlations in discrete and polymeric complexes. The nitrogen μ-azido may give end-to-end (EE) or end-on (EO) coordination modes, where normally, the first one cause antiferromagnetic coupling and the latter would result in ferromagnetic coupling (see Fig. 1).

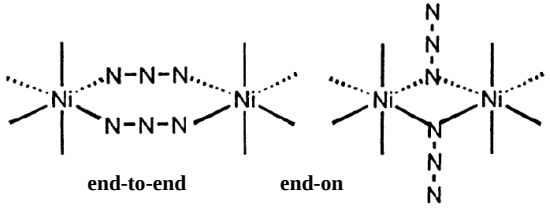

Fig. 1

Magnetization plateaus occur both in antiferromagnetic and ferromagnetic materials and they play a great role in understanding of a large family of nontrivial quantum phenomena. For the first time K. Hida [2] in a pioneering work has shown the appearance of magnetization plateau in ferromagnetic-ferromagnetic-antiferromagnetic trimerized Heisenberg model. Since then tremendous works have been done in the field out of which, we can mention the experimental data of the magnetic properties of low dimensional diamond chains in [3 - 5] and the corresponding theoretical investigations that has been presented in [5 - 7] . In section 3, the magnetic properties of spin-1 Ni-containing polymer [Ni (NN'-dmen) $(\mu\text{-}N_3)_2]_n$ are demonstrated. Following the same track, in section 4, we look into negativity in the polymer system as a measure to observe quantum correlations and entanglement. Entanglement is a property of the states of quantum systems composed of many parties that expresses particularly strong correlations between these parties, persistent even in the case of large separations among the parties. The term "entanglement" was first introduced by Erwin Schrödinger [8] in 1935 in order to describe an intrinsic feature of quantum mechanics. In antiferromagnetic systems entanglement has been observed to be an essential trait to understand the quantum behavior [9].

This manuscript would be structured as follows. In section 2, we introduce spin-1 Ni-containing polymer [Ni (NN'-dmen) $(\mu\text{-}N_3)_2]_n$ and the corresponding Hamiltonian. The next section would present the details about the magnetization plateaus and magnetic susceptibility. Section 4, would be devoted to the study of thermal negativity as the entanglement measure of the polymer. Finally, the conclusions are mentioned in Sec. 5.

2. Hamiltonian of Ni ^{II} Containing Polymer

The following Hamiltonian in Eq. (1)

$$H = -\sum_{i=1}^{N} J_H S_{4i-2}.S_{4i-1} + J_1(S^z_{4i-3}S^z_{4i-2} + S^z_{4i-1}S^z_{4i}) + J_2 S^z_{4i}S^z_{4i+1} + g\,\mu_B\, h(\frac{1}{2}S^z_{4i-3} + S^z_{4i-2} \quad (1)$$

$$+ S^z_{4i-1} + S^z_{4i} + \frac{1}{2}S^z_{4i+1}) - D[\frac{1}{2}(S^z_{4i-3})^2 + (S^z_{4i-2})^2 + (S^z_{4i-1})^2 + (S^z_{4i})^2 + \frac{1}{2}(S^z_{4i+1})^2]$$

shows the interaction structure in the polymer [Ni (NN'-dmen) $(\mu\text{-}N_3)_2]_n$, which is experimentally studied in [10] and is a highly unusual one-dimensional polymer containing at the same time both kinds of coordination mode (EE and EO) and showing tremendous magnetic properties (Fig. 2). In order to compare experimental magnetic results reported in the literature, it is necessary to establish the general spin-1 Heisenberg-Ising Hamiltonian with bilinear (dipolar) Ising ferromagnetic coupling constants, J_1 and J_2, Heisenberg exchange coupling J_H, single-ion anisotropy D, and magnetic field h. In the following sections, when talking about the behavior of the magnetization curves, magnetic susceptibility, and thermal negativity, we always consider the specific values of $J_1 = 20$ cm^{-1}, $J_2 = 37$ cm^{-1}, $J_H = -120$ cm^{-1}, $D = -6$ cm^{-1}, and $g = 2.39$ from experimental data [1, 10]. In Eq. (1) $\boldsymbol{S}$ is the vector operator of spin-1 particles at the corresponding sites and S^z is its Z-component.

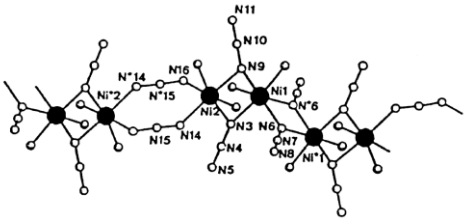

Fig. 2. Polymer [Ni(NN'- dmen)(μ-$N_3)_2]_n$ with the $F_1 - AF - F_1 - F_2$ azido bridging ligands

According to Eq. (1), the polymer actually is composed of separable blocks each of which consists of 5 spins. Calculating partition function would result in the product of the transfer matrices.

3. Magnetization Plateaus in a Spin-1 System

While applying the classical transfer matrix method of separated blocks, we have exploited the relations:

$$Z = tr\prod_{i=1}^{N} e^{-\beta H_i}\ ,\ F = -\frac{1}{\beta}\log Z \propto -\frac{N}{\beta}\log\lambda_{Max}\ ,\ M = -\frac{\partial F}{\partial h}\ ,\ \chi = \frac{\partial M}{\partial h}\ ,$$

where Z is the partition function, F the free energy, M the magnetization, χ the susceptibility, and β is the inverse temperature $(k_B T)^{-1}$. The following figures show magnetization plateaus at $T = 0.05K$.

4. Thermal Negativity as an Entanglement Measure for Ni^{II} Containing Polymer

Entanglement is an essential phenomenon in quantum physics, bearing the strongest contradictions between quantum mechanics and the very foundations of classical physics. It shall primarily be seen as a resource for performing various tasks, such as quantum computation, teleportation, error correction, or quantum cryptography [11, 12].

By definition, a system is called entangled when its quantum state cannot be factored out into a product of states of its local constituents; Simply speaking, two (or more) particles are entangled, if each of them cannot be fully described without the other so that as a whole they are inseparable. As a simple example of an entangled bipartite state, one can consider any of the Bell states. There are

many different definitions of entanglement, one of which is "negativity (Ne)" that is a simple quantification of the nonpositivity of the partially transposed density matrix of a state [13] and for a bipartite system is defined as $Ne=\sum_i |\mu_i|$, where μ_i 's are the negative eigenvalues of ρ^T which is the partial transpose of the bipartite density matrix, ρ, with respect to one of the subsystems. In an alternative way negativity can be formulated as $Ne=\frac{\|\rho^T\|_1-1}{2}$, where $\|\rho^T\|_1$ is the trace norm of the matrix ρ^T.

For temperature $T=0.5$ and with the specific choice of the coupling constants which is mentioned in section 2 and is compatible with the experimental data in [1, 10], *Ne* for the spin-1 Ni-containing polymer [Ni (NN'-dmen) (μ-N_3)$_2$]$_n$ in Eq. (1) is shown in the below plot.

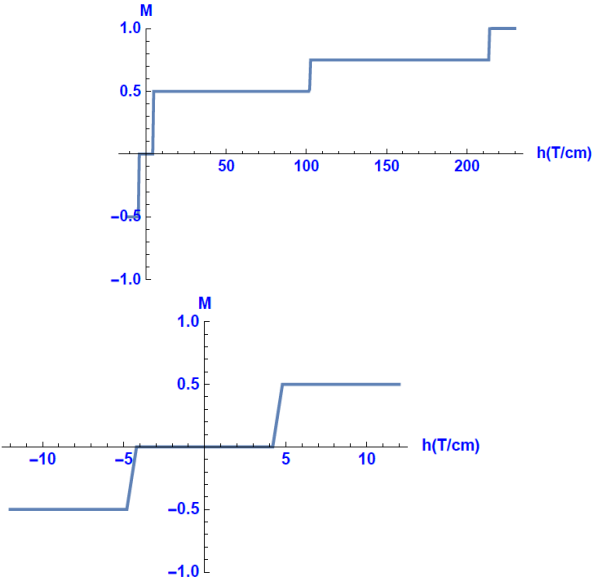

Correspondingly, the magnetic susceptibility is shown below:

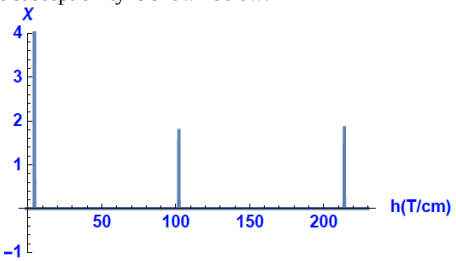

5. Conclusion

In this talk a compatible theory model of a Nickel-containing polymer is introduced and studied that can fully cover and explain the experimental data which was gained and reported in [1, 10]. This study will improve our understanding of nitrogen μ-azido ligand as one of the most adaptable entities that can be immensely exploited to create new materials both discrete and polymeric and acts as a key ingredient in determining the relative magnetic properties in those materials.

The authers acknowledge financial support by the MC-IRSES (612707, DIONICOS) under FP7-PEOPLE- 2013, CS MES RA in the frame of SCS 15T- 1C114 grants, and also the financial support from ICTP Office of External Activities (OEA) within NET68 and OEA-AC-100 programs.

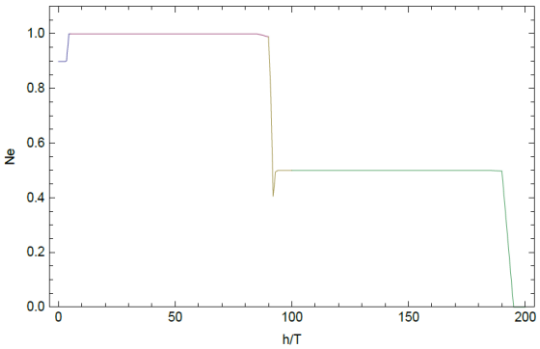

References

1. ***J. Ribas, A. Escuer, M. Monfort, R. Vicente, R. Cortés, L. Lezama, T. Rojo.*** Coordination Chem. Rev., **193**, 1027 (1999); ***F.A. Mautner, M. Scherzer, C. Berger, R.C. Fischer, R. Vicente, S.S. Massoud.*** Polyhedron, **85**, 329 (2015).
2. ***K. Hida.*** J. Phys. Soc. Jpn., **63**, 2359 (1994).
3. ***H. Kikuchi, Y. Fujii, M. Chiba, S. Mitsudo, T. Idehara, T. Tonegawa, K. Okamoto, T. Sakai, T. Kuwai, H. Ohta.*** Phys. Rev. Lett., **94**, 227201 (2005).
4. ***S. Konar, P.S. Mukherjee, E. Zangrando, F. Lloret, N.R. Chaudhuri.*** Angew. Chem. Int. Ed., **41**, 1561 (2002).
5. ***H. Jeschke, I. Opahle, H. Kandpal, R. Valentí, H. Das, T. Saha-Dasgupta, O. Janson, H. Rosner, A. Brühl, B. Wolf, M. Lang, J. Richter, S. Hu, X. Wang, R. Peters, T. Pruschke, A. Honecker.*** Phys. Rev. Lett., **106**, 217201 (2011).
6. ***N. Ananikian, H. Lazaryan, M. Nalbandyan.*** Eur. Phys. J. B, **85**, 223 (2012).
7. ***V. Abgaryan, N. Ananikian, L. Ananikyan, V. Hovhannisyan.*** Solid State Comm., **224**, 15 (2015).
8. ***E. Schrödinger.*** Naturwissenschaften, **23**, 807 (1935).
9. ***M. Wieśniak, V. Vedral, Č. Brukner.*** *New J. Phys.*, **7**, 258 (2005).
10. ***J. Ribas, M. Monfort, I. Resino, X. Solans, P. Rabu, F. Maingot, M. Drillon.*** Angew. Chem. Int. Ed. Engl., **35**, 2520 (1996).
11. ***A. Barenco, D. Deutsch, A. Ekert, R. Jozsa.*** Phys. Rev. Lett., **74**, 4083 (1995).
12. ***A.K. Ekert.*** Phys. Rev. Lett., **67**, 661 (1991).
13. ***G. Vidal, R.F. Werner***. Phys. Rev. A, **65**, 032314 (2002).

MODIFICATION OF PLASTIC LUBRICANTS USING FEW-LAYERED GRAPHENE

D. Al-Saadi[1], V. Pershin[1], E. Galunin[1], G. Shmavonyan[2], A. Tkachev[1], V. Ostrikov[3]

[1] Tambov State Technical University, Tambov, Russia, E-mail: evgeny.galunin@gmail.com
[2] National Polytechnic University of Armenia, Yerevan, Armenia, E-mail: gshmavon@yahoo.com
[3] All-Russian Scientific Research Institute for the Use of Machinery and Petroleum Products in Agriculture, Tambov, Russia, E-mail: viitinlab8@bk.ru

Introduction

Graphene has a very low coefficient of friction and, in our opinion, it seems very promising to use this material for modification of plastic lubricants, which are widely used in various industries. This material is usually synthesized as graphene nanoplatelets (GNPs) via exfoliation of crystalline, intercalated or expanded graphite [1-4]. Besides, it is also possible to implement shear exfoliation [5, 6].

In the present paper, the results of experimental studies on the modification of plastic lubricants using few-layered GNPs are described.

Experiment and Methods

To modify plastic lubricants, a masterbatch consisting of I-20A oil ("Devon" Lubricant Factory JSC, Ufa, Russia) and 10-% few-layered GNPs was used herein. The GNPs were synthesized at the "NanoTechCenter" JSC (Tambov, Russia) from GSM-2 natural crystalline graphite (carbon content 99.5 %, ash content < 0.5 %, "Resurs-S" JSC, Ekaterinburg, Russia) using ultrasound. The oxidative intercalation of the graphite was carried out with ammonium persulfate (reagent grade, "Reakhim" JSC, Moscow, Russia) dissolved in sulfuric acid containing 5-% free sulfur trioxide. The experimental details of intercalation were described elsewhere [7].

Plastic lubricants of "Solidol-Zh" and "Litol-24" trademarks (both – from "Devon") were used as initial (starting) materials. The former is a plastic lubricant for general purposes and represents a mixture of petroleum oils with medium viscosity index thickened using hydrated calcium soaps of higher fatty acids which are part of natural (vegetable and animal) fats, whereas the latter is a plastic lubricant obtained by thickening petroleum oils using lithium soaps of 12-hydroxystearic acid. With each lubricant, five compositions (pastes) containing 0.25, 0.5, 1.0, 3.0 and 6.0 % of the masterbatch were prepared. We tried to mix the compositions on different types of mixers (blade, frame, anchor, planetary, and propeller). Depending on the type of mixer, the rotation speed varied from 12 to 300 rpm, and the agitation time – from 5 to 30 min. The quality of mixing (homogenization) was determined both visually by the lubricant appearance and by the coefficient of sliding friction. As a result of the experiments, it was found that the mixtures do not become uniform and the coefficient of sliding friction remains practically unchanged. Considering this finding, we decided to pre-mix the compositions for 2-3 min using a conventional propeller mixer, and the final homogenization was performed in a special laboratory setup, similar to the one described in our earlier work [5].

This device presented a stainless steel cylinder-shaped container with an internal diameter of 60.0 mm and a height of 50 mm and a steel rotor inside the container. In the experiments, two rotors with diameters of 59.8 mm and 59.9 mm and a height of 25 mm were used. The paste was fed through a hole in the bottom of the container by means of a piston. During the tests, the rotation speed of the rotor was changed from 400 to 2,500 rpm, whereas the rate of feeding the paste to the container was changed from 0.3 to 1.0 g s^{-1}.

First, the paste moved in the gap between the bottom of the container and the rotor, and then between the inner cylindrical surface of the container and the cylindrical surface of the rotor at a fixed gap. The linear speed of the paste movement in the gap changed according to the law close to that of parabolic rate from 0 in the immediate vicinity of the fixed surface of the container to a certain maximum value in close proximity to the rotating surface of the rotor.

The numerical value of the maximum speed of the paste movement is almost impossible to determine, since the coefficient of the paste slippage relative to the moving surface of the rotor is unknown. Nevertheless, it is quite obvious that the paste moves with large gradients of linear speed, and the particles of graphite and graphene are subjected to very active shearing effects. Earlier, in one of our papers [5], it was demonstrated that even with sufficiently large gaps between the container and the rotor (0.35 mm), few-layered GNPs are formed. After all the paste passed through the gap between the container and the rotor, it was unloaded from the container, and the process was repeated. The efficiency of the modification of the GNP-base lubricant was determined according to two methods. First of all, the coefficient of sliding friction was found for the standard lubricant and the one modified using a universal friction and wear machine. The test method was based on mutual movement of the elements pressed against each other with a specified force. The first element was a fixed (static) circular plate with a diameter of 50 mm, and the second one was an annular plate with an outer diameter of 36 mm and inner diameters of 0, 10, and 20 mm. The contact scheme was as follows: the end of the annular rotating plate and the plane of the fixed (static) circular plate. The assembly for fixing the static circular plate through a thrust bearing was mounted on a balance with a measuring limit of 15,000 g and an error of ± 0.1 g, which made it possible to accurately record the clamping force of the friction couple elements. The force *G* (N) generated by the friction torque *M* (N m) of the thread through the unit was passed to the weight set on the second balance with a measurement accuracy of 0.001 g. The numerical value of the force *G* was determined as the difference between the weight mass and the current value of the balance.

The friction torque can be estimated according to Equation (1):

$$M = G \times h\,, \tag{1}$$

where *h* is the arm (m) of the force *G*.

On the other hand, the moment can be found according to Eq. (2):

$$M = \int_A \tau \rho dA\,, \tag{2}$$

where τ are the shearing stresses acting in the contact zone of the friction couple elements (N m^{-2}), ρ is the current radius (m), which can vary from the inner radius R_1 (m) of the ring to the outer radius R_2 (m), and *A* is the integration (ring) area (m^2). After the integration, the following expression can be obtained:

$$M = \int_{R1}^{R2} 2\pi\tau\rho^2 d\rho = 2\pi\tau \int_{R1}^{R2} \rho^2 d\rho = 2\pi\tau \frac{R_2^3 - R_1^3}{3}\,. \tag{3}$$

By equating (1) and (3), the following equation can be written:

$$\tau = \frac{3Gh}{2\pi(R_2^3 - R_1^3)}\,. \tag{4}$$

The numerical value of the coefficient of sliding friction *f* (dimensionless) was determined as follows:

$$f = \tau / \sigma\,, \tag{5}$$

where $\sigma = P/A$ are the normal stresses in the contact zone of the friction couple elements, *P* – normal force (N), and A is the contact area (m^2). In addition, the contact spot diameter was determined on a four-ball friction and wear machine. The temperature of the lubricant heating during the tests was found to be at 100 °C, whereas the normal load on the upper rotating ball was

80 N. When determining the coefficients of friction for each combination of P and n (rotation speed, rpm), 30 experiments were performed with subsequent statistical processing of the results obtained. As an example, Table 1 presents the average values for a series of experiments at n = 1000 rpm. The coefficients of sliding friction were determined at different concentrations of the GNPs in the plastic lubricants under study. The results of these tests showed that at the concentrations above 0.1 %, the coefficient of sliding friction decreases by about 30 %, and further increase in the GNP content does not significantly reduce this coefficient. Figure1 demonstrates the dependencies of the changes in the contact spot diameter (D) on the percent masterbatch content (C) after testing the "Litol-24" and "Solidol-Zh" lubricants on the four-ball friction and wear machine. As seen from the graphs, a fairly pronounced extremum of the minimum can be observed for "Solidol-Zh" at the masterbatch content of 1 % (0.1 % as related to the solid phase), whereas for "Lithol-24", a significant decrease in the contact spot diameter with an extremum of the minimum, not less pronounced, is also observed. Special attention should be paid to the fact that the masterbatch containing 10 % of the solid phase with graphite and graphene was used herein. It was not possible to quantitatively estimate the amount of the few-layered GNPs in this solid phase. Anyway, with the masterbatch content of 1 %, there is actually only 0.1 % of the solid phase in the lubricant. In the course of the experiments, it was found that when the content of the GNP-modified masterbatch is up to 1%, a rotor providing the gap of 0.05 mm with the container can be used, and at larger concentrations the gap should be increased to 0.1 mm. This is due to the fact that at the concentrations above 1 % and the gap of less than 0.1 mm, separation of the solid phase from the plastic lubricant took place.

Table 1. Values of the coefficient of friction coefficient found depending on normal pressures in friction vapor.

No.	**σ, N m^{-2}**	**Initial lubricant - "Litol-24"**		**"Litol-24" based on 1-% GNP-modified masterbatch**	
		τ, N m^{-2}	***f***	**τ, N m^{-2}**	***f***
1	51,990	14,557	0.28	11,437	0.22
2	67,584	17,571	0.26	14,193	0.21
3	82,227	20,557	0.25	20,557	0.24
4	91,207	24,625	0.27	20,977	0.23
5	97,240	27,227	0.28	23,338	0.24
		Initial lubricant - "Solidol-Zh"		**"Solidol Zh" based on 1-% GNP-modified masterbatch**	
6	51,990	18,716	0.36	11,958	0.23
7	67,584	23,654	0.35	16,896	0.25
8	82,227	27,135	0.33	18,089	0.22
9	91,207	33,746	0.37	23,713	0.26
10	97,240	34,034	0.35	24,310	0.25

Besides, it was established that performance has the greatest impact on the modification quality of the modification, i.e. the speed of the lubricant movement in the gap between the container and the rotor. For the laboratory setup described herein, the optimum performance was found to be 0.7 g/s. Furthermore, bench tests were performed for the thrust sliding bearing using the Solidol-Zh and Litol-24 lubricants, as well as the modified lubricants containing the GNP-based 1-% masterbatch. During this experiment, the temperature was measured in the contact zone of the fixed (static) and rotating surfaces. It was found that when the thrust bearing is operated for 60 min, the temperature during the use of the modified lubricant is 15-20% less than that obtained in the case of using the standard lubricants. This may be due to the fact that the thermal conductivity of the modified lubricants is 15 % higher than that of the non-modified ones. Finally, it was established that when using the modified lubricants, a very thin layer of the graphene nanostructures is formed on the

friction surfaces (Fig. 2), which not only reduces the coefficient of sliding friction, but also the coefficient of wear. In fact, new GNP-based surfaces are formed, and they contact each other, and the metal surfaces are fully protected from wear.

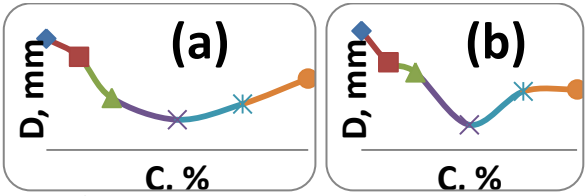

Fig. 1. Dependencies of the changes in the contact spot diameter (*D*) on the percent masterbatch content (*C*) after testing the "Litol-24" (a) and "Solidol-Zh" (b) lubricants on the four-ball friction and wear machine.

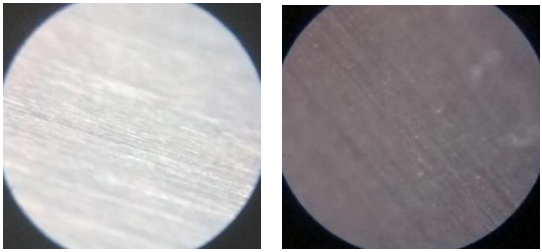

(a) (b)

Fig. 2. Surfaces of the fixed (static) element afer 600-second contact with the rotating element: (a) when using the initial lubricant, and (b) when using the GNP-modified lubricant.

Conclusions

The present work experimentally proves that the few-layered GNPs are an efficient modifier for plastic lubricants. It was found that 1 % of the masterbatch containing 10 % of the few-layered GNPs decreases the coefficient of friction by 15-30 % and reduces the contact spot by 15-25 %. The shear impact during movement in thin layers between the static and rotating surfaces appears to be the most effective way to homogenize the plastic lubricant and the GNPs. Apart from improving the frictional characteristics of the lubricants, the few-layered GNPs form protective layers on the surfaces of the contacting elements, thereby reducing wear and, possibly, regenerating these surfaces, i.e. eliminating the surface defects which occur during the manufacture of the elements and operation thereof.

References

1. ***M. Lotya, Y. Hernandez, P. J. King, et al.*** J. Am. Chem. Soc., **131** (10) 3611 (2009).
2. ***Y. Hernandez, V. Nicolosi, M. Lotya, et al.*** Nat. Nanotechnol. **3**, 563 (2008).
3. ***A.V. Nikolaeva.*** Preparation and study of aqueous suspensions of graphene particles in the presence of surfactants, Extended Abstract of Cand. Sci. (Tech. Sci.) Dissertation, Res. Inst. Graphite-Based Struct. Mater. NIIGRAFIT, Moscow, 2015.
4. ***J.H. Lee, D.W. Shin, V.G. Makotchenko, et al.*** Adv. Mater. **21**, 4383 (2009).
5. ***A.V. Melezhik, V.F. Pershin, et al.*** Nanotechnol. Russ., **11** (7-8), 421 (2016).
6. ***G.Sh. Shmavonyan, V.M. Harutyunyan, G.G. Sevoyan.*** Arm. J. Phys., **6** (1), 1 (2013).
7. ***A.V. Melezhyk, A.G. Tkachev.*** Nanosyst. Phys., Chem., Math., **5** (2), 294 (2014).

PECULIARITIES OF OBTAINING A CATALYST FOR THE SYNTHESIS OF NANOSTRUCTURED CARBON MATERIALS VIA THERMAL DECOMPOSITION

E. Burakova[1], G. Besperstova[1], A. Rukhov[1], T. Dyachkova[1], E. Bakunin[1], E. Galunin[1], G. Shmavonyan[2], A. Tkachev[1]

[1]Tambov State Technical University, Tambov, Russia,
E-mail: elenburakova@yandex.ru
[2]National Polytechnic University of Armenia, Yerevan, Armenia,
E-mail: gshmavon@yahoo.com

Introduction

Since the discovery of carbon nanotubes (CNTs), special attention has been paid to studying various methods for synthesis there of (Shmavonyan et al., 2011). At present, there exist several ways of CNT industrial production, one of which is chemical vapor deposition (CVD) characterized by the relative simplicity in hardware design and process implementation. In the synthesis of CNTs via the CVD, much attention is given to the catalyst as a key factor that allows forregulating the morphology and structure of nanomaterials. Controlling changes in the elemental composition of the catalyst and the mode parameters of its production, it is possible to achieve controlled synthesis of nanostructured materials. Due to the fact that CNTs are widely used in various industries, the synthesis of nanostructured materials with specified characteristics on an industrial scale remains the actual problem. To synthesize CNTs of a certain quality, it is very important to be able to control the properties of the catalyst at all stages of its preparation, and to know atwhich mode parameters of the process one can regulate its efficiency.

Experiment and Methods

A Co-Mo / Al_2O_3-MgO catalyst was chosen herein as the object under study. It is known that Co is one of the most active metals of the Fe group, and the use of binary carriers, as well as promoters in catalysts, leads to a significant increase in its catalytic activity (Wang et al., 2014).

In the present paper, the features of the process of obtaining the Co-Mo/Al_2O_3-MgO catalyst through the thermal decomposition method, namely the effect of the quality of reagents, conditions for carrying out thermal decomposition stages and calcinating the catalyst on the parameters of the synthesized nanoproduct are studied. To reproduce the catalyst with the required properties, the method of its preparation should describe in detail all the operations performed (Pakhomov, 2011). The Co-Mo/Al_2O_3MgO catalyst was prepared by dissolving the initial components and heat-treating the resulting system. The dissolution process of the initial components – $Co(NO_3)_2 6H_2O$ (chemically pure), $Mg(NO_3)_2 6H_2O$ (chemically pure), $Al(NO_3)_3 9H_2O$ (chemically pure), $(NH_4)_6Mo_7O_24 4H_2O$ (reagent grade), and citric acid – was carried out for 40-60 min at 50-60 °C. The resulting solution was subjected to thermal decomposition at 500 °C for 15 min and then to calcinationat 600 °C for 60 min. The catalyst synthesizedby this way has a porous flake-like structure of a dark grey color (Fig. 1).

Fig. 1. Morphology of the Co-Mo/Al_2O_3-MgO

To conduct the CVD process, the catalyst was ground to obtain a working fraction of 50-100 µm. The specific yield of a carbon nanostructured material was chosen as a parametercharacterizing the efficiency of the catalyst.Thisindicator allows for judging on the activity of a catalytic system.

The efficiency of the $CoMo/Al_2O_3$-MgO catalyst in the CVD process was studied using a quartz laboratory reactor, the schematic diagram and the exterior of which are presented in Fig. 2. The catalyst was deposited on the substrate (3) and placed into the reaction chamber (2), which was first purged with an inert gas, and then the carbon-containing gas – ethylene (Russian National Standard – GOST No. 25070-2013) – was supplied into it. The CVD process was carried out for 30 min at 650 °C. To evaluate the reproducibility of the $CoMo/Al_2O_3$-MgO catalyst preparation procedure, 12 catalyst batches were obtained under the similar conditions. Each batch was used in the CNT synthesis for at least 3 times, and the specific yield value of the carbon nanostructured material was fixed. The CNT specific yield on the obtained catalysts was found to be within the range 9.3-15.0$g_{CNTs}/g_{catalyst}$, thereby indicating the instability of the $CoMo/Al_2O_3$-MgO catalyst system characteristics.

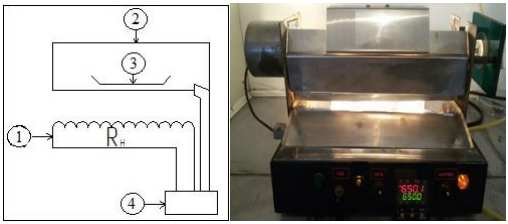

Fig. 2. Diagram and exterior of the laboratory reactor:
1 - Heater, 2 - reaction chamber, 3 - substrate, 4 - thermostat.

The analysis of the obtained results led to the conclusion that a clear implementation of the existing method for preparing the $CoMo/Al_2O_3$-MgO catalyst is not sufficient to prepare a stable and efficient catalyst system, since the process of its production is multifactorial. For instance, the additional air supply at the stage of thermal decomposition and calcination promotes a 15-20 % increase in the efficiency of the $CoMo/Al_2O_3$-MgO catalyst. The use of the prepared catalyst in the CVD process (carbon source – propane-butane mixture, t = 650 °C, 40 min) makes it possible to obtain CNTs with a diameter of 10-30 nm and a length of more than 2 μm (Fig. 3). However, the instability of the characteristics of the catalyst hinders the reproduction of the synthesis of nanostructures with given parameters, which is quite important nowadays.

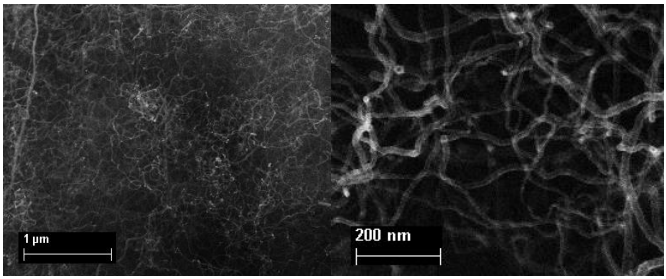

Fig. 3. SEM images of the CNTs synthesized over the $CoMo/Al_2O_3$-MgOcatalyst.

Controlling the catalyst quality at all the production stages may allow for achieving the reproducibility of obtaining an effective $CoMo/Al_2O_3$-MgO system through the thermal decomposition technique. To this end, procedures for validating initial reagents (regarding their solubility in water and decomposition of crystalline hydrates) and their solutions (regarding their density, electrical conductivity and pH) were developed herein. The procedure for evaluation of reagents regarding their solubility in water enablesfast determination of the reagent suitability for

the catalyst preparation. The decomposition of the crystalline hydrate during the validation of the initial reagents provides an opportunity to weed out partially decomposed initial components. The control of the density, electrical conductivity and pH of the initial component solutions also makes it possible to determine their suitability for the preparation of an effective CNT synthesis catalyst. To measure the electrical conductivity and the pH of the catalyst initial component solutions, a Hanna HI2550multifunctional multiparameter device (Eco Instrument Ltd, Moscow, Russia) was used. The validation regarding the reagent solubility allows to identify $(NH_4)_6Mo_7O_{24}\cdot 4H_2O$batches which meet the Russian National Standard (GOST) requirements, but do not appear to be suitable for the preparation of the CNT synthesis catalyst (due to incomplete dissolution). The incomplete dissolution of this reagent may be related to its partial decomposition. The X-ray diffraction analysis showed that the insoluble impurity in $(NH_4)_6Mo_7O_{24}\cdot 4H_2O$ corresponds to oblong $(NH_4)_2MoO_4$ crystals (Fig. 4). The presence of this impurity in the solution of the $CoMo/Al_2O_3$-MgO catalyst initial components is highly undesirable. Therefore, to solve this problem, two options were proposed herein: 1) additionally introducing a small NH_4OH amount into the solution, and 2) recrystallizing the reagent.

To determine the best way of solving the problem of the solubility of this reagent, four samples with $(NH_4)_6Mo_7O_{24}\cdot 4H_2O$ of different quality were prepared: satisfying (No. 1), not satisfying (No. 2) the solubility requirements, soluble but supplemented with the NH_4OH (No. 3) and recrystallized reagent (No. 4). The quality of the $(NH_4)_6Mo_7O_{24}\cdot 4H_2O$ preparation and dissolution was evaluated by the CNT specific yield on the catalyst containing this reagent. The analysis of this parameter suggested that the NH_4OH addition and the reagent recrystallization promote the transfer of the reagent from an unsatisfactory state to a state that satisfies the requirements for the preparation of carbon nanostructured material synthesis catalysts. However, the presence of an excess of the NH_4OH in the pre-catalyst solution may have a negative effect on the $CoMo/Al_2O_3$-MgO catalyst, since ammonium citrate may be formed after adding citric acid, which is highly undesirable. It should be noted that the need for precise control of the NH_4OH excess amount introduced at the $(NH_4)_6Mo_7O_{24}\cdot 4H_2O$dissolution stepcomplicates the process of obtaining the catalyst. That is why the recrystallization appears to be the most appropriate way of adapting the reagent that does not meet the solubility requirements for the preparation of the $CoMo/Al_2O_3$-MgO catalyst. The experimental results also showed that the highest value of the CNT specific yield is observed overthe catalyst prepared using the recrystallized $(NH_4)_6Mo_7O_{24}\cdot 4H_2O$. The validation of the reagents regarding their solubility in water and the degree of crystalline hydrate decomposition, as well as the reagent solutions regarding their density, electrical conductivity and pH, enables control over the quality of the solution of the initial components of the $CoMo/Al_2O_3$-MgO catalyst. The optimum density (1,510-1,515 kg/m^3) and electrical conductivity (1.54-1.72 μS/cm) values experimentally found for the catalyst initial component solution allow for obtaining a stable pre-catalyst. However, this is not enough, because the thermal treatment step, which consists of the thermal decomposition and calcination stages, plays a special role in the catalyst formation process. The experimental investigation of these stages made it possible to propose and test the methods for estimating mass losses of the catalyst system during heating and calcination and the pH of theresulting catalyst suspension, which allow for indirectly judging on the presence of undecomposed organic matter. It was found that when obtaining an effective $CoMo/Al_2O_3$-MgO catalyst, the loss of its mass after the calcination should not exceed 10 wt.%. In the suspension, the main component of which is the effective $CoMo/Al_2O_3$-MgO catalyst, the pH should be 10.1-10.4.

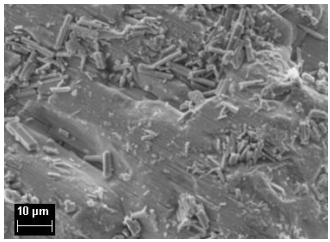

Fig. 4. Microstructure of $(NH_4)_6Mo_7O_{24}\cdot 4H_2O$ unsuitable for preparing the catalyst.

By implementing the catalyst validation procedures proposed at all the preparation stages, 15 batches of the $CoMo/Al_2O_3$-MgO catalyst samples were prepared and tested during the CVD

process under the same conditions. The analysis of the obtained data showed that the application of these procedures in the preparation of the catalyst stabilizes its efficiency. When using such a catalyst in the CVD process, the average CNT yield ranges from 10.3 to 11.9 $g_{CNTs}/g_{catalyst}$. Thus, the use of the proposed methods for validating the catalyst during its preparation makes it possible to obtain a stable effective catalyst for the synthesis of multi-walled CNTs with a diameter of 5-30 nm. The SEM images of the synthesized CNTs are presented in Fig. 5.

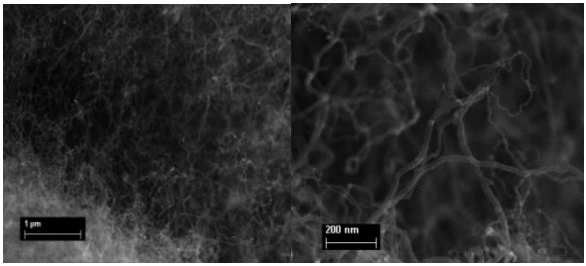

Fig. 5. SEM images of the CNT synthesized over the $CoMo/Al_2O_3$-MgO catalyst (obtained considering the validation procedures).

The use of the $CoMo/Al_2O_3$-MgO catalyst in the CVD process (a propane-butane mixture act allows for synthesizing CNTs with a specific yield of 20.3-23.0 $g_{CNTs}/g_{catalyst}$.

Conclusions

The present work experimentally proves that the process of $CoMo/Al_2O_3$-MgO catalyst preparation through the thermal decomposition method has its own peculiarities. The reagent quality and heat treatment conditions play an important role in obtaining the catalyst for the CNT synthesis, and that is why it is so important to carry out the catalyst validation at all production stages. The proposed procedures for validatingreagents regarding the solubility and degree of crystalline hydrate decomposition are what it exactly allows for eliminating the use of $(NH_4)_6Mo_7O_{24}\cdot 4H_2O$ which meets the GOST requirements but is not suitable for the catalyst preparation, even at the initial stage of obtaining the $CoMo/Al_2O_3$-MgO catalyst. Besides, the efficient way of adapting $(NH_4)_6Mo_7O_{24}\cdot 4H_2O$ which does not satisfythe solubility requirements for the production for the catalyst production for the CNT synthesis was elucidated herein. The optimum density and electrical conductivity values of the catalyst initial component solution were determined experimentally. They make it possible to obtain a stable pre-catalyst. Using the methods for estimating the mass loss of the $CoMo/Al_2O_3$-MgO catalyst during calcination and the pH of the resulting catalyst suspension allows for indirectly judgingon the presence of undecomposed organic matter in the sample, which is extremely undesirable, and to eliminate this, it is required to increase the duration of thecatalyst calcination process. The implementation of the catalyst validation procedures at all the preparation stages promotes the production of an effective (the nanoproduct yield of 10.3-11.9 $g_{CNTs}/g_{catalyst}$) $CoMo/Al_2O_3$-MgO catalyst, the application of which in the CVD process leads to obtaining CNTs with a diameter of 5-30 nm.

The work was funded by the Russian Science Foundation under Project No. 15-13-10038.

References

1. ***G.Sh. Shmavonyan, S.M. Zendehbad***. ScientiaIranica: Nanotechnology, **18** (3), 816 (2011).
2. ***G.Wang, J.Wang, H. Wang, J. Bai***. J. Environ. Chem. Eng., **2**, 1588 (2014).
3. ***N.A. Pakhomov***. Scientific Foundations for the Preparation of Catalysts: an Introduction to the Theory and Practice, SBof the RAS Publ., Novosibirsk, 2011 (in Russian).

STUDY OF RADIATION DEFECTS CREATED BY HIGH INTENSITY SHORT DURATION PULSE IRRADIATION IN SILICON CRYSTALS

Armenuhi Khachatryan

National Institute of Measurements CJSC, Armenia, www.nim.am

Introduction

A lot of works are devoted to the investigation of radiation defects in semiconductors, particularly, in silicon and germanium. This is explained by increase of interest on wide application of radiation methods to solve problems of semiconductor electronics, as well as development of new directions such as optoelectronics, microwave electronics and so on. One of the most promising techniques is radiation defects introduction method, i. e. directional modification of the properties of semiconductors under the action of various types of radiation.

The irradiation sources applied in usually investigations are conventional sources based on micro - second pulse beams (accelerators, nuclear reactors and so on) allowing to accumulate a large amount of irradiation doses in a short time and, consequently, quickly affect properties of irradiated materials. It is important to note that at the same irradiation dose, the irradiation intensity (amount of particles per 1sec. on 1 cm^2 cross-section of the beam) was proved to play an important role in affecting the properties of semiconductors [1-2]. The case when the irradiation source has a beam with a pulse shorter than "microsecond", is important, because it is scientific and practice interest (pulse nuclear reactors, space particle interactions, etc.). For understanding very short pulse beam influence on the materials, it is better to describe steps and time intervals of radiation interactions which take place at usual "microsecond" irradiation with materials.

The first stage of radiation influence is elastic transfer of irradiation energy to the atoms; the collision time with atoms is estimated to be 10^{-16} [2]. Atoms and electrons with excessive energy and impulse come into interaction with other atoms of matter, loosing energy through this action. This stage is called "energy exchange" from primary exciting particle and transition of the system to quasi-equilibrium state. At the inter-atomic distances this time is about $10^{-14} – 10^{-13}$ second [3-4].

The next process, relaxation of excessive energy received by atoms and electrons in crystal, takes place at time which is typical for the period of atomic oscillations, i. e., $10^{-13} – 10^{-12}$ second in solid states [3]. Further consideration relates to processes at average-statistic kinetic energy in order of kT (k is the Bolzman`s constant, T the absolute temperature). The system which is excited by irradiation passes through different quasi-equilibrium states and reconstruction of primary radiation defects occur. The speed of the latter exponentially depends on temperature and can extend over time. Secondary radiation defects are formed which are stable at room temperatures. In their formation both primary radiation defects (vacancies and interstitial atoms) and chemical impurities which were present in samples before irradiation, participate.

Experimental procedure and results

Irradiation of samples was carried out at room temperatures in linear accelerator of CANDLE Synchrotron Radiation Institute (Armenia) by electrons with 3.5 MeV energy, $4x10^{-13}$ sec. pulse duration, 12 Hz frequency, charge in impulse was 30 pico-Coulomb (we called pico- second pulse irradiation). The samples of n-Si were cut out in double-cross shape having 6 Ohmic contacts for electrical measurements, at 0.8 – 1.0 mm thickness, and $3x10mm^2$size.

Irradiation dose was defined:

$$D = 6.25 \times 10^{12} \times \frac{It}{S} \ [\text{el/cm}^2], \quad (1)$$

where I is the mean current in μA, t is exposition time in seconds and S is the cross-section of the beam in cm^2.

The beam current was measured by accumulated charge in Faraday cup. Electrical conductivity and charge carriers' mobility were measured applying known Hall effect method at different temperatures. Electrical conductivity was calculated by $\sigma = e\mu n$, where μ is the charge carriers' (Hall) mobility, n is the concentration of main charge carriers', e is the electron charge. The charge carriers` mobility was defined by Hall effect measurements:

$$\mu = \frac{U_H l}{U_\rho b B}, \quad (2)$$

where U_H is the potential difference between Hall contacts, U_ρ the potential difference between conductivity contacts, B the magnetic field induction, l and b are the sample`s length and width.

The measurement results are presented in Fig. 1-3 as a graphics of dose and temperature dependencies of electrical conductivity and charge carriers' mobility for samples of different specific resistivity. An obvious "critical dose" is seen on Fig. 1, after which the electrical conductivity of samples smoothly decreases and then sharply falls down. This effect depends on their initial specific resistivity, i.e. for higher specific resistivity the "critical dose" is reached rapidly. The charge carrier mobility has similar dependence. Note that for samples with specific resistivity 100 Ω·cm and 700 Ω·cm this dependence is almost the same; even at numerical values this dependence is only slightly different, in spite of significant difference in initial carrier concentrations. For samples with specific resistivity 950 Ω·cm and 700 Ω·cm the difference in carrier concentration is not so high but there is a significant difference in dose dependences. From comparison of Fig.1 and Fig.2 it is obvious that point radiation defects accumulation kinetics has a marked influence on the mechanism of charge carriers scattering. Note that these measurements were carried out at room temperatures.

Temperature dependencies of carrier mobility were studied to clarify the physical nature of their variations after irradiation (Fig. 2-3). The carrier mobility measurement results at the 120-300K temperatures for samples with specific resistivity100 Ω·cm are presented in Fig.3. It is obvious that the behavior of carriers' mobility temperature dependence before and after irradiation is almost the same up to maximum applied irradiation dose of 6 x 10^{13} el/cm^2.

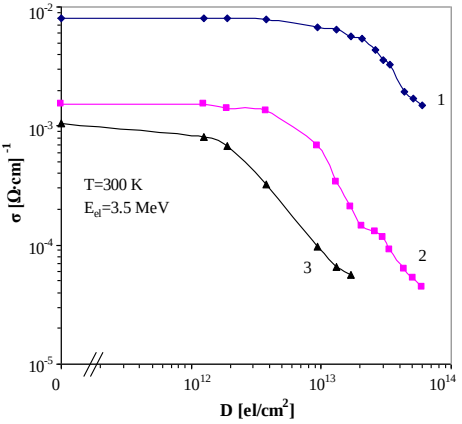

Fig. 1. Silicon crystal (n-Si) electrical conductivity dose dependence by electron pico-second beam irradiation (energy 3.5 MeV). Samples specific resistivity: 1 - 100 Ω·cm, 2 - 700 Ω·cm, 3 - 950 Ω·cm. Maximum irradiation dose is 6x10^{13} el/cm^2.

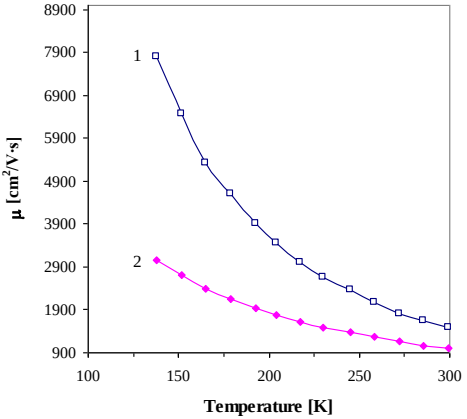

Fig. 2. Silicon crystal (n-Si) charge carriers' mobility temperature dependence after electron pico-second beam irradiation (energy 3.5 MeV). Sample specific resistivity100 Ω·cm: 1 – before irradiation, 2 – after irradiation by dose 6 x 10^{13} el/cm^2.

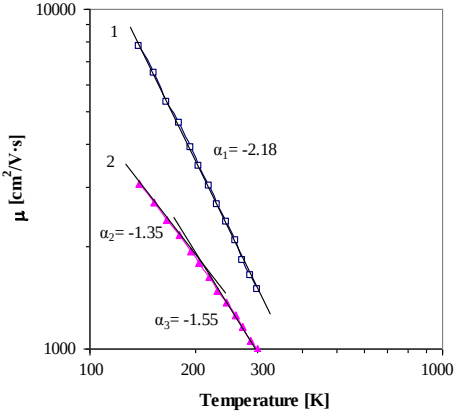

Fig. 3. Silicon crystal (n-Si) charge carriers' mobility temperature dependence after electron pico-second beam irradiation (energy 3.5 MeV). Sample specific resistivity100 Ω·cm: 1 – before irradiation, 2 – after irradiation by dose 6 x 10^{13} el/cm^2.The graphs are in log-log scale for better demonstration. The mathematical expression $\mu \sim T^{\alpha}$ gives possibility to explain charge carriers scattering mechanism for α_1=-2.18 before irradiation and α_2=-1.55; α_3=-1.35 after irradiation. Such behavior of carriers' mobility (line 2) is explained by carriers' scattering on the lattice defects.

However, detailed study of carriers' mobility temperature dependence in log-log scale points to a difference between these dependences (Fig. 3). Almost a straight line over entire temperature interval (line 1) before irradiation indicates the existence of uniform mechanism for carriers' scattering, i. e., scattering on the ionized impurity of phosphorus in n-Si. After irradiation there are two mechanisms for carrier scattering (line 2). The mathematical expression for the mentioned cases is as follows: $\mu \sim T^{\alpha}$, α_1=-2.18 before irradiation and α_2=-1.55; α_3=-1.35 after irradiation. Such behavior of carriers' mobility (line 2) is explained by carriers' scattering on the lattice defects

[4]; in the given case, scattering on the radiation defects created by pico-second pulse irradiation with energy 3.5 MeV.

It is worth mentioning that the behavior of samples with low specific resistivity (i.e. having high impurity concentration) is significantly different from others at low temperatures, where the region of scattering on ionized impurities seen; whereas in samples with high specific resistivity, this region is not observed, although the measurements are difficult at these temperatures because the conductivity is near intrinsic. The primary defect capture by different centers, that were present in samples before irradiation, plays an important role during these processes [4]. However, at sufficiently high doses ("critical dose") these channels may be exhausted , i.e. the centers saturated, but, on the other hand, concurrent radiation defects are accumulated, which act as channels for new reactions, leading to the changes of secondary radiation defects spectrum with irradiation dose. Along with this, the charge state of formed radiation defects changes, consequently the electrical-physical properties of the crystal also change.

Conclusions

From the above given results the following conclusions can be drawn:

1. Pico-second electron irradiation, in spite of low intensity has a significant effect on the electrical physical properties of silicon crystal.
2. The known "radiation annealing" which is typical to conventional micro- second pulse beam irradiation, at given pico-second pulse beam irradiation doesn't take place, because the thermal processes (duration $10^{-6} – 10^{-7}$second) don't have enough time to develop.
3. Study of temperature dependence of charge carrier mobility helped to reveal their scattering mechanism: scattering on the ionized impurities and on the radiation defects. At the same time it became possible to observe formation of point defects, followed by their cluster formation.
4. It was shown that the "critical dose" corresponding to sharp changes of electrical-physical properties depends on specific resistivity. In these cases it is found to be more appropriate to use an expression "dose threshold" of cluster formation instead of the more commonly used "energy threshold".

Acknowledgement: *The author is thankful to the scientific community of Applied Physics Division of Yerevan Physics Institute for great assistance to carry out this work.*

References

1. ***C. Leroy and P.G. Rancoita*.** Reports on Progress in Physics, **70**, 493 (2007).
2. ***S. Duzellier.*** Aerospace Science and Technology, **9**, 93 (2005).
3. ***P.G. Coleman, C.J. Edwardson, A.P. Knightsand, R.M. Gwilliam.*** The open access journal for physics. **4,** 025007 (2012).
4. ***V.V. Emtsev, A.M. Ivanov, et all.*** Physics and Technics of Semiconductors. **46,** 473 (2012).

FABRICATION OF MO/CUINSE$_2$ THIN FILMS BY DC MAGNETRON SPUTTERING

S. Petrosyan[1,2], N. Yeranyan[1], A. Musayelyan[1]

[1]Institute of Radiophysics and Electronics, NAS RA, Ashtarak, Armenia
[2]Russian-Armenian (Slavonic) University, Yerevan, Armenia,
E-mail: eranyan.narek@gmail.com

Introduction

Among group IV quantum dot nanostructures, which are highly promising for future generation solar and photovoltaic cell applications [1], copper indium diselenide (CIS) thin films have received considerable attention due to its high absorption coefficient, radiation stability, direct band gap and other features [2]. The current world record of 22.6% efficiency for such devices has been achieved by Zentrum Sonnenenergie & Wasserstoff Forsch Baden in 2016 [3]. Currently various techniques are available for $CuInSe_2$ films production, such as molecular beam epitaxy, thermal co-evaporation from Cu, In, and Se elemental sources, spray pyrolysis method, ink printing method, electrodeposition or a two-step process, which consists of DC magnetron sputtering of metallic indium and copper precursors followed by their selenization in Ar + Se atmosphere [4-6]. Among this methods, the last one offers a high level of control over film thickness and deposition sequence, as well as a not overly sophisticated process for manufacturing high-quality CIS thin films. The highest efficiencies for CIS based solar cells have been obtained by using alkali-aluminosilicate and soda-lime glass (SLG) as a / nsubstrate material [7]. The substrate is coated with molybdenum (Mo), which serves as the back contact for the solar cell. The choice of this metal is due to its high melting point (2623°C), mechanical strength and low resistivity [8-10]. It can be considered as the main transport gate for the sodium out-diffusion from SLG to the CIS thin film during its growth process at substrate temperatures close to the softening point of the substrate, when Na ions start to diffuse from the SLG into the semiconducting material through Mo back electrode [11]. The same process occurs in case of perlite-glass-ceramic substrates, containing 3.29wt. % of Na [12].

The main purposes of this work were the optimization of the growth parameters of CIS thin films on a soda-lime glass substrate from high purity elemental metallic targets by sequential DC magnetron sputtering in an argon atmosphere, with further selenization of thus prepared samples placed in graphite container inside the heated vacuum chamber and the study of Mo coated SLG with CIS thin film on it.

Experimental details

One micrometer CIS thin films were grown by a two-step process. In the first step, Cu and In metallic precursors with 99.999% purities were sputtered on a 1x1 cm square shaped soda-lime glass substrates by DC magnetron sputtering. In case of Mo coated SLG substrate, Mo film of thickness 0.5-0.6 μm was deposited by the same technique with working current of 600 mA and sputtering pressure of $1.3x10^{-2}$ mbar. Targets were positioned at 10 cm distance from the substrate and the base pressure in the chamber was 10^{-2} mbar. The magnetron was operated in DC mode with working current of 400 mA and duration of 200 minutes for the deposition of Cu and 200 mA with the duration of 50 minutes for In. For the second step, Cu-In deposited samples were placed in the special graphite container with several compartments: one for the granules of pure selenium and the others for the samples. A base pressure of nearly 10^{-2} mbar was established by a mechanical pump for the selenization process, which was performed in three steps. The first step at 120°C was to obtain a good Cu–In alloy where its physical properties become stable [13]. The second step was to heat up to 200°C and keeps them at this temperature for 20 minutes to encourage complete saturation of the alloy precursor with Se [14]. After that, depending on a batch they were kept at 400°C, 450°C, 500°C and 550°C temperature for 30 minutes, with the

ramp of 40°C per minute for the formation of CIS and the recrystallization process. The three steps of the selenization process are shown in Fig. 1. The total selenization time was 60 minutes. The structural and compositional properties of obtained $CuInSe_2$ and $Mo/CuInSe_2$ thin films were investigated by grazing incidence X-ray diffraction (XRD).

Results and discussion

The phase and crystallographic structure of Mo-coated glass and selenized films were analyzed by XRD. The XRD patterns of sputtered molybdenum film and $CuInSe_2$ films selenized at different temperatures are shown in Fig. 2 and Fig. 3 respectively. The experimental parameters and structural properties of CIS thin films obtained from XRD analysis are summarized in Table 1.

It can be seen, that Mo crystallites exhibit cubic crystal structure according to the

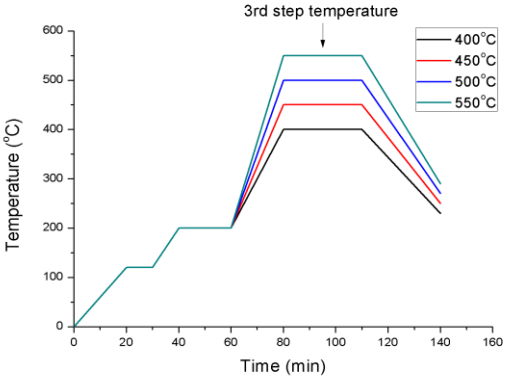

Fig. 1. Temperature profile of the selenization process.

ASTM 4-809 standards. From Fig. 2 it is obvious, that single peak was observed with preferred crystallographic orientation along (110) direction. The average crystallite size for both Mo and CIS thin films was

calculated using the following equation [15]:

$$L = \frac{K\lambda}{B\cos\theta},$$

where K is the Scherrer constant (K=0.94), λ is the wavelength of the incident monochromatic X-ray beam ($CuK_\alpha = 1.5404$Å) and B is the FWHM of diffraction peak at corresponding θ.

In Fig. 3, the XRD spectra corresponding to the films selenized at different temperatures (from 400℃ up to 550℃) are plotted. These spectra showed the presence of indium and copper oxides, $Cu_{2-x}Se$ binary compound (Berzelianite) and CIS chalcopyrite phase. The formation of above mentioned phases assumed to be represented by the following chemical reactions [16]:

$2Cu_{11}In_9 + 29Se \Rightarrow 11Cu_2Se + 18InSe$ or $2Cu_{11}In_9 + 20Se \Rightarrow 11Cu_2Se + 9In_2Se$,

then

$Cu_2Se + 2InSe + Se \Rightarrow 2CuInSe_2$ or $Cu_2Se + In_2Se \Rightarrow 2CuInSe_2$

respectively, and separately

$4In + 3O_2 \Rightarrow 2In_2O_3$ and $2Cu + O_2 \Rightarrow 2CuO$.

The average crystallite size of obtained $CuInSe_2$ phase and the thickness of the layer show identical behavior with the increase of selenization temperature (Fig. 4). At lower temperatures both parameters increase with the increase of the temperature. But in case of 500℃ percentage of $CuInSe_2$ starts to decrease along with the decrease in the crystallite size and thickness of the film due to the evaporation of the precursors.

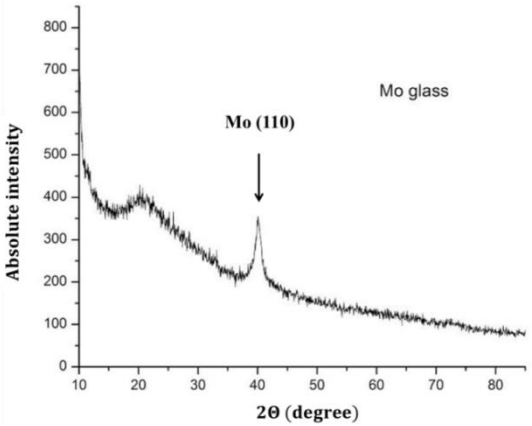

Fig. 2. XRD spectra of Mo-coated soda-lime glass.

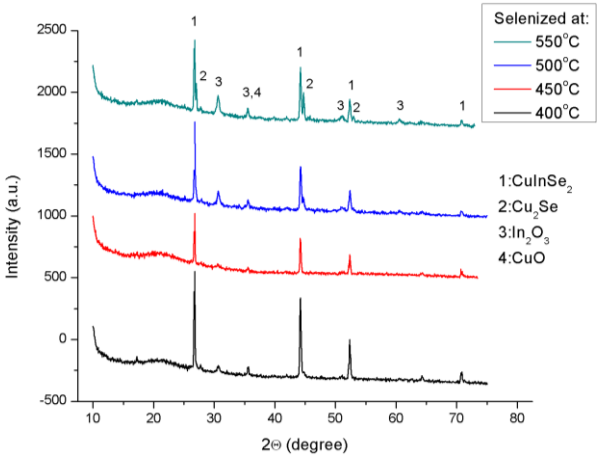

Fig. 3. XRD spectra of all samples without Mo layer selenized at different temperatures.

The X-ray diffraction pattern of CIS thin film grown on Mo-coated glass, which was selenized at 450℃ for 30 minutes, is shown in Fig. 5. The film, as it was expected, shows three intense peaks, which correspond to the reflections from (112), (220/204), and (116/312) directions, that indicate the crystalline phases of CIS. One can notice, that the splitting of two doublets 220/204 and 116/312 does not exist in the XRD pattern of this sample due to the right choice of the selenization temperature. Additionally, all the films have two preferred orientations perpendicular to the (112) and (220/204) planes. It is also noticeable from Fig. 5 that Mo peak has a large amount of FWHM (full width at half maximum) due to the high sputtering pressure, which has certain impact on the electrical and structural properties of the Mo film, especially on the resistivity and porosity [17]. On the other hand, the growth parameters were chosen to provide good adhesion to the glass substrate.

The calculated lattice parameters of the last sample with Mo back contact are a = 5.784±0.003Å, c = 11.615±0.01 Å and the axial ratio is c/a = 2.008 for $CuInSe_2$ phase, which is in good agreement with [18] and α_{Mo} = 3.1788 Å for molybdenum.

Table 1. Structural properties of DC-plasma sputtered Mo and CIS thin films calculated from XRD

Sample	T, °C	Phases	Amount (%)	Thickness of the layer (nm)	$CuInSe_2$ crystallite size (nm)
a	400	$CuInSe_2$+Cu_2Se+CuO	78.3/12.5/9.2	1260±170	320
b	450	$CuInSe_2$+In_2O_3	95.7/4.3	1310±205	440
c	500	$CuInSe_2$+Cu_2Se+In_2O_3	47.1/32.4/20.5	1200±210	400
d	550	$CuInSe_2$+ In_2O_3+ Cu_2Se	57.8/12.9/29.3	820±200	360
Mo-coated glass	RT (startig point)	Mo	100	550±30	10

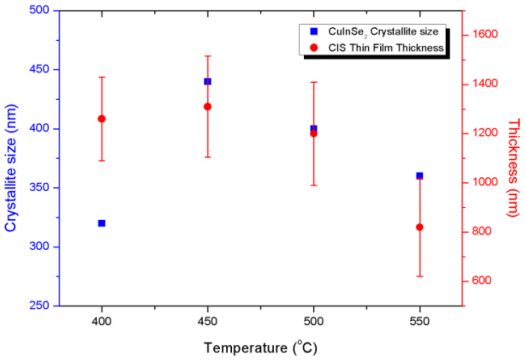

Fig. 4. The average crystallite size and thickness of CIS thin films as a function of selenization temperature.

Conclusions

In this work, single-phase chalcopyrite CIS thin films have been obtained by selenization at different temperatures varying from 400 to 550℃. Average crystallite size of the desired $CuInSe_2$ phase increased with the increase of selenization temperature from 400℃ to 450℃, but in case of 500℃ percentage of $CuInSe_2$ starts to decrease along with the decrease in the crystallites size. Both of those values go down with the further increase of the selenization temperature. Thickness of the layer shows the same behavior as the crystallites average size value. The optimal temperature for selenization process was established to be 450℃ and applied during the preparation of SLG/Mo/CIS structure. All the films exhibit two preferred orientations along (112) and (220) planes. Among CIS phase, In_2O_3, CuO and Cu_2Se phases also were presented in the XRD patterns of the films. The lattice parameters obtained for all phases are in good agreement with the known data.

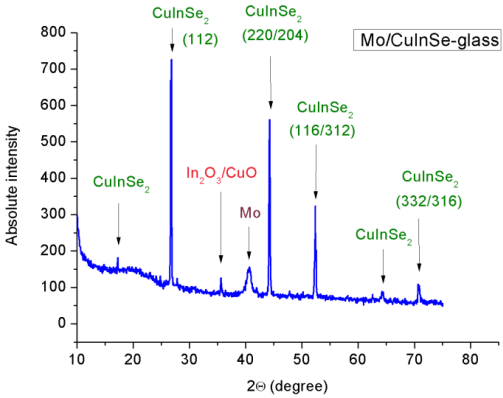

Fig. 5. XRD pattern of CIS thin film grown on Mo-coated soda-lime glass and selenized at 450 °C.

References

1. ***G. Conibeer, M. Green, W.C. Cho et al***. Thin Solid Films **516** (20), 6748 (2008).
2. ***D. Cahen, J.-M. Gilet, C. Schmitz, L. Chernyak, K. Gartsman, A. Jakubowicz.*** Science **258** (5080), 271 (1992).
3. ***P. Jackson, R. Wuerz, D. Hariskos, E. Lotter, W. Witte, M. Powalla***, Phys. Status Solidi RRL, **10,** 583 (2016).
4. ***Sho Shirakata et al***. *Jpn. J. Appl. Phys.*, **38,** 4997 (1999).
5. ***V.K. Kapur, A. Bansal, P. Le, O.I. Asensio***. Thin Solid Films **431-432,** 53 (2003).
6. ***K. Ramanathan, et al.*** Prog. Photovolt: Res. Appl., **11,** 225 (2003).
7. ***M.A. Contreras, B. Egaas, K. Ramanathan, J. Hiltner, A. Swartzlander, F. Hasoon, R. Noufi***. Prog. Photovolt. Res. Appl., **7,** 311 (1999).
8. ***D.W. Hoffmann, R.C. McCune***, Handbook of Plasma Processing Technology, Noyes, Park Ridge, NJ, 1989.
9. ***S. Ashour et al***. Thin Solid Films, **226,** 129 (1993).
10. ***K. Granath, A. Rockett, M. Bodegard, C. Nender, L. Stolt***. 13th European Photovoltaic Solar Energy Conference, Nice, France, 1995, pp.1983-1986.
11. ***H.A. Al-Thani, F.S. Hasoon, M. Young, S. Asher, J.L. Alleman, M.M. Al-Jassim, D.L. Williamson***. Photovoltaic Specialists Conference, IEEE, 2002, pp. 720-723.
12. ***S.G. Petrosyan et al.*** Eur. Phys. J. Appl. Phys., **62** (3), 30103 (2013).
13. ***T. Nakano, T. Suzuki, N. Ohnuki, S. Baba***. Thin Solid Films, **334,** 192 (1998).
14. ***R. Caballero, C. Guillen***. Solar Energy Materials & Solar Cells, **86**, 1 (2005).
15. ***M. Khan, M. Islam***. Sov. Semicond. Phys. (FTP), **47**(12), 1636 (2013).
16. ***S. Verma, N. Orbey, R. Birkmire, T. Freser Russel***. Progress in Photovoltaics: Research and Applications, **4**, 341 (1996).
17. ***J.H. Scofield, A. Duda, D. Albin, B.L. Ballard, P.K. Predecki***. Thin Solid Films, **260**, 26 (1995).
18. ***J.J.M. Binsma, L.G. Giling, J. Bloem.*** Journal of Crystal Growth, **50**, 429 (1980).

ABOUT MAGNETIC PROPERTIES OF THE COMPOUND $K_3Cu_3AlO_2(SO_4)_4$

N. Ananikian[1], R. Kenna[2], H. Lazaryan[1], and M. Nalbandyan[1]

[1]*Alikhanyan National Science Laboratory, Alikhanian Br. 2, 0036 Yerevan, Armenia*
[2]*Applied Mathematics Research Centre, Coventry University, Coventry, CV1 5FB, UK*

Using the density matrix renormalization group method, the magnetic behavior of the compound $K_3Cu_3AlO_2(SO_4)_4$, which represents the physical realization of the diamond chain, was studied. For the numerical calculations, we used the ALPS (Algorithms and Libraries for Physics Simulations) library.

1. Introduction

Low-dimensional systems are particularly attractive since they provide opportunities for approbation of condensed-state physics models. The fact is that models for low-dimensional systems can be more easily analyzed than large-scale models, on the one hand, on the other hand, they reveal a wide range of the most diverse and interesting physical properties, being, thus, a touchstone for the above-mentioned field. The more interesting are the physical implementations of low-dimensional systems, which make it possible to compare theoretical results with experimental ones. The so-called diamond chain model, which is a quasi-one-dimensional structure, was proposed to explain the properties of the compound $Cu_3Cl_6(H_2O)_2{\cdot}2H_8C_4SO_2$ [1]. Presently, more than a dozen compounds having the structure of parallel located diamond chains are known [2-5]. Among them – the long-known natural mineral azurite $Cu_3(CO_3)_2(OH)_2$ [2,3], attracted the great interest both in the experimental and theoretical sectors. Such interest was caused by the following reasons. On the one hand, attempts have been made to describe the azurite in the approximation of parallelly placed diamond chains, such that the interaction between them is much less than the interactions inside the diamond chain, or the effect of the interchain couplings is transferred to the couplings inside the diamond chain (the effective diamond chain model). On the other hand, within the framework of this model, the researchers, using various theoretical approaches, came to different, sometimes contradictory, values for coupling constants, nevertheless, with good consistency of theoretical to particular experimental results. For example, the Kikuchi group established $J_1 : J_2 : J_3 = 1 : 1.25 : 0.45$ [2.3], Gu and Su [6,7] proposed the anisotropy of the Heisenberg bond, with the presence of a ferromagnetic component, for the best coincidence with the experimental magnetic susceptibility: $J_1 : J_2 : J_{3z} = 1 : 1.9 : -0.3$ and $J_{3x} / J_{3z} = J_{3y} / J_{3z} = 1.7$. In the researches, for the coupling J_3, both antiferromagnetic [8,9] and ferromagnetic [10,11] values were proposed. Extensive research undertaken by a group of researchers [12] established the values of the coupling constants for the model of an effective diamond chain, in which the best consistency with all experimental data is observed. Taking into account direct nodal couplings here was significant. It should also be noted a number of theoretical works directly related to experimental data, or revealing the properties of diamond chains with an arbitrary spin in general, without binding them to specific materials [13-22]. Recently, a group of Japanese researchers synthesized a compound $K_3Cu_3AlO_2(SO_4)_4$ with a diamond chain structure [5]. The dependence of the magnetic susceptibility on temperature was measured in the work, as well as the dependence of the magnetization on the external magnetic field up to 50 T.

In Paragraph 2 of this paper the Hamiltonian for an antiferromagnetic diamond chain studied. In Section 3, for numerical values of the coupling constants obtained in [5], we numerically calculate the magnetization curve using DMRG method for 300 spins (100 diamonds) by means of the ALPS (Algorithms and Libraries for Physics Simulations) library. The Conclusion contains the main results.

2. The Hamiltonian of the model

On the basis of the result of Ref. [23], using the high-temperature series expansion method, they, under the assumption of symmetric diamond chain, obtain the coupling constants values for which the best fit of the theoretically calculated magnetic susceptibility curve is observed with the experimental curve in the temperature range from 100 to 300 K.

We use an antiferromagnetic Heisenberg Hamiltonian with spins 1/2 for our diamond chain:

$$H = J_1 \sum_i \left(\vec{S}_{3i-1}\vec{S}_{3i} + \vec{S}_{3i}\vec{S}_{3i+1} \right) + J_2 \sum_i \vec{S}_{3i+1}\vec{S}_{3i+2} + \\ + J_3 \sum_i \left(\vec{S}_{3i-2}\vec{S}_{3i} + \vec{S}_{3i}\vec{S}_{3i+2} \right) + J_m \sum_i \vec{S}_{3i}\vec{S}_{3i+3} - g\mu_B h \sum_i S_j^z . \quad (1)$$

where $\vec{S}_i$ are the spin operators 1/2, J_i are the interaction constants between the Cu^{2+} ions. h, μ_B and g is the value of the z projection of the external magnetic field, the Bohr magneton and the gyromagnetic ratio (2.06), respectively. The Figure 1 illustrates two diamonds clusters from the chain.

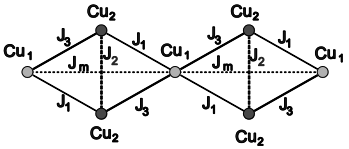

Fig. 1. Structure of the rhombus.

3. Magnetic properties of the model

For the values of $J_1 = J_3 = 132, J_2 = 336$ (symmetric diamond chain) taken from [5], we performed a numerical calculation using the density matrix renormalization group method (DMRG) [24] and the matrix product of states method (MPS) [25, 26] diamond chain containing 300 spins (100 diamond clusters). For the calculations, we used the ALPS library [27,28]. The calculations were performed on a super cluster of the Yerevan Physical Institute (SuperServer 7047GR-TRF) using parallel computations. The Figure 2 shows the magnetization curve. It can be seen that it has a 1/3-plateau in the 50-300 T region. According to the experimental results obtained in the above work, the magnetic plateau is not observed up to 70 T. According to this, we can say that fitting the coupling constants and the gyromagnetic ratio, using only the behavior of the magnetic susceptibility, turns out to be insufficient for a correct description of the magnetic behavior of the mentioned compound. Quite recently a publication [29] appeared, in which the model of an asymmetric diamond chain for the compound $K_3Cu_3AlO_2(SO_4)_4$ is considered. In this publication, along with antiferromagnetic, ferromagnetic interactions are also introduced, and the value of the gyromagnetic ratio is also revised. Calculations were made at zero temperature by the renormalization-group approach of the density matrix (DMRG) at 120 spins. In the article appears 1/3-plateau of magnetization in the region 110-250T from the external magnetic field.

4. Conclusion

We obtained the magnetization curve for the $K_3Cu_3AlO_2(SO_4)_4$ compound model by the density matrix renormalization group (DMRG) method and the matrix product state (MPS) method using the ALPS library. The chosen number of spins in our model of a periodic and symmetrical diamond chain is quite sufficient to predict with great accuracy the appearance of a magnetic 1/3 plateau on the magnetization curve in the framework of this model. Thus, we show that the values obtained in the work [5] cannot be correct and in spite of the fact that they give a good coincidence of the magnetic susceptibility in the temperature range 100-300 K, nevertheless they contradict the experimental data on the magnetization, leading to the appearance in model 1/3-plateau with an external magnetic field from 50T, whereas in the experiment it is not observed up to 70T.

The authors acknowledge financial support by the MC-IRSES (612707, DIONICOS) under FP7-PEOPLE- 2013, CS MES RA in the frame of SCS 15T- 1C114 grants.

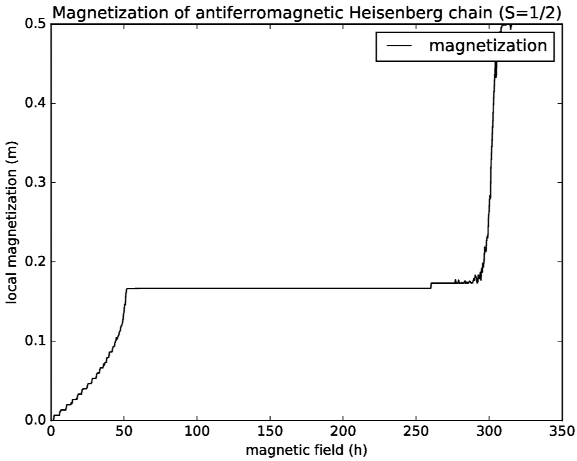

Fig. 2. Magnetization curve of the rhombus.

References

1. ***K. Okamoto, T. Tonegawa, et al.*** J. Phys.: Cond. Mat., **11,** 10485 (1999).
2. ***H. Kikuchi, Y. Fujii, M. Chiba, S. Mitsudo, et al.*** Phys. Rev. Lett., **94,** 227201 (2005).
3. ***H. Kikuchi et al.*** Prog. Theor. Phys. Suppl., **159,** 1 (2005).
4. ***S. Yoneyama, T. Kodama, et al.*** CrystEngComm, **16,** 10385 (2014).
5. ***M. Fujihala, H.Koorikawa, et al.*** J. Phys. Soc. Jpn., **84**, 073702 (2015).
6. ***B. Gu and G. Su.*** Phys. Rev. Lett., **97,** 089701 (2006).
7. ***B. Gu and G.j Su.*** Phys. Rev. B, **75,** 174437 (2007).
8. ***H-J. Mikeska and C. Luckmann.*** Phys. Rev. B, **77,** 054405 (2008).
9. ***J. Kang, C. Lee, R.K. Kremer and M-H. Whangbo***. J. Phys.: Cond. Mat., **21**, 392201 (2009).
10. ***Y-C. Li.*** J. Appl. Phys., **102**, 113907 (2007).
11. ***K.C. Rule, A.U.B. Wolter, et al.*** Phys. Rev. Lett., **100**, 117202 (2008).
12. ***H. Jeschke, I. Opahle, H. Kandpal, et al.*** Phys. Rev. Lett., **106,** 217201 (2011).
13. ***N. Ananikian, H. Lazaryan, M. Nalbandyan.*** Eur. Phys. J. B, **85,** 223 (2012).
14. ***M. Nalbandyan et al.*** Journal of the Phys. Soc. of Japan **83**, 074001 (2014).
15. ***H. Lazaryan et al.*** Int. Journal of Modern Phys. B, **30,** 1650135 (2016).
16. ***L. Canova, J. Strecka and M. Jascur.*** J. Phys.: Condens. Matter, **18,** 4967 (2006)
17. ***B. Lisnyi and J. Strecka.*** J. Magn. Mater., **346**, 78 (2013)
18. ***Onofre Rojas, M Rojas, N. S. Ananikian, S. M. de Souza.*** Phys. Rev. A, **86,** 042330 (2012).
19. ***O. Rojas, S.M. de Souza, V. Ohanyan, M. Khurshudyan*.** Phys. Rev. B, **83**, 094430 (2011).
20. ***J. Torrico, M. Rojas, et al.*** EPL **108**, 50007 (2014)
21. ***V. Abgaryan, N.S. Ananikian, et al.*** Solid State Communications, **224,** 15 (2015).
22. ***V. Hovhannisyan, J. Strecka, N. Ananikian.*** J. Phys.: Condens. Matter **28,** 085401 (2016).
23. ***A. Honecker, A. Lauchli.*** Phys. Rev. B, **63,** 174407 (2001) .
24. ***S.R. White.*** Phys. Rev. Lett., **69**, 2863 (1992).
25. ***A. Klumper, A. Schadschneider, J. Zittartz.*** J. Phys. A, **24**, L955 (1991).
26. ***D. Perez-Garcia, F. Verstraete, M.M. Wolf, J.I. Cirac.*** Quantum Inf. Comput., **7**, 401 (2007).
27. ***B. Bauer and et al.*** J. Stat. Mech. P05001 (2011).
28. ***A.F. Albuquerque et al.*** Journal of Magnetism and Magnetic Materials, **310**, 1187 (2007).
29. ***K. Morita et al.*** arXiv:1701.02198 [cond-mat.str-el].

MAGNETORESISTAMCE AND HALL RESISTANCE OF Sb_2Te_3 NANOFLAKES

S.R. Harutyunyan[1], Wei-Han Tsai[2], Yang-Yuan Chen[2]

[1]Institute for Physical Research, NASRA, Ashtarak, Armenia
[2]Institute of Physics, Academia Sinica, Nankang, Taiwan
E-mail: sergeyhar56@gmail.com

Introduction

Antimony Telluride (Sb_2Te_3) compound is known as a semiconductor with good thermoelectric properties [1]. Recently, Sb_2Te_3 attracts increased attention of researchers as it is also a topological insulator (TI) [2]. The surface states of TIs are non-dissipative and highly conductive, as protected by the time reversal symmetry. TIs are considered as promising materials for spintronics and quantum computations [3, 4]. In topological insulators the phenomena such as non-saturated and linear magneto-resistance as well as the anomalous Hall effect have been registered [5-11]. Anomalous Hall effect has previously been detected in ferromagnetic conductors where it was induced due to spin-dependent scatterings of charge carriers [12]. The origin of the nonlinear Hall resistance in TIs is attributed to the contribution of the surface states and results from anomalous Hall effect described by the Dirac theory [5-9].

This paper presents the results on experimental study of thickness dependent Hall resistance and magneto-resistance of Sb_2Te_3 nanoflakes at temperatures from 2K to 300 K. Sb_2Te_3 is a p-type semiconductor with multivalley valence band which consists of the upper (light hole) and the lower valence band (heavy holes) responsible for conductivity [13]. To observe effects related to the contribution of the surface states to the conductivity thin samples are required. In this work the samples of different thickness (25 nm, 34 nm and 450 nm) were selected for comparison.

The results and discussions

Sb_2Te_3 nanoflakes of different thickness were grown by vapor phase deposition method using polycrystalline Sb_2Te_3 compound as a source material [14, 15]. Scanning electron microscope (SEM) and transmission electron microscope (TEM) images confirm that the samples are single-crystalline (Fig. 1). Energy-dispersive x-ray spectroscopy showed a similar ratio Sb/Te = (41 ± 1)/(59 ± 1) in all three samples. The resistance of the nanoflakes were measured by a standard four-probe method in perpendicular to the plane of the sample magnetic fields up to 9 T and at temperatures from 2 to 300 K. Magneto-resistance was defined as MR = (100%) × $(R_B\text{-}R_0)/R_0$, where $R_B = R(B)$ resistance of the sample in a magnetic field B, and R_0 is the resistance of the sample out of a magnetic field.

The resistance and magneto-resistance of the nanoflakes show a strong dependence on their temperature and thickness. The normalized resistance R_T/R_{300} demonstrates metallic behavior in the temperature region of measurement, which is typical for Sb_2Te_3 compound. The steepness of $R(T)$ curves decrease and the residual resistance grows when thickness of the nanoflakes decreases. This is caused by increasing number of defects in the nanoflakes, as well as by increasing of scattering from the boundaries (Fig. 2).

The ordinary positive MR is caused by Lorentz force and is quadratic function of the magnetic field and mobility of charge carriers, i.e. magneto-resistance MR ~ $(\mu B)^2$. The strong dependence of the mobility of charge carriers on the thickness of the nanoflakes has direct impact on MR curves. MR at high temperature is reduced significantly because mobility is further suppressed by the intense electron-phonon scattering. The transverse resistance $R_{xy}(B)$ of the nanoflakes with thickness of 25 nm and 450 nm are depicted in Fig. 3. While $R_{xy}(B)$ dependence of 25 nm thick sample is almost linear at 300 K and 2 K, the $R_{xy}(B)$ dependence of 450 nm thick sample is nonlinear and transformed from concave at 2 K to convex at 300 K. Based on $R_{xy}(B)$ results we obtained the values of mobility $\mu = R_H/\rho = 0.0145$ m^2/Vs and 0.0075 m^2/Vs and number of charge

carriers $p = 1/(R_H q) = 3\times10^{26}$ m^{-3} and 2×10^{26} m^{-3} at 2 K and 300 K respectively for the 25 nm thick sample, where $R_H = (R_{xy}d)/B$ is Hall coefficient, ρ is the resistivity and q is elementary charge. The concentration of holes in this sample exceeds the concentrations usually observed in bulk Sb_2Te_3, and confirms previously observed dependence of the number of charge carriers on the thickness of nanoflakes [16]. $R_{xy}(B)$ dependence of the 34 nm thick sample is also nonlinear but is straightened gradually with temperature and at 300 K it becomes linear (Fig. 4).

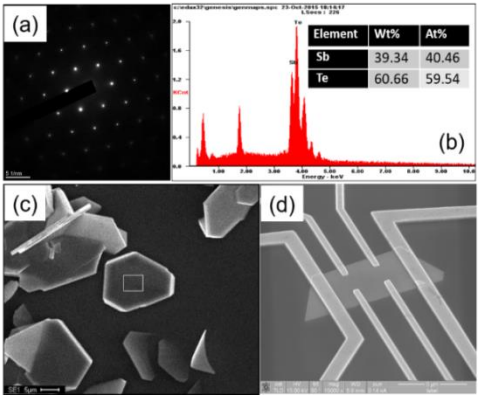

Fig.5. (a) TEM diffraction image one of the nanoflakes. (b) EDX spectrum one of the nanoflakes. (c) SEM image of the grown nanoflakes with marked area where the EDX probe was taken. (d) SEM image of one of the nanoflakes with

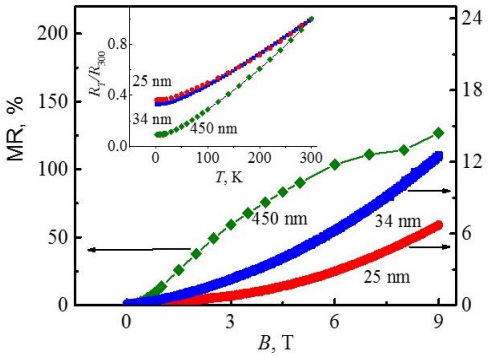

Fig. 2. Magneto-resistance of the nanoflakes of different thickness at 2 K. Inset; Temperature dependences of the normalized resistance of the nanoflakes.

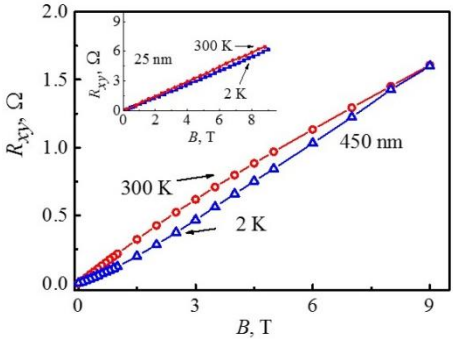

Fig. 3. R_{xy}(B) dependences of the nanoflakes with thickness 450 nm at 2 K and 300 K. Inset; R_{xy}(B) dependences of the nanoflakes with thickness 25 nm at 2 K and 300 K.

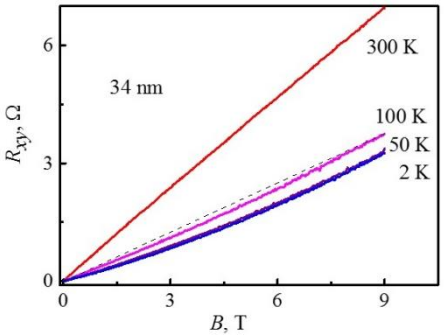

Fig. 4. R_{xy}(B) dependences of the nanoflake with thickness 34nm at 2 K, 10 K, 50 K, 100 K and 300 K. The dot line is guide for eyes.

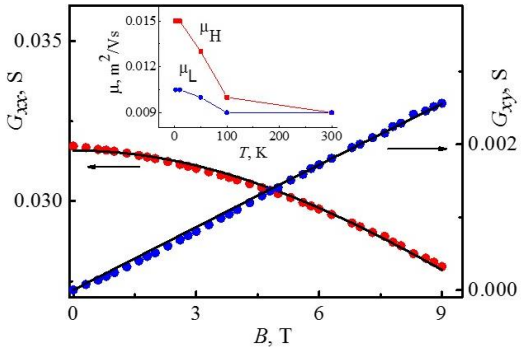

Fig. 5. G_{xx}(B), G_{xy}(B) dependencies (dots) and the fitting curves of the sample with thickness 34 nm at 2 K. Inset; Temperature dependences of the fitting parameters of mobility μ_L (heavy holes) and μ_H (light holes).

The obtained dependencies of the longitudinal R_{xx} and transverse R_{xy} resistances of the nanoflakes are analyzed, considering the resistance as functions of relevant magneto-conductivity tensor components. In the case of an electric field is applied in the *X* direction and the magnetic field *B* in the *Z*-direction it is given by an expressions:

$$R_{xx} = \frac{G_{xx}}{G_{xx}^2+G_{xy}^2}, \quad R_{xy} = \frac{G_{xy}}{G_{xx}^2+G_{xy}^2}, \quad G_{xx} = \frac{R_{xx}}{R_{xx}^2+R_{xy}^2}, \quad G_{xy} = \frac{R_{xy}}{R_{xx}^2+R_{xy}^2}, \tag{1}$$

where G_{ij} are the components of magneto-conductance. The $G_{ij}(B)$ dependencies were calculated from expression (1). Applying Drude model and using the fitting parameters μ_f and p_f, the right side of the expression (3) is fitted to the received $G_{ij}(B)$ dependences:

$$G_{xx}(B) = \frac{qp_f\mu_f}{[1+(\mu B)^2]}, \; G_{xy}(B) = \frac{qp_f\mu_f^2 B}{[1+(\mu B)^2]}. \tag{3}$$

The model of single-channel transport fits well with the $G_{ij}(B)$ dependencies in the case of 25 nm thick sample at 2 K and 300 K, as well as for the sample with thickness of 34 nm at 300 K. The fitting parameters μ_f and p_f are in good agreement with the experimental values of μ and p of an order of magnitude. The parameters μ and p obtained from $G_{xy}(B)$ dependence do not match with those obtained from $G_{xx}(B)$. This is a common discrepancy for semiconductors and stems from the fact that the scattering mechanisms are not energy-independent. Thus, measured Hall mobility and the number of charge carriers will differ from the actual drift mobility and the number of charge carriers through the multiple scattering factor $r = \langle\tau^2\rangle/\langle\tau\rangle^2$, where τ is the average time between collisions of charge carriers [17]. Nonlinear Hall effect, observed in samples with thicknesses 34 nm and 450 nm, indicates the presence of a multichannel transport. Here the two-channel transport model has been applied, where both channels have *p*-type charge carriers, but of different number and motility. The total conductivity is the sum $G = G_1 + G_2$:

$$G_{xx}(B) = \frac{qp_1\mu_1}{[1+(\mu_1 B)^2]} + \frac{qp_2\mu_2}{[1+(\mu_2 B)^2]}, \; G_{xy}(B) = \frac{qp_1\mu_1^2 B}{[1+(\mu_1 B)^2]} + \frac{qp_1\mu_2^2 B}{[1+(\mu_2 B)^2]}, \tag{4}$$

where μ_i and p_i are the mobility and the number of charge carriers of the *i*-th channel.

The comparison of the fitting parameters μ_i and p_i ($\mu_1 = 0.63$ m^2/Vs, $p_1 = 5.9\times10^{25}$ m^{-3}, $\mu_2 = 0.1$ m^2/Vs, $p_2 = 0.8\times10^{25}$ m^{-3} at 2 K and $\mu_1 = 0.26$ m^2/Vs, $p_1 = 0.24\times10^{25}$ m^{-3}, $\mu_2 = 0.065$ m^2/Vs, $p_2 = 4.5\times10^{25}$ m^{-3} at 300 K) of 450 nm thick nanoflake revealed that the majority charge carriers at 2 K are carriers with high mobility while the majority of carriers at 300 K have low mobility. Perhaps this inversion between the numbers of the majority and minority carriers is the main reason for changing the shape of the $R_{xy}(B)$ curves from concave to convex. The strong electron-phonon scattering at high temperatures causes a substantial decrease in the number of carriers of high mobility. As for the 25 nm thick sample the scattering here is so intense that it overwhelms the carriers with high mobility and leads to ordinary (linear) Hall effect. The sample with thickness 34 nm is in an intermediate position. The scatterings are considerably stronger in it than in the 450 nm thick sample but it still contains a sizeable number of carriers with high mobility, resulting in nonlinear $R_{xy}(B)$ at low temperatures. However, the $R_{xy}(B)$ dependence is transformed into a linear at 300 K due to suppression of high mobility carriers. Figure 5 shows the $G_{xx}(B)$, $G_{xy}(B)$ dependencies and the fitting curves of the sample with thickness 34 nm at 2 K. Temperature dependence of fitting parameters of mobility of this nanoflake is shown in the Insert of Fig. 5 and demonstrates quite expected trend of increasing intensity of scatterings with temperature. We can conclude that non-linear behavior of $R_{xy}(B)$ is not related to the surface states. Otherwise, the effect would be stronger in the sample with thickness of 25 nm. It can be assumed that even if the effect exists it is masked by the strong scattering processes. Most likely the observed nonlinear effect is attributed to the contribution of both valence band with light and heavy effective masses holes. The model does not account for the spin-dependent current (or spin-dependent scattering), which is not negligible in case of strong spin-orbit interaction.

Conclusion

Sb_2Te_3 nanoflakes of different thickness were grown by vapor phase deposition method. Hall resistance and magneto-resistance of the samples were measured in magnetic fields up to 9 T at

temperatures from 2 K to 300 K. The magneto-resistance and Hall resistance of the nanoflakes show a strong dependence on the thickness of the samples. Relatively thick samples show a nonlinear dependence of Hall resistance on magnetic field. The measurement data are analyzed within Drude model of multichannel transport. The Hall resistance behavior is attributed to the existence of two channels of charge transfer with high and low mobility. The two-channel transport is responsible for non-linear Hall effect in the Sb_2Te_3 nanoflakes.

References

1. ***C. Wood***. Rep. Prog. Phys. **51,** 459 (1988).
2. ***M.Z. Hasan, C.L. Kane*.** Rev. Mod. Phys. **82,** 3045 (2011).
3. ***J.E. Moore***. Nature **464**, 194 (2010).
4. ***Y. Ando, S.-C. Zhang***. Physics **1**, 6 (2008).
5. ***D.X. Qu, Y.S. Hor, J. Xiong, R.J. Cava, N.P. Ong***. Science **329**, 821 (2010).
6. ***Z.J. Yue, X.L. Wang, Y. Du et al.*** EPL **100**, 17014 (2012).
7. ***H. Tang, D. Liang, R.L.J. Qiu, X.P.A. Gao***. ACS Nano **5**, 7510 (2011).
8. ***H. He, B. Li, H. Liu, X. Guo, Z.Wang et al***. Appl. Phys. Lett. **100,** 032105 (2012).
9. ***H-J. Kim, Ki-Seok Kim et al*.** Phys. Rev. B **84**, 125144 (2011).
10. ***A.A. Abrikosov***. Europhys. Lett. **49,** 789 (2000).
11. ***B.A. Assaf, T. Cardinal, P. Wei, F. Katmis, J.S. Moodera, D. Heiman***. Appl. Phys. Lett. **102**, 012102 (2013).
12. ***N. Nagaosa, J. Sinova et al***. Rev. Mod. Phys. **82**, 1539 (2010).
13. ***V.A. Kulbachinskii et al.*** Semicond. Sci. Technol. **17**, 1133 (2002).
14. ***Y. Takagaki et al*.** Semicond. Sci. Technol. **26,** 125009 (2011).
15. ***H. Li, J. Cao, W. Zheng, Y. Chen, D. Wu, W. Dang, K. Wang, H. Peng, Zh. Liu***. J. Am. Chem. Soc. **134**, 6132 (2012).
16. ***Y.S. Kim, M. Brahlek et al.*** Phys. Rev. B, **84**, 073109 (2011).
17. ***D.K. Schroder***. Semiconductor Material and Device Characterization, IEEE Press, New Jersey, 2006.

TWO-DIMENSIONAL POSITION-SENSITIVE PHOTODETECTORS BASED ON (p)InSb–(n)CdTe HETEROJUNCTION

A.V. Margaryan[1], S.G. Petrosyan[1, 2], L.A. Matevosyan[1], K.E. Avjyan[1]

[1]Institute of Radiophysics and Electronics, NAS RA, Ashtarak, Armenia
[2]Russian–Armenian (Slavonic) University, Yerevan, Armenia
E-mail:artsrunmargaryan@gmail.com

Introduction

Since the 60s to the present day, the semiconductor position-sensitive photodetectors are widely used in the control systems of movement, positioning, and definition of linear and angular coordinates [1–5]. Generally, position-sensitive photodetectors (PSD) are the semiconductor structure with one or more *p–n* junctions having several ohmic contacts on the sufficiently large photosensitive surface, the output signals from which are proportional to the position of the light spot relative to the center of structure. The principle of PSD operation is based on the lateral photoelectric effect, which was observed experimentally by Wellmark in 1957 [6]. If in the one region of *p–n* junction two distant electrodes symmetrically arranged and the voltage is measured between them, then during the local illumination of surface of such photodiode by the focused light beam shifted from the center, the magnitude and sign of arising photovoltage will vary with the change in the beam location. If the photocurrents flowing between these contacts and the common contact in the collector region are measured, the magnitude and the sign of the differences of these currents also gives an unambiguous information regarding the displacement of the light spot from the center of the structure. To maximize the value of the lateral photosensitivity it is necessary to provide complete separation by *p–n* junction of the electron–hole pairs generated by the light, and the high resistance of the junction layer on contacts of which the photovoltage is measured. From this point of view, the use of heterojunctions to generate the lateral photoelements is very interesting [7]. In heterojunction, the generation of electron–hole pairs by the light illumination with the photon energies lesser than the band gap of the material of the top layer takes place directly in the space charge region of *p–n* junction. At low density of the surface states and the small size or the absence of the band edges discontinuity in one of the energy bands, the almost complete separation of electron–hole pairs generated by the light takes place.

This work presents the results of the study of *X–Y* sensitivity of locally illuminated photodetectors based on the heterojunction (*p*)InSb–(*n*)CdTe, which are operating in the mid-IR range of (0.8–5) μm. It is known that the semiconductor compounds, selected for the heterojunction in this case, have the close lattice parameters and coefficients of thermal expansion, and form an ideal heteropair, while the main bands discontinuity being in the valence band and does not interfere with the separation of photocarriers [8]. As in the case of nonuniformly illuminated *p–n* junction [9], the arising of photovoltage (at short-circuit and at photocurrent) not only caused by the local separation of nonequilibrium charge carriers but also due to the lateral spreading of the majority carriers out of the generation region followed by their reinjection through the contact barrier. Note that due to the large gap areas in the valence band of heterojunction considered by us, the electrons give the main contribution to the current through the heterojunction.

Experiment

To manufacture the (*p*)InSb–(*n*)CdTe heterostructure, we used the method of pulsed laser deposition [10], which enables the epitaxial growth of CdTe films on the InSb substrates at relatively low temperatures (T = 200–225°C). As a substrate, the polished, high resistance (*p*)InSb(100) plates were used with the thickness of 450 μm and the acceptor concentration N_A = 4.17×10^{14} cm^{-3}. The pulsed laser deposition device consists of YAG:Nd3+ laser (wavelength 1.064 μm, the pulse width of 30 ns, the energy per pulse of 0.35 J, the intensity of radiation on the CdTe target ~2×10^8 W/cm^2) and the vacuum chamber with the residual pressure of 4 × 10–5 mm

of mercury (Figure 1). In both areas of heterostructure the ohmic contacts are formed by the thermal spraying of the metal indium (In) after the laser deposition of CdTe layer with the thickness of the order of 0.4 μm. This is the sufficiently high-resistance layer, since the donor concentration therein of no more than 10^{15} cm^{-3} [10]. From the side of (*p*)InSb, the layer of In covers the entire surface of the substrate, and from the side of (*n*)CdTe 4 contacts with the maximum diameter at most 0.4 mm are made on the illuminated surface.

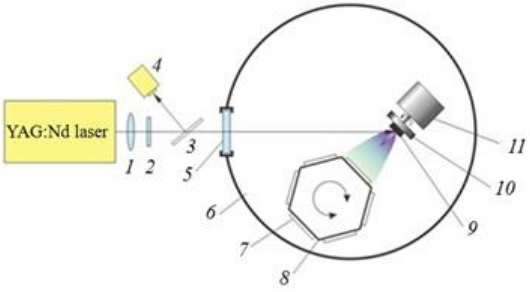

Fig. 1. Scheme of the installation of laser-pulsed deposition: 1–quartz lens, 2–filter, 3–beam separator, 4–calorimeter, 5–quartz window, 6–vacuum chamber, 7–substrate, 8–the substrate holder and heater, 9–target, 10–the target holder, 11–motor.

Research results

The two-dimensional PSD based on (*p*)InSb–(*n*)CdTe heterojunction, the scheme of which is shown in Fig. 2, is investigated. As a source of IR radiation, the iron plate heated to 300°C, and lacquered white with the emissivity ε ≈ 0.8 was used [11]. The unmodulated radiation has been focused by the converging lens of lithium fluoride (LiF) and the diaphragm in such a manner that the beam diameter does not exceed 0.3 mm. According to the Wien displacement law, the body which is heated to 300°C has the maximum spectral density at 5 μm, and the main part of it is in the mid-infrared region. Since the band gap of CdTe is 1.6 eV, the CdTe layer is the wide-range optical window for the radiation in the wavelength range from $\lambda_1 = 0.8$ μm to $\lambda_2 = 5$ μm, which is confirmed also by the measurements of the spectral distribution of photocurrent [10]. The difference of components of photocurrents flowing through the contacts A, B, C and D are the desired signals, and they were measured at different positions of the light beam by the picoamperemeter KEITHLEY 6845.

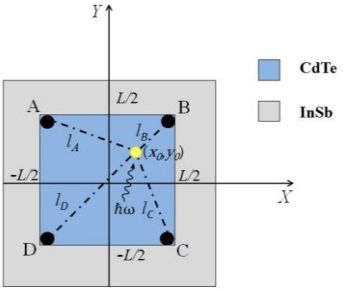

Fig. 2. The scheme of two-dimensional PSD

Figure 3 shows the dependences of the photocurrents differences through the contacts arranged in the half-planes $y > 0$ and $x > 0$, as the functions of the displacements along the coordinate axes x and y. It is seen that the PSD is characterized by the linear coordinate dependence of the photoresponse at the displacement of the beam in sufficiently large area near the center of the surface of the PSD with the sign changing response. The value of coordinate sensitivity Γ showing the change of current at the unit change of coordinate of the light spot is about 30 nA/μm. Measuring the values of output currents I_i (i = A, B, C, D) for the given position of the light spot center (x_0, y_0), it is possible to determine x_0, y_0. Assuming that the lateral resistance of CdTe film between the illumination point and given contact R_i (i = A, B, C, D) linearly increases with the distance between them at small deviations of the beam from the center of structure (x_0, $y_0 << L/2$), the I_A current, for example, can be represented in the following form:

$$I_A \sim \frac{1}{R_A} \sim \frac{1}{l_A} \approx \frac{\sqrt{2}}{L\left(1+\frac{x_0 - y_0}{L}\right)}. \quad (3)$$

Similar expressions are true for the other components of the photocurrent. Then it is easy to show that

$$\frac{(I_B+I_C)-(I_A+I_D)}{(I_B+I_C)+(I_A+I_D)} = \frac{R_A R_D (R_B+R_C) - R_B R_C (R_A+R_D)}{R_A R_D (R_B+R_C) + R_B R_C (R_A+R_D)} \approx \frac{x_0}{L}, \frac{(I_A+I_B)-(I_D+I_C)}{(I_A+I_B)+(I_D+I_C)} \approx \frac{y_0}{L}. \quad (4)$$

Such linear dependence of photocurrent on coordinates when the light spot is moving in the central region of the structure with the dimensions approximately equal to 1x1 mm^2 is really observed in the experiment (Fig. 3a, b).

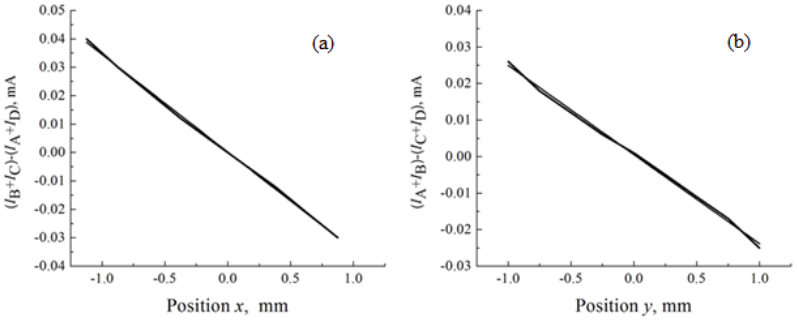

Fig. 3. Dependence of current on the coordinate at the scanning (a) along the x-axis at $y = 0$ and (b) along they-axis at $x = 0$.

Conclusion

The results on the creation and study of two-coordinate IR photodetector based on the (p)InSb–(n)CdTe heterojunction are presented. The heterostructure is obtained with the use of the relatively simple low-temperature technology of laser-pulsed deposition. It is shown that the PSD has the linear characteristic and enables to determine the coordinates of the beam position along the X and Y axes with the high spatial resolution. The photodetectors sensitive in the near and mid-infrared ranges (0.8–5.8 μm) have the parameters that are not in ferior to the traditional homo-junction photodetectors based on InSb [12], and they can be used to determine both linear and angular coordinates of the light beam, and for the tracking of moving objects.

References

1. ***G. Wieglen***, Sensoren., Franzis-Verlag GmbH, 1986.
2. ***A.A. Samarin*.** Elektronnye komponenty (Electronics Components), **7**, 103 (2003).
3. ***N.T. Gurin, C.G. Novikov, I.V. Korneev, A.A. Shtan'ko, V.A. Rodionov.*** Datchiki i sistemy (Sensors and Systems), **11**, 54 (2011).
4. ***N.T. Gurin, C.G. Novikov, I.V. Korneev, A.A. Shtan'ko, V.A. Rodionov*.** Techn. Phys. Lett., **37**, 271 (2011).
5. ***V.M. Aroutiounian, C.G. Petrosyan, V.A. Gevorkyan, A.S. Khachaturyan*.** Author's Certificate of the USSR, № 1018559, 1982.
6. ***J.T. Wallmark*.** Proc. IEEE, **45**, 474 (1957).
7. ***Zh.I. Alferov, V.M. Andreev, E.A. Portnoy, I.I. Protasov***, FTP, 3, 1324 (1969).
8. ***A.G. Aleksanyan, R.K. Kazaryan, L.A. Matevosyan.*** Electronnaya promyshlennost' (ElectronicIndustry), **107**, 55 (1981).
9. ***G. Lucovsky.*** J. Appl. Phys, **31**, 1088 (1960).
10. ***L.A. Matevosyan, K.E. Avjyan, S.G. Petrosyan, A.V. Margaryan.*** Uspekhy prikladnoi fiziki (Advancesin Applied Physics), **2**, 403 (2014).
11. ***L.Ya. Kriksunov*.** Spravochnik po osnovam infrakrasmoy tekhniki. (Handbook on the Basics of Infrared Technology), Moscow: Sov. Radio, 1978.
12. Characteristics and use of PSD, Hamamatsu technical information.

DIELECTRIC LOSSES POWER METER USING MICROCONTROLLER

B.M. Mamikonyan, D.S. Nikoghosyan

National Polytechnic University of Armenia, Gyumri, Armenia, E-mail: bomam@yandex.ru

Introduction

Dielectric losses of energy in form of heat occur in real dielectric materials under an applied voltage by both DC and AC. When DC voltage is applied to the insulating material the periodic polarization does not exist, however, leakage currents arise, since the values of bulk and surface electrical conductivities of the insulating material are not equal to zero. Leakage currents cause heating of the insulating material. With AC voltages, currents of periodic polarization are added to the leakage currents, this increases thermal energy allocated in material and may cause different defects that lead to a deterioration of the insulating properties of the material. Therefore, in the manufacturing and exploitation process of electrical equipment, the quality of insulation material is tested in order to detect possible defects [1, 2].

Theory

Real insulation material is a capacitor having capacitance C_x and active resistance R_X. Capacitance C_X characterizes property of material to store electrical energy $W = C_X U^2/2$ by applying external electric voltage U. The resistance R_X shows thermal energy $Q = \left(U^2/R_X\right)\cdot t$ allocated in the material by the leakage currents in the same conditions, for the time t. In electrical equivalent circuit of capacitor the parameters R_X and C_X may be connected in series or in parallel, wherein serial circuit is preferable for small losses, parallel - for large ones. However, only calculation formulas depend on substitution scheme but the result of power measurement of dielectric losses remains unchanged. [3]. For example, the following formula is used to calculate the power dissipation of the parallel equivalent circuit (Fig. 1).

$$P_a = U \cdot I_R = U \cdot I_C \cdot tg\delta = U \cdot \frac{U}{X_C} \cdot tg\delta = U^2 \omega C_X \cdot tg\delta\,, \tag{1}$$

where $X_C = 1/\omega C_X$, δ is dielectric loss angle and ω is the angular frequency of the applied sinusoidal voltage U.

From (1) it is clear that the dielectric losses are particularly important for materials used in high-voltage installations, in high-frequency equipment and especially in high voltage - high frequency devices. High dielectric losses in the insulating material causes intense heating of the product manufactured from it and may lead to its failure. From (1) it also follows that it is impractical to produce the assessment of the insulating properties of the dielectric by value of power of dielectric loss, as P_a also depends on the applied voltage. Therefore, the insulating properties of the insulator were evaluated by a value of $tg\delta$, which is equal to the ratio of active and reactive power, and can also be expressed in terms of parameters R_X and C_X (Fig. 1.).

$$tg\delta = \frac{I_R}{I_C} = \frac{I_R \cdot U}{I_C \cdot U} = \frac{P_a}{P_p}\,, \qquad tg\delta = \frac{I_R}{I_C} = \frac{U}{R_X \cdot U/X_C} = \frac{X_C}{R_X} = \frac{1}{\omega R_X C_X}\,.$$

In contrast to the P_a, the value $tg\delta$ is also independent from geometric dimensions of the dielectric, which is easily proved by applying the concept of the complex permittivity [4].

To measure $tg\delta$, the sample of controlled dielectric (e.g., transformer oil) is placed in the space between the plates of a capacitive transducer (Fig. 2). In the diagram: 1 is the measuring

circuit; 2 the capacitive transducer CT; 3 the programmable generator of sinusoidal signals; 4 the electronic switch; 5 the programmable microcontroller (MC); 6 the digital reading device (DRD); 7 the Interface Converter (UART-USB); 8 the computer.

In measuring circuit, in series with the CT, two model resistors are connected: base (R_1) and an additional (R_2). The resulting circuit in the form of a voltage divider is connected to a generator of sinusoidal signals. The measuring circuit has two output voltages relative to the total point, which are input to the MC: the common voltage u_S of the voltage divider, taken from the general contact switch and voltage u_X from clamps of CT. The output signal of measuring circuit is a phase shift angle between the voltage u_S and u_X . It should be noted that in most cases of measurement of $tg\delta$ it is also necessary to have appropriate values of parameters C_X and R_X , therefore when designing the meter has been tasked to provide separate measurements of these three parameters.

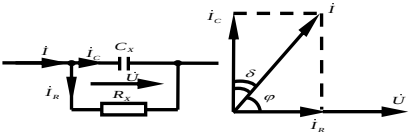

Fig. 1

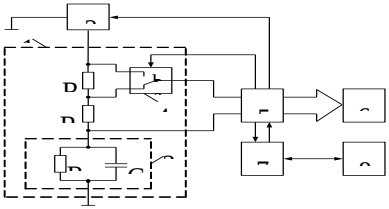

Fig. 2

Let us find the relationship between the parameters of the CT and the angle φ . In the initial position a of switch for value of φ_1 of angle φ we can write:

$$tg\varphi_1 = \frac{\mathrm{Im}\left(\dot{U}_S/\dot{U}_X\right)}{\mathrm{Re}\left(\dot{U}_S/\dot{U}_X\right)} = \frac{\mathrm{Im}\left\{\dot{I}\left[R_1 + R_X/\left(1+ j\omega R_X C_X\right)\right]/\dot{I}\left[R_X/\left(1+ j\omega R_X C_X\right)\right]\right\}}{\mathrm{Re}\left\{\dot{I}\left[R_1 + R_X/\left(1+ j\omega R_X C_X\right)\right]/\dot{I}\left[R_X/\left(1+ j\omega R_X C_X\right)\right]\right\}}. \qquad (2)$$

The result is:

$$tg\varphi_1 = \frac{\omega R_1 R_X C_X}{R_1 + R_X}. \qquad (3)$$

In b position of switch

$$tg\varphi_2 = \frac{\omega\left(R_1 + R_2\right)R_X C_X}{R_1 + R_2 + R_X}, \qquad (4)$$

where, ω is the angular frequency of the generator, I is the current of measuring circuit.

From (3) and (4) we have: $ctg\varphi_1 - ctg\varphi_2 = \dfrac{R_2}{\omega R_1\left(R_1 + R_2\right)C_X}$, from which we obtain:

$$C_X = \frac{R_2}{\omega R_1\left(R_1 + R_2\right)} \cdot \frac{1}{ctg\varphi_1 - ctg\varphi_2}. \qquad (5)$$

We divide formula (4) into formula (3): $\dfrac{tg\varphi_2}{tg\varphi_1} = \dfrac{\left(R_1 + R_2\right)\cdot\left(R_1 + R_X\right)}{R_1\left[\left(R_1 + R_2\right) + R_X\right]}$, which implies:

$$R_X = \frac{R_1\left(R_1 + R_2\right)m}{R_2 - R_1 m}, \qquad (6)$$

where the notation $m = \left(tg\varphi_2 / tg\varphi_1\right) - 1$. Let us transform the formula (3) and (4) as follows:

$$R_1 \cdot ctg\varphi_1 = \frac{R_1 + R_X}{\omega R_X C_X},\ \left(R_1 + R_2\right) \cdot ctg\varphi_2 = \frac{R_1 + R_2 + R_X}{\omega R_X C_X},\ \ \left(R_1 + R_2\right) \cdot ctg\varphi_2 - R_1 \cdot ctg\varphi_1 = \frac{R_2}{\omega R_X C_X} \cdot$$

Consequently,

$$tg\delta = \frac{1}{R_2}\left[\left(R_1 + R_2\right) \cdot ctg\varphi_2 - R_1 \cdot ctg\varphi_1\right] \cdot \tag{7}$$

The resulting formulas (5), (6), (7) allow us carry out separate measurement of the three parameters of the CT on alternating current. This requires only measuring the angle of the phase shift between the two output voltages of the two-pole measuring equipment.

In the process of measuring, MC controls the position of the switch and measures the values of the φ_1 and φ_2 angles in the corresponding switch positions. With the measured values of these angles MC calculates parameters C_X, R_X, $tg\delta$ according to the formulas (5), (6), (7), and outputs the measurement results on a digital display, as that seven-segment LEDs are used. To improve the reliability of measurement results at every point the MC performs 10 measurements and displays on the display the average result of these measurements. If necessary, the digitized signals of φ_1 and φ_2 can be sent from the MC through the interface converter (*e.g.*, AVR309) to computer, where they can be processed and the measurement results are displayed on monitor. Since, in general, the results of measurements of the CT parameters also depend on the frequency of the supply current of measurement circuit, as the power supply of the measuring chain, the programmable generator of sinusoidal signals AD9833 is used. At each measurement MC sets the generator frequency, and uses this value in calculating of CT parameters, whereby the generator frequency changes do not affect the measurement. Generator voltage stability is not essential, as in (5), (6) and (7) the generator voltage does not appear. Thus, the accuracy of the CT parameters depends only on the accuracy of measurement of the angle φ that is performed in this device by discrete calculation method, so the measurement accuracy is significantly higher than with methods using potentially - current signals. In the MC, the φ angle is converted into a time interval τ. The time intervals τ and T are measured by digital accounts by filling them with pulses of f_0 exemplary frequency of clock generator of MC with use of its integrated timer counter. Further, the angle φ is calculated by the obvious formula

$$\varphi = \left(\tau / T\right) \cdot 360^o \cdot \tag{8}$$

To measure the angle φ in the MC, we consider two methods.

1. Using the internal ADC of MC (Fig. 3, 4). At the beginning, multiplexer transmits the voltage u_S to the input of ADC, which converts it to a digital code. ADC writes value of digital code ("Value 1") at the time t_1 in output register. MC starts the internal timer and via the multiplexer transmits the voltage u_X to the input of ADC. Then the MC considers the value of the output register until the moment t_2 when it receives on u_X the "Value 2" equal to "Value 1". At the moment t_2, the MC stores the timer value and again transmits the voltage u_S to the ADC input. Then twice receiving value equal to "Value 1" (the moment t_3), the MC again remembers the timer value and stops the timer. By the number of the pulses of clock timer n for the time $t_2 - t_1$ and the value of the pulses N during $t_3 - t_1$, the angle φ is calculated by formula

$$\varphi = (n/N)\cdot 360^{o}, \tag{9}$$

obtained from (8) by substituting the values $\tau = n/f_0$ and $T = N/f_0$, where f_0 is clock frequency.

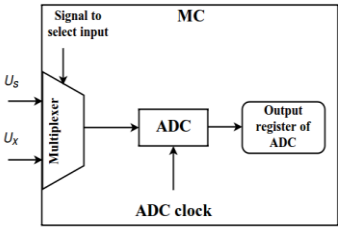

Fig. 3

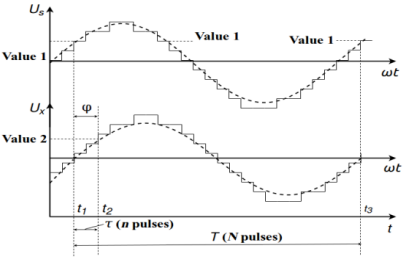

Fig. 4

This method of measuring the angle φ has a significant limitation: the period of the ADC should not be more than the minimum value of τ. From condition $\tau_{\min} = 1/f_D$ where f_D is the ADC sampling rate, from (9) we find the minimum value of the angle φ, which can be measured by this method at the signal frequency f:

$$\varphi_{\min} = (f/f_D)\cdot 360^{0}. \tag{10}$$

In device developed according to the scheme in Fig. 2, the measuring circuit is supplied by sinusoidal current with frequency $f = 50$ kHz. Even if you use the MK LPC4370FET100 type [5], the ADC of which has a sufficiently high sampling frequency $f_D = 80$ MHz, from (10) we obtain for $\varphi_{\min}$ the value $\varphi_{\min} = 0,225^{0}$. In addition, for the nominal value of the measuring range $\varphi_N = 45^{0}$ the sensitivity threshold of error will be $\delta_S = (\varphi_{\min}/\varphi_N)\cdot 100 = 0,5\%$ which is unacceptable. Therefore, the use of this method is inexpedient.

2. Using the internal comparators of MC (Fig. 5 and 6). To implement this method, we need MC with two internal comparators. Inverted inputs of comparators are grounded, and the direct inputs are connected to u_S and u_X, and thus forming a zero voltage comparators. As a result, each of the comparators can perform three types of interrupts:

- "Transition 0-1" (Rising edge) - when the signal at the direct input passed through 0 up;
- "Transition 1-0" (Falling edge) - when the signal at the direct input passed through 0 down;
- "Transition 1-0 / 0-1" (Toggle) - when the signal at the direct input passed through 0 up or down.

At the moment t_1, the MC receives an interrupt "Transition 0-1" from the first comparator and starts a timer. Then at the moment t_2, again the MC receives an interrupt "Transition 0-1" from the second comparator. At this moment, the MC saves the value of the timer. When for the second time (at the moment t_3) the MC receives an interrupt "Transition 0-1" from the first comparator it again stores the value of the timer and stops the timer. By the obtained numbers of pulses n and N, the angle φ is calculated as in the first method.

Let us estimate the φ angle measurement error. It follows from (9), that the φ angle measurement error is caused by the error in determining the number of pulses n and N. This

error is the sum of the random error of discreteness, i.e. the possibility of loss in numbers n and N with one count pulse. Absolute measurement error

$$\Delta\varphi = \frac{\partial\varphi}{\partial n}\Delta n + \frac{\partial\varphi}{\partial N}\Delta N = \left(\frac{\Delta n}{N} - \frac{n}{N^2}\Delta N\right)\cdot 360^o,$$

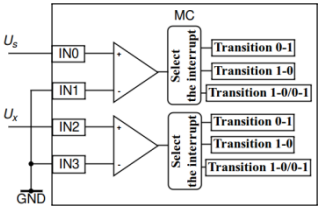

Fig. 5

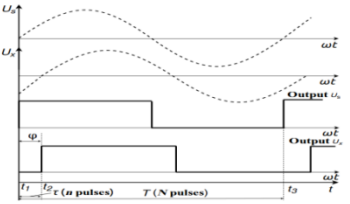

Fig. 6

and the relative error - $\delta(\varphi) = \frac{\Delta\varphi}{\varphi} = \frac{\Delta n}{n} - \frac{\Delta N}{N}$. The worst case occurs when $\Delta n = 1$, $\Delta N = -1$:

$$\delta(\varphi) = \frac{1}{n} + \frac{1}{N} = \frac{1}{\tau f_0} + \frac{1}{T f_0} = \frac{1}{f_0}\cdot\left(\frac{1}{\tau} + \frac{1}{T}\right).$$

It obvious that the error of measurement of the angle φ can be reduced by increasing the frequency f_0 of the timer of MC. A technique for experimental investigation of the metrological characteristics of meter has been developed. In the circuit of Fig. 2 the measured parameters R_X and C_X are modeled by a high-precision model store of resistance P4851 and a model store of capacities P544. Absolute measurement error is estimated as a difference between the output of the digital reading device 6 (Fig. 2) and the values of R_X and C_X on P4851 and P544. The results of the experiments show that the developed device can provide a separate measurement of the parameters C_X, R_X, $tg\delta$ with a basic relative error of measurement not exceeding 0.2%.

Conclusion

The phase method for dielectric loss measurement makes it relatively easy to implement invariant parameters measuring of capacitance of the primary transducer without the use of potentially-current signals. You need to measure only the angle of the phase shift between the two output voltages of measuring circuit. To convert the measured phase shift angle to a digital code, it is advisable to use the internal comparators of microcontroller instead of embedded ADC. This significantly reduces the error from the threshold sensitivity of the device, in addition ADC is more sensitive to noises and interferences.

References

1. ***D.M. Kazarnovsky, B.M. Tareev.*** Testing of electrical insulating materials and products. L.,Energia, 1980. (In Russian)
2. ***B.M. Tareev.*** Physics of dielectric materials. M., Energoizdat, 1982. (In Russian)
3. ***L.N. Tatyantshenko, V.I. Stashko.*** Insulation control by tangent of dielectric loss angle: Teaching-methodical manual. Barnaul, PH ASTU. I.I. Polzunova, 2014. (In Russian)
4. ***K.S. Demirchyan, L.R. Neiman, N.V. Korovkin.*** Theoretical bases of electrical engineering: Textbook for high schools. Volume 2, St. Petersburg: Peter, 2009. (In Russian)
5. NXP Semiconductors. LPC4370 Product data sheet / Rev. 2.3 /. - 2016. (In Russian)

PHOTOELECTRIC PROPERTIES OF A-C/P-Si HETEROSTRUCTURE FABRICATED BY PULSED LASER DEPOSITION TECHNIQUE

K.E. Avjyan[1], L.A. Matevosyan[1], G.A. Dabaghyan[2]

[1]Institute of Radiophysics & Electronics, NAS RA, E-mail:avjyan@gmail.com
[2]National Polytechnic University of Armenia

Introduction

Different forms of carbon (diamond, graphite, fullerenes, nanotubes, DLC, etc.) has made carbon one of the most interesting elements in nature. The wide variety of structures and unique properties of carbon are due to its ability to form various types of hybridization. Over the past few years carbon based materials have become increasingly interesting for use in electronic applications. The range of its application varies from disposable electronics for consumer goods, to UV sensors, dosimeters and large area flat panel displays.

Thin film amorphous carbon has many attractive features for electronic use: a band gap which can be varied from ~0.5 eV up to ~4.0 eV, potential to produce n, p and intrinsic material, and large area deposition at room temperature. Each one of these potential applications depends upon the production of high quality, reproducible and well characterized material. Their main application has been in their use as cold cathode field emitters [1]. However, attempts have also been made to produce metal semiconductor metal structures [2], diodes [3] and thin film transistors [4], with varying degrees of success. The utilization of carbon thin films in solar cells has also been attempted [5, 6]. The use of the various diamond-like or/and amorphous carbon (a-C) in electronic devices is limited by their high defect state density and charge low mobility. The paper [7] shows the possibility of using a-C/p-Si heterostructure (HS) as a radiation detector. However, it should be noted that the properties of such detectors are explained by silicon. a-C films only for the internal barrier of HS.

This paper presents the results of photoelectric properties of carbon on silicon structure fabricated by pulsed laser deposition (PLD) technique. In advance, we will say that a uniform photo response is obtained in a wide range of waves (550-1100 nm), which can have an excellent practical value for visible range photo electronics. Nowadays, PLD being the part of laser technologies and a kind of flexible, universal vacuum deposition, recognized as a simple and versatile method for deposition of thin films and structures based on them [8-10]. This method based on the using of physical phenomena occurring under the influence of laser radiation on solid targets, which reduced to ablation of a substance from the irradiation zone. The method holds of unique characteristics:

1. Possibility of evaporation practically all the materials including as well high-melting.
2. Short times of deposition (~10^{-6} sec.), which is equivalent to improve the "effective vacuum" on a several orders.

Practically all materials needed for functional electronics are obtained by this technology. PLD is indispensable for synthesis of a number of complex composite materials with extraordinary properties. Nevertheless, the wide application of PLD method in production of electronic components is limited due to the difficulty of obtaining films with required qualities on relatively large areas. PLD there is still an alternative technology as yet.

Experiment

Carbon films were obtained by the PLD method on factory quality polished pSi (~10^4 ohm cm, thickness - 500 μm) substrates at room temperature from carbon target. The deposition unit consists of a Q-switched YAG: Nd^{3+} laser (1.064 μm wavelength, 30 ns pulse duration, laser energy - 0.35 J per pulse, repetition rate - 1 Hz) and a vacuum chamber with residual gas pressure $2 \cdot 10^{-5}$ mm Hg (fig. 1). Laser intensity on a target was $6 \cdot 10^8$ W/cm^2. Silicon wafers were degreased

in pure acetone, washed in redistilled water and dried in air jet. Before the deposition of carbon films short-time (20-30 min) annealing of silicon substrates were made under vacuum of $2 \cdot 10^{-5}$ mm Hg at 100°C. The thickness of deposited layer from a single laser pulse was determined by dividing measured by optical interference method of a thick layer on a number of laser pulses (0.5 nm per pulse). Low-resistance contact to the carbon film is made by PLD of silver (Ag) with subsequent metallization of indium (In) by physical vapor deposition (PVD). Low-resistance contact to the p- type Si substrate is made by PLD of In with subsequent PVD metallization of In. Carbon on silicon structure with contact pads is shown schematically in fig. 2. The carbon film crystal structure was investigated by reflection high-energy electron diffraction method (accelerating voltage 75 kV). Dark volt ampere (I-U) characteristic of fabricated structure (carbon film thickness - 100 nm) was investigated by means of sub-femtoamp source meter KEITHLEY-6430. Photo response of fabricated structure was investigated on monochromator MDR-12 (0.2 - 2 μm).

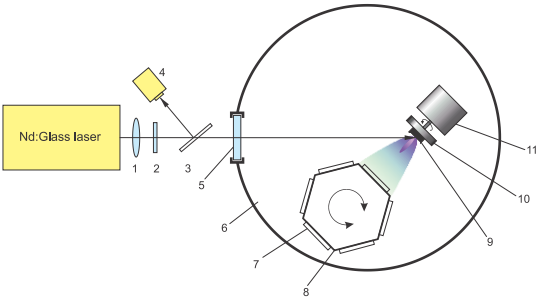

Fig. 1. PLD system.
1-Quartz lens, 2- filter, 3- beam splitter, 4- calorimeter, 5- quartz window, 6- vacuum chamber, 7- substrate, 8- sSubstrate holder and heater, 9- target, 10- target holder, 11- motor

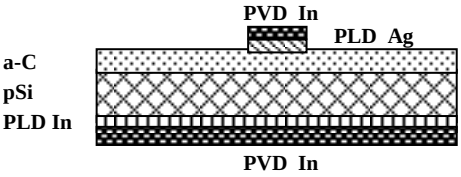

Fig. 2. Carbon on silicon structure.

Results

Electron diffraction studies (Fig. 2) shows that deposited on silicon substrate carbon films has an amorphous structure (a-C), and so our structure is a-C/p-Si HS.

Figure 3 shows dark I-U curve of a-C/pSi HS. We have a rectifying junction with rectifying coefficient k (ratio of forward current to reverse) of $2.7 \cdot 10^3$ at 0.6 V. Higher than 0.5 V direct current (+ on pSi) is characterized by linear dependence of $I = (U - U_{Icut\ off})/Rd$, with current cut-off voltage $U_{Icut\ off} = 0.46$ V and residual differential resistance Rd = 300 ohm. The numerical value of $U_{Icut\ off}$ equals to the n- and p-areas total contact potential (Anderson model). I-U characteristic of junction at direct biases $0.01\ V < U < 0.45\ V$ satisfactory fits with the expression $I=I_0\exp(eU/nkT)$ (I_0 – saturation current, n – non-ideality coefficient).

Figure 4(b) shows the photo response (relative units) of a-C/p-Si HS. For comparison, the photo response of Sb/p-Si barrier structure fabricated by PLD in the framework of presented article

also is given (Fig. 4(a)). It can be seen that a-C/p-Si structure at the level of 0.8 has a uniform photo response in the spectral range 550-1100 nm, and the tail reaches up to 400 nm (level 0.1). The spectral characteristic of Sb/p-Si structure looks like a conventional silicon photodiode. The physics and corresponding interpretation of such a photo response of a-C/p-Si HS are not known to us at this moment. *There is an assumption that the* a-C *film has a semiconductor property with electronic conductivity and the structure* a-C/p-Si *behaves itself as an ordinary p-n junction.*

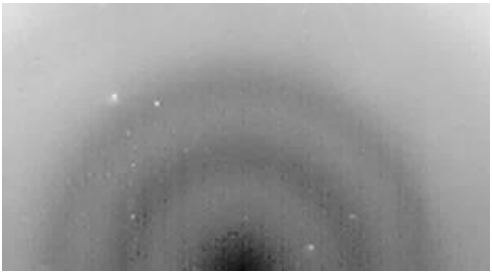

Fig. 3. Electron diffraction pattern from carbon film.

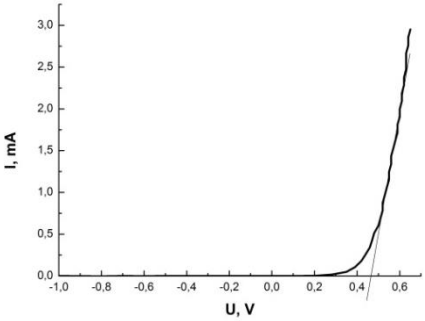

Fig. 4. Dark I-U characteristic of a-C/pSi HS.

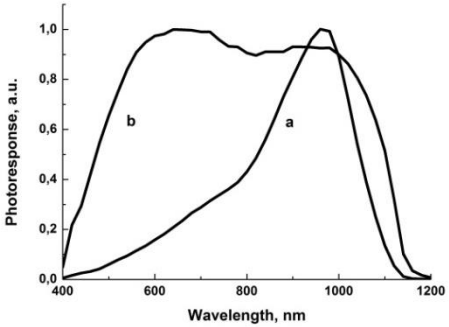

Fig. 5. Photo response of Sb/p-Si structure (a) and a-C/p-Si HS.

Conclusions

The results of photoelectric properties of a-C/p-Si HS fabricated by PLD of carbon on a silicon substrate are presented in this paper. Uniform photo response is obtained in a wide range of waves (550-1100 nm). The tail of this photo response reaches up to 400 nm (level 0.1). Such photoelectric properties of a-C/p-Si HS can have an excellent practical value for visible range photo electronics.

References

1. ***W.I. Milne, J. Robertson, B.S. Satyanarayana and A. Hart.*** Int. J. Mod. Phys., **B 14**, 301-7 (2000)
2. ***S. Egret, J. Robertson, W.I. Milne and F.J. Clough.*** Diam. Relat. Mater. **6**, 879 (1997).
3. ***S. Paul and F.J. Clough.*** MRS Symposium Proceedings, 2000, **593**, p. 427.
4. ***F.J. Clough, W.I Milne, B. Kleinsorge, J. Robertson, G.A. Amaratunga and B.N Roy.*** Electron. Lett., **32**, 498 (1996).
5. ***A. Vohra, W.I Milne and G.A Amaratunga.*** Proc. 16th European Photovoltaic Solar Cell Conference, Glasgow, 1–5 May, 2000.
6. ***C.H Lee and K.S. Lim.*** Appl. Phys. Lett., **75**, 569 (1999).
7. ***K.E. Avjyan L.A. Matevosyan K.S. Ohanyan L.G. Petrosyan.*** Instruments and Experimental Techniques, **59**(1), 60 (2016).
8. ***J.C. Miller.*** Laser Ablation - Principles and Applications, Springer-Verlag, Berlin, 1994.
9. ***R. Eason.*** Pulsed Laser Deposition of Thin Films, John Wiley & Sons Ltd, 2006.
10. ***A.G. Alexanian, N.S. Aramyan, K.E. Avjyan, A.M. Khachatryan, R.P. Grigoryan and A.S.Yeremyan***. Combinatorial and High-Throughput Discovery and Optimization of Catalysts and Materials (edited by R.A. Potirailo and W.F. Maier), CRC/Taylor & Francis 2006, p. 447.

REMOTE MONITORING SYSTEM USING GSM FOR PHOTOVOLTAIC STATIONS

D.V. Aghabekyan[1], A.G. Ayvazyan[2], A.A. Vardanyan[3]

[1]National Polytechnic University of Armenia, Yerevan, Armenia, E-mail: adav3@mail.ru
[2]Nokia-Siemens Network Co., Tbilisi, Georgia, E-mail: armayvaz@mail.ru
[3]Barva Innovation Center, Talin, Armenia, E-mail: a.vardanyan@barva.am

1. Introduction

Armenia has a significant advantage in terms of solar energy: the country is situated in the proximity of subtropical zone; most territory of the country has favorable climatic conditions that make wide use of solar energy possible. There are on average more than 2500 sunny hours per year and the average annual amount of solar energy flow per square meter of horizontal surface is about 1720 kWh (the average European 1000 kWh). One fourth of the country's territory is endowed with solar energy resources of 1850 kWh/m^2. Up to now in Armenia different photovoltaic (PV) demonstrating stations have been installed with small capacities.

At the end of 2016 the Government of the Republic of Armenia approved the investment project for the construction of photovoltaic solar stations, the total investment cost of which is estimated about $129 million. Within the project, it is planned to build utility-scale PV stations with a capacity of up to 110 MW in various regions of Armenia [1]. Currently construction 55 MWh PV station near the village of Masrik in Gegharkunik marz is launched.

Power generation from PV stations is variable in nature due to changes in solar irradiance, temperature and other factors. In the operation of such stations especially with large size (kilowatt or megawatt scales), the station performance should be carefully monitored and a proper decision must be taken in time. For better output and performance of PV stations they should be monitored properly. Remote monitoring is an online technique that is used to transmit real time data from the station to database unit. The role of monitoring system is to discover drawbacks and inform the operator by the type and location of the failure to take decision or act a fault tolerant system if the monitored hardware is supported. Till now many techniques of remote monitoring for PV stations are developed [2-6]. These techniques involve monitoring using ZigBee network, Wi-Fi, GSM and Ethernet cable network. Remote monitoring based on ZigBee technology is proven inefficient in large scale because it can't face up huge distance. Moreover, ZigBee network demands high cost and complexity. Wi-Fi is offer high data rate, but this solution is suitable for microgrid local network architecture. Ethernet uses network cable to transmit data. Hence, it is affected by geographical environment. GSM network provides a monitoring system that is wide signal coverage, has low error rate, highly reliable data delivery, no geographical constraints and less complexity. Due to the availability of SMS the cost for data transmission becomes very low.

This paper describes the hardware and software design for PV remote monitoring system using GSM. The given system was implemented and experimentally tested on PV station in Barva Innovation Center.

2. System Architecture

The overall architecture of the PV remote monitoring system is shown in Fig. 1.

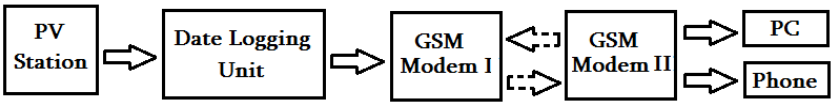

Fig. 1. Architecture of the PV remote monitoring system

The parameters that are required for monitoring a PV station properly are voltage, current, solar irradiance, temperature and humidity. All the data collected from different sensors is sent to the

data logging unit (DLU). The heart of the DLU is microcontroller, through which data is converted from the analog to digital form in the processing.
We have selected GSM network for the PV remote monitoring system. The SMS service was favored, because it is remarkably simple and cheap. SMS can contain 160 alphanumeric characters. These characters can be coded for security reasons or they can be directly utilized as data as per the requirements. One major advantage of SMS is that it is supported by 100% GSM mobile phones. Generally the message delivery takes 0,5÷2 s depending on the momentary traffic on the network [7].
The information from the sensors goes to the DLU where it is processed and it is passed by an RS 232 or USB interface to the GSM Modem I (SIM card), and later sent to a connected remote PC or Mobile Phone by GSM Modem II after a specific interval of time. Received data are monitored by the software and are displayed on PC monitor or mobile phone screen.

3. Hardware Design

GSM Modem.

F2003 modem is a kind of cellular terminal device that provides SMS function by public GSM network. It adopts high-powered industrial 16/32 bits CPU and embedded real time operating system. It supports RS232 and RS485 (or RS422) port that can conveniently and transparently connect one device to a cellular network. Mode for usage of GSM modem in this research will be text mode.

Sensors.

The choice of sensors depends on interfacing it with microcontroller, the design should simplify the I²C (Inter-Integrated Circuit) modification of the role of a node by simple adding or modifying or suppressing a sensor. A better solution for that would be to use digital sensors with I²C communication port [8]. In the light of the above -mentioned we selected the following sensors:

- SFH 5712 solar irradiance sensor detects ambient brightness in the same way as the human eye and offers high speed rates of up to 3.4 MHz. With 150 μA during operation and only 1.5 μA in stand-by mode, the sensor consumes extremely little power.
- SHT21 humidity and temperature sensor utilizes a capacitive sensor element to measure humidity, while the temperature is measured by a band gap sensor. Relative humidity operating range: 0-100% RH (resolution of 0.03%), and temperature operating range: -40 to +125°C (resolution of 0.01°C).
- LV 25-P voltage and LA 25-NP multi-range current transducers provide easy to use precision voltage/current measurements.

Microcontroller.

AVR Atmega microcontroller is featured by:

- Thirty two 8-bit general purpose registers.
- 64k bytes of in-system programmable flash memory, 512 bytes of EEPROM and 1 bytes of internal SRAM.
- 10 bit in-built and six channel analog to digital converter (ADC).
- On chip analog comparator.

A hardware assembly for DLU is shown in Fig. 2.

4. Software Design

In software design we have used the C programming language to program the microcontroller. The microcontroller is then interfaced with the GSM module. AT commands are instructions used to control a modem [9]. Few GSM AT commands that are used for specific operations are: AT = Initialize Modem; AT+CMGF=1 = Set Modem in Text Mode; AT+CNMI = New Message Indicator; AT+ECHO = Turns Echo On/Off; AT+CMGS = Send Message; AT+CMGR = Read Message; AT+CMGD = Delete Message These are the few commands for F2003 GSM IP modem which will do our task.

The microcontroller algorithm was shown in Fig. 3.

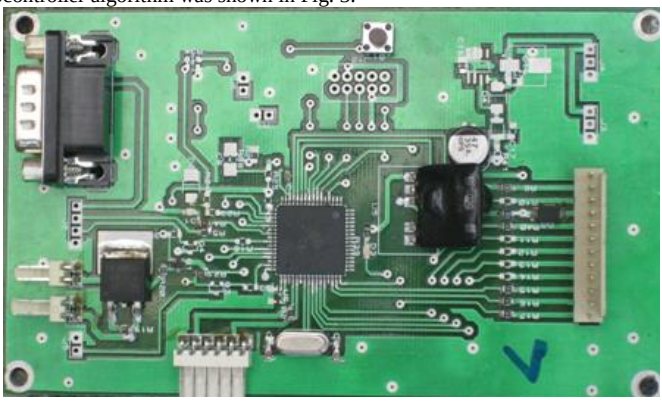

Fig. 2. Hardware assembly for DLU

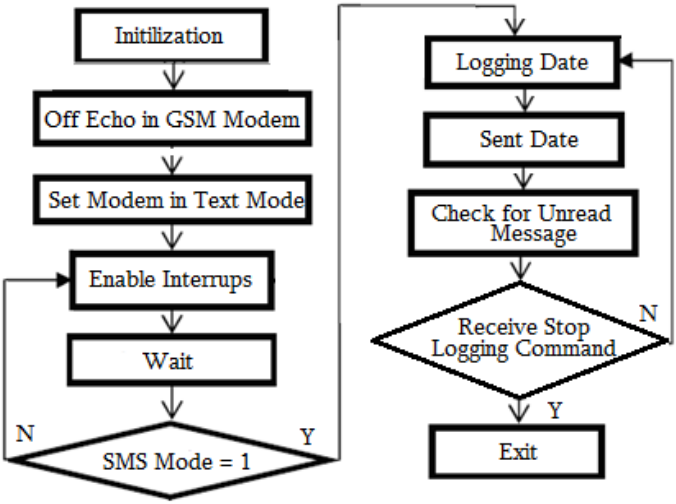

Fig. 3. Microcontroller algorithm

The first stage is initialization of microcontroller. Next, AT command were used to switch off echo function in GSM modem to easily identify feedback from modem. AT+CMGF=1 command is sent to enable GSM modem I to operates in text mode. Then, interrupts is enabled if any text received. After that, microcontroller will wait for command from GSM modem II which will be sent from PC. If GSM modem I received text message, microcontroller will start logging data. If not, microcontroller will continue waiting until it receives command. Microcontroller will log data and send SMS to GSM modem II. Then, it will check for any unread messages. If it receives stop logging command from GSM modem II, it will exit the system and keep in standby mode. If not it will continue monitoring until it receives stop command.

5. *Testing*

Developed remote monitoring system has been tested on demonstration PV station with an installed capacity of 5.0 kWh in Barva Innovation Center (Talin, Aragatsotn marz). As an illustration Fig. 4 shows daily (March 02, 2017) variations of output power *P* of PV station, solar irradiation *I* and ambience temperature *T*, which are displayed based on provided monitoring using GSM.

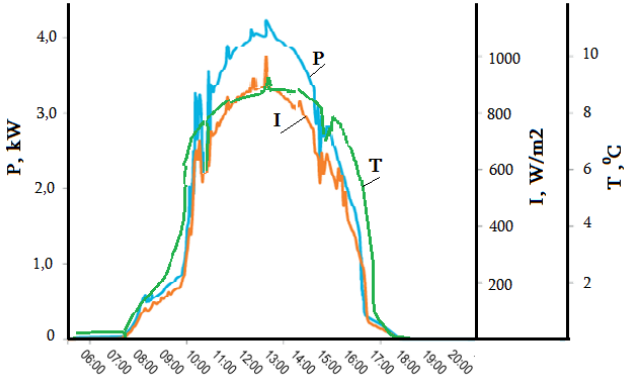

Fig. 4. Daily variations of output power, solar irradiation and ambience temperature

The results of the testing depicts that the monitoring system operates well under the severe conditions without any data loss and transmission delay.

6. *Conclusions*

Remote monitoring system using GSM has been designed, emulated, implemented, and experimentally tested. This system ease user in monitoring PV station placed at remote area. GSM is preferred over other techniques due to its highly reliable data transmission and its cost. The monitoring system is working properly in all conditions. It can be efficiently used in the new utility-scale PV stations in Armenia.

References

1. ***C.J. Muth.*** PV Magazine, February 2, 2017. Available online: /www.pv-magazine.com/2017/02/02/armenia-to-built-its-first-solar-power-plant/.
2. ***F. Shariff, N. Rahim, W. Hew.*** Expert Syst. Appl., **42**, 1730 (2015).
3. ***S. Adhya, D. Saha, A.t Das, J. Jana.*** Proc. of Int. Conf. on Control, Instr., Energy & Commun., 432 (2016).
4. ***H. Belmili, S.M Cheikh, M. Haddadi, C. Larbes.*** Renew. Energy, **35**, 1484 (2010).
5. ***R. Tejwana, G. Kumar, C. Solanki.*** Energy Procedia, **57,** 1526 (2014).
6. ***P. Ppadmaja, M.U. Shamili.*** Int. J. Sci. Eng. & Techn. Research, **4**, 4663 (2015).
7. ***A.G. Ayvazyan.*** Proc. of Eng. Academy of Armenia, **14,** 324 (2017).
8. ***I.M. Moreno-Garcia, E.J. Palacios-Garcia, V. Pallares-Lopez.*** Sensors, **16**, 770 (2016).
9. ***S.M. Sajaad, A. Lone.*** Int. J. of Comp. Appl., **117**, 28 (2015).

PASSIVATION OF BLACK SILICON SOLAR CELLS BY THERMAL SILICON DIOXIDE

G.Y. Ayvazyan, K.G. Ayvazyan, L.M. Lakhoyan

National Polytechnic University of Armenia, Yerevan, Armenia,
E-mail: agag@arminco.com

1. Introduction

Black silicon (b-Si) or silicon grass is a needle-shaped surface structure where needles are made of single-crystal silicon and have a height 0.3-10 μm and diameter 0.05-1.0 μm [1]. These surfaces can be fabricated by reactive ion etching (RIE) in a self-masked procedure. For instance, sulfur hexafluoride (SF_6) and O_2 plasmas have been used for texturing Si wafers. It is known that fluorine radicals easily etch silicon, and moreover the addition of oxygen to fluorine enhance the texturing process. On SF_6/O_2 plasmas two opposite effects take place: an etching process due to fluorine radicals which are very efficient for etch silicon, and a re-deposition process due to residual SiO_xF_y film, which produce a masking effect. Those micro-masks enhance the texturing process of the Si surface. The unusual optical characteristics, combined with the semiconducting properties of silicon make b-Si interesting for solar cells applications as antireflection layers [1-3]. Although an especially low surface reflection ratio has been achieved by nanostructured b-Si, the final energy-conversion efficiency of solar cells was not satisfied at present.

The b-Si solar cells suffer from increased surface recombination rates due to the larger surface area resulting in poor spectral response especially at short wavelengths [4-6]. This effect is often more detrimental for the final device operation than the gain from the reduced reflectance. In addition, b-Si suffers from aging phenomena; the huge internal surface of the needles tends to be progressively oxidized or contaminated by impurities when in contact with air. The low stability of structural and optical properties over time is crucial for b-Si solar cells.

For surface passivation and stabilization of conventional Si solar cells both plasma enhanced chemical vapour deposition (PECVD), liquid phase deposition (LPD) or thermal silicon dioxide (SiO_2), silicon nitride (SiN), zinc oxide (ZnO), amorphous silicon (a-Si) and aluminum oxide (Al_2O_3) have been used with varying results [7, 8]. Among these materials, SiO_2 is one of the obvious candidates to realize the above purpose due to low density of interface states and dangling bonds. Considering the fact that the gaps among the needles on b-Si is difficult to be covered with low-temperature LPD or PECVD methods, thermal oxidation was proposed to be an effective passivation method to solve this difficulty because oxygen can reach the surface of the b-Si anywhere during the process of thermal oxidation [9]. However, thermal oxidation passivation has to be carried out at high temperature. The high temperature will destroy the original structure of the b-Si (the long thin needles are not very strong and can be wiped off easily) and accordingly degrade the performance of solar cells.

In this paper we report that the usage of the b-Si surfaces with the thermal SiO_2 passivation films can be one of the methods to increase the efficiency and protection of the solar cells simultaneously.

2. Solar Cells Fabrication

The following process steps for fabrication of b-Si solar cells were performed: (i) pre-cleaning and removal; (ii) formation of p-n junction; (iii) formation of b-Si layer; (iv) surface passivation; (v) formation of metal back contact; (vi) formation of metal front contact (Fig.1). There is no additional antireflection coating on either type of nanostructured solar cell under study.

i. **Pre-cleaning and removal.** The 10x10cm^2 Si wafer is double-sided polished boron-doped P-type Si (100) FZ with resistivity of ~ 2.8 Ω-cm and thickness of ~ 300 μm. Si wafers were first chemically cleaned and acid-etched to remove the saw damage and randomly textured in an

$HF:HNO_3:H_2O=2.5:1:2.5$ etching solution. The process is completed by washing in deionized water and drying in N_2.

ii. **Formation of p-n junction. N**-type emitters were formed by phosphorus diffusion at 890°C for about 80 min. Edge isolation was done in plasma equipment and phosphosilicate silicon glass was removed in diluted HF solution. The emitter sheet resistance is around 75 Ω/□ with junction depths of ~ 0.85 μm.

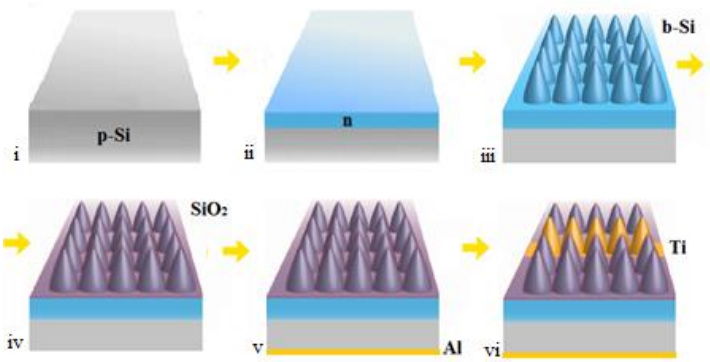

Fig. 1. Process steps for production of b-Si solar cells

iii. **Formation of b-Si layer.** The b-Si layers on the front surfaces of Si wafers were fabricated by RIE method in a gas mixture of SF_6 and O_2 by multi-cathode RIE equipment (home-making). The process pressure was 55 mTorr and gas flow rates were 75 cm^3/min and 40 cm^3/min for SF_6 and O_2, respectively. Samples were placed on the water-cooled (23°C) bottom electrode that was powered by a 13.56 MHz RF generator. The etch durations were kept constant at 10 min.

iv. **Surface passivation.** Thermal oxidation of the b-Si was processed in a quartz furnace tube at 800°C for 20 min under atmospheric pressure. The passivation oxide was removed from the back surface of all samples by HF etching.

v. **Formation of metal back contact.** The contact for back surface were covered by a 40 nm thick Al layer using vacuum evaporation and then were annealed at 550°C for 15 min. The purpose of this treatment is to reduce the contact resistance and recombination by Al/Si alloying and p+-type doping of the rear-contact region.

vi. **Formation of metal front contact.** An array of slits – 70 μm wide, parallel to one side of the cell and separated by 2 mm pitch – was opened in the passivation SiO_2 film on the front surfaces of all samples by photolithographic patterning and HF etching. The slits were covered by a 40 nm thick Ti layer using vacuum evaporation and lift-off of photoresist.

We made several b-Si solar cells of neighbor wafers processed with- and without passivation thermal SiO_2 films allowing for a direct comparison of the performance parameters.

3. Solar Cells Characterization

Samples of solar cells were investigated immediately after their fabrication, as well as after expiration for 30 days.

For the investigation of the b-Si structure, scanning electron microscopy imaging (SEM) was applied with a SEMXL 40 Philips. Fig. 2 shows SEM image of a Si_2O - b-Si sample in cross section. By the RIE process, a needle-shaped surface is created. The typical height of needles was around 650 nm and diameter around 150 nm. The thermal SiO_2 film follows the surface geometry and covers completely the b-Si surface. The thermal SiO_2 film thickness was 25-30 nm.

The reflectance was measured using a Spectrophotometer T70 UV-VIS with an integrating sphere. The incident direction was close to the surface normal.

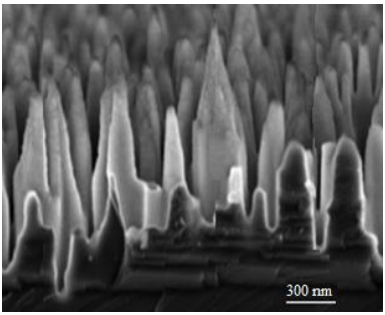

Fig. 2. SEM image of a Si_2O - b-Si sample in cross section

Fig. 3 shows the reflectance of conventional (polished surface) and bi-Si samples with- and without passivation SiO_2 films. The results of the spectroscopic studies confirmed that the b-Si and b-Si - SiO_2 surfaces have low reflectance (2-8 %) in the visible region of the spectrum compared with the conventional samples (40-50 %). Both b-Si samples have similarly low reflectance, indicating that the thermal oxidation does not interfere with the antireflection of the b-Si surface. Solar spectrum-weighted average reflectance from 450-1000 *nm* wavelength is 5% and 4% for b-Si - SiO_2 and b-Si surfaces, respectively. Minor difference in the reflectivity spectrum is likely the result of slight variation of b-Si etching during high temperature oxidation. The repeated spectroscopic analysis of the b-Si - SiO_2 samples showed the stability of the optical properties after their expiration for 30 days.

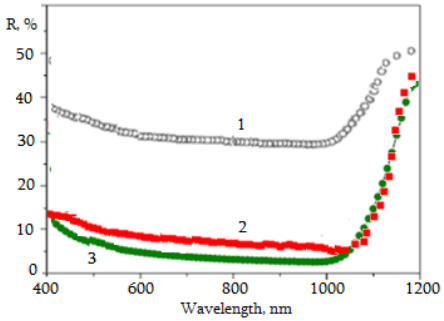

Fig. 3. Reflectance spectra of the samples. 1 - conventional; 2 - b-Si - SiO_2; 3 - b-Si

The IV-characteristics of the solar cells was investigated under air mass 1.5 (AM 1.5, 1000 $W.m^{-2}$) illumination with a solar simulator. Table shows the performance parameters (such as open circuit voltage - V_{oc}, short-circuit current - I_{sc}, fill factor - FF, and conversion efficiency - μ) of b-Si solar cells with- and without passivation SiO_2 film.

As shown in Table, the efficiency of b-Si solar cell samples with passivation SiO_2 can be insignificantly improved. The passivation mechanism can be given as follows: the SiO_2 film does not only have low surface state density at Si-SiO_2 interfaces but also reduces the surface doping concentration via thermal oxidation processing leading to the lower Auger recombination. It also provides very good chemical passivation, reducing silicon interfacial defects to 10^9 to 10^{10} $eV^{-1}.cm^{-}$

^{2} and contains a small amount of positive fixed charge with a density of 10^{10} to 10^{11} cm^{-2}, affording a weak field passivation effect [3]. It was found that the performance parameters of b-Si solar cells protected by the thermal SiO_2 film in comparison with b-Si solar cells without SiO_2 film did not change during 30 days.

The performance parameters of solar cells

Solar Cells	After fabrication				After expiration for 30 days			
	V_{oc}, mV	I_{sc}, mA/cm^2	FF	μ, %	V_{oc}, mV	I_{sc}, mA/cm^2	FF	μ, %
with SiO_2 film	628	37.0	0.770	17.9	628	36.8	0.767	17.7
without SiO_2 film	627	36.4	0.772	17.6	627	35.2	0.764	16.9

4. Conclusions

Thus, the combination of b-Si and thermal SiO_2 demonstrates promising results. The thermal oxidation: i) retains low reflectivity of the b-Si surface; ii) does not degrade performance parameters; iii) provides better surface-passivation quality and iv) has a protective function and stabilizes the properties of the b-Si surface at the time. Further optimization of the key processing steps - such as b-Si formation and thermal oxidation - could promise extremely high-efficiency b-Si solar cells. It is also problematic to form good metal contacts on nanostructured surfaces. In b-Si that contains deep pores, metal cannot completely bridge the gaps between nanostructures, resulting in poor contact.

References

1. ***M. Steglich, T. Kasebier, M. Zilk.*** J. of Appl. Phys., **116**, 173503 (2014).
2. ***K. Svetoslav, B. Martins,S. Stutzmann.*** Appl. Phys. Lett., **100,** 19 (2012).
3. ***X. Liu, P. Coxon, M. Peters, B Hoex.*** Energy Environ. Sci., **7**, 3223 (2014).
4. ***Y. Tang, Z. Chunlan, W. Wenjing, Z. Su.*** J. of Semiconductors, **33**, 118801 (2012).
5. ***J. Shieh, C. You, C. Chiu, J. Liu, P. Shih.*** Nanoscale Res. Lett., **11**, 489 (2016).
6. ***Oh Jihun, Y. Hao-Chih, H. Bran.*** Nature Nanotechnology, **7,** 743 (2012).
7. ***A. Aberle.*** Progress in Photovoltaics: Research and Appl., **8**, 473 (2000).
8. ***J. Schmidt, F. Werner, B. Veith.*** Energy Procedia, **15**, 30 (2012).
9. ***K.G. Ayvazyan, G.Y. Ayvazyan, A.R. Barseghyan.*** Proc. of Eng. Academy of Armenia, **12**, 355 (2015).

DETERMINATION OF DEFECTS OF SEMICONDUCTOR SOLAR CELL WAFERS BY INFRARED IMAGE PROCESSING

A.L. Hovhannisyan, R.R. Vardanyan

National Polytechnic University of Armenia, Yerevan, Armenia,
E-mail: anna.l.hovhannisyan@gmail.com
National Polytechnic University of Armenia, Yerevan, Armenia, E-mail: rvardan@seua.am

1. Introduction

Solar power is a growing renewable technology that provides promising solutions to the world's energy. Engineers and scientists worldwide are collaborating to lower the material costs of solar cells, increase their production efficiency, and viably introduce technologies to the mainstream market [1].

Since defects in solar cells critically reduce their conversion efficiency and usable lifetime, the determination of defects of solar cells is very important in the stage of manufacturing as well as during exploitation process.

Typically, failures of Photovoltaic (PV) modules are divided into the following three categories: Infant-failures, midlife-failures, and wear-out-failures. Figure 1 shows examples for these three types of failures for PV modules. Besides these module failures many PV modules show light-induced power degradation (LID) right after installation. The LID is a failure type which occurs anyhow and the rated power printed on the PV module is usually adjusted by the expected standardized saturated power loss due to this failure [2].

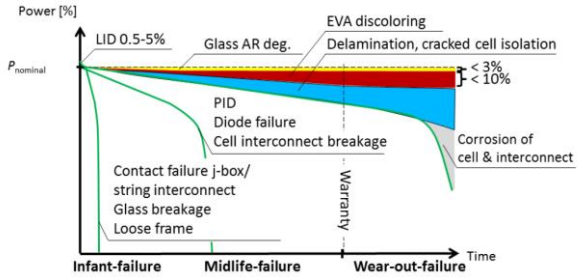

Fig. 1: Three typical failure scenarios for wafer-based crystalline photovoltaic modules are shown. Definition of the used abbreviations: LID – light-induced degradation, PID – potential induced degradation, EVA – ethylene vinyl acetate, j-box – junction box.

Some fatal defects, such as small cracks lying within the wafer surface and subtle finger interruptions, may not be visually observed in the image captured by a typical CCD camera. To highlight the intrinsic and extrinsic deficiencies that degrade the conversion efficiency of a solar cell, the electroluminescence (EL) imaging technique has been proposed in recent years. In the EL imaging system, the solar cell is excited with voltage, and then a cooled Si-CCD camera or a more advanced InGaAs camera is used to capture the infrared light emitting from the excited solar cell. The defect areas are inactive, resulting in dark regions that are visually observable in the sensed EL image. The EL imaging system not only shows the extrinsic defects as dark objects but also presents the dislocation and grain boundaries with dark gray levels in the sensed image [3].

In this paper different image processing approaches to find solar cell defects by using infrared images captured by electroluminescence method are suggested. The methodology is also considered the final application in use and the algorithms are chosen based on the working speed on the embedded hardware for the real-time test solution.

2. The approach and algorithm

There are different methods of solar cell investigation and defect detection. In this paper the electroluminescence method is used which is a contactless, precise and cheaper method of investigation. Measurements had been done by the system presented in Figure 2. At the end of acquisition phase from the infrared camera, infrared images are captured which should be pass the digital image processing.

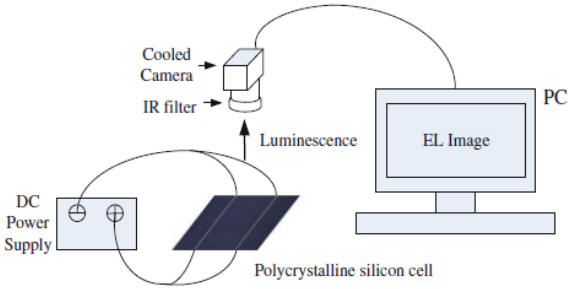

Fig. 2. The hardware architecture of the proposed measurement system

For this research, initially we have a color (infrared) image, acquired from IR camera. It contains thermal information about the surface in camera field of view. Hot parts are colored by red color, warmer parts with yellow, cool parts with green and cold parts with blue color. So, the treated parts are those, which colored red. It means, that the color detection could be implemented directly, but color operators are time consuming, and if it is not only a research, but should be used in real production line, then we should think about algorithm complexity and speed as well.
In this paper two approaches of digital image processing algorithms are proposed. The first algorithm is used for the defect localization and the second one is for defect's contour analysis.
The algorithm used for the defect detection of solar cells is presented below:

- Capturing Original Image
- Color Plane Extraction
  Extracts the three-color planes (RGB, HSV, or HSL) from an image. In the proposed case the treated (defected) part of image is colored by red, so the R plane from RGB is taken for processing.
- Filter (Median filter is used)
  The median filter is a lowpass filter. It assigns to each pixel the median value of its neighborhood, effectively removing isolated pixels and reducing detail.
  For each pixel $P(i, j)$ in an image where i and j represent the coordinates of the pixel, the convolution kernel is centered on $P(i, j)$. Common cases for median filter are 3x3, 5x5, 7x7 windows.
  $P(i, j)$ = median value of the series $[P(n, m)]$
- Thresholding
  Thresholding segments an image into a particle region—which contains the objects under inspection—and a background region based on the pixel intensities within the image. The resulting image is a binary image.
- Particle Analysis
  Particle analysis consists of a series of processing operations and analysis functions that produce information about particles in an image. Using particle analysis, we can detect and analyze any 2D shape in an image. A typical particle analysis process scans through an entire image, detects all the particles in the image, and builds a detailed report on each particle. We can use multiple parameters such as perimeter, angle, area, and center of mass to identify and

classify these particles. Using multiple parameters can be faster and more effective than pattern matching in many applications [3, 4].

After the defect localization, the defect's contour analysis is done. The algorithm used for that is presented below:

- Capturing Original Image
- Color Plane Extraction (R plane from RGB is taken for processing)
- Lookup Table
  Logarithmic Power 1/Y Square Root is used to increases the brightness and contrast in dark regions.
- Contour Analysis
  Contour analysis involves three steps. First, curves are extracted from the image. Next, the curves are connected based on the connection parameters. Finally, the step selects a single connected curve to represent the contour.
- Clamp
  Finds edges along a rectangular region of interest (ROI) that is drawn in the image and measures the distance between the first and last edges found. The edges are located along multiple parallel search lines drawn within a rectangular ROI. Edges are determined based on their contrast and slope.
- Defect's Contour Definition and classification

3. The experimental results

In the figures 3 – 8 step by step results of the algorithm for the defect localization are presented.
In the figures 14, 15 the estimated time needed both for the first particle analysis and second, contour analysis are presented. So, the whole image processing for the solar cell wafer defect detection can be done in 33.58ms which is faster than the existing approaches. This gives an opportunity to test up to 30 DUTs per second in real-time.

4. Conclusion

The methodology presented in this paper allows defining and detecting solar cell defects using IR images. The proposed approach is precise as it uses two algorithms. The algorithms have been tested on a real embedded hardware where the resources are limited than on the usual personal computer.

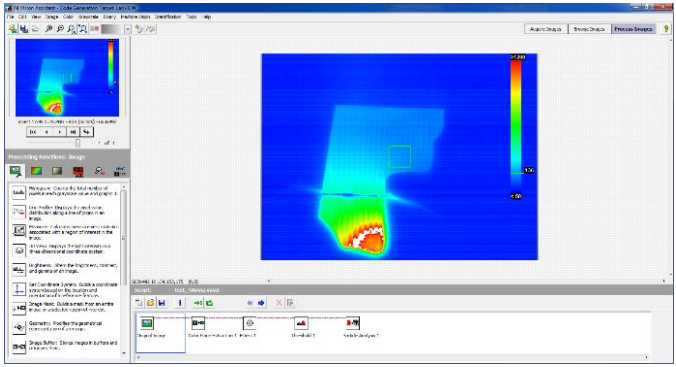

Fig. 3. Original Infrared Image

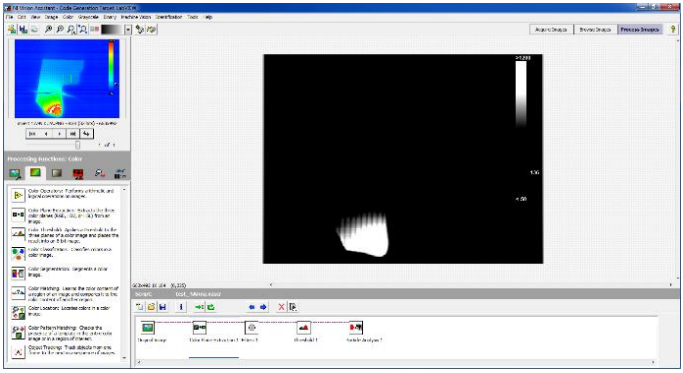

Fig. 4. Color Plane Extraction result (red plane is taken)

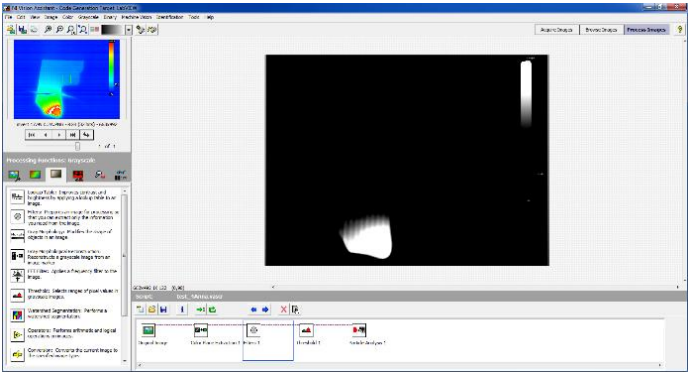

Fig. 5. Result after filtering (median filter is implemented)

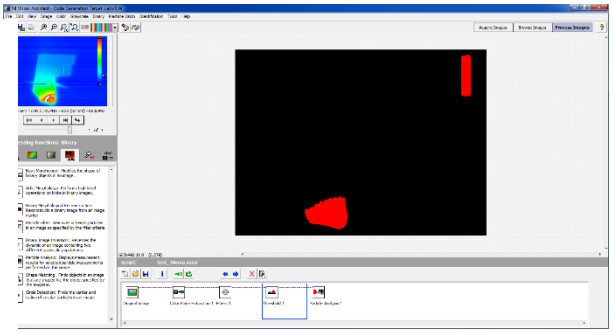

Fig. 6. Threshold (manual or automatic)

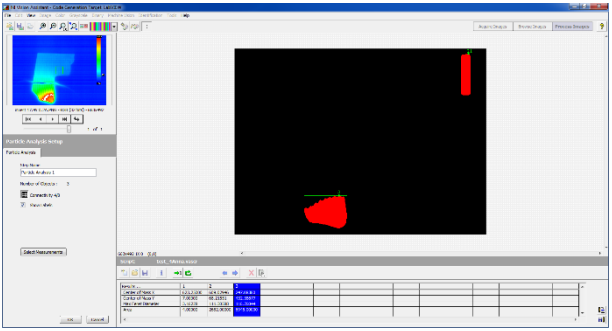

Fig.7. Particle analysis (finds separate particles in binary image)

Results ...	1	2	3
Center of Mass X	623.25000	609.02946	247.08380
Center of Mass Y	7.00000	68.21551	432.38877
Max Feret Diameter	3.16228	111.30588	116.76044
Area	4.00000	2682.00000	6945.00000

Fig. 8. Particle analysis Results

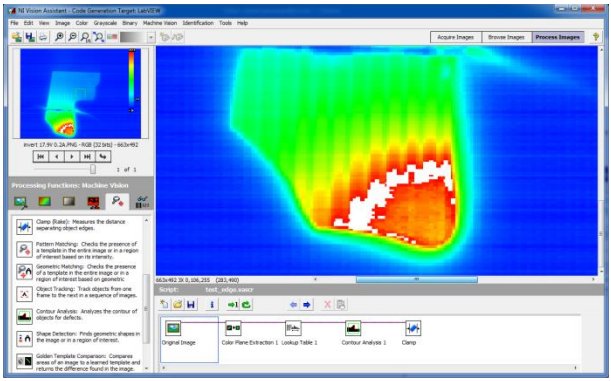

Fig. 9. Capturing Original Image

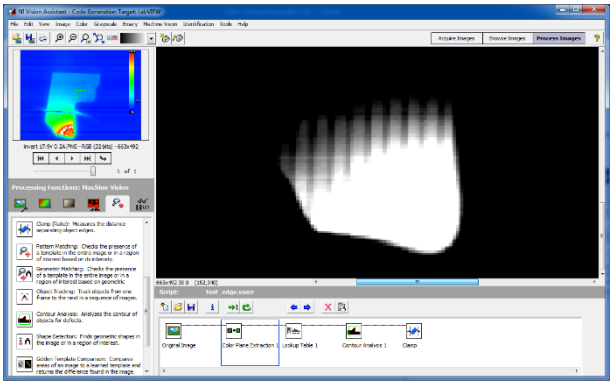

Fig. 10. Color Plane Extraction Result (red plane is taken)

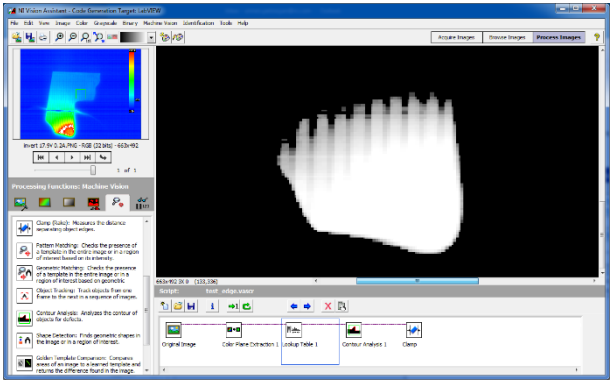

Fig. 11. Lookup Table Result

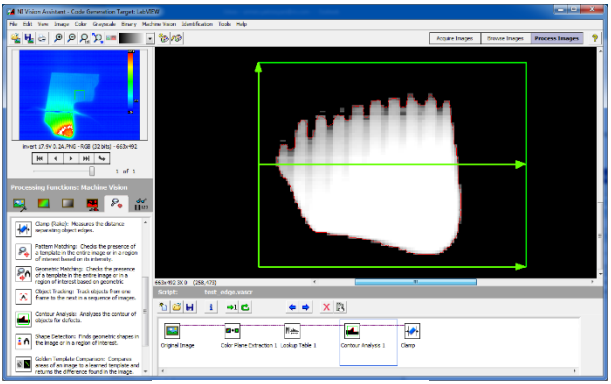

Fig. 12. Contour Analysis

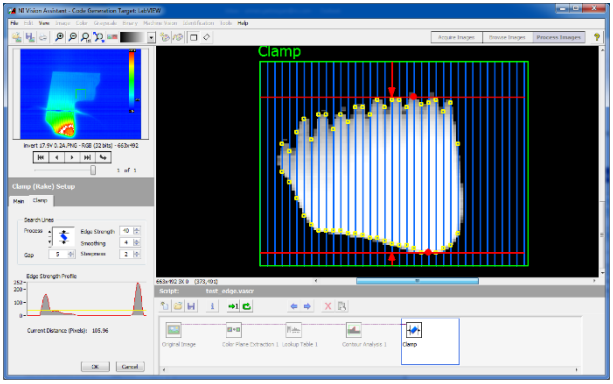

Fig. 13. Clamp Result

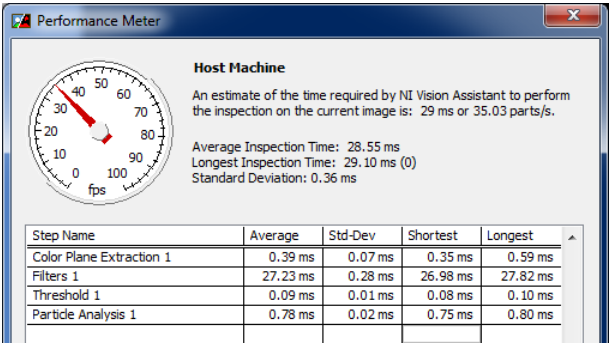

Fig. 14. An estimated time required for solar cell defect detection by particle analysis

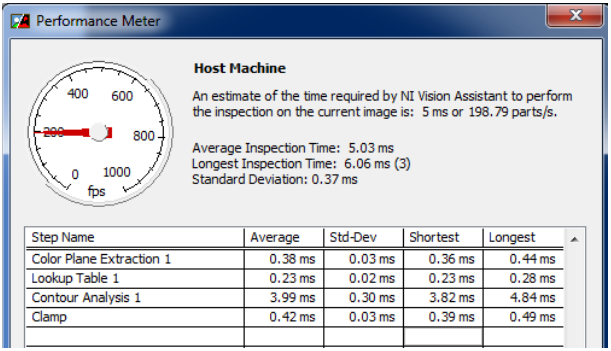

Fig. 15. An estimated time required for solar cell defect by contour analysis

References

1. ***ni.com***
2. ***M. Köntges, S. Kurtz, C. Packard, U. Jahn, K.A. Berger, K. Kato, T. Friesen, H. Liu, M. Van Iseghem.*** Review of failures of photovoltaic modules, 2014
3. ***Y.-H. Tsai, D.-M. Tsai, W.-C. Li and S.-C. Wu.*** Defect Detection of Solar Cells Using EL Imaging and Fourier Image Reconstruction, Proc. of the Institute of Industrial Engineers Asian Conference 2013, pp 53-62, 2013.
4. ***E.R. Davies.*** Computer and Machine Vision: Theory, Algorithms, Practicalities, Fourth Edition, Elsevier, 2012.
5. ***National Instruments Corporation.*** "NI Vision Concepts Manual", 2008.

OBTANING OF GRAPHENE BY CHEMICAL VAPOR DEPOSITION

H.L. Margaryan, N.H. Hakobyan, V.K. Abrahamyan, H.S. Chilingaryan, Arpi S. Dilanchian Gharghani

Yerevan State University, e-mail: marhakob@ysu.am

Introduction

The discovery of graphene has opened a new and very promising area of new physics and potential applications [1, 2]. Graphene, a monolayer of carbon atoms arranged in a honeycomb structure, is a unique material with outstanding properties: high optical transmittance, exceptional electronic transport, outstanding mechanical strength, and chemical stability. The striking electrical [3], mechanical [4, 5] and chemical [6, 7] properties of graphene make it suitable for use in flexible and transparent optoelectronics [8-10], biological sensors, energy storage conversion devices and etc.

However, efforts to make transparent conducting films from graphene have been hampered by the lack of efficient methods for synthesis, transfer and doping of graphene at the scale and quality required for applications. Theoretical studies of graphene have begun long before obtaining the real samples. In the 30-40's on the past century the calculations showed that a free two-dimensional film should be thermodynamically unstable. For this reason monolayer structures were obtained only on the surface of bulk materials. The first steps for making single carbon layers were made in the 60-70's., using colloidal solutions of graphite oxide [11] and using methods of chemical vapor deposition of hydrocarbons on metal substrates [12] or on their carbides [13]. Another method showed that the high-temperature treatment of silicon carbide with silicon evaporation leads to the epitaxial growth of a single-layer carbon film [14, 15]. However, in all the works listed above, the films with the thickness of no less than 20-30 layers were obtained, which in their essence were not graphene.

A new stage of graphene development began with obtaining of single-layer and two-layer samples in 2004 [16], when the scientists, by multiple using of an adhesive tape, separated a monolayer of graphene from the bulk graphite and transferred it to the silicon substrate with oxide of 300 nm thickness. After demonstration of the unique electronic properties of graphene in these works, a rapid development of research of this material and the development of new methods for its production began.

Methods for obtaining graphene

The method of obtaining graphene is divided into several categories: detached graphene [16, 17, 18]; chemical graphene [19-21]; epitaxial graphene on metals [22-27] or on SiC [28-30]; chemical vapor deposition (CVD) graphene on nickel [31, 32] or on copper [33-36]. In order to obtain detached graphene from a plate of bulk well-oriented pyrolytic graphite by means of an adhesive tape multiple using, it is possible to separate the film into a single monolayer, which can be transferred to another substrate. The undisputed advantage of this method today is the obtaining of a graphene monolayer of the highest quality. Such samples are ideal for conducting experiments for electronic properties study, measurement of its conductivity or creation of prototypes based on graphene. The only and very significant drawback of this method is its inability to use it on production scale. Chemically graphene is obtained either by restoration of graphite oxide or by liquid-phase stratification of graphite. In the first case, a highly disordered material is obtained, which is far from its pure graphene properties. Liquid phase stratification of graphite, prolonged ultrasonic treatment and fine graphite centrifugation in the presence of a surface-active substance leads to the suspension formation containing not only single-layer graphene flakes, but also curved sheets and two-layer or multilayer graphene samples. When graphene is grown epitaxially on the metal surface (ruthenium, iridium, platinum, palladium, nickel, etc.) at a temperature exceeding 1000 °C, the metal saturates as a result of the chemical deposition of carbon from the gas phase. Further, in high or ultrahigh vacuum, when the substrate temperature decreases, the solubility of carbon in metal significantly decreases, and due to the thermal compression of crystal grating,

carbon appears on the surface, forming graphene domains of large area. The given method allows forming extremely thin and large-scale samples containing one or two layers, and having dimensions of highly oriented clusters up to 200 μm. On the other hand, graphene formed on the surface of the metal substrate cannot be transferred to any other substrate without damaging the metal. The fourth method is chemical vapor deposition (CVD). At 900 °C, a graphite film with thickness of ~400 Å is formed on metal substrate, the formation mechanism of which is quite simple. In a mixture of carbon-containing gas, hydrogen and argon at various pressures, gas decomposition takes place during heating. Further, with increase in temperature starting from 650 °C, the carbon atoms are deposited on a nickel substrate and at temperatures above 800 °C they begin to diffuse into the volume of nickel. The heating stops at temperatures 950-1000 °C and then, when the sample is cooled to room temperature, the crystal grating of the metal (due to thermal compression) squeezes out carbon atoms to the surface where they form a graphite-like structure, since the grating constant of nickel is very close to the constant graphite grating. When selecting certain synthesis parameters, like the nickel foil thickness, the maximum synthesis temperature, the synthesis time and the cooling rate of the sample, it is possible to achieve the formation of a thin graphene film - up to obtaining a monolayer of graphene. The formation of a graphene film on the surface of copper polycrystalline substrate is different. Since the solubility of carbon in copper is about 1000 times less than in nickel, then after the decomposition of carbon-containing gas and the deposition of carbon on the copper surface, diffusion into volume does not occur. As the temperature of the copper substrate increases, both the probability of graphene film formation and the covered area increase. In this case, the formation of multilayer graphene sheets is impossible on copper, since copper is a catalyst in the deposition of carbon. When the graphene monolayer is coated with a copper surface, the formation of subsequent layers becomes very unlikely. Today this method is used for a large-scale production of graphene.

The device description and experiment

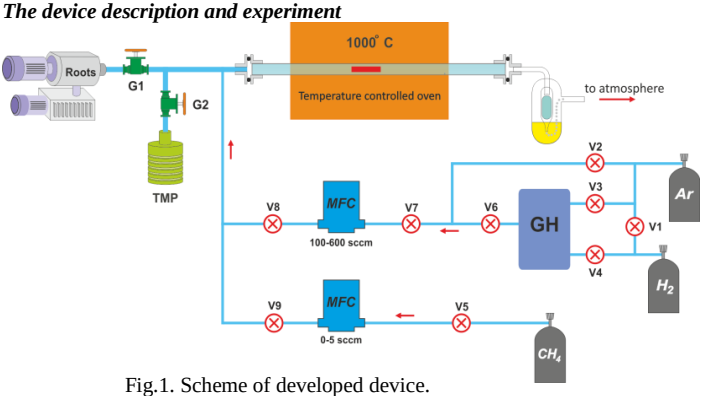

Fig.1. Scheme of developed device.

At the center of semiconductor devices and nanotechnologies of YSU an installation has been developed and assembled for graphene obtaining by the method of chemical vapor deposition from the gas phase. The scheme of the developed installation is shown in Fig.1. The installation consists of three main parts - a thermal reactor, a vacuum system and a gas distribution system. *The reactor* is a quartz tube of 22 mm diameter, placed in a heat furnace. In this case the furnace is installed on the base, which smoothly moves along the rails for withdrawal of the substrate- catalyst from the hot zone (synthesis zone) in order to cool the substrate after the end of the process. The temperature of the hot zone is controlled by FU-72 temperature controller in the range of 10-1200 °C with an accuracy of ~0.5°C. At the outlet of the reactor, a bubbler is installed to exclude backflow from the atmosphere into the quartz tube and neutralize the exhausted gas mixture before

discharge to the atmosphere. *The vacuum system* consists of a Roots pump and a turbomolecular pump designed to clean the quartz tube and provide vacuum in the reactor. *The gas distribution system* consists of a tank for gases mixing with a reducer, gas pipes, a valve system and two programmable gas flow regulators. The control of gas flow regulators and vacuum valves (V1-V9) is carried out by specially created software in the LabVIEW medium. A technological process for graphene obtaining on copper foil has been also developed. After chemical cleaning and electropolishing, the copper foil is placed in a quartz tube and dried in a stream of argon. At that the chamber is heated uniformly to a synthesis temperature of 1000 °C at a rate 20 °C/min in a stream of argon at a flow rate 300 N/cm^3/min. When the temperature reaches 1000 °C, the copper foil is annealed within 10 minutes. After the copper foil annealing, the process of graphene deposition begins, which lasts for 20 minutes. For this a 2% mixture of argon in hydrogen Ar:H_2 (80 sccm) and methane CH_4 (1sccm) is supplied into the chamber through MFCs. The heat anneals the copper increasing its domain size. The hydrogen catalyzes a reaction between methane and the surface of the Cu substrate, causing carbon atoms from the CH_4 to be deposited onto the surface of Cu through chemical adsorption. Then the furnace is abruptly moved along the rails in order to remove copper foil from the hot reaction zone. This keep the deposited carbon layer from aggregating into bulk graphite, and it crystallizes into a contiguous graphene layer on the surface of Cu. Once the graphene/copper foil has been removed from the furnace and cooled the graphene layer can be transferred an arbitrary substrate. As pilot samples graphene films on copper foil were obtained. The mono-layer graphene film was then transferred from the Cu foil to a pre-cleaned glass substrate by using a polymer support layer of polystyrene (PS, Mw 35k, 2% w/w in toluene) and an etchant acid ($FeCl_3$ aq, 0.5 M) to remove the Cu, as described elsewhere [37]. This was followed by a wash in a warm ethyl acetate bath to dissolve the supporting polymer layer. The obtained graphene was used as a transparent electrode in a liquid crystal cell. At that, for comparison with a hybrid LC cell, containing two sections with different transparent conductive layers - graphene and ITO, have been made. The work of the prepared cell as an optical valve was observed (Fig. 2).

a b c

Fig. 2. Images of the graphene-ITO hybrid LC cell, obtained between crossed polarizers: voltage not applied (a), voltage applied to LC cell with graphene electrodes (b), voltage applied to LC cell with ITO

The transmission spectra of the both sections have measured in the visible range (Fig.3).
As it seen from the figure, the cell with ITO electrodes is more transparent for the 400-500 nm wavelengths, and the cell with graphene electrodes - for wavelengths exceeding 800 nm. The transparency is the same for the 550-800 nm wavelengths range.

Conclusion

A device for graphene obtaining by CVD method is developed and assembled. A liquid crystal cell consisting of two sections with various transparent electrodes is made: graphene and ITO. The work of the obtained cell as an optical valve is shown, both sections of the cell function identically. Graphene can be successfully used as a transparent electrode in optical elements based on LC.

This work was supported by State Committee Science MES RA, in frame of the research project № SCS 15T-1C157.

References

1. K.S. Novosolov, A.K. Geim, et al. Nature, **438**, 197 (2005).
2. A.K. Geim and K.S. Novoselov. Nat. Mater., **6**, 183 (2007).
3. H.W. Kroto, J.R. Heath, S.C. O'Brien, R.F. Curl, R.E. Smalley**.** Nature, **318**, 162 (1985).

4. C. Lee, X. Wei, J.W. Kysar, & J. Hone. Science, **321**, 385 (2008).
5. J.S. Bunch, et al. Nano Lett., **8**, 2458 (2008).
6. D.C. Elias, et al. Science **323**, 610 (2009).
7. X. Wang, et al. Science **324**, 768 (2009).
8. K.S. Kim, et al. Nature **457**, 706 (2009).
9. D.-H. Kim, et al. Science **320**, 507 (2008).
10. T. Sekitani, et al. Science **321**, 1468 (2008).
11. H.P. Boehm, et al. Proc. of the Fifth Conf. on Carbon, Pergamon Press, London, 1962, p.73.
12. M. Eizenberg, J.M. Blakely. Surface Science **82(1)**, 228 (1979).
13. T. Aizawa, et al. Physical Review Letters **64**, 768 (1990).
14. A.J. Van Bommel, J.E. Crombeen, A. Van Tooren. Surface Science **48(2)**, 463 (1975).
15. I. Forbeaux, J.-M. Themlin, J.-M. Debever. Phys. Rev., **B 58**, 16396 (1998).
16. K.S. Novoselov, A.K. Geim, S.V. Morozov, et al. Science **306**, 666 (2004).
17. K.S. Novoselov, et al. Proc. of the Nat. Acad. of Sci. of the USA **102(30)**, 10451 (2005).
18. J.C. Meyer, et al. Nature (London) **446**, 60 (2007).
19. K.P. Loh, Q. Bao, P.K. Ang, J. Yang. Journal of Mat. Chem. **20**, 2277 (2010).
20. S. Park, R.S. Ruoff. Nature Nanotechnology **4**, 217 (2009).
21. O.C. Compton, S.T. Nguyen. Small **6**, 711 (2010).
22. Y. Pan, H. Zhang, D. Shi, et al. Advanced Materials **21**, 2777 (2009).
23. P.W. Sutter, J.-I. Flege, E.A. Sutter. Nature Materials **7**, 406 (2008).
24. T. N'Diaye1, J. Coraux, et al. New Journal of Physics **10**, 043033 (2008).
25. P. Sutter, J.T. Sadowski, E. Sutter. Physical Review B **80**, 245411-1 (2009).
26. M. Gao, Y. Pan, et al. Appl. Phys. Lett., **98**, 033101-1 (2011).
27. S.-Y. Kwon, C.V. Ciobanu, et al. Nano Letters **9 (12)**, 3985 (2009).
28. E. Rollings, G. Gweon, et al. J. of Phys. and Chem. of Solids **67(9-10)**, 2172 (2006).
29. L.B. Biedermann, M.L. Bolen, et al. Phys. Rev. B **79,** 125411-1 (2009).
30. K.V. Emtsev, et al. Nature Materials **8**, 203 (2009).
31. Q. Yu, J. Lian, et al. Appl. Phys. Lett. **93**, 113103-1 (2008).
32. H. Cao, Q. Yu, et al. J. of Appl. Phys. **107**, 044310-1 (2010).
33. X. Li, W. Cai, et al. Science **324**, 1312 (2009).
34. X. Li, Y. Zhu, W. Cai, et al. Nano Letters **9(12)**, 4359 (2009).
35. S. Bae, H. Kim, et al.Nature Nanotechnology **5**, 574 (2010).
36. C. Mattevi, H. Kim, M. Chhowalla. J. of Mat. Chem., **21**, 3324 (2011).
37. M.M. Qasim, et al. Nanoscale. **7**, 14114 (2015),

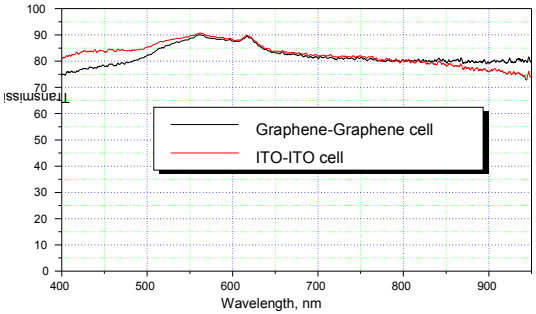

Fig.3. The transmission spectra of hybrid LC cell with graphene and ITO sections.

THz SPECTROSCOPIC PROPERTIES OF HUMAN SPONGY BONE AND COLLAGEN IN THE TERAHERTZ SPECTRAL RANGE 0.2 TO 2.5 THz

A.S. Nikoghosyan[1], H. Ting[2], J. Shen[2]

[1]*Yerevan State University, Yerevan, Armenia, nika@ysu.am*
[2]*Capital Normal University, Beijing, China*

1. Introduction

A bone material is composed of an organic matrix of collagen fibers and mineral hydroxyapatite ($Ca_5(PO_4)_3OH$) nanoparticles. An average tooth dentin contains 70% hydroxyapatite crystals, 20% collagen (e.g., proteins), and 10% water. The organic constituents provide flexibility, whereas the mineral provides strength and quality. Up to now, very few studies have been conducted concerning the study of the human bones [1, 2] and its anisotropy by THz radiation [3]. A structure of parallel dielectric fibrils (mineralized collagen fibrils) immersed in isotropic homogeneous ground substance behaves as a positive uniaxial birefringent medium. The hidroxyapatite can be found in space between fibrils - in layers that transverse across the fibrils and both within and outside the collagen fibrils. The collagen fibrils periodically separated by a tiny gap from 1 nm to 67 nm.

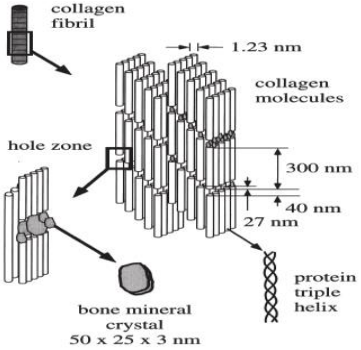

Fig. 1. System of long dielectric cylinders array (mineralized collegen fibrils of turkey) with major components.

THz wave (frequency range from 0.1 to 10 THz) found the most widespread practical use in THz time-domain spectroscopy [4,5] and in the THz imaging [6,7]. It is known that the time of vibrational motion of biological molecules have the order of picoseconds, and therefore, the frequency of vibrations is in the terahertz frequency range. Intermolecular interactions are usually weaker than the intramolecular and only THz spectroscopy in the time domain is sensitive to resolve their spectrum in the THz range.

In this paper we report the results obtained from a study of dielectric properties ($n(\omega)$ and $\alpha(\omega)$) of a spongy bone and collagen in transmission geometry using THz time-domain spectroscopy (THz -TDS).

2. Experimental study of human spongy bone and collagen by THz TDS

To measure the optical properties human spongy bone and collagen jawbone, the THz TDS method was applied. The experimental setup of the THz spectrometer is shown in [8]. The fiber femtosecond laser (Fx-100, IMRA) with the pulse duration 113 fs, central wavelength 800 nm, pulse repetition rate 75 MHz, and the power 120 mW was used to pump and detect the THz pulses [8]. During the measurements, the air temperature was 21°C, the humidity < 1.5%, the dynamic

range was more than 1000, and the signal/noise ratio at the peak position was about 400. The temporal forms for the THz pulses transmitted through the air and human spongy bone with the thickness 1.21 mm and the corresponding THz spectra of field obtained after the fast Fourier transform are shown in Fig.2a–e. To control the reproducibility of the experiment, the results of the three measurements are shown on the figure. The THz spectra of electric field after the fast Fourier transform E(ω) are shown in Fig. 2c, and the refractive indices and absorption coefficients at Fig. 2d,e. The absorption coefficient changes with the rise of frequency from 23.8 cm^{-1} to a value of 19.6 cm^{-1}, showing the several resonance absorption lines in low frequency range from 0.2 THz to 1.1 THz. The refractive index of the human spongy bone changes between the values of 1.09 and 0.99.

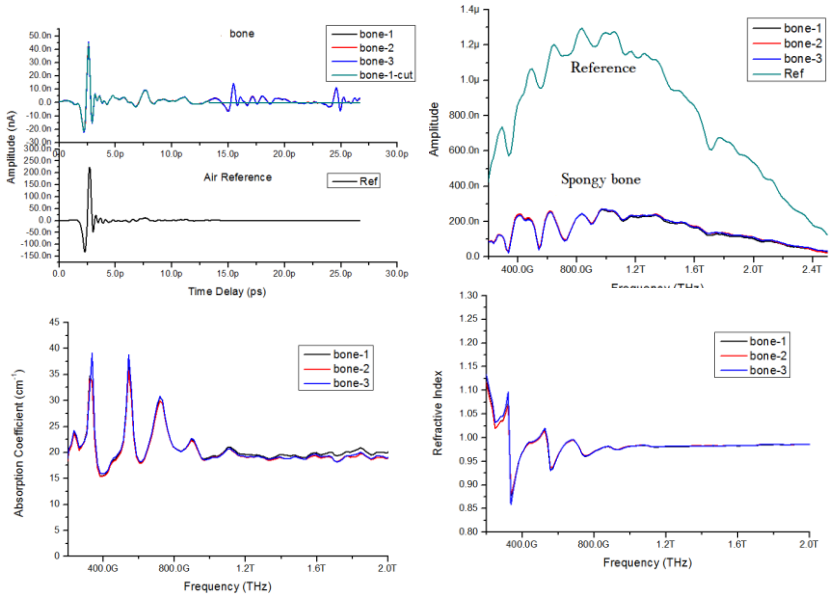

Fig. 2. Temporal waveforms of the THz pulses passing through (a) air and (b) the spongy bone; (c) spectra of electric field after the fast Fourier transform; (d) the adsorption coefficient and (e) the refractive index.

Conclusion

By the method of the terahertz time-domain spectroscopy (THz TDS) in a wide frequency range from 0.2 THz to 2.5 THz in vitro, the refractive indexes and absorption coefficients of the human spongy bone and the collagen are determined. The fiber femtosecond laser (Fx-100, IMRA) with a pulse width of 113 fs, a central wavelength of 800 nm and an average power of 120 mW was used as a laser source for pumping and detecting terahertz pulses. Transmission measurements were made through tissue slices of a spongy bone and collagen with thickness d=1.21mm and d=1.65 mm correspondly. As the results of studies, it was found that the refractive index of the human spongy bone changes between the values of 1.09 and 0.99 and for the collagen between 1.022 and 1.0245. The absorption coefficient of the human bone changes with the frequency from 23.8 cm^{-1} to a value of 19.6 cm^{-1}, showing the several resonance absorption lines in low frequency range from 0.2 THz to 1.1 THz. Absorption coefficient of the collagen increases from 1.45 cm^{-1} to 7.44 cm^{-1}.

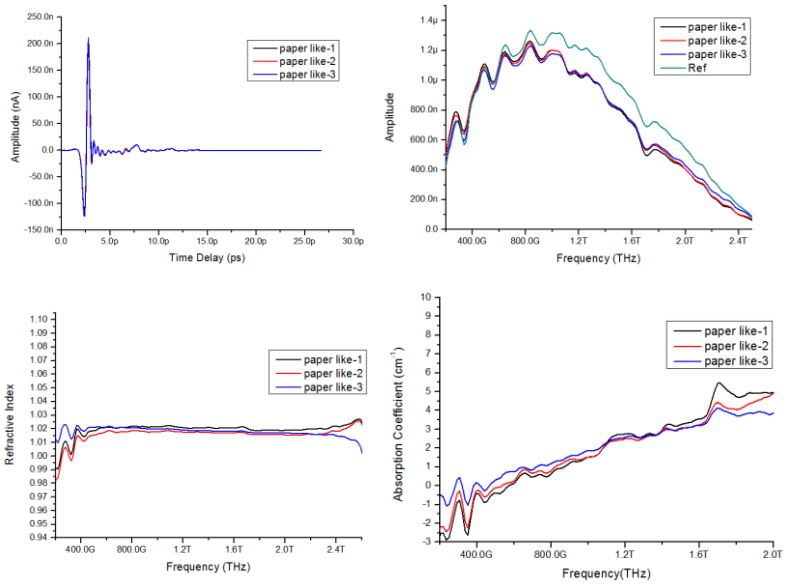

Fig. 3. Temporal waveform of the electric field of the THz pulse which has passed through (a) the collagen, (b) its spectrum after the fast Fourier transform, (c) the refractive index, (d) the absorption coefficient. .

Acknowledgments: This research was supported by the National Instrumentation Program (Grant No.2012YQ140005), the National Nature Science Foundation of China (Grant Nos. 61505125), the Nature Science Foundation of Beijing (Grant No. 4144069) and Science and Technology Project of Beijing Municipal Education Commission (Grant No. KM201410028004).

References

1. ***A. Magal, R. Reznikov, N. Shahar, R. Weiner.*** J. Struct. Biol., **186** 253 (2014).
2. ***E. Berry, A.J. Fitzgerald, et al. Physics*** of Medical Imaging, **5030,** 459 (2003).
3. ***V.V. Tuchin.*** J. of Biomedical Photonics & Eng, **1,** 3 (2015).
4. ***A.J. Fitzgerald, E. Berry, et al.*** J. Biol. Phys. **29,** 123 (2003).
5. ***E. Berry, A.J. Fitzgerald, N.N. Zinov'ev, et al.*** Proc. SPIE **5030,** 459 (2003).
6. ***N.N. Zinov'ev, A.S. Nikoghosyan, and J.M. Chamberlain. Proc***. SPIE, **6257,** 62570P1 (2006).
7. ***E. Pickwell, V.P. Wallace, B.E. Cole, S. Ali, C. Longbottom, R. Lynch, and M. Pepper***. Caries Res., **41,** 4955 (2007).
8. ***A.S. Nikoghosyan, H. Ting, J. Shen, R.M. Martirosyan, M.Yu. Tunyan, A.V. Papikyan and A.A. Papikyan***. J. of Contemp. Phys. (Armenian Academy of Sciences), 2016, **51**, 256 (2016).

DESIGN AND MODELING OF INTEGRATED CIRCUITS

ON-CHIP DECOUPLING CAPACITOR FOR FINFET TECHNOLOGY

V. Melikyan, T. Hakhverdyan, T. Khazhakyan, K. safaryan, A. Avetisyan, A. Hayrapetyan

Yerevan State University, Yerevan, Armenia, Synopsys Armenia CJSC,
E-mail: tigranha@synopsys.com

Introduction

Modern integrated circuits (ICs) are very sensitive to noise due to the presence of a big amount of noise generators that decrease the noise margins. The power grid: power supply and ground signals, are among the most critical sources of noise, since supply voltage variations are extremely large, it may lead to problems such as timing unpredictability, delay variation, or even improper functionality. Usually used metric, noise budget, is defined as the maximum permissible noise amplitude [1]. Signal integrity is appearing as a limiting factor in the VLSI chip designs as technology scales. This is especially true on power/ground networks, a common technique for reducing power supply and ground noise and keeping the noise within the noise budget is through the use of on-chip decoupling capacitors (decaps). Decaps are capacitors that hold a reservoir of charge and are placed close to any large drivers. Decaps provide instantaneous current to the drivers to reduce IR drop, once large drivers switch, and hence keep the supply voltage approximately constant. As shown in Fig.1 [1], the on-chip decap delivers current to charge up the load capacitance of the second inverter when it switches. The supply voltage level is relatively constant at the inverter tap point since the decap is nearby [1, 2].

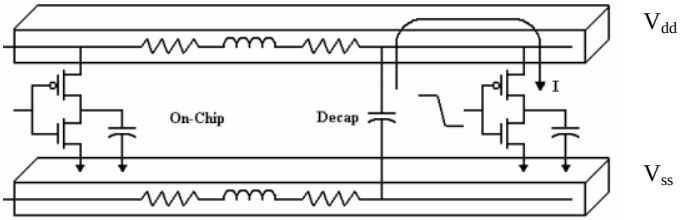

Fig. 1. Use of decoupling capacitor to reduce power grid noise

It has become common in the past decade to add decap to the areas of an IC that otherwise have no cells, or add dcaps directly to high speed block areas. However, decaps normally come with a quite serious down-side. Too many decaps in a design can increase leakage power of circuit as the cells bring their own leakage current.

In this paper has been proposed a new decal cell scheme which gives better parameters for circuit design with FinFET technologies as well as decreased ESD risk [2].

Types of decap cells

Standard: A standard decap is usually made from NMOS transistors in a CMOS process. The gate of the NMOS transistor is connected to VDD, whereas source, drain and substrate of the transistor are tied to VSS, as shown in Fig. 2. This approach is considered effective because the thin-oxide capacitance of the transistor gate provides a higher capacitance than any other oxide capacitance available in a standard CMOS fabrication process. For this MOS decap, the first-order calculation of the capacitance is WLC_{OX}, where W is the transistor width, L is the transistor length, and C_{OX} is the oxide capacitance per unit area. The effective capacitance and resistance at low frequencies can be written as:

$$C_{eff} = C_{OX}WL + 2C_{OL}W \qquad R_{eff} = \frac{L}{6\mu C_{OX}W(V_{GS} - V_T)}$$

where C_{OX} is the oxide capacitance per unit area, C_{OL} is the overlap and fringing capacitance per unit width, and W and L are the width and length of the transistor, μ is the channel mobility, V_{GS} (V_{GD}) is the voltage across the oxide, and V_T is the threshold voltage. R_{eff} is proportional to the channel length L. So for faster transient response, a decap design should use a small L to keep R_{eff} small. Both R_{eff} and C_{eff} can be considered constant at low or moderate operating frequencies, but they are degraded at high frequencies.

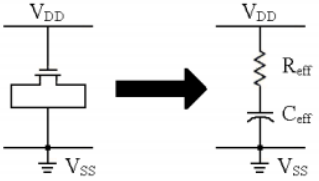

Fig. 2. Decoupling capacitor implemented using an NMOS device and modeling as a series RC circuit.

The channel length L of the decap controls its frequency response, with small enough L the effective capacitance remains relatively constant at high frequencies. As a result a fingering technique in decap layout is commonly used to support its frequency response. Also it needs to note that NMOS has better frequency response than PMOS. So the use of PMOS decaps should be limited, from the frequency response perspective [2].

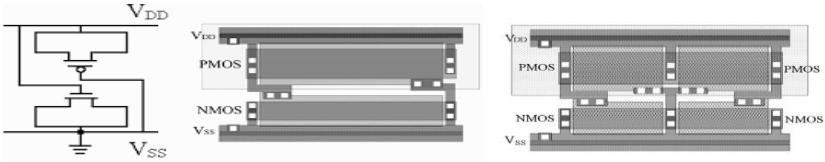

(a) (b) (c)

Fig. 3. Standard cell N+P decap

Standard-Cell Decap: As mentioned decaps are usually made of NMOS devices, within standard cells, it is more convenient to make decaps using both types of NMOS and PMOS to form a decap filler cell, as shown in Fig. 3 (a). That's why the n-well is already implemented and reserved for PMOS devices. Only the lower half-cell area is for NMOS devices. One sample standard-cell decap layout is illustrated in Fig. 3 (b). The capacitor areas are the polysilicon gates placed on the top of the channel regions of the MOS transistors. A fingering technique is used to improve the frequency response for Standard cell N+P decap. Fig. 3 (c) depicts the same decap cell but with two fingers [1, 2].

The overall effective capacitance is the sum of the two individual decoupling capacitances, and the overall effective resistance is the parallel combination of the two individual effective resistances.

$$C_{eff\_overall} \approx C_{eff\_n} // C_{eff\_p} = C_{eff\_n} + C_{eff\_p} \qquad R_{eff\_overall} \approx R_{eff\_n} // R_{eff\_p} = \frac{R_{eff\_n} R_{eff\_p}}{R_{eff\_n} + R_{eff\_p}}$$

Cross Coupled Decap: The standard N+P decap design for standard cells may no longer be suitable for 90nm and smaller technology due to increased ESD risk. This issue is solved in cross-coupled decap design. In the cross coupled design (Fig. 4 (a)), the drain of the PMOS connects to the gate of the NMOS, whereas the drain of the NMOS is tied to the gate of the PMOS. Both transistors in this design are still in the linear region. In the standard decap design, depending

on the transistor type the gates of the transistors are directly connected to either V_{DD} or V_{SS}. In this case, the gate of the NMOS device is connected to VDD through the channel resistance of the PMOS device. The gate of the PMOS device is tied the channel resistance of the NMOS device and then connected to V_{SS} [1, 2]. The added channel resistance to the gate provides the input resistance R_{in} for ESD protection. The input resistance can help to limit the maximum current flow to the decap so that the voltage seen from the gate of the decap is also limited. From the layout perspective (Fig. 4 (c,d)), this cross-coupled circuit can be seen simply as the standard decap. So the decap transistor areas don't need to modify, while only the metal wire connections are modified. Thus, this design does not require additional area in layout.

The design can be modeled as a series connection of R_{eff} and C_{eff} (Fig. 4 (b)), similar to the standard decap. The overall C_{eff} is roughly the same, while the overall R_{eff} increases significantly. Both transistors are still in the linear region, but the channel resistance is modified. Specifically, where C_{eff_n}, C_{eff_p}, R_{eff_n} and R_{eff_p} are the intrinsic effective capacitances and resistances, and R_{on_p} and R_{on_n} are the channel resistances of the NMOS and PMOS transistors. Since R_{on_p} and R_{on_n} are at least one order of magnitude larger, $R_{eff\ p}$ and $R_{eff\ n}$ can be ignored in the overall R_{eff} calculation.

$$C_{eff\_overall} \approx C_{eff\_n} // C_{eff\_p} = C_{eff\_n} + C_{eff\_p}$$

$$R_{eff\_overall} \approx (R_{eff\_p} + R_{on\_n}) // (R_{eff\_n} + R_{on\_p}) \approx R_{on\_n} // R_{on\_p} = \frac{R_{on\_n} R_{on\_p}}{R_{on\_n} + R_{on\_p}}$$

where R_{eq} is the process-dependent square resistance (kΩ

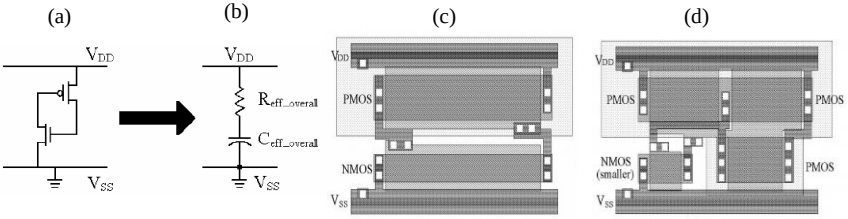

Fig.4. Cross-coupled decap schematic, modeling and layouts

Proposed decap cell

For integrated circuits made by FinFet technology need to note that transistor width change is discrete and it is difficult to meet required parameters for corresponding design [3, 4]. Also design standard N+P or cross-coupled decap cells no longer appropriate for FinFet technology due to controllability of capacitance value. As compared with planar technology where width of transistor can change continuously, in FinFet technology transistor width can be changed only discrete, via changing FINs count [3]. The new circuit is required, which will give opportunity to get corresponding value of capacitance.

As well as reducing on chip variation by matching corresponding transistors. The new decap cell circuit is made by merging cross coupled (Fig.5 (a)) and standard N+P decap cells. As shown in Fig.5 (b) the gate of M6 NMOS transistor is tied to left couple of standard decap cells gates, similare M9 PMOS transistor connect to right standard decap cells gates. The fingering technique is used to improve the frequency response for proposed decap cells as in standard cell N+P decap, also it inherits low ESD risk from cross coupled decap cell. As in proposed ciruit used capacitance which are connected series and parallel, is is posible to get capacitance value which are require.

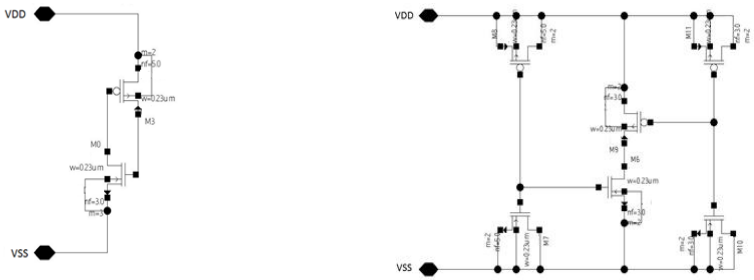

a) b)

Fig.5. Cross-coupled (a) and proposed (b) decap cell schematic view

Simulation Results

In table 1 show parameter comparison of proposed and cross-coupled decap cells. With proposed method it was posibled to design decap cells with different capacitance value, as described in previous section, while with cross-coupled method only get X4, X8, X16 and X64 decap cell, due to discrete of transistor width. From table 1, it is evident that area and leakage power of proposed method is higher due to number of transistor, these are disadvantages of proposed method. As advantages need to mention the minimum on chip variation, as with physical implementation corresponding transistors have benn merge/match (m7-with-m10, m8-with-m11), less ESD risk compare with stnadard decap cell, as well as improved frequency response.

Table 1. Proposed and Cross-coupled decap cells

Proposed Decap	area	Leakage (1nW)	Cross Coupled Decap	area	Leakage (1nW)
DCAP_X2	0.03231	0.00855412	NA		
DCAP_X3	0.04261	0.01014216	NA		
DCAP_X4	0.05133	0.01254412	DCAP_X4	0.02781	0.077521
DCAP_X6	0.08208	0.02107592	NA		
DCAP_X8	0.10944	0.03105181	DCAP_X8	0.05208	0.0157592
DCAP_X12	0.13854	0.04703721	NA		
DCAP_X16	0.21888	0.06562907	DCAP_X16	0.11934	0.0423451
DCAP_X64	0.87552	0.30549251	DCAP_X64	0.55521	0.2154925

Also were done frequency response C_{eff} and R_{eff} for diferent decap architecutre (Fig. 6)

Conclusions

Proposed circuit has the following advantages compared with the existing decap cell discussed in the second parts: a) compatibility with FinFET technology, b) minimum on chip variation, c) low ESD risk, d) improved frequency response. There are also disadvantages, usage of extra transistors, which increase total area of cells, but in 10nm and below technology core utilization is 60%, so designer will have enough free area to place decap cells. And leakage power is also increase, due to extra cells, it is compensating with using low power techniques [5, 6].

References

1. ***X. Meng, K. Arabi.*** IEEE Transactions On Very Large Scale Integration (VLSI) Systems, **16**, 1 (2008).
2. ***X. Meng, K. Arabi, R. Saleh.*** Novel Decoupling Capacitor Designs for sub- 90nm CMOS Technology, 7th International Symposium on Quality Electronic Design (ISQED) 2006, pp. 1-6.

3. ***V. Melikyan.*** Challenges and Solutions of IC Design Using FinFET Transistors, Proceedings of Engineering Academy of Armenia. Jubilee Publication, Yerevan, **11**. 91 (2014).
4. ***V. Melikyan, K. Safaryan, A. Avetisyan, T. Hakhverdyan.*** On-Chip Decoupling Capacitor Optimization Technique, Electronics and Nanotechnology Elnano (ELNANO), 2017, pp. 1-4.
5. ***V. Melikyan, T. Hakhverdyan, A. Gevorgyan, D. Babayan S. Manukyan.*** Low Power OpenRISC Processor with Power Gating, Multi-VTH and Multi-Voltage Techniques, East West Design and Test Symposium (EWDTS), 2016, pp. 33-36.
6. ***D. Babayan, E. Babayan, P. Petrosyan, E. Kagramanyan, T. Hakhverdyan.*** 1.9 GHz 1.05V 16-bit RISC Core for High Density and Low Power Operation in 28nm Technology, East West Design and Test Symposium (EWDTS), 2016, pp. 459-462.

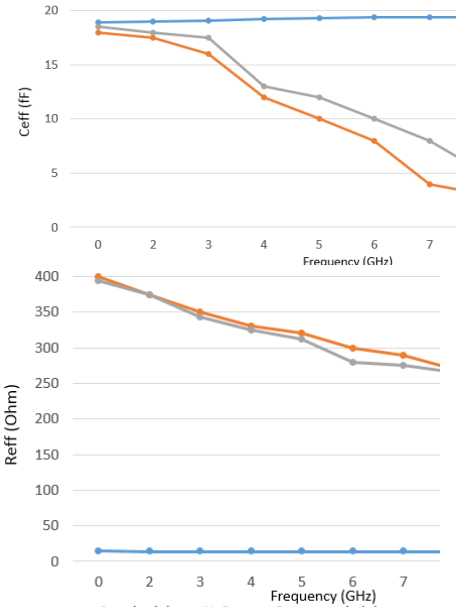

Fig. 6. Frequency response of Standard Cross-coupled and proposed decap cells

POWER SUPPLY NOISE REJECTION IMPROVEMENT IN HIGH-SPEED TRANSMITTER

A.K. Hayrapetyan

Yerevan State University, Yerevan, Armenia, E-mail:and@synopsys.com

Introduction

Has been researched famous architecture of transmitter, which has a big role in integral I/O circuits. Produced a test-bench of transmitter. Simulated and measured the key parameters of circuit, as a result observed the weak regions, due to which the circuit has a low noise immunity. Proposed to decrease the effect of weak regions on the output stage to enhance noise immunity.

Theory

The continues growth of amount of information transmitted from one device to another, makes it necessary to have high-frequency transmitters and receivers, but on the other hand the high frequency schemes create more noises, which will have a big impact on real data. Besides of speed growth, the continuous scaling of CMOS technologies makes circuits to be more sensitive and more vulnerable from noises. Supply voltages are scaled as well to keep constant the electric field, which also make circuits to become more sensitive to noise. The same picture appears in high-speed transmitters as well.

In transmitter-channel-receiver systems output resistance of transmitter, input resistance of receiver and characteristic impedance of channel, also called transmission line, should be equal to provide best termination of data reflection.

The characteristic impedance of a uniform transmission line is the ratio of the amplitudes of voltage and current of a single wave propagating along the line, that is a wave travelling in one direction in the absence of reflections in the other direction. Characteristic impedance is determined by the geometry and materials of the transmission line. For a uniform line, it is not dependent on it's length.

$$Z_0 = \frac{V_x}{I_x},$$

Z_0 is the characteristic impedance, V_x the voltage phasor at distance x , I_x the current phasor at distance x .

The characteristic impedance can be expressed as

$$Z_0 = \sqrt{\frac{R+j\omega L}{G+j\omega C}}:$$

The voltage phasor and current phasor can be expressed in the frequency domain as

$$\frac{\delta V(x)}{\delta x} = -(R+j\omega L)I(x), \quad \frac{\delta I(x)}{\delta x} = -(G+j\omega C)V(x).$$

When the elements R and G are negligibly small the transmission line is considered as a lossless structure. In this case, the model depends only on the L and C elements which greatly simplify the analysis. For a lossless transmission line, equations are:

$$\frac{\delta^2 V(x)}{\delta x^2} + \omega^2 LC * V(x) = 0, \quad \frac{\delta^2 I(x)}{\delta x^2} + \omega^2 LC * I(x) = 0.$$

If R and G are not neglected, the equations will be:

$$\frac{\delta^2 V(x)}{\delta x^2} = \gamma^2 V(x), \qquad \frac{\delta^2 I(x)}{\delta x^2} = \gamma^2 I(x).$$

Here γ is the propagation constant

$$\gamma = \sqrt{(R + j\omega L)(G + j\omega C)}.$$

The solution for V(x) and I(x) are:

$$V(x) = V^+ e^{-\gamma x} + V^- e^{\gamma x}, \qquad I(x) = \frac{1}{Z_0}(V^+ e^{-\gamma x} - V^- e^{\gamma x}).$$

The constants $V^{\pm}$ and $I^{\pm}$ must be determined from boundary conditions. For a voltage pulse , starting at x=0 and moving in the positive direction, then the transmitted pulse at position x can be obtained by computing the Fourier Transform.

In metallic conductor systems, reflections of a signal traveling down a conductor can occur at a discontinuity or impedance mismatch. The ratio of the amplitude of the reflected wave to the amplitude of the incident wave is known as the reflection coefficient.

$$\Gamma_0 = \frac{V_r}{V_i}$$

Γ_0 is the reflection coefficient, V_r the voltage amplitude of reflected wave, V_i the voltage amplitude of incident wave.

When the source and load impedances are known, the reflection coefficient is given by

$$\Gamma_0 = \frac{Z_L - Z_S}{Z_L + Z_S},$$

Z_L is the load impedance, Z_S the source impedance

In high-speed circuits, signals do not always flow in one direction. If the impedance is mismatched at any point, the signal will be reflected at that point. Impedance mismatching is easier to under if it is likened to a water pipe. If the inner diameter of the water pipe, which corresponds to impedance, changes at a point along the pipe, the water, which corresponds to signal, will not flow smoothly. Matching the impedance is an important aspect to consider in high-speed circuits.

For the approach resistance calibration circuits exist, which provide bias voltages to output stage transistors of transmitter to regulate output resistance. The bias voltages should be very precise to provide right resistance values. In this case noise from power supply could have crucial impact. The impact of power supply noise usually represented by power supply rejection ratio.

Power supply rejection ratio is a measure of a circuit's power supply's rejection expressed as a log ratio of output noise to input noise. PSRR provides a measure of how well a circuit rejects ripple, of various frequencies. PSRR is a measure of the regulated output voltage ripple compared to the input voltage ripple over a wide frequency range.

$$\text{PSRR} = 20\log \frac{Input\ Ripple}{Output\ Ripple}$$

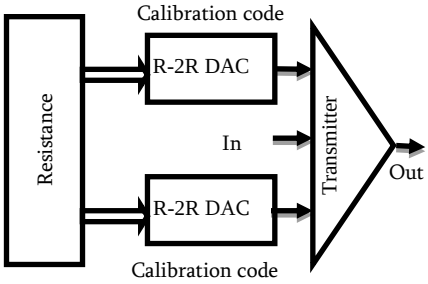

Fig. 1. Transmitter with resistor calibrator

Proposed to add two capacitors at calibration voltage net to vdd and to gnd. In this case noise from power supply will appear on calibration voltage net, so calibrated transistor gate and source voltages will get same noise and the difference will be equal to zero. Capacitors could be made from metal layers or from transistors. Both versions are investigated and compared. For both capacitors were used the same area.

Experiments

Simulated AC analysis. Frequency changed from 1 kHz to 10GHz. Measured power supply noise rejection ratio (PSRR) with metal and with transistor capacitors. Measured variations caused by process and temperature variations and from production variations.

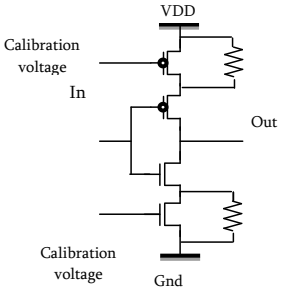

Fig. 2. Transmitter circuit

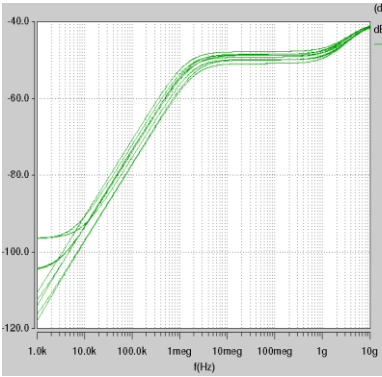

Fig. 3. PSRR plots, transistor capacitor case

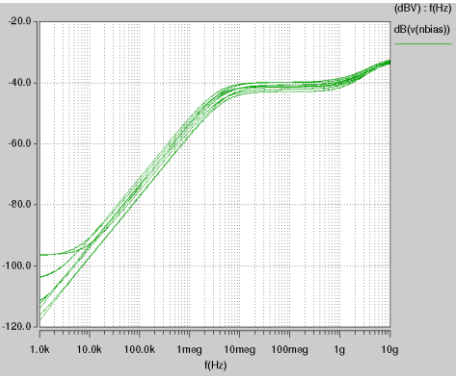

Fig. 4. PSRR plots, metal capacitor case

Results

Table 1. Worst rejection of both cases

Measurment	Metal cap	Transistor cap	difference [%]
psrr_max_bias [db]	-40.41	-32.56	24.11%
freq_max_bias [MHz]	10000	10000	0.00%
psrr_500_bias [db]	-47.28	-39.3	20.31%

psrr_max_bias – over frequency the worst PSRR value;
freq_max_bias – frequency value when PSRR is the worst;
psrr_500_bias – PSRR at 500MHz frequency.

Table 2. Process and temperature variations impact

	Measurment	Min	max	difference [%]
Metal cap	psrr_max_bias [db]	-42.58	-40.41	5.10%
	freq_max_bias [MHz]	10000	10000	0.00%
	psrr_500_bias [db]	-51.39	-47.28	8.69%
Transistor cap	psrr_max_bias [db]	-33.79	-32.56	3.78%
	freq_max_bias [MHz]	10000	10000	0.00%
	psrr_500_bias [db]	-42.56	-39.3	8.30%

Table 3. Production variations impact

	Measurment	min	max	difference [%]
Metal cap	psrr_max_bias [db]	-40.73	-37.04	9.06%
	freq_max_bias [MHz]	10000	10000	0.00%
	psrr_500_bias [db]	-55.6	-47.95	15.95%
Transistor cap	psrr_max_bias [db]	-37.09	-31.46	17.90%
	freq_max_bias [MHz]	10000	10000	0.00%
	psrr_500_bias [db]	-49.23	-39.3	25.27%

Conclusion

1. Investigated famous architecture of transmitter and observed weak regions, due to which circuit had a low power supply noise rejection ratio (PSRR).
2. Proposed two methods to improve PSRR.
3. Comparison of two methods shows:
    a. Metal caps provide about 20% more PSRR improvement than transistor caps.
    b. Transistor caps are more stable to process, temperature variations.
    c. Metal caps are more stable to production variations.

References

1. ***B. Razavi.*** Design of integrated Circuits for Optical Communications, John Wiley and Sons, Inc, 2012.
2. ***Z. Dixian, P. Reynaert.*** CMOS 60-Ghz and E-band Power Amplifiers and Transmitters, Springer International Publishing Switzerland 2015.
3. ***E. Musaelyan, V. Melikyan, A. Durgaryan, A. Khachatryan, H. Manukyan.*** Self Compensating Low Noise Low Power PLL design, East-West Design & Test Symposium 2013, pp.1-4.
4. ***S. Pithandia, S. Lester.*** LDO PSRR Measurement Simplified, Texas Instruments SLAA414, 2009, pp.1-5.

HIGH SPEED PRE-CHARGE CIRCUIT

A.V. Avetisyan

Synopsys Armenia CJSC, Arshakunyats 41, Yerevan, Armenia,
E-mail:aramav@synopsys.com

1. Introduction

Nowadays the large portion of the System-on-Chip (SoC) area takes Static random-access memory (SRAM). One of the main problems in SRAM's is the total power consumption. To solve this problem in the designs often used cells with smaller sizes, but this cause noise margin impairs. One of the solutions is using 8T SRAM cells, which has detached read path, controlled by read word-line (RWL) and the read data appropriately stored by read bit-line (RBL). When the RWL is enabled and the logical "0" is stored in the cell, current flows through the read path, and the RBL voltage becomes "0", and vice versa if stored data is "1" the RBL voltage remains "1". Thus the speed of this operation is very important. Moreover, the performance of the previous solutions is limited, when number of cells is plenty, it takes time to discharge RBL capacitance. In previous method to speed up the pre-charge path, which was controlled by pre-charge clock signal (PCS), used the simple circuit solution to generate PCS from signals. This paper demonstrates an 8T bit-cell SRAM with proposed circuit is presented to improve the timing for pre-charge path.

The rest of the paper is organized as follows. In Section 2, the schematic and operation of the conventional schemes are described. The proposed scheme for single-ended bit line architecture is detailed explained in Section 3 and 4. The Section 5 summarizes this paper.

2. Conventional Circuit.

Conventional scheme for pre-charge clock is shown in Fig. 1. The local write clock pin (LWCLK) is connected to the one of the inputs of NAND gate and second input pin is test enable (TE). LWCLK pin is inverse of memory internal clock signal, which is used to synchronize the writhe cycle. TE signal is a test pin and responsible to stress bit cells, but not corrupt data. When it is enabled, it puts the memory bitcell in stress mode for the address applied by turning on the word line and at same time keeping the bit-lines pre-charged. Read and write operations are disabled in this mode. The NAND_1 generate WCLKB signal, which connected to next NAND_2 gate, thus formed PCS. Second input of NAND_2 is inverse of CS signal. CS pin used in memory for power down mode, which will allow periphery supply to turn off completely and keep memory content. After write cycle, before read cycle starts bit-line (BB) and bit-line inverse (BT) should be charged to "1".

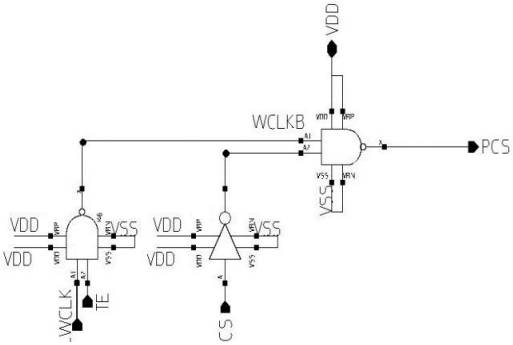

Fig. 1. Pre-charge clock scheme.

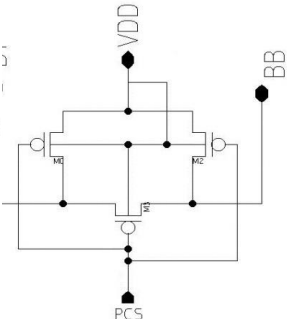

Fig. 2. Pre-charge circuit.

.

PCS signal is used to pre-charge BB and BT shown in Fig.2. When PCS is “0”, the pMOS transistors are turned ON and charges BB/BT for next read cycle. In this approach between the read/write operations LWCLK is toggling from “0” to “1”, the TE signal is “1” for this cycle, therefore WCLKB becomes from “1” to “0” and CS remains “0”, so output PCS toggling from “0” to “1”. Thus pre-charge operati3on stops. This operation takes around 34.68ps shown in Fig. 3.

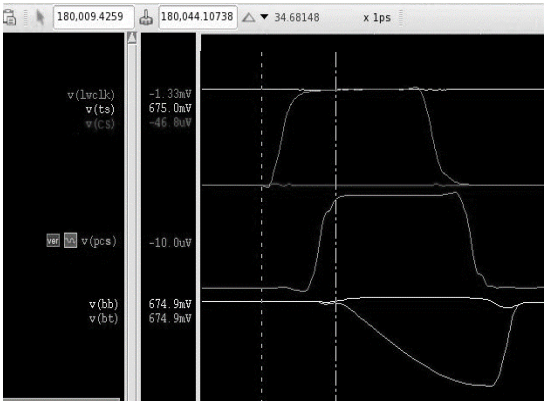

Fig. 3. Signals of Pre-charge clock scheme.

3. Proposed Circuit

To speed up the pre-charged clock path, the high speed pre-charge (HSP) circuit was proposed. The top structure of the HSP circuit is shown in Fig. 4. In this case the whole structure was revisited. Unlike previous scheme the control signal was inverse of memory internal clock, which was adding additional delay and delayed WCLKB signal was used to generate PCS. Instead of using WCLKB in the scheme is used write clock signal (WCLK), which is used to synchronize the write cycle. 2 NAND gate circuit was replaced with HSP scheme, shown in Fig. 5. The first input WCLK of HSP is connected to the M1 and M2 transistors, while the second CS and third LSB to (M3/M4 and M5/M6), this signals are for delayed control.

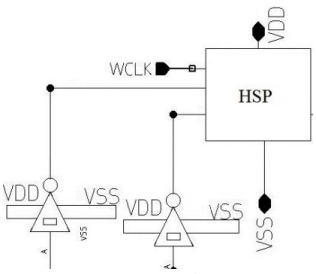

Fig. 4. Top level of HSP

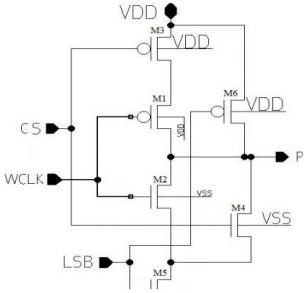

Fig. 5. HSP

The truth table for HSP scheme is shown in Table 1. The No5/6 cases are not allowed during this cycle (between read and write), which cause the short connection. Other than that the output PCS is used in pre-charge cells, to stop or start the discharge operation.

Table. 1 Truth table for HSP circuit

#No	CS	LSB	WCLK	PCS
1	0	0	0	1
2	0	0	1	1
3	0	1	0	1
4	0	1	1	0
5	1	0	0	X
6	1	0	1	X
7	1	1	0	0
8	1	1	1	0

The implemented scheme permits discharge the BL faster than the previous scheme. The appropriate discharge speed is achieved via a word-line (WL) enable. The signal which triggers a latch operation called sense amplifier enable (SAE), is generated via the reference bit cell. Activation of SAE and the discharging speed of the reference bit cell change, which force a SAE activation time to ensure correct sensing.

4. Simulation Results

512-b SRAM with the proposed scheme has been designed in a 28nm CMOS technology node. The memory array is created with 64 physical rows and 8 physical columns. The simulations have been run using Synopsys Hspice/VCS simulators, SS (slow-slow) 0.675v -40c PVT under 1600MHz. The memory passed the Verilog functional check. Timing parameters and values for PVT corner with conventional and proposed circuits is presented in the Table 2.

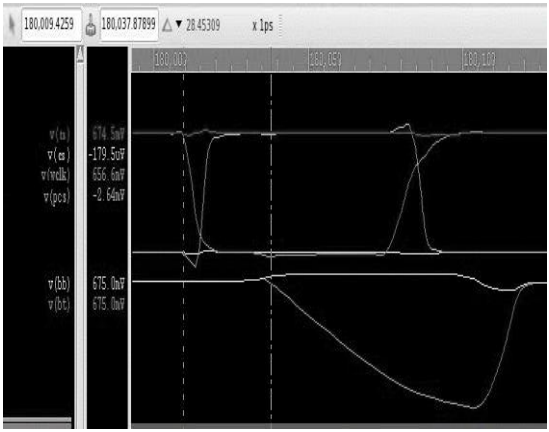

Fig. 6. HSP scheme.

Table. 2 Timing parameters comparison between Conventional and Proposed circuits.

Techniques	Wclk to BT/BB (ps)	Precharge (ps)	Total Difference (%)
Conventional Circuit	34.68148 ps	28.56122 ps	3.414e+00
Proposed Circuit	28.45309 ps	24.23782 ps	2.230e+00

Table. 3 Percentage advantage of Proposed circuits with respect to Conventional.

Parameters	Total Differance (%)
WCLK to BT/BT	17.95 %
Pre-charge	15.13

5. Conclusion

The characteristics of the two compared schemes are summarized in Table 2/3. Compared with the conventional scheme, the HSP scheme achieve 17.95% better performance for WCLK to BT/BT time by taking advantage of HSP architecture and write clock signal usage. The HSP scheme is able to decrease pre-charge time before read cycle 15.13% better performance than the previous solution. The disadvantage of this circuit is the bigger area with respect to old scheme around 16 % area increase.

References

1. ***H. Jeong, T. Kim, T. Song, G. Kim, S. Jung.*** IEEE transactions on very large scale integration (vlsi) systems, **23**, no. 7 (2015).
2. ***A. Sindwani***, ***S. Saini.*** Proc. of 2014 RAECS UIET Panjab Univ. Chandigarh, 06-08 March, 2014.
3. ***M. Qazi, K. Stawiasz, L. Chang, and A. P. Chandrakasan***. IEEE J. Solid-State Circuits, **46** (1), 85 (2011).
4. ***S. Nalam, V. Chandra, C. Pietrzyk, R. C. Aitken, and B. H. Calhoun***. in Proc. 11th Int. Symp. Qual. Electron. Des. (ISQED), Mar. 2010, pp. 139–146.

DYNAMIC VOLTAGE DROP ANALYSIS FOR UNIVERSAL SERIAL BUS TEST CHIP

K. Safaryan

Chair of Microelectronic Circuits and Systems National Polytechnic University of Armenia Yerevan, Armenia
Synopsys Armenia Educational Department,e-mail: karosaf@synopsys.com

Abstract: Dynamic voltage (IR) drop is vector dependent and circuits switching activity. In this paper emphasized the common design closure methodology and issues based on dynamic voltage drops. Reasons that can affect the accuracy of dynamic IR analysis and the related metrics for Universal Serial Bus (USB) Test Chip (TC) design closure are discussed. A structured approach to planning the power distribution and grid for power managed designs is presented. Care-about and solutions to avoid and fix the Dynamic voltage drop issues are also presented. Results are from Universal Serial Bus Test Chip industrial designs in 16nm process are presented.

I. Introduction

Designing an optimal power grid which is robust across multiple operating scenarios of an integrated circuit continues to be the main challenge. [1][2] The problem becomes enormous with technology shrinking, allowing more performance to be realized in a smaller area, from one node to another. The power distribution on the Universal Serial Bus(USB) Test Chip needs to ensure circuit robustness not only to current requirements, but also needs to ensure timing or functionality is not affected due to Dynamic IR drop, caused by in high frequency area power demand and switching patterns. [3]

Additional, today's integrated circuits power management methods like power gating and switch power supplies are the norms. In the case of switched power supplies, typically, power switch cells are regularly distributed across the standard cell logic (logic gates) area of the floorplan. There may be additional separation in the switched power grid in the form of power domains. These power switches add an extra dimension to the power distribution problem. Frequently limit the response of the power grid to dynamic power or current needs. By increasing the quantity of power switching the power network robustness can be improved but it will impact on the leakage current. So, the requirement is to minimize the number of switches used as well as minimize the signal routing resources utilized on the power grid. This paper discusses the issues related to timing closure and signoff (IR Drop, EM, etc.) at the same time estimate Dynamic IR drop effects realistically for the USB Test Chips. On one hand, the aspects that introduce pessimism in Dynamic voltage drop analysis have to be removed, although on the other hand the method ensures strong coverage of various corners and design operating scenarios must be ensured. The power distribution and power grid planning methodology was discussed. Also demonstrated some of the efficient power grid enhancements like robust automated switch placement and switched supply resistance minimization through DRC-aware power metal fill for USB TC. All the discussions and results are based on production implementations of low power Universal Serial Bus Test Chip.

II. Common Design Closure Method for USB TC

- Overview of Static Vs Dynamic IR Drop

Static IR drop is average voltage drop for the design [6], while Dynamic IR drop depends on the switching activity of the logic [5], hence is vector dependent. Dynamic IR drop depends on the switching time of the logic, and is less dependent on the clock period. The average current depends totally on the time period, whereas the dynamic IR drop depends on the instantaneous current which is higher while the cell is switching. Static IR drop was good for signoff analysis in older technology nodes where sufficient natural decoupling capacitance from the power network and non-switching logic were available. While Dynamic IR drop Evaluates the IR drop caused when

large amounts of circuitry switch simultaneously, causing peak current demand [1] [6]. This current demand could be highly localized and could be brief within a single clock cycle (a few hundred ps), and could result in an IR drop that causes additional setup or hold-time violations. Typically, high IR drop impact on clock paths and causes hold-time violations, although IR drop on data path causes setup-time violations.

- Disadvantages of Dynamic Analysis On A "Good" Power Grid

A typical power grid and power switches are designed to meet static IR drop targets and not for Dynamic IR drop. In the initial stage of the design, static IR drop can be tested. This is because of Voltage change Drop file (VCD) doesn't available. For instance, the switch and metal grid densities in the marks area can meet the static IR drop criteria, because the average power density in this region is not enormous. But when a particular procedure is run, notch area could have higher power density because of localized switching in that area and the switches combined with metal grid (Switched supply is distributed to cells by lower layers like Metal1 and Metal2) may not be enough to support the current density in the notch area. In that area can be very high dynamic IR drop. Refer to notch area as shown in Fig. 1.

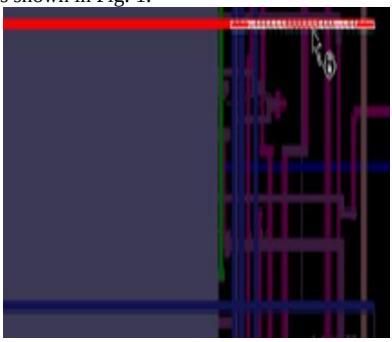

Fig. 1. Voltage map for small region

Here due to a lesser amount of switch cells combined with not so strong power grid is the main cause of high dynamic IR drop. Metal2 voltage drop are the dominant factors in the overall voltage drop for that region. A similar equivalence on the power density can be to the larger region. Fig. 2 shows, that the original Metal2 grid, static IR drops was within the budget. However, to meet the dynamic IR drop goals, an increase of the Metal2 grid by 2 times, was needed. The drop across the Metal2 and related vias reduced by 32%, after the improvement. This is another example of a robustness issue which was missed in static analysis. The number of power switches is calculated based on the static IR drop requirement. For our design, with the switch density that is calculated as per average power and with "calculated" optimal cell density and optimal decap cells density. Static IR drop and vectorless dynamic results runs were within the budgets. For Pin VPN Metal2 voltage drop is 7.21mV and for updated Pin VPN Metal2 voltage drop is 49.03mV. Vectorless dynamic IR drop was 4.302mV, but vector based dynamic IR drop was 7.412 mV, which is beyond the budget. The high dynamic IR drop region has high power density, which is not satisfied by the existing power switch density in that region, and as a result there is high Dynamic voltage drop. This shows that the affected region is not really a poorly designed power grid, but more of the very high power density, due to the design architecture combined with the placement of cells. In any case, the power grid has to eventually be able to support the design's power demands in that area, which requires a little bit different approach.

III. Accuracy of Analysis

- Comprehending delays in gate level simulation

There are several factors that affect the accuracy of the dynamic IR drop analysis. One of the main basics is to generate a realistic VCD file. Typically, VCD file was created by annotating an SDF in the gate simulation. Another common approach is to use a VCD file from a zero-delay simulation, which often results in non-realistic Dynamic IR drop.

- Comprehending realistic glitch propagation

Combinational logic switching can cause glitches. If the glitches have very weak amplitude, the chances of them getting filtered out by the (cell + interconnect) delay of the path is very high. Remains only comparable glitches. Form this approach the pessimism in the dynamic voltage drop reduced by 20%.

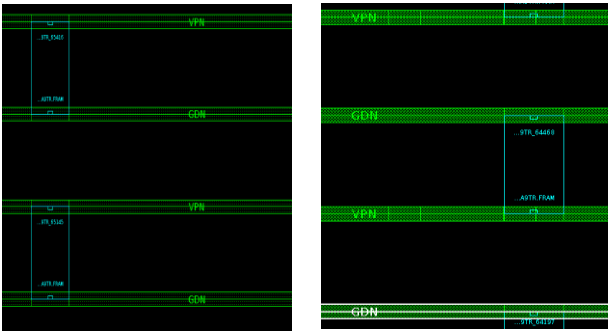

Fig. 2. Metal 2 original grid (left) and updated

- Choice of technology specs for signoff

Frequently, worst case conditions are chosen for timing closure checks. However, it is also dangerous to attack a balance between preference bounding conditions and being overly pessimistic. In an effort to get results closer to realistic silicon conditions, and to detect potentially issues, selectively evaluated designs under both worst case and best case conditions. For instance, if compared the effect of the worst via resistance specification in contradiction of the nominal via specs, the drop across vias alone reduce by 37%, as show in Table 1.

TABLE 1. VOLTAGE DROPS WORST AND BEST CORNERS

Worst Case		Best Case	
Pin VPN	Voltage Drop	Pin VPN	Voltage Drop
Met2	3.4 mV	Met2	3.09 mV
Via23	4.31 mV	Via23	2.75 mV
Met3	2.78 mV	Met3	2.14 mV
Via34	4.07 mV	Via34	2.56 mV
Met4	2.54 mV	Met4	2.33 mV

IV. Method for Robust Power Grid Design

Knowledge of the USB TC design operating scenarios and architecture play a vital role in ensuring the robustness across scenarios. Some methods to improve power grid robustness discussed below.

- Choosing the right average power

The vital problem is to choose the right average power value for which the power distribution is designed. It is common

practice to design for the average power seen in the use case that consumes the highest power. Hence, choosing the right average power for designing the power grid would help the design scale up to not just dynamic IR drop issues, but even to tolerate the average value more strongly.

- Early Dynamic IR Analysis

One of the problems in estimating the dynamic IR influence on USB TC is to get vectors for necessary scenarios, and to get them in time to detect issues before the design tapes out. This Early Analysis flow regards to this issue. In this flow, the switching activity of a macro blocks is integrated at the top level, and switching activity at the top level is created, for use in dynamic IR analysis. Via this flow, hot-spots for dynamic IR was detected.

- Power Switch Density and Placement

For designs with power switches, in most cases, high voltage drops cause by using small quantity of switches than needed for localized power density in certain regions. From common power analysis methods, it is possible to get a list of macro blocks which need more power than the rest of the design. This means that these IPs need higher current. Creating more VCD files will excite different parts of design and will show any weak connected power network.

- Power/Ground Metal Fill

Alternative method is Power/Ground Metal fill. After the design is frozen, final step is to add metal fill in the areas where the free metal tracks are available. These inserted metal straps are connected power or ground. By doing that, the power and ground grid becomes stronger and hence would help in reducing voltage drop.

- Other Methods to Reduce Dynamic IR Drop

Load and Slew violation can cause from high power. There can be high current demands for higher loads/slews. When fixing load/slew violation it can reduce dynamic IR drop. One more method to reduce Dynamic IR is addinf decoupling capacitors near Clock tree cells. This will help in reducing the voltage drop in clock tree cells due to switching.

V. Simulation Results

Simulation has been completed using the Synopsys Inc. Power Rail analysis tool for USB TC, including SS (slow-slow) case, with the supply voltage and temperature variations. Simulation performed with and without dynamic IR drop reduction which are talked above. The simulation results are shown in the Table 2.

TABLE 2. DYNAMIC VOLTAGE DROPS WITH AND WITHOUT REDUCTION

	Without optimization	Using Reduction
Dynamic Voltage Drop	13.488 mv	10.203 mv
Static Voltage Drop	5.04 mv	4.71 mv
Worst Slack	1.319 ns	1.520 ns

VI. Conclusion

We have emphasized the common issues faced in the USB TC design closure of power managed. Main accuracy and signoff method issues were talked and improvements made in reproducing the same operating conditions in analysis. A comprehensive set of methods adopted in our designs to create a strong power grid, and to ensure timing robustness considering dynamic voltage drop, was presented. This covered the choice of the correct power values, power switch planning, using design individuality and power routing methods. From above mentioned reductions dynamic IR drop reduced up to 24%, static IR drop reduced about 6.5%, worst timing path grow about 13%, but timing issues do not appear.

References

1. ***Sh. Lin, N. Chang.*** Int. Conf. on Computer Aided Design, 2001, pp. 651 – 654
2. ***Y. Zhong, M.D.F. Wong.*** Quality Electronic Design, 2008. ISQED 2008. 9th Int. Symposium.
3. ***R. Vishweshwara, R. Venkatraman.*** VLSI Design, 22nd Int. Conf., 2009.
4. ***Sh.H. Weng, Y.M. Kuo.*** Computer Design, 2008. ICCD 2008. IEEE Int, Conf. 12-15 Oct. 2008, pp. 532 – 537.
5. ***K. Arabi, R. Saleh, X. Meng.*** Design & Test of Computers, 2007 **24**, 236 (2007).
6. ***B. Rishi, P. Bindu.*** VLSI – SoC 2007. IFIP Int. Conf. 15-17 Oct. 2007, pp. 292-295.

APPROACH TO MATRIX BASED THERMAL PLACEMENT

Tigran Gasparyan[1], Ashot Harutyunyan[2]

[1]*Synopsys Armenia CJSC, Armenia, Yerevan E-mail:tigrangs@synopsys.com*
[2]*National Polytechnic University of Armenia: harash@seua.am*

Introduction

With the development of microelectronic technology and increase of integration of ICs, requirements for their design increase. According to the international index of semiconductor technology, currently the dominant requirements are performance and power consumption [1].

Increasing IC integration brings to increasing power consumption of semiconductor crystal. In contemporary IC working temperature of semiconductors can reach more than 100^0C and the temperature differences between different areas of the crystal can reach more than 10^0-20^0C. High temperature has negative influence on timing parameters of VLSI ICs. Each change of working temperature by 10^0C brings to decreasing of driving power of MOS transistors. So the increase of temperature in IC semiconductor crystal leads to a rapid decline in its reliability [2]. There are several ways of solving temperature distribution issues. One of them is using power distributers and coolers but the using of this method is not always possible. For example in mobile devices using of coolers doesn't possible at all. Other methods are based on thermal reliability increasing methods during IC design. It is important not only semiconductor crystal temperature but also temperature gradient during IC physical design. From this point of view it is productive to decrease temperature differences among different parts of semiconductor crystal. This approach is related to cells placement stage. During placement stage if cells with higher temperature will be surrounded by low temperature cells then whole temperature of the crystal will be distributed as low temperature cells will distribute temperatures from higher cells. From point of view cells placement the problem of reliability of ICs brings to temperature evenly distribution problem on semiconductor crystal.which could be represented by following:

$$\sum_{i=1}^{N} (T_i - T_{mid})^2 \rightarrow \min, \qquad (1)$$

Where T_i is temperature value of each cell and T_{mid} is middle value of all cells temperature.

There are two known categories of algorithms for thermal placement [3]:

- Algorithms which are based on dividing
- Matrix based algorithms

These algorithms are used during primary placement stage. They are based on cells primary placement using their powers consumption values. This paper is about matrix based algorithms. We will discuss two approximation methods.

Problem definition

Cells temperature does not known in the placement stage, but powers are known. So for using (1) we must do some modifications in it. Let consider that powers of IC cells, coefficients of thermal conductivity of individual parts of the IC chip and heat transfer coefficients do not depend from temperature. In that case, based on superposition principle, temperature of any *i* element is defined by mutual thermal influence of all cells [4]:

$$T_i = T_{En} + \sum_{k=1}^{N} P_k F_{ki}, \qquad (2)$$

where T_{En} is the environment temperature, P_k is the power of *k* element, F_{ki} is the thermal coefficient between *i* and *k* elements. From (1) using (2), the even distribution of the temperature on crystal surface will be defined by the following:

$$f_T = \sum_{i=1}^{N} \sum_{\substack{j=1 \\ j \neq i}}^{N} |P_i - P_j| d_{ij} \rightarrow \min \tag{3}$$

where $d_{i,j}$ is the distance between the *i* and *j* positions.

We will use matrix synthesis problem (MSP)[5] definition by making few changes in it.Given integers *w*, *n* and a list of nonnegative real numbers $x_0, x_1, \ldots, x_{n*n-1}$. Purpose is to synthesize *nxn* matrix M out of , $x_1, \ldots, x_{n*n-1}$such that $W_w(M) \rightarrow \min$. Where $W_w(M)$ is sum of cells in each sub matrix (window) of *w x w* size from M matrix.

It is proven that in case of $w \geq 2$ MSP is NP-complete [5].

Approximation algorithms

We will discuss two simple approximation algorithms which will solve defined problem. For simplifying let define n=w*p. $S_{i,j}$ is defined as *w x w* window where i = 0, …, p; j = 0, …, p; and mapped to *p x p* size grid.

Algorithm 1

1. Sort given $x_0, x_1, \ldots, x_{n*n-1}$ numbers.
2. For each $S_{i,j}$ took items x_k where $(i * p + j) * w^2 \leq k \leq (i * k + j + 1) * w^2 - 1$
3. Fill chosen items from left to right, from top to bottom.
4. If there is any $S_{i,j}$which is empty then return to step 2

This algorithm will not give evenly distributed items and their values will increase from top left corner of the matrix to bottom right (Fig.1).

As shown in Fig1 there are areas with very high cell values and areas with lowest cell values. So this is not a good placement method.

Algorithm 2

Define $a_{i,j}(c,d)$ as elements of $S_{i,j}$ sub matrix where c = 0,…,w; d = 0,…,w.

1. Sort given $x_0, x_1, \ldots, x_{n*n-1}$ numbers.
2. For each $S_{i,j}$ took items x_k from beginning of sorted values if $(c*w + p) \leq w^2/2 - 1$ in other case from the end.
3. Fill chosen items from left to right, from top to bottom.
4. If there is any $S_{i,j}$ which is empty then return to step 2

This algorithm will virtually divide our numbers in to two groups and each sub matrix will have half items from each group. In this case we got better distribution.

10	10	16	17	21	22	27	27
15	15	17	18	24	26	27	28
30	34	43	46	49	49	51	53
36	36	47	49	50	51	56	58
58	61	62	64	66	68	69	70
62	62	65	65	68	68	71	73
73	76	77	80	84	85	90	91
76	76	81	82	86	86	92	94

Fig. 1. Matrix generated by Alogrithm1 where n = 8, w = 2, values are random generated.

10	10	14	18	19	25	27	29
100	99	98	97	97	94	93	89
30	33	33	34	34	35	35	35
88	86	83	81	80	80	80	80
36	38	38	41	43	44	45	45
77	72	72	71	68	68	67	67
45	47	47	47	48	48	50	50
67	65	63	57	56	54	52	50

Fig. 2. Matrix generated by Algorithm2 where n = 8, w = 2, x_k values are random generated.

As shown in Fig.2 each sub matrix with size 2 x 2 has half elements from lower part of input values and half from higher value part.
Algorithm2 is better than Algorithm1 as it does have better distribution of items, there is no well-defined direction from where items values start to increase. Also second algorithm gives better values for evenly distribution formula.

Experiments

Program was written to for testing both methods. Matrix size, sub matrix size and item value ranges are passed as in input. With given input program generates two matrixes (one with each algorithm). Also calculate evenly distribution factor using Form.1.
Tests were made by generating ~100 matrixes using input: n = 30; w = 2; items value range is [15 - 65].
As a result in all cases Algorithm2 generate matrix with better distributed cells values. Evenly distribution factor for algorithm2 was near ~4K and for algorithm1 ~2.6M.

Conclusions

As a conclusion we can say that two approximation methods were provided for solving MSP. With experimental results it was proven that given second algorithm is much better for solving MSP as its item are evenly distributed.

References

1. Semiconductor Industry Association, International Technology Roadmap for Semiconductors, 2010, http://public.itrs.net/.
2. ***A. Ajami, K. Banerjee, A. Mehotra, and M. Pedram.*** Analysis of IR-Drop Scaling with Implications for Deep Submicron P/G Network Designs. Fourth International Symposium on Quality Electronic Design. 2003 (ISQED'03). P.35-40.
3. ***V.Sh. Melikyan, A.G. Harutyunyan.*** Physicaldesign methods for microelectronic circuits. PFWM, "Synopsis Armenia" CJSC, 2015(in Armenian).
4. ***G. N.Dulnev*.** The theory of heat and mass transfer, St. Petersburg, ITMO University, 2012 (in Russian).
5. ***C.C.N. Chu, D.F. Wong.*** IEEE Trans on Comp.-Aided Design, **17**, 1166 (1998).

ADVANCED METHOD FOR POWER SWITCH PLANNING IN POWER GATING TECHNIQUES

T.A. Hakhverdyan

Yerevan State University, Yerevan, Armenia, Synopsys Armenia CJSC,
E-mail: tigranha@synopsys.com

Introduction

Wide distribution of electronic devices in the last decades, as well as the rise of computing capabilities of new generation of diverse mobile and household devices sets new requirements for their main components: integrated circuits (IC). One of the significant problems in modern integrated circuits (ICs) is power (dynamic and static) consumption. Nowadays, unacceptably high power consumption of ICs became one of the main bottlenecks of ICs. Various low power design techniques for digital ICs were developed. Low-power ICs design techniques have been around for quite a while and it is hard to make modern big ICs without using one of them [1, 2]. One of the low power techniques types is power gating.

The aim of power gating is to minimize leakage current by turning off supply voltage in a low-power domain with power switches. There are two approaches for power gating: fine grain and coarse grain. In fine grain (Fig.1 (a)) power gating the switch is placed locally inside of each standard cell in the library. Since this switch must supply the worst case current required by the cell, it has to be quite large in order not to impact performance. The area overhead of each cell is significant (of the 2x-4x the size of the original cell) [1]. The key advantage of fine grain power gating is that the timing impact of the IR drop across the switch and the behavior of the clamp are easy to characterize as they are contained within the cell.

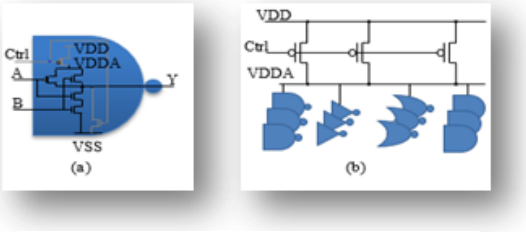

Fig. 1. Power switching fine (a) and coarse (b) grain

In coarse grain power gating (Fig.1 (b)), a block of gates has its power switched by a collection of switch cells. The sizing of a coarse grain switch network is more difficult than a fine grain switch as the exact switching activity of the logic it supplies is not known and can only be estimated. But coarse grain gating designs have significantly are less penalty than fine grain (Table 1).

Coarse grain power gating as the preferred method. The area penalty for fine grain power gating has just not proven worth the savings in design effort [2].

Thus goal of this paper is to research and develop methods for power switch planning in coarse grain power gating designs. As well as new switch transistor cell circuit was creation for increasing efficiency and controllability of power gating method, which provides high current efficiency while allowing control of tradeoff between voltage island wake-up time and rush current.

Proposed power switch cells

Another key issue in modern ICs is power supply noise, since supply voltage variations is extremely large, it may lead to problems such as timing unpredictability, delay variation, or even improper functionality [3]. A common technique for reducing power supply and ground noise and keeping the noise within the noise budget is using on-chip decoupling capacitors (decaps) [4]. In coarse grain

power gating design power is spread through power switches, that is why decap cell is placed close to power switches. In proposed method need place decap cells between virtual and global supply. Analyzing all points, the new cells were created, by merging power switch and decap cells into PSD cell. In Fig.2 illustrated different types of PSD cell, which differ in different parameters such as ESD risk, on chip variation, frequency response, area, and power consumption [5].

Table 1. Proposed and Cross-coupled decap cells

Parameter	Fine grain	Coarse grain
Reduce leakage	10x	50x
Wakeup time	Fast	Slow
Wakeup power	Small	Large
Library requirements	New cell library	New footer or header cell
Sensitive to PVT variation	Large	Small
Can be implemented by usual physical synthesis	Yes	No
IR-drop variations	Large	Small
Chip Area	Large	Small

Proposed power switch cells

Another key issue in modern ICs is power supply noise, since supply voltage variations is extremely large, it may lead to problems such as timing unpredictability, delay variation, or even improper functionality [3]. A common technique for reducing power supply and ground noise and keeping the noise within the noise budget is using on-chip decoupling capacitors (decaps) [4]. In coarse grain power gating design power is spread through power switches, that is why decap cell is placed close to power switches. In proposed method need place decap cells between virtual and global supply. Analyzing all points, the new cells were created, by merging power switch and decap cells into PSD cell. In Fig.2 illustrated different types of PSD cell, which differ in different parameters such as ESD risk, on chip variation, frequency response, area, and power consumption [5].

Modern digital circuits are made by considering switching activity information file, that data was used in proposed power switch planning. Switching activity is essential to measuring power in digital circuits, and it is also important for optimizing digital designs. Power can be static, caused by leakage, or dynamic, caused by switching. Switching activity is crucial because dynamic power is, after all, proportional to the switching activity in the design.

Background for switching activity

Switching activity interchange format (SAIF) is an open standard [6]. SAIF is the measurement of changes of signal values. And it is obtained from digital simulation(s) of the design. It also is an essential part of the power equation and optimization. The quality of the results of power analysis and power optimization is strongly influenced by the quality of the switching activity data. For power analysis, the estimated dynamic power is calculated from the switching activity data. The result is the estimated power consumed by that circuit when used in that way. If this is not representative, then the results will not be representative. Similarly, for power optimization, the resulting power savings will not be as good as they could be. Some power will be wasted. Also must be noted that unknown states in the simulation have a negative impact on the power analysis and optimization processes. Another important consideration is the ability to propagate switching activity through the design. There are situations where the switching activity is incomplete. One example is a complex expression in RTL, where there are nodes that are not named because they are internal to the expression. In power analysis or optimization, the tool will propagate switching activity information from annotated signals through the logic, making calculations as it moves through the logic. In this case, a sequential analysis (one which reaches beyond register boundaries) will produce more accurate results than a simple Boolean approach. Switching activity is a critical element of power analysis and power optimization. For power analysis, switching activity provides a

key piece of the power equation. For optimization, switching activity helps to identify which optimizations are most useful. The quality of the switching activity information has a direct effect on the quality of results [6].

Advanced method for power switch planning

As power switch planning supposed the choosing and placement power switch cells. A new switch transistor cell circuit was created for increasing power supply noise influence and controllability of power gating method (Fig. 2). So during coarse grain power gating design instead of common power switch cells, used proposed power switching cells.

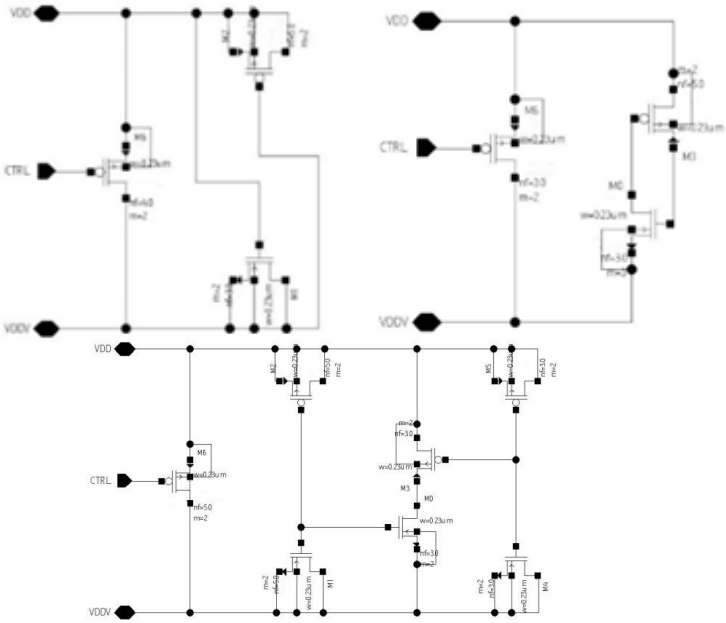

Fig. 2. New power switches + decap cells with different

There is some methodology for power switch placement and each of them can be implemented using proposed power switch cells [7]. But in this article two new methods were proposed for power switch placement considering SAIF data. For both methods were created PSD cells with different capacitance values. First method called pre-std. placement approach and the second method called post-std. placement approach. The place and route flow are based on common flow [8]. Block diagram for both methods are illustrated in Fig. 3.

- Classify each logic gates into placement group in the following way:

$$K_i = T_i / \Sigma T,$$

K_i is the classification coefficient, T_i the maximum value of the timing delay for the timing path, wherein the i-th element includes

- Calculate PSD factor for each group by following way:

$$Fj = Ki*Avg\ (SAIF)*(\Sigma Pj/j),$$

Fi is the PSD factor for corresponding group, K_i the logic gates classification coefficient, SAIF – SAIF coefficient, Pj the coresponding power value for j placemnet group

- Choose PSD cell for each group based on PSD factor (Fj) (Table 2).

- After determination of Fj for each group, the replacement coordinates of power switches are calculated according to the following formula:

$$X = \Sigma(Fj \cdot X_i),\ Y = \Sigma(Fj \cdot Y_i),$$

X_i *and* Y_i- The coordinate for i-th logic cell for current group, X and Y - The replacement coordinate for power switches.

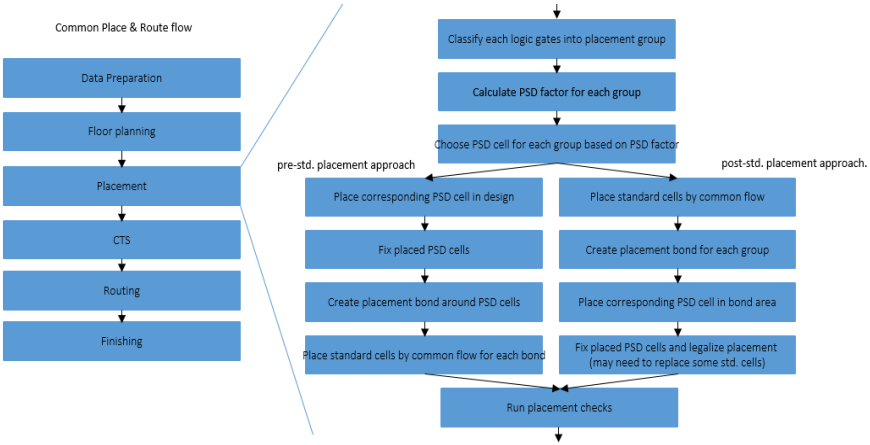

Fig. 3. Pre-std. placement and post-std. placement for power switch placement approaches

Simulation Results

As a simulation result in Fig. 4 is illustrated placement design with proposed two methods. In Fig. 4 (a) is shown post-std. PSD placement (highlighted PSD cells), and with green is showed placement bond for each placement cell group, the picture is zoomed for better illustration. In Fig. 4 (b) is shown pre-std. PSD placement (highlighted PSD cells.

Table 2. PSD cell and PSD factor mapping

PSD cell	Fj	PSD cell	Fj	PSD cell	Fj	PSD cell	Fj
PSDCA_X2	0.0-~0.2	PSDCAP_X4	0.5-~0.7	PSDCAP _X8	1.0-~1.3	PSDCAP _X16	1.8-~2.5
PSDCAP _X3	0.2-~0.5	PSDCAP_X6	0.8-~1.0	PSDCAP _X12	1.3-~1.8	PSDCAP _X64	2.5-~5.0

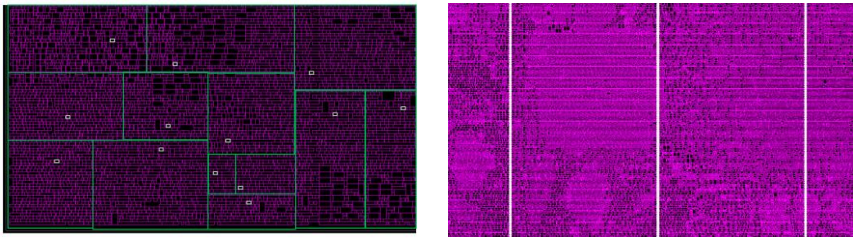

(a) (b)

Fig. 4. Post-std. and pre-std. power switch placement approaches

Conclusions

A new cell is introduced for reducing power supply noise affection on course grain power gating technique. The cell was created by merging power switch and decaps cells into PSD cell. PSD cells were designed with different driver factors. SAIF data was used for proposed post-std. and pre-std. power switch placement approaches. In pre-std. method timing results is worst compare with post-std. approach, as standard cells should place in limited area. Standard cell placement configuration is less than in post-std. method, as during post-std. method first placed usual standard cells with timing driven approach, then PSD cell. In post-std. method power consumption is less due to minimum count of PSD cells and temperature distribution is better as for each bound PSD cells coordinates are decided especial. Compare with pre-std. method post-std. require much running time and will take long time for design.

References

1. ***M. Keting, D. Flynn, R. Aitken, A. Gibbons, K.Shi*****.** Low Power Methodology Manual For System-on-Chip Design, Synopsys, Inc. & ARM Limited. 2007, p. 297.
2. ***V. Melikyan, T. Hakhverdyan, A. Gevorgyan, D. Babayan S.Manukyan*****.** Low Power OpenRISC Processor with Power Gating, Multi-VTH and Multi-Voltage Techniques, East West Design and Test Symposium (EWDTS), 2016, pp.33-36.
3. ***J.-H. Liu, J.-K. Zeng, A.-S. Hong.*** Process-Variation Statistical Modeling for VLSI Timing Analysis, 9th International Symposium on Quality Electronic Design, Washington. p. 730-733, 2008.
4. ***V. Melikyan, K. Safaryan, A. Avetisyan, T. Hakhverdyan*****.** On-Chip Decoupling Capacitor Optimization Technique, Electronics and Nanotechnology Elnano (ELNANO), pp. 1-4, 2017.
5. ***X. Meng, K. Arabi.*** IEEE Transactions On Very Large Scale Integration (VLSI) Systems, **16**, 1 (2008).
6. ***S.A. Lozhkin. S. Shupletsov.*** Switching activity of Boolean circuits and synthesis of Boolean circuits with asymptotically optimal complexity and linear switching activity, October 2015, **36**, Issue 4, pp 450–460.
7. ***T. Hakhverdyan.*** Power Switch Planning Technique for Power Gatin.g Designs, Information Systems, Electronics And Scientific Instrumentation, pp. 1-6. 2017.
8. ***R. Goldman, K. Bartleson, T. Wood, A.Watson, V. Melikyan, E. Babayan, T. Hakhverdyan.*** IC Design Course Based on the Synopsys DesignWare ARC 600 Processor Core and 32/28nm Educational Design Kit, Interdisciplinary Engineering Design Education Conference (IEDEC). pp.66-69, 2014.

CONTENTS

PHYSICAL PHENOMENA IN MICRO- & NANOSTRUCTURES

GAS, BIO- & CHEMICAL SENSORS

MATERIAL SCIENCE AND ENGINEERING

DESIGN AND MODELING OF INTEGRATED CIRCUITS

ԿԻՍԱՀԱՂՈՐԴՉԱՅԻՆ ՄԻԿՐՈ- ԵՎ ՆԱՆՈԷԼԵԿՏՐՈՆԻԿԱ
ՏԱՍՆՄԵԿԵՐՈՐԴ ՄԻՋԱԶԳԱՅԻՆ ԳԻՏԱԺՈՂՈՎԻ ՆՅՈՒԹԵՐ

ԵՐԵՎԱՆ, 23-25 ՀՈՒՆԻՍ

Տպագրվել է Գևորգ - Հրայր ՍՊԸ-ում
Ք. Երևան, Գր. Լուսավորչի 6

Տպաքանակ՝ 70:

ԵՊՀ հրատարակչություն
ք. Երևան, 0025, Ալ. Մանուկյան 1
www.publishing.ysu.am